UNDERSTANDING AND PREDICTING CHANGES IN PRECIPITATION AND WATER AVAILABILITY UNDER THE INFLUENCE OF LARGE-SCALE CIRCULATION PATTERNS: RIO GRANDE AND TEXAS

A Dissertation

by

CHUNDUN PRAKASH KHEDUN

Submitted to the Office of Graduate Studies of
Texas A&M University
in partial fulfillment of the requirements for the degree of

DOCTOR OF PHILOSOPHY

Approved by:

Co-Chairs of Committee,	Vijay P Singh
	John R Giardino
Committee Members,	Anthony T Cahill
	Gerald R North
Intercollegiate Faculty Chair,	Ronald A Kaiser

December 2012

Major Subject: Water Management and Hydrological Science

ABSTRACT

Large-scale circulation patterns have a significant modulating influence on local hydro-meteorological variables, and consequently on water availability. An understanding of the influence of these patterns on the hydrological cycle, and the ability to timely predict their impacts, is crucial for water resources planning and management. This dissertation focusses on the influence of two major large-scale circulation patterns, the El Niño Southern Oscillation (ENSO) and the Pacific Decadal Oscillation (PDO), on the Rio Grande basin and the state of Texas, US. Both study areas are subject to a varying climate, and are extremely vulnerable to droughts, which can have devastating socio-economic impacts.

The strength and spatial correlation structure of the climate indices on gauged precipitation was first established. Precipitation is not linearly related to water availability; therefore a land surface model (LSM), with land use land cover constant, was used to create naturalized flow, as it incorporates all necessary hydro-meteorological factors. As not all ENSO events are created equal, the influence of individual El Niño and La Niña events, classified using four different metrics, on water availability was examined. A general increase (decrease) in runoff during El Niños (La Niñas) was noted, but some individual events actually caused a decrease (increase) in water availability. Long duration El Niños have more influence on water availability than short duration high intensity events. Positive PDO enhances the effect of El Niño, and dampens the negative effect of La Niña, but when it is in its neutral or transition phase, La Niña tends to dominate climatic conditions and reduce water availability.

LSM derived runoffs were converted into 3-month Standardized Runoff Indices (SRI 3) from which water deficit durations and severities were extracted. Conditional probability models of duration and severity were developed and compared with that based on observed precipitations. It was found that model derived information can be used in regions having limited ground observation data, or can be used in tandem with observation driven conditional probabilities for more efficient water resources planning and management.

Finally a multidimensional model was developed, using copulas, to predict precipitation based on the phase of ENSO and PDO. A bivariate model, with ENSO and precipitation, was compared to a trivariate model, which incorporates PDO, and it was found that information on the state of PDO is important for efficient precipitation predictions.

To Mum, Dad, and Hema

ACKNOWLEDGMENTS

Several individuals, in one way or another, contributed and extended their valuable assistance, and made this dissertation possible.

First and foremost, I express my sincere gratitude to my co-advisors for their valuable guidance and advice. Dr. Vijay P Singh gave me the latitude to explore my research interests, but was always present to help me climb the walls I encountered along the way. Dr. John R Giardino introduced me to the world of geomorphology, and helped me put my ideas in a larger perspective. Thanks are due to Dr. Anthony T Cahill and Dr. Gerald R North for their time, guidance, and generous advice throughout my studies.

The most important person, that really made this research possible, is Dr. Ronald A Kaiser, the Chair of the water program, who financially supported me through the years. Every semester, when I faced the challenge of finding enough funds for tuition and fees, Dr. Kaiser stepped in, and helped me through. Dr. Kaiser is a unique person; he is not a man who works for an award. He likes to be around eager minds, to help them achieve excellence in all they do. He has made it his mission to educate the next generation of water professionals; professionals who are going to solve water problems around the world. It has been an honor and a privilege to be his research and teaching assistant.

Late Dr. Valeen “Val” Silvy, the first WMHS program coordinator, was an important pillar of the water program and a generous soul. Every day, she welcomed me with a smile, and was always willing to listen to me. Val, thank you!

Thank you to the Fulbright Program, the flagship international educational exchange program sponsored by the US government, for giving me the opportunity to study for my doctorate at Texas A&M University. Thank you to the donors of the various scholarships and grants I received during my stay, and to the Office of Graduate Studies for awarding me the Dissertation Fellowship to help me complete my research.

Throughout the years, I have had the opportunity to meet new people and build new friendships; to y'all, thanks for making the daily grind a bit more tolerable. Thanks to Ashok for all the discussions over coffee. A special thanks to Dr. Rosario Sanchez Flores, the current WMHS program coordinator, for her help in getting data from Mexico and for securing funding from the Comisión Estatal de Aguas y Saneamiento del Estado de Coahuila, Mexico, which supported part of this research. Financial support from the USGS, Grant No. 2011TX395B, is also acknowledged. Thanks are also due to the Goddard Earth Sciences and Technology Center for supporting my stay at NASA Goddard Space Flight Center, Greenbelt, Md. I am grateful to the scientists in the Hydrological Sciences Branch, especially Dr. John D Bolten and Hiroko K Beaudoing, for their help and advice.

Thank you to my brother Vinay and his wife, my grandfather, uncles and aunts, Dient and all my cousins, for always being there for me.

A loving thought to my wonderful parents; thank you for your dedication and unwavering support. Mum, I love you and I miss you!

Heartfelt thanks to my loving wife Hema, for her unyielding support as I toiled through my research.

NOMENCLATURE

AAR	Area-averaged Runoff
AIC	Akaike Information Criteria
ALMA	Assistance for Land Modeling Activities
BIC	Bayesian Information Criteria
CMORPH	CPC Morphing Technique
COADS	Comprehensive Ocean-Atmosphere Data Set
CONAGUA	Comisión Nacional del Agua
CONUS	Continental United States
COOP	Cooperative Observer Program
CPC	Climate Prediction Center
EMI	El Niño Modoki
ENSO	El Niño Southern Oscillation
EOS	Earth Observing System
ESMF	Earth System Modeling Framework
FAO	Food and Agriculture Organization
FNEP	Full Network Estimated Precipitation
GCM	General Circulation Model

GFS	Global Forecast System
GLDAS	Global Land Data Assimilation System
GSFC	Goddard Space Flight Center
GSWP	Global Soil Wetness Project
IBWC	International Boundary and Water Commission
IRI	International Research Institute
JISAO	Joint Institute for the Study of the Atmosphere and Ocean
K-S	Kolmogorov-Smirnov
LIS	Land Information System
LSM	Land Surface Model
MEI	Multi-ENSO Index
NAM	North American monsoon
NASA	National Aeronautics and Space Administration
NCDC	National Climatic Data Center
NCEP	National Centers for Environmental Prediction
NLDAS	North American Land Data Assimilation System
NLDAS-2	North American Land Data Assimilation System – Phase 2
NOAA	National Oceanic and Atmospheric Administration
NSOI	Negative Southern Oscillation Index

NWS	National Weather Service
PDO	Pacific Decadal Oscillation
PDSI	Palmer Drought Severity Index
PILSPS	Project for Intercomparison of Land-surface Parameterization Schemes
PRISM	Parameter-elevation Regressions on Independent Slopes Model
RG	Rio Grande/Río Bravo del Norte
RMSD	Root Mean Square Deviation
SMN	Servicio Meteorológico Nacional
SOI	Southern Oscillation Index
SPI	Standardized Precipitation Index
SRI	Standardized Runoff Index
SST	Sea Surface Temperature
SSTA	Sea Surface Temperature Anomaly
UMD	University of Maryland
US	United States
USHCN	United States Historical Climatology Network
VIC	Variable Infiltration Capacity

TABLE OF CONTENTS

Page

ABSTRACT ii

DEDICATION iv

ACKNOWLEDGMENTS v

NOMENCLATURE vii

TABLE OF CONTENTS x

LIST OF FIGURES xiii

LIST OF TABLES xvii

1 INTRODUCTION 1

1.1 Problem Statement 1
1.2 Objectives 3
1.3 Structure of Dissertation 5

2 INFLUENCE OF LARGE-SCALE CIRCULATION PATTERNS ON PRECIPITATION 7

2.1 Overview 7
2.2 Introduction 7
2.3 Large-scale Circulation Patterns 8
2.3.1 El Niño Southern Oscillation 8
2.3.2 El Niño Modoki 9
2.3.3 Pacific Decadal Oscillation 11
2.4 Methodology 13
2.5 Study Area: Rio Grande/Río Bravo del Norte 13
2.6 Data 16
2.6.1 Precipitation 16
2.6.2 Climate Indices 18
2.7 Results and Discussion 21
2.7.1 Hydroclimatology of the Basin 21
2.7.2 ENSO Events 27
2.7.3 Climate Teleconnection and Precipitation 34
2.8 Conclusions 40

3 UNDERSTANDING CHANGES IN WATER AVAILABILITY UNDER THE INFLUENCE OF LARGE-SCALE CIRCULATION PATTERNS USING A LAND SURFACE MODEL 41

3.1 Overview 41
3.2 Introduction 42
3.3 Land Surface Modeling 43
3.3.1 Noah LSM 44
3.3.2 Land Information System 47
3.3.3 Forcing Data and Parameters for LSM 48
3.4 Results and Discussions 50
3.4.1 Runoff and Water Availability 50
3.4.2 Effects of Large-scale Circulation Patterns on Water Availability 60
3.5 Conclusions 67

4 WATER DEFICIT DURATION AND SEVERITY ANALYSIS BASED ON RUNOFF DERIVED FROM THE NOAH LAND SURFACE MODEL 70

4.1 Overview 70
4.2 Introduction 71
4.3 Data and Methdology 72
4.3.1 Runoff Modeling 72
4.3.2 Standardized Runoff Index 72
4.3.3 Univariate Water Deficit Duration and Severity Model 74
4.3.4 Copulas 74
4.3.5 Conditional Distribution for Drought Duration and Severity 77
4.3.6 Return Periods 77
4.4 Results and Discussion 78
4.4.1 Water Deficit Duration and Severity 78
4.4.2 Copula Parameter Estimation and Selection 86
4.4.3 Joint CDF of Duration and Severity 89
4.4.4 Conditional Probability of Water Deficit Duration and Severity 90
4.4.5 Return Periods 98
4.5 Conclusions 101

5 PROBABILISTIC PREDICTION OF PRECIPITATION USING LARGE-SCALE CIRCULATION INDICES AS PRECURSORS – EFFECT OF INTERDECADAL MODULATION 103

5.1 Overview 103
5.2 Introduction 104
5.3 Study Area: Texas 105
5.3.1 Climate of Texas 105
5.4 Data 111
5.4.1 Precipitation 111
5.4.2 Climate Indices 111

5.5 Methodology 115
5.5.1 Marginal Distribution Selection 115
5.5.2 Copula Selection 116
5.6 Results and Discussion 120
5.6.1 Temporal Changes in Precipitation and Major Events 120
5.6.2 Climate Teleconnection and Precipitation 122
5.6.3 Marginal Selection 130
5.6.4 Copula Selection 137
5.6.5 Simulation 148
5.6.6 Prediction 159
5.7 Conclusions 161

6 CONCLUSIONS 163

REFERENCES 166

LIST OF FIGURES

Page

Figure 1. The Rio Grande/Río Bravo del Norte basin. 15

Figure 2. Location of precipitation stations used in this study. 17

Figure 3. Time series of PDO, Niño 3.4, MEI, and EMI indices. The PDO, MEI, and EMI series are overlain with a running, centered 13-month average to highlight yearly variations. The normalized monthly Niño 3.4 index series is overlain with a centered 3-month running mean and ± 0.5°C thresholds (see section 2.7.2.1)..... 20

Figure 4. (a) Isohyet of annual mean precipitation and coefficient of variation of monthly precipitation across the Rio Grande basin, and (b) mean monthly precipitation for each region. 22

Figure 5. Smoothed series of average monthly gauged precipitation (mm/month) for each region. The broken horizontal line is the long-term average. The scales of the ordinates are arbitrary to illustrate variability. The top panel shows the phases of PDO and ENSO. 25

Figure 6. Time series of standardized anomaly for stations in the US, Mexico, and Río Conchos (Stations are latitudinally arranged with numbers corresponding to Figure 2). 26

Figure 7. Comparison of major El Niño and La Niña events between 1979 and 2008 (transparent gray band shows ±0.5°C neutral range). 32

Figure 8. Plots of seasonal correlation coefficients between PDO and precipitation anomaly. Inset gives the *p*-values for the regression coefficients. 36

Figure 9. Plots of seasonal correlation coefficients between (a) Niño 3.4, (b) MEI, and (c) EMI and precipitation anomaly. Inset gives the *p*-values for the regression coefficients. 37

Figure 10. A snapshot of the model run showing daily precipitation and runoff within the catchment. 51

Figure 11. Scatter plot of area-averaged monthly NLDAS-2 precipitation and observed precipitation for the (a) Upper-Middle RG, (b) Río Conchos, and (c) Lower RG region (Mexican stations only). 53

Figure 12. (a) Modeled, naturalized, and measured streamflow in the Río Conchos sub-basin, (b) sliding-window correlation. 56

Figure 13. Continuous wavelet power spectrum of (a) climate indices and (b) AAR for each region. Period is in days. The thick black contours designate the 5% significance level against red noise and the thin black line demarcate the cone of influence beyond which, shown in a lighter shade, the image may be distorted since the data is not padded at the edges. 58

Figure 14. Lag correlation for each section of the basin. 62

Figure 15. Percentage change in water availability during (a) El Niño and (b) La Niña events. 64

Figure 16. AAR anomaly overlain with SRI(3) for (a) the whole Rio Grande (RG) Basin and (b) each region. 79

Figure 17. Scatter plot of severity versus duration for the whole basin and for each region (inset shows an exceptional drought event in the Río Conchos). 84

Figure 18. Observed duration with exponential fit and observed severity with gamma fit for Lower-Middle RG. 85

Figure 19. Contours of joint probabilities of severity versus duration for Lower-Middle RG. 90

Figure 20. Conditional distribution of water deficit severity given that duration exceeds d'month(s). 91

Figure 21. Conditional distribution of water duration given that severity exceeds s'. 92

Figure 22. Scatter plot of monthly area-averaged monthly NLDAS-2 precipitation and averaged observed precipitation for Lower-Middle RG. 96

Figure 23. Comparison of conditional probability of (a) severity given duration d' and (b) duration given severity s' for Noah LSM runoff (solid line) and averaged observed precipitation (dashed line) in Lower-Middle RG. 97

Figure 24. Conditional return period of water deficit duration given that severity exceeds s' for RG. 100

Figure 25. Conditional return period of water deficit severity given that duration exceeds d' months for RG. 100

Figure 26. Climate divisions and climate regions of Texas (adapted from [*Larkin and Bomar*, 1983]). 106

Figure 27. Violin plots of monthly precipitation in each climate division in Texas. Thick black line and blue dot shows the 25^{th} and 75^{th} percentile range and median respectively, and thin black line shows the 5^{th} and 95^{th} percentile range. 108

Figure 28. Monthly mean precipitation for each month (in mm) in each climate division based on data for 1900 to 2011. Solid black line represents the mean monthly precipitation for the whole state. 110

Figure 29. Time series of monthly precipitation for each climate division. The time series has been smoothed with a 13-month centered running mean filter. The dotted line represents the means for the dataset (mm). The time series were not padded at the ends. 112

Figure 30. Time series of monthly NSOI and PDO indices. The NSOI series is overlain with a 5-month centered running mean filter and ± 0.5 and ± 1 thresholds. The PDO series is smoothed with 10 passes of a 13-month centered running mean filter. 114

Figure 31. Boxplots of cold season ($October^0$ – $March^+$) average precipitation in each climate division in Texas. 123

Figure 32. Plots of correlation coefficients between $June^0$ – $November^0$ average NSOI and cold season ($October^0$ – $March^+$) average precipitation anomalies and cold season average PDO index and cold season average precipitation anomalies. 125

Figure 33. Scatter plot of cold season ($October^0$ – $March^+$) average precipitation anomalies versus (a) $June^0$ – $November^0$ average NSOI and (b) cold season average PDO indices for climate division 8. Positive (negative) anomalies during El Niño (La Niña) events are shown in blue (red). 127

Figure 34. Histograms and Q-Q plots of $June^0$ – $November^0$ average NSOI and $October^0$ – $March^+$ average PDO indices. NSOI follows GEV and PDO follows Weibull. Negative (positive) values are show in blue (red). 131

Figure 35. (a) Histogram of cold season ($October^0$ – $March^+$) average precipitation anomaly and (b) plot of selected marginal distribution, for each climate division. 134

Figure 36. Dependence between $June^0$ – $November^0$ average NSOI and cold season average precipitation anomaly for climate division 8 illustrated through (a) Kendall's plot and (b, c, and d) chi-plots. 138

Figure 37. Comparison of observed data with 1,000 random samples generated from the Gaussian and Clayton copula (solid light gray dots). Observed positive

(negative) anomalies during El Niño (La Niña) events are shown in blue (red) and other events are shown in solid black dots. 142

Figure 38. Boxplots of observed and simulated cold season precipitation anomalies for different NSOI ranges for climate divisions 5, 7, and 8. Boxplot with light gray background is for complete NSOI range. 149

Figure 39. Boxplots of observed and simulated cold season precipitation anomalies for different NSOI and PDO ranges for climate divisions 5, 7, and 8. Boxplot with light gray background is for complete NSOI and PDO ranges while light blue (red) is for different NSOI ranges and negative (positive) PDO. 154

Figure 40. Scatter plot of predicted versus observed predicted cold season average rainfall anomaly for (a) NSOI and precipitation anomaly model and (b) NSOI, PDO, and precipitation anomaly model. 160

LIST OF TABLES

Page

Table 1. El Niño and La Niña events between 1979-2008 following NOAA's definition. Braces indicated coupled events. 29

Table 2. The three strongest ENSO events since 1979 based on different ranking criteria. 33

Table 3. Lag correlation of Niño 3.4 index with Noah runoff for the whole of the basin. 61

Table 4. PDO phase for major ENSO events. 63

Table 5. Statistics for AAR and SRI(3) for each region and the whole basin. 82

Table 6. Parameters for exponential and gamma distribution fitted to observed duration and severity respectively. 86

Table 7. Probability function, parameter space, generating function, and relationship of non-parametric dependence measure with association parameter for the copulas considered in this study. 87

Table 8. Water deficit durations (months) for different return periods. 99

Table 9. Water deficit severities for different return periods. 99

Table 10. Number and percentage of time the June^{0} – November^{0} average NSOI and cold season (October^{0} – March^{+}) average PDO index are in different phases. 128

Table 11. Amount (mm) and percentage change (*in italics*) in cold season (October^{0} – March^{+}) average precipitation for different phases of June^{0} – November^{0} average NSOI and cold season average PDO index. 129

Table 12. Marginal distribution, parameters, chi-square statistic, and *p*-value for cold season (October^{0} – March^{+}) average precipitation anomaly for each climate division. 132

Table 13. Statistics of cold season (October^{0} – March^{+}) average precipitation anomaly for each climate division. 136

Table 14. Probability function, generating function, parameter space, lower and upper tail dependence, and relationship of non-parametric dependence measure

with association parameter for bivariate form of the ten copulas used in this study..... 139

Table 15. Parameter(s), Kendall's tau, AIC, BIC, and Cramér-von Mises and Kolmogorov-Smirnov goodness-of-fit statistics, along with their respective *p*-values, for each copula for climate division 8..... 143

Table 16. Parameter(s) and Cramér-von Mises and Kolmogorov-Smirnov goodness-of-fit statistics, along with their respective *p*-values, for the copula selected for modeling the dependence between June^0 – November^0 average NSOI and cold season average precipitation anomaly for each climate division..... 144

Table 17. Parameter and Cramér-von Mises goodness-of-fit statistic along with its *p*-value, for the Clayton, Frank, and Gaussian copulas modeling the dependence between June^0 – November^0 average NSOI, cold season average PDO, and cold season average precipitation anomaly for climate divisions 5, 7, and 8. 147

Table 18. Statistics of observed and simulated cold season precipitation anomalies for different NSOI ranges for climate divisions 5, 7, and 8. 151

Table 19. Statistics of observed and simulated cold season precipitation anomalies for different NSOI and PDO ranges for climate divisions 5, 7, and 8. 156

1 INTRODUCTION

Climate variability is an inherent characteristic of the climate related to temporal changes about the long term mean of meteorological variables. The time period can be in terms of months, years, or even decades. Such variations have a noticeable effect on the hydrological cycle and hence on water availability. If not anticipated and planned accordingly, an increase in short duration high intensity precipitation may cause devastating floods, and an acute shortage of rainfall may lead to blistering droughts. Different parts of the world are often subjected to a combination of more than one large-scale circulation patterns. An understanding of the influence of these phenomena on the hydrological cycle can help in precipitation prediction and efficient short and long term water resources planning and management.

1.1 PROBLEM STATEMENT

Several studies have investigated the influence of climate variability using either a single index or a combination of indices on precipitation [e.g., *McCabe and Dettinger*, 1999; *Piechota and Dracup*, 1996; *Ropelewski and Halpert*, 1986; *Woolhiser et al.*, 1993], streamflow [e.g., *Barlow et al.*, 2001; *Kahya and Dracup*, 1993; *Redmond and Koch*, 1991], and drought [e.g., *Özger et al.*, 2009; *Schoennagel et al.*, 2005] in the United States (US). In the southern US, the Pacific Decadal Oscillation (PDO) and the El Niño Southern Oscillation (ENSO) have been found to be the two most dominant climate teleconnections influencing regional hydrological conditions.

ENSO is a coupled ocean-atmosphere phenomenon related to sea surface temperature (SST) anomalies (SSTA) in the central and eastern equatorial Pacific and associated sea-level pressure difference known as the Southern Oscillation [*Rasmusson and Carpenter*, 1982]. It has a recurrence pattern of 3 to 6 years and every event normally lasts for about a year. El Niño events, the positive or warm phase of ENSO, are often, but not always, followed by La Niña events, also referred to as the negative or cold phase of ENSO. More recently, a new type of El Niño, occurring more frequently, with inter-annual variability, has been observed [*Ashok*

et al., 2007]. It has been named El Niño Modoki (Japanese for "similar but different"). It occurs with a shift in the warming center from the eastern equatorial Pacific, which is the case with regular El Niño, to central equatorial Pacific, and both the eastern and western regions are flanked by anomalously cool temperatures, thus resulting in an SST gradient that generates a two-cell Walker Circulation in the troposphere with a wet region over the central Pacific. When coupled with other ongoing atmospheric disturbances, a dry rim arises around the wet central tropical Pacific. Given the similarities between canonical ENSO and this new occurrence, it is easy to confuse between their impacts. Partial correlation and regression analyses suggest that they are distinct phenomena in both space and time and do not appear as an evolving phase of one or the other [*Weng et al.*, 2007].

PDO is a long-lived El Niño-like pattern of Pacific climate variability with a cycle of about 20 to 30 years [*Mantua and Hare*, 2002]. PDO influences the hydrological cycle in the same way as ENSO, but with more pronounced influence in the extra tropics and secondary influence in the tropics. The similarities in the signature between ENSO and PDO have led to the hypothesis that the two teleconnections may be related, or PDO may be forced by ENSO [*Zhang et al.*, 1997]. Statistical analysis by *Newman et al.* [2003] showed that PDO is dependent on ENSO on all timescales. When the PDO is in its positive or warm phase, above normal SST is observed along the west coast of North America and below normal SST along the central and western North Pacific around 45°N. The Aleutian low strengthens and winter precipitation increases in the southern US [*Mantua et al.*, 1997].

Recently *Kurtzman and Scanlon* [2007] examined the impacts of ENSO and PDO on winter precipitation in 165 climate divisions in southern and central US and found a significant increase (decrease) with respect to El Niño (La Niña). The correlation with PDO was weaker, but when both indices were combined, it was noted that La Niñas occurring during the cold phases of PDO exhibited a strong influence in central US and El Niños occurring during the warm phases of PDO dominated southwest and southeast US. *Redmond and Koch* [1991] noted that if events in the Pacific Ocean are causally related to remote meteorological variables, it would be separated by a time lag. They found statistically significant correlations with lags ranging between 0 to 6 months between the Southern Oscillation Index (SOI) and

precipitation in the western US. *Kumar and Hoerling* [2003] found that the maximum correlation between observed zonal mean tropical 200-mb heights and SST in the Pacific occurs with a lag of 1 to 3 months and this results in a lag of one season between rainfall in the tropical Pacific and Niño 3.4 SSTA. The robustness of these results was confirmed using an atmospheric general circulation model (GCM).

Climate change is expected to influence the temporal and spatial variability of climate teleconnections but there still remains considerable uncertainty as to how exactly anthropogenic forcings will affect the climate system [*Karl and Trenberth*, 2003]. The effect of global warming on ENSO has received considerable attention, unlike other climate teleconnections. In their analysis on the change in global temperature over the past century, *Hansen et al.* [2006] showed that the warming in the Western Equatorial Pacific was larger than in the Eastern Equatorial Pacific, increasing the West-East temperature gradient, hence leading to stronger El Niños, like those in 1983 and 1998.

While this information on the degree of association between hydrologic variables and climate patterns is valuable, it is only of qualitative nature and its use in water management is limited. Water planning and management is driven by demand, priority, and availability. Demand is influenced by demographic and economic changes, while priority is an institutional variable defined by legal, social, and economic constraints. Availability, on the other hand, is a natural variable, subjected to the whims of climate.

1.2 OBJECTIVES

The main goal of this research is to extend the findings on the influence on ENSO and PDO on hydrometeorological variables into applications for short and long term water resources planning and management. The tasks to be undertaken are:

(i) Assess the influence of ENSO and PDO on precipitation. Two canonical ENSO indices (Niño 3.4 and the Multi-ENSO index (MEI)) are compared to those of the El Niño Modoki index (EMI) to determine which index shows maximum correlation and is best suited for water management.

(ii) Generate runoff using a land surface model for use as a proxy for water availability, given that gauged streamflow in highly engineered basins is impaired by land use land cover and other changes.

(iii) Compare different ENSO events based on their recorded durations, maximum (or minimum) SSTA, and intensities and assess the influence of individual events on water availability. Further, quantify the changes in water availability under the influence of ENSO and PDO.

(iv) Develop joint probabilities of water deficit duration and severity, conditional probability distribution charts of severity given a threshold duration, and of duration given a threshold drought severity, and conditional return periods of severity and duration.

(v) Develop a probabilistic framework for predicting precipitation using ENSO and PDO indices as precursors.

Two study areas are chosen for this research: the Rio Grande/Río Bravo del Norte (RG) watershed and the state of Texas, US. The reasons directing the choice of these two areas are given below.

RG is a transboundary basin shared between three states in the US and straddles US and Mexico, two countries very dissimilar economically. It is a vital source of water for the region, but is already in a state of absolute water scarcity, with less than 500 m^3/person/day; the only transboundary basin in this category [*Wolf*, 2002]. This region is also extremely vulnerable to droughts; records show that it suffers from both short-term and long-term droughts [*Quiring and Goodrich*, 2008]. Subjected to a burgeoning population, which will further increase the stress on water allocation, and climate change, which will likely result in a decrease in precipitation [*IPCC*, 2007], the potential for conflicts cannot be overlooked. It is therefore imperative to understand the mechanisms driving water availability and quantify any change for long-term sustainable water planning and management.

Texas is the second largest, with a total land and inland water area of 691,146 km^2, and the second most populous state (25.67 million in 2012), in the United States. Of the 50 states, it registered the largest population growth between 2000 and 2010, and the population is further

projected to increase by 82%, to 43.6 million by 2060. Lack of water, however, can lead to serious social, economic, and environmental consequences across the state. The drought of the 1950s, once considered the drought of record, caused an estimated annual loss of $3.5 billion (adjusted to 2008 dollars) [*Texas Water Development Board*, 2012]. Recently, in 2011, the state suffered the worst single year drought and harshest drought in recorded history. Economic losses to the agricultural sector alone have been evaluated at $7.62 billion, making it the costliest drought on record [*Fannin*, 2012].

1.3 STRUCTURE OF DISSERTATION

The objectives enumerated above are discussed in four sections. In section 2 a brief review of the influence of ENSO and PDO is given. An analysis of how ENSO and PDO influence precipitation in each of the four seasons, in RG, is presented. A comparison of major ENSO events (both El Niño and La Niña) using different metrics is also presented.

Section 3 gives a description of how the most appropriate LSM for modeling runoff in RG was chosen. The forcing and other parameters for running Noah, the chosen LSM is given. The procedure adopted in validating precipitation, the most important input, and runoff for the basin is presented. The influence of large-scale circulation on the temporal patterns of runoff in different parts of the basin is discussed. Changes in water availability are quantified for different ENSO events and compared along with lags between the events and response in runoff. The combined influence of ENSO and PDO is also explored.

In section 4, using runoff derived from Noah and copulas joint distribution functions of water deficit duration and severity are developed. Conditional probability models of duration and severity are presented and compared for two regions – one experiencing alpine climate at the headwaters and one in the semi-arid portion of the basin. Conditional probabilities derived from model runoff are also compared with that based on observed precipitation. Finally, univariate and conditional return periods based on duration and severity are computed for the regions and their significance in long-term water resources planning is discussed.

Section 5 builds on the findings from the previous sections and explores the effect of interdecadal modulation on precipitation in the southern US to predict precipitation using ENSO and PDO as precursors. The state of Texas is chosen as the study region for this analysis. Three different climate divisions, the most arid, the wettest, and one in between, are chosen for evaluating the proposed methodology.

In section 6 the main conclusions drawn from this research are listed along with future directions.

2 INFLUENCE OF LARGE-SCALE CIRCULATION PATTERNS ON PRECIPITATION*

2.1 OVERVIEW

It can be argued that precipitation is the most important hydrological variable when it comes to water management. Local precipitation conditions have been found to be teleconnected to large-scale circulation patterns. An assessment of the relationship and degree of correlation between dominant large-scale climate patterns is therefore important for water management at all timescales. In this study, the correlation between El Niño Southern Oscillation (ENSO) and Pacific Decadal Oscillation (PDO) on precipitation in the Rio Grande basin is examined. Three ENSO indices (Niño 3.4, MEI, and EMI) and one PDO index are considered. Except for the headwaters region, a positive correlation between the climate indices and gauged precipitation was found. However, the correlation was not consistent across the seasons. For PDO, the highest correlations were in winter and spring. In winter higher correlation was observed in the lower part of the basin, and the correlation pattern shifted in spring, with the northern part of the basin exhibiting higher correlation. For ENSO, the correlation patterns of all three indices considered were similar, but Niño 3.4 and MEI exhibited stronger correlations. Again, correlations for winter and spring were higher than that for summer and fall. Finally, given that ENSO events are not created equal, a comparison of major El Niño and La Niña events is presented, using different metrics (duration, SSTA, and intensity).

2.2 INTRODUCTION

Large-scale circulation patterns have a significant influence on local atmospheric and hydrologic variables, and consequently on water availability. The southern United States (US)

* Part of this section is reprinted with permission from "Understanding changes in water availability in the Rio Grande/Río Bravo del Norte basin under the influence of large-scale circulation indices using the Noah land surface model" by C. P. Khedun, A. K. Mishra, J. D. Bolten, H. K. Beaudoing, R. A. Kaiser, J. R. Giardino, and V. P. Singh, 2012, *J. Geophys. Res.*, 117(D5), D05104, doi: 10.1029/2011jd016590, Copyright 2012 American Geophysical Union.

is subject to two major large-scale circulation patterns: the El Niño Southern Oscillation (ENSO) and Pacific Decadal Oscillation (PDO).

In this section the correlation of the ENSO and PDO with gauged precipitation in RG is determined. Two canonical ENSO indices (Niño 3.4 and the Multi-ENSO index (MEI)) are compared to that of the El Niño Modoki index (EMI) to determine which index shows maximum correlation and is best suited for water management within the basin.

Further, El Niño (La Niña) events are not similar and coincide with different phases of PDO (positive, negative, or transitioning from one phase to another). Individual El Niño and La Niña events are compared and ranked based on their recorded durations, maximum (or minimum) SSTA, and intensities – a new metric that we propose in this study.

2.3 LARGE-SCALE CIRCULATION PATTERNS

2.3.1 EL NIÑO SOUTHERN OSCILLATION

ENSO is a coupled ocean-atmosphere phenomenon related to sea surface temperature (SST) anomalies in the central and eastern equatorial Pacific and the associated sea-level pressure difference, the Southern Oscillation [*Rasmusson and Carpenter*, 1982]. The Southern Oscillation Index is the fluctuation in air pressure between Tahiti and Darwin. Negative (positive) pressure is accompanied by sustained warming (cooling) in the central or eastern Pacific. In non El Niño years, the easterly trade winds, which are the surface component of the Walker circulation, drive warm moist air over the Pacific towards the Indonesian region. El Niño disrupts and weakens the Walker circulation [*Bjerknes*, 1969; *Julian and Chervin*, 1978]. In certain strong El Niño years westerly winds can be observed in the tropical and central Pacific. ENSO has a recurrence pattern of 3 to 6 years and every event normally lasts for around a year. El Niño events are often, but not always, followed by La Niña events, also referred to as the cold phase of ENSO. They have a direct effect on the hydrological cycle both regionally and globally, especially on precipitation patterns. The effect of ENSO is neither distributed uniformly across the globe, not even across a single continent, nor in time during its period of occurrence [*Lyon*, 2004].

In the North American region, ENSO alters the path of the jet stream and hence affects the weather and storm tracks. El Niño causes a dip in the position of the jet stream in the Eastern Pacific which results in warmer winters in western Canada and southern Alaska and north eastern US, while the southern US has cooler and wetter weather. During summer the southern part of Mexico becomes warm and dry. During La Niña the dip in the jet stream shifts west of its normal position towards the Central Pacific. It causes cooler winters in eastern Canada while the southern US becomes warm and dry. The shift in the jet stream, during warm ENSO events, forces storms south of their normal position in the Pacific Northwest into California. Stronger El Niño can force storms even further south into Southern California, while the Pacific Northwest becomes drier as the moisture flux is transported southward. California thus benefits from above average precipitation during El Niño and flash floods are very common [*Mo and Higgins*, 1998; *Schonher and Nicholson*, 1989]. This influx of moisture also increases snowfall in the Sierra Nevada mountain range [*Kunkel and Angel*, 1999]. In the Rocky Mountains, the effect of ENSO varies with opposite effects at the northern and southern ends [*Baker*, 2003]. The Rockies can be divided into three sections: the northern Rocky Mountains in Montana, the central Rocky Mountains extending from southern Montana into central Wyoming, and the southern Rocky Mountain stretching from southern Wyoming into New Mexico and Arizona. El Niño (La Niña) winters bring higher (lower) snowfall in the southern Rockies [*Kunkel and Angel*, 1999]. The effect of ENSO on the central and northern Rockies is less pronounced.

In its cold (warm) phase ENSO bring higher (lower) snowfall over the Pacific Northwest in early and midwinter and over the northern Rocky Mountains in midwinter [*Patten et al.*, 2003; *Smith and O'Brien*, 2001]. The central Rockies receive 30% less heavy precipitation events [*Gershunov and Barnett*, 1998b].

2.3.2 EL NIÑO MODOKI

A new type of El Niño, occurring more frequently, with interannual variability, has been observed since 1990 [*Ashok et al.*, 2007]. This phenomenon has been called El Niño Modoki (EMI; Japanese for “similar but different”). It occurs with a shift in the warming center from

the eastern equatorial Pacific, as is the case with regular El Niño, to central equatorial pacific, and both the eastern and western regions are flanked by anomalously cool temperatures. The resulting sea surface temperature gradient generates a two-cell Walker Circulation in the troposphere with a wet region over the central Pacific. When coupled with other ongoing atmospheric disturbances, a dry rim arises around the wet central tropical Pacific. Given their similarities it is easy to confuse between the impacts of these two occurrences. Partial correlation and regression analyses suggest that they are distinct phenomena in both space and time and do not appear as an evolving phase of one or the other. Hence, in order to understand the actual impact of each one, it is important to differentiate canonical El Niño from EMI. Events occurring in 1991-92, 1994-95, 2002-03, 2004-05 [*Weng et al.*, 2007] and 2009-10 [*Lee and McPhaden*, 2010] have been associated with this central Pacific El Niño. *Weng et al.* [2007] looked at the hydrological impacts of EMI on the Pacific rim using observational data for the period 1979 to 2005 and compared their features with the regular El Niño. Focusing on China, Japan, and US, using in-situ data, they concluded that the warm temperature during EMI exacerbates droughts in areas suffering from large rainfall deficits.

The location of the warming in the Pacific affects the cyclogenesis and track of tropical cyclones. The warming in central Pacific has an impact on the frequency and impacts of North Atlantic tropical cyclones. They are likely to form closer to the US coast, and consequently increasing the probability of making landfall [*Kim et al.*, 2009]. *Lee and McPhaden* [2010] utilized satellite observations to compare El Niño events and found that the one in the central equatorial pacific has almost doubled in intensity in the last three decades. Sea surface temperature in the same region for neutral and La Niña years on the other hand have remained constant, implying that the background increase in global temperature may not influence ENSO. *Yeh et al.* [2009] compared the frequency of occurrence of central Pacific El Niño to canonical El Niño events under projected global warming scenarios and found that central Pacific El Niño may increase by a ratio of five.

2.3.3 PACIFIC DECADAL OSCILLATION

The Pacific Decadal Oscillation (PDO) is a long-lived El Niño-like pattern of Pacific climate variability with a cycle of about 20 to 30 years [*Mantua and Hare*, 2002]. This past century has witnessed two full PDO cycles, a cold regime in 1890-1924 and again from 1947-1976 and a warm regime between 1925-1946 and 1977 through late 1990s. Based on a 13 k.y. record of drought variability at subdecadal resolution, inferred from fossil diatom assemblages recovered from a lake in northwestern Montana, *Stone and Fritz* [2006] found that drought periodicities associated with the PDO has changed over time, with strongest periodicity occurring during mid-Holocene when temperature were warmer than present. *Gedalof et al.* [2002] combined a set of five published proxy records of tree rings and corals to study the Pacific basin climate variability and concluded that it provide a good record of PDO extending back to 1840. They found that the PDO is not a phenomenon that manifested solely in the 20th century, but was present in the previous century as well which means that its influence on fluvial geomorphology has been continuous. However, the influence of the PDO in the 19th century was not as robust as in the last century.

When the PDO is its positive or warm phase, above normal SSTs is observed along the west coast of the North America and below normal SSTs along the central and western North Pacific around 45°N. The effect of PDO on the hydrological cycle is similar to ENSO, but with more pronounced influence in the extra tropics and secondary influence in the tropics, whereas for ENSO the reverse is true. Its influence has been observed in both the northern and southern hemisphere [e.g., *Hessl et al.*, 2004; *Krishnan and Sugi*, 2003; *Mantua et al.*, 1997; *Neal et al.*, 2002; *Verdon et al.*, 2004]. In its positive, or warm, phase the PDO has been observed to correlate with anomalously dry weather in eastern Australia and Asia, Central America and northern South America and above average precipitation in coastal Gulf of Alaska, southwest US and Mexico, southeast Brazil, south Central America, and west Australia [*Mantua and Hare*, 2002]. Further November to April temperatures tend to be anomalously higher in northwestern North America, southern South America and northwestern Australia and below average in eastern Asia, southeast US and Mexico. This period coincides with winter in the Northern Hemisphere and therefore has a direct impact on

precipitation, snow accumulation, and the timing of snowmelt and runoff in the alpine regions. On the other hand, in its negative phase, the PDO enhances spring snow pack [*Selkowitz et al.*, 2002]. *McCabe and Dettinger* [2002] showed that PDO is more important than ENSO in regulating the variability in the April snowpack in the western US. *Malanson et al.* [2009] explain the importance of climate, both at the large and micro scale, to ecotone dynamics, and argue that PDO will have an important influence on treeline dynamics, especially in the Pacific Northwest and northern Rockies. Large scale climate fluctuations influence local weather which for the Rocky Mountains implies modification of the mean summer and winter position of the polar jet stream which translates into the modification of the wind strength and direction, and precipitation amount which ultimately affects the needles, stems, and roots of plants [*Malanson et al.*, 2009].

The similarities in the signature between ENSO and PDO have led to the hypothesis that the two teleconnections may be related or PDO may be forced by ENSO [*Zhang et al.*, 1997]. Statistical analysis by *Newman et al.* [2003] showed that the PDO is dependent on ENSO at all timescales.

Kurtzman and Scanlon [2007] looked at the impact of ENSO and PDO on the winter precipitation in 165 climate divisions in southern and central US and found that there is a significant increase (decrease) with respect to El Niño (La Niña). The correlation with PDO was weaker, but when both indices are combined, it was noted that La Niña occurring during the cold phase of the PDO and El Niño occurring during the warm phase of the PDO exhibited strong influence in the precipitation in the central US, and the southwest and southeast US, respectively.

Macias Fauria and Johnson [2006] showed the influence of PDO/ENSO and the Arctic Oscillation in the frequency of occurrence of large scale wildfires in Alaska and Canada in the last four decades. Since the climate fingerprints of PDO and ENSO are the same, but with different scales, events occurring at larges time scales were associated with PDO while those occurring at higher frequencies were associated with ENSO or the Arctic Oscillation. *Schoennagel et al.* [2005] investigated ENSO-PDO related drought-induced fires in the subalpine forests of the Rocky Mountains and found that large fires occurred in years of

extreme droughts. These drought events were not always strongly correlated with ENSO or PDO alone but the combination of these two indices showed strong correlation with the occurrence of large fires across the region. In the central and northern Rockies large fires appeared when El Niño occurred during the positive phase of the PDO and in the southern Rockies, large fires tend to occur when La Niña coincided with the cold phase of the PDO. *Dixon et al.* [2008] used a similar approach and four teleconnection patterns for the prediction of wildfires in Mississippi and endorsed such index combination approach for wildfire prediction. With global warming, a loss of moisture in the alpine forests is expected which may lead to changes in the temporal dynamics of fire-climate relationships, area destroyed, mean age of the forest, and species composition [*Macias Fauria and Johnson*, 2008].

2.4 METHODOLOGY

Pearson correlation is used to determine the relationship between climate indices and gauged seasonal precipitation data. The Pearson correlation coefficient, ρ_{xy}, is a measure of linear association between two time series: x and y. The lag-correlation coefficient, $\rho_{xy}(k)$, is the cross-correlation for lag k between the time series. The range for $\rho_{xy}(k)$ is $[-1, 1]$, with larger $|\rho_{xy}|$ implying greater ability of x to predict y [*von Storch and Zwiers*, 2003]. The correlation coefficient can be used as a statistical test of independence to help make inferences about the degree of association between variables. The null hypothesis is that the two time series are independent and identically distributed (iid) normal random variables($\rho_{xy} = 0$).

Kriging interpolation is employed to map the spatial variation of the correlation coefficient across the study area.

2.5 STUDY AREA: RIO GRANDE/RÍO BRAVO DEL NORTE

RG is the fifth longest river in North America. It originates in the snow dominated San Juan range in the Rocky Mountains in southern Colorado, at an altitude of around 3,700 m amsl, and flows through arid/semi-arid plains in a south-eastward direction over a distance of approximately 3,100 km before discharging into the Gulf of Mexico. The basin encompasses

an area of 557,722 km^2 straddling three states in the US and five states in Mexico (Figure 1). The river catchment is narrow, with its length being considerably longer than its width, and has a dendritic drainage pattern. The watershed contains a number of endorheic sub-basins, such that only 468,374 km^2 (242,994 km^2 on the US side and 225,380 km^2 on the Mexican side) actually contribute to flow in the river [*Patiño-Gomez,* 2005].

Winter precipitation and spring runoff sustain flow in the basin. The flow is impounded in a number of dams and regulated by major diversions. Elephant Butte Dam in southern New Mexico supports agricultural production in the region. The release from the dam is apportioned between the US and Mexico under the 1906 Convention for the Equitable Distribution of Waters of the Rio Grande [*International Boundary & Water Commission*, 1906]. From El Paso to Ojinaga/Presidio the river flows through one of its driest stretches [*US Army Corps of Engineers,* 2008]. At El Paso (station 45 in Figure 2), for example, the mean annual rainfall is 219 mm, while the yearly pan evaporation is around 1,500 mm. At Ojinaga/Presidio, RG is regenerated from flow from the Río Conchos, which is one of its most important tributaries, originating in the Sierra Madre Occidental in northwestern Mexico at around 3,500 m amsl. Two international reservoirs, Amistad and Falcon, store and apportion the water between the US and Mexico. Without any dam or diversion along its course, the virgin flow of RG is estimated at above 100 m^3/s [*Revenga et al.*, 2003]. However, the over anthropogenization of the basin has constantly impacted flow, such that the actual mean historical flow is 37 m^3/s, but in recent years the flow in the river has reduced considerably, and on several occasions the river failed to reach the sea.

Land cover in RG is mainly desert shrubland and grassland, covering about 81%, while irrigated agriculture constitutes only 2.6% of the basin, and urban and industrial area covers 6% of the basin [*Revenga et al.*, 2003].

Given its size, the varied climatology it is subjected to, and the major dams and diversions partitioning the system, RG cannot be studied as one watershed, nor can it be divided into sub-basins, as some tributaries, like the Pecos, runs along the main stem, crossing several latitudes, thus subjected to different climate teleconnection influences. Higher snowfall at the headwaters, for example, does not necessarily result in higher flow into the international

reservoirs or at the mouth. Moreover, climate divisions from one US state do not align with that from another state. The basin is therefore divided into six sub-regions (Figure 2) by considering the latter constraints and other geomorphological features in the system.

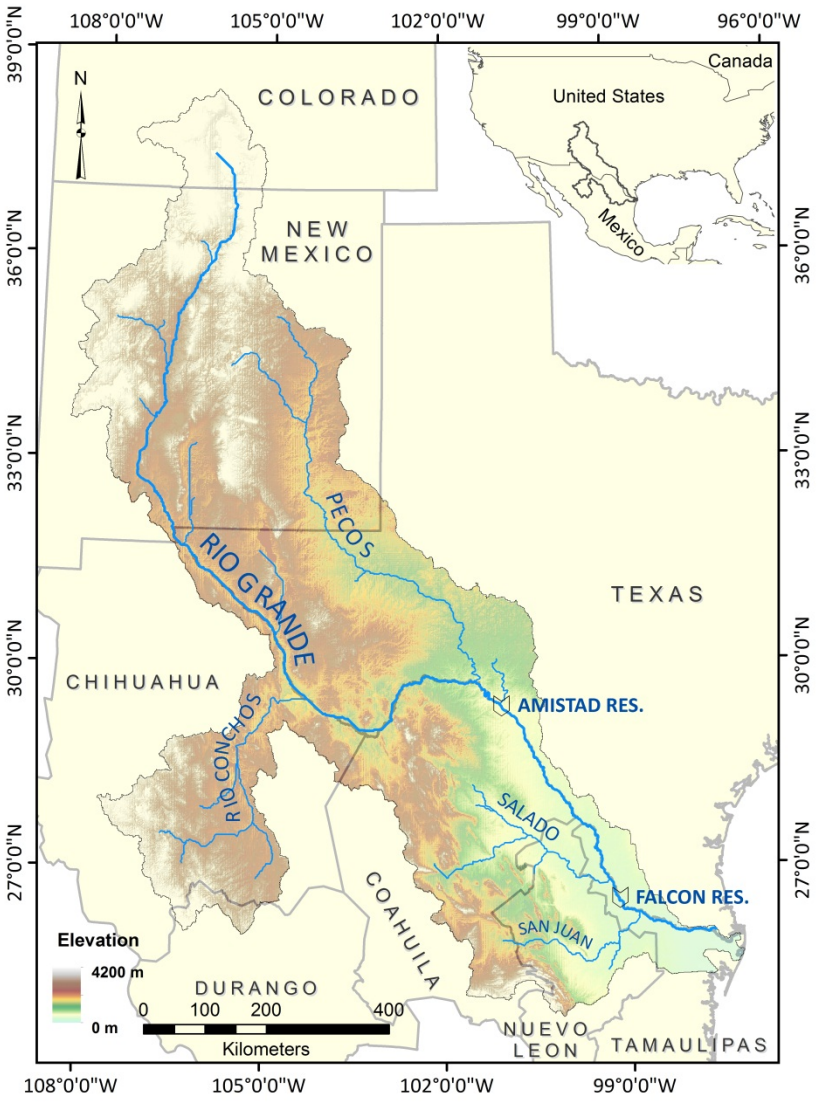

Figure 1. The Rio Grande/Río Bravo del Norte basin.

2.6 DATA

2.6.1 PRECIPITATION

2.6.1.1 United States

The National Climatic Data Center (NCDC) has an extensive archive of publicly available weather data from NOAA's Cooperative Observer Program (COOP) stations in the US. The COOP data contains gaps and only a few stations have continuous records. NCDC also houses the United States Historical Climatology Network (USHCN) version 2 dataset which is a designated subset of the COOP network [*Karl et al.,* 1990]. The dataset undergoes extensive quality control including adjustment for any time-of-observation bias. Only 27 stations out of the 1,221 stations in the USHCN are serially complete [*McRoberts and Nielsen-Gammon,* 2011], while missing data in the others have been filled using a weighted average of values from highly correlated neighboring stations. However, the density of the USHCN network is not adequate within RG for purposes of this study (see Figure 1 of USHCN Version 2 Serial Monthly Dataset, available from http://www.ncdc.noaa.gov/oa/climate/research/ushcn/ which shows the distribution of both COOP and HCN sites).

McRoberts and Nielsen-Gammon [2011] proposed the full network estimated precipitation (FNEP, available from http://atmo.tamu.edu/osc/fnep) which utilizes as many COOP observations from the network of more than 24,000 stations and an inverse distance weighting scheme, using stations that have at least 10 years of overlap data and highest correlation, to fill missing data and extend the record, thus creating a continuous series from 1895 to present. There are a total of 332 FNEP stations within the US portion of RG, but only those that have a sufficiently long record of observational data, while ensuring adequate spatial coverage, were chosen, hence taking advantage of the filled gaps. The time period considered in the analysis is January 1935 to December 2008, thus giving 74 years of data. Figure 2 shows the spatial distribution of the 63 stations (4 in Colorado, 40 in New Mexico, and 19 in Texas) selected.

2.6.1.2 Mexico

Historical monthly precipitation data for the Mexican section of the basin was obtained from the Servicio Meteorológico Nacional (SMN), Comisión Nacional del Agua (CONAGUA),

Mexico. SMN is the state entity responsible for the observation, recording, interpretation and dissemination of weather information in Mexico. The most updated observational dataset obtained contained data up to December 2006 only, and any record beyond that date is not yet publicly available. For the Río Conchos sub-basin the latest available data is only up to December 2003.

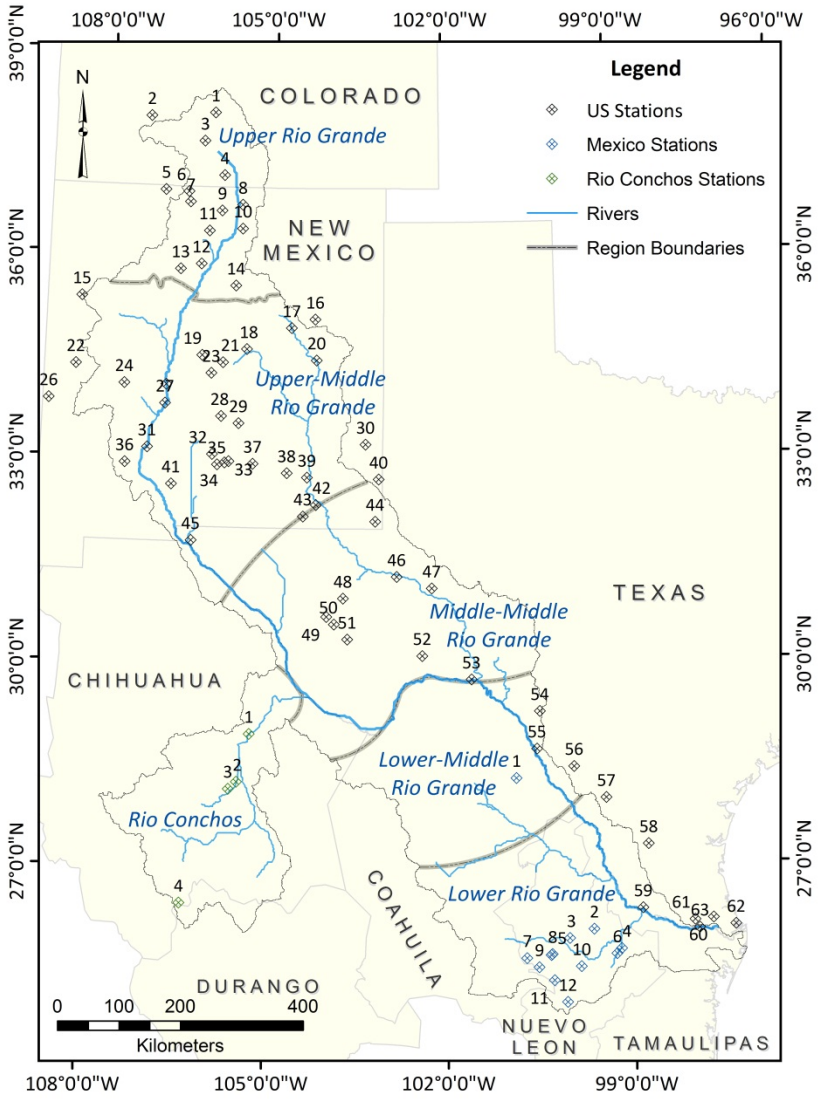

Figure 2. Location of precipitation stations used in this study.

Of all the stations within the Mexican section of the basin, excluding the Río Conchos, 52 are operational and have records that extend up to 2006. However, most of these stations are very recent and only a few have records of at least 50 years, but have several years of missing data. A careful selection of viable stations, while ensuring maximum possible coverage, limited the number of stations that can be used in the study to only 12. The time period extended from January 1954 to December 2006. Records show that 9 stations are operational in the Río Conchos, but only 4 had sufficiently long records, extending from 1964 to 2003, for this study. Data gaps were filled from neighboring stations that had sufficient amounts of overlapping data with the target stations. Any data missing from both the target and neighboring stations were filled with the long term monthly mean. The spatial distribution of the selected stations is shown in Figure 2.

2.6.2 CLIMATE INDICES

2.6.2.1 Pacific Decadal Oscillation (PDO)

Monthly PDO indices for the period 1935 to 2008 were obtained from the Joint Institute for the Study of the Atmosphere and Ocean. The PDO index is defined as the leading principal component of the North Pacific, poleward of 20°N, mean monthly SSTA [*Mantua et al.*, 1997]. The data is not influenced by global warming trends as monthly mean global average SSTA have been removed. A plot of monthly indices, with a centered 13-month moving average to highlight multi-decadal frequency, is given in Figure 3. Positive (negative) values indicate warm (cold) phases of PDO. Between 1935 and 2008, 51% of warm months and 49% of cold months were recorded.

Independent studies have shown two full PDO cycles in the last century [*Mantua and Hare*, 2002; *Minobe*, 1997], cool regimes that lasted from 1890 to 1924 and from 1947 to 1976, and warm phases that lasted from 1925 to 1946 and from 1977 to 1998. From 1998, PDO has been in a cold phase until 2002 and in a warm phase from 2002 to 2007. Occasional shifts, within the 20-30 year cycle, from cool (warm) to warm (cool) are visible in the record.

2.6.2.2 Niño 3.4

There are four Niño regions along the equatorial Pacific, chosen in the early 1980's to describe and monitor SST. The warming across this region is not uniform and no single region can capture the whole ENSO phenomenon. *Barnston et al.* [1997] proposed the Niño 3.4 index as one that has both maximum correlation with the core ENSO phenomenon and strongest influence on remote teleconnection events. It is the area-averaged SSTA over the region bounded by 5°N–5°S and 120°W–170°W, straddling the Niño 3 and Niño 4 regions. Monthly data for the Niño 3.4 index was obtained from the International Research Institute (IRI) on Climate and Society Data Library. Figure 3 gives a plot of the Niño 3.4 index.

2.6.2.3 Multi-ENSO Index (MEI)

MEI is not based solely on SST but is a multivariate index based on six variables recorded over the tropical Pacific and published in the Comprehensive Ocean-Atmosphere Data Set (COADS): sea-level pressure, zonal and meridional components of the surface wind, sea surface temperature, surface air temperature, and total cloudiness fraction of the sky. It is the first unrotated principal component of all the six observed fields combined [*Wolter and Timlin*, 1993], and is analyzed separately for twelve sliding bi-monthly seasons, which removes most intra-seasonal noise. For correlation studies, it is advised that the MEI values for month $(i-1)$ and month (i) be treated as for month (i). Monthly data for MEI for 1950 to 2008 was obtained from NOAA's Earth System Research Laboratory. Figure 3 gives a plot of MEI.

2.6.2.4 El Niño Modoki (EMI)

EMI is available from the Japan Agency for Marine-Earth Science and Technology. It is defined as

$$EMI = [SSTA]_C - 0.5[SSTA]_E - 0.5[SSTA]_W \quad \textbf{(1)}$$

where [SSTA] is the area-averaged SST anomaly for the following regions: C (central, 165°E–140°W, 10°S–10°N), E (eastern, 110°W–70°W, 15°S–5°N), and W (western, 125°E–145°E, 10°S–20°N) [*Ashok et al.*, 2007]. The time series for EMI is given in Figure 3.

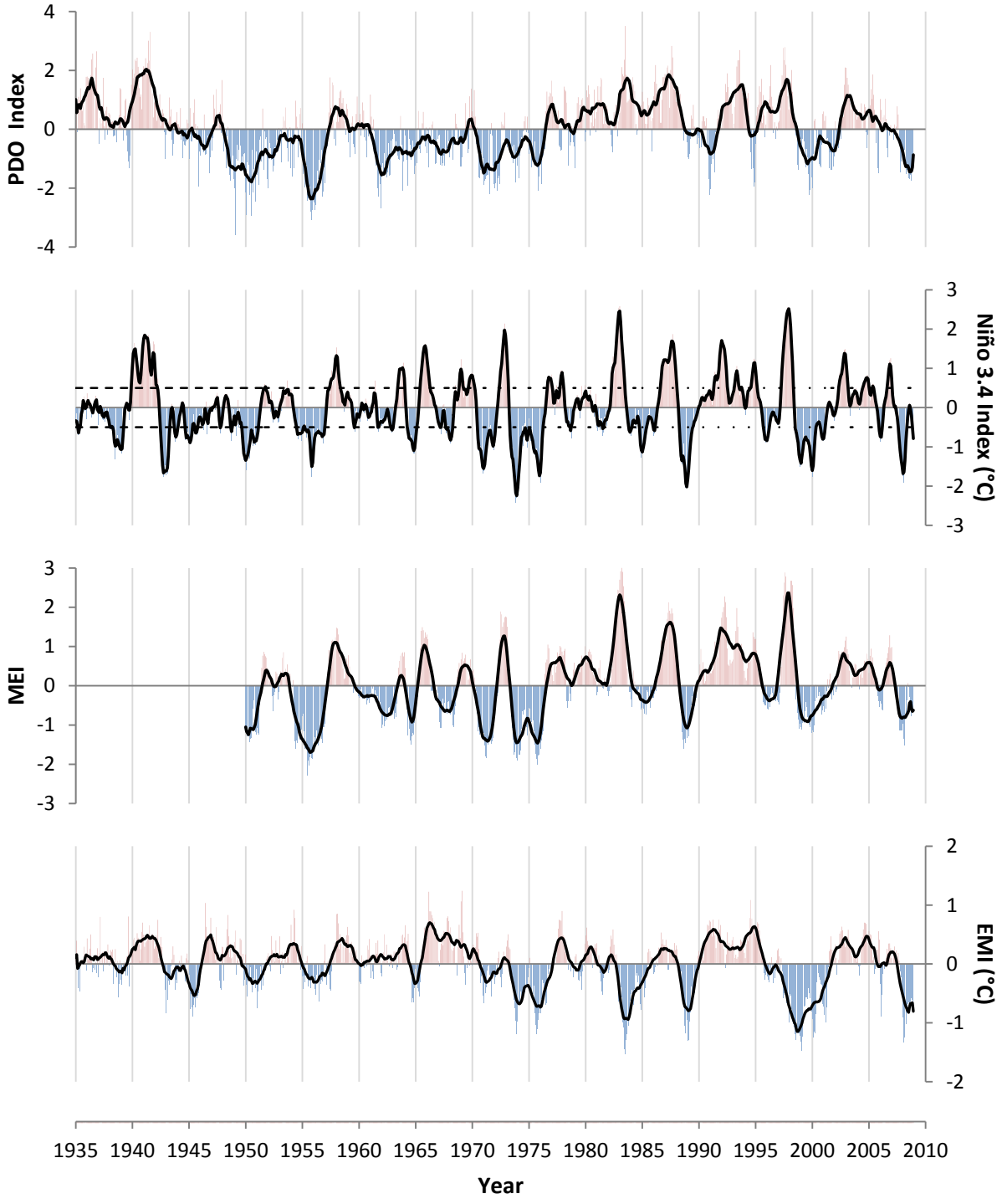

Figure 3. Time series of PDO, Niño 3.4, MEI, and EMI indices. The PDO, MEI, and EMI series are overlain with a running, centered 13-month average to highlight yearly variations. The normalized monthly Niño 3.4 index series is overlain with a centered 3-month running mean and ± 0.5°C thresholds (see section 2.7.2.1).

2.7 RESULTS AND DISCUSSION

2.7.1 HYDROCLIMATOLOGY OF THE BASIN

2.7.1.1 Spatial Variation

RG trends across different climatic zones – alpine in southern Colorado and northern New Mexico, desert in southern New Mexico and west Texas, humid continental in east Texas, and humid sub-tropical in south Texas and north-eastern Mexico [*Dahm et al.*, 2005] – making it an interesting study basin from both a hydrological and ecological perspective. Average annual precipitation varies from northwest to southeast across the basin, with a minimum of 187 mm at Manassa, in the San Juan Mountains, and a maximum of 698 mm at Port Isabel at the mouth of the basin. In the Río Conchos sub-basin, precipitation varies from southwest to northeast with a maximum annual mean of 781 mm at El Vergel, in the Sierra Madre Occidental, and a minimum of around 290 mm around the mouth as it discharges into RG. Figure 4 shows the isohyet of the annual mean precipitation and the coefficient of variation (C_v) of monthly precipitation across the basin. C_v is a statistical measure of variability, where a $C_v < 1$ indicates less variation, while a $C_v > 1$ indicates high variability.

The basin exhibits wide disparity in precipitation regime, with C_v ranging between 0.7 and 1.7. The Upper RG region has low variability. It receives around 20 mm of precipitation every month except for JAS with August being the wettest month (Figure 4b). The middle portion of the basin exhibits high variability. It has a unimodal precipitation regime, typical of the southwestern US where, for most of the year, the average precipitation is below 20 mm except for May/June to September/October when the North American monsoon (NAM) brings most of the yearly rainfall. Río Conchos follows a similar pattern. NAM is a regional-scale circulation that develops over southwest North America, bringing substantial rainfall to this otherwise arid region. It is associated with a subtropical ridge shifting poleward during the summer months over the northwestern Mexican plateau and southwestern US. As evidenced in the mean monthly precipitation distribution (Figure 4b) of the Río Conchos basin, the Upper-Middle and Middle-Middle RG, NAM starts to develop in late May to early June in southern Mexico quickly spreading along the western slopes of the Sierra Madre Occidental and into

New Mexico and the western edge of Texas in early July and into southwestern US in the middle of July and decays in September/October [*Adams and Comrie*, 1997; *Higgins et al.*, 1997]. The strength and path of the subtropical ridge is influenced by ENSO conditions. El Niño (La Niña) influences NAM by causing a weaker (stronger) southward (northward) displaced monsoon ridge [*Castro et al.*, 2001]. The lower part of the basin has a slightly bimodal precipitation pattern with May and June, and September and October as the two wettest periods. Atlantic hurricanes bring copious amounts of rainfall in a very short period of time, often resulting in major flooding in this region. A strong relationship between ENSO and the frequency of Atlantic hurricanes has been noted, with El Niño (La Niña) favoring a decrease (increase) in activity [*Pielke and Landsea*, 1999].

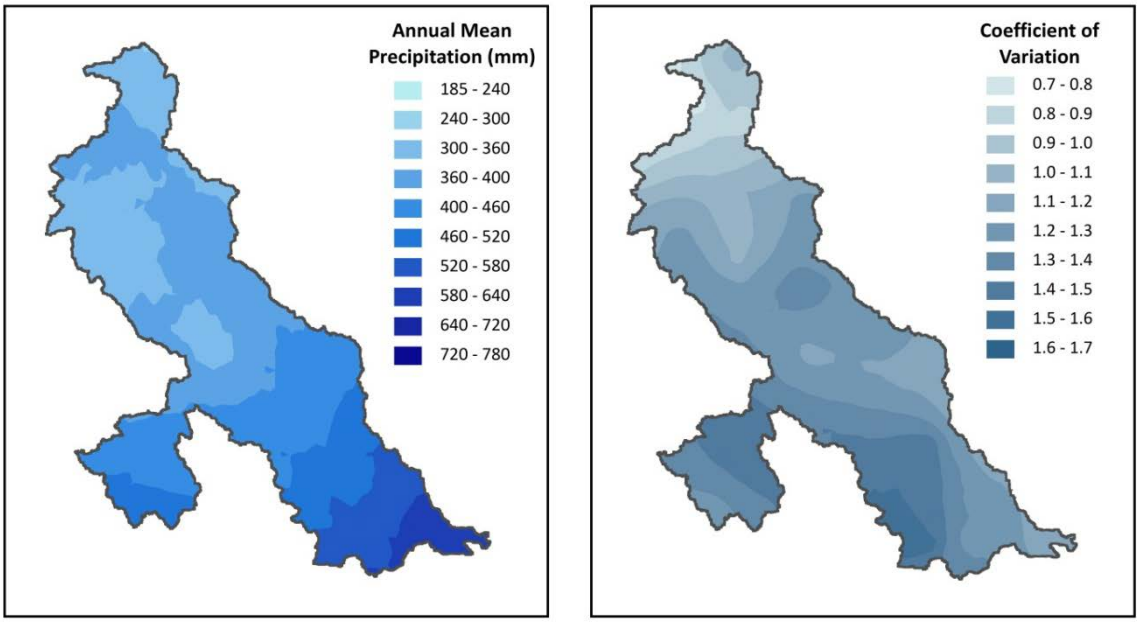

(a)

Figure 4. (a) Isohyet of annual mean precipitation and coefficient of variation of monthly precipitation across the Rio Grande basin, and (b) mean monthly precipitation for each region.

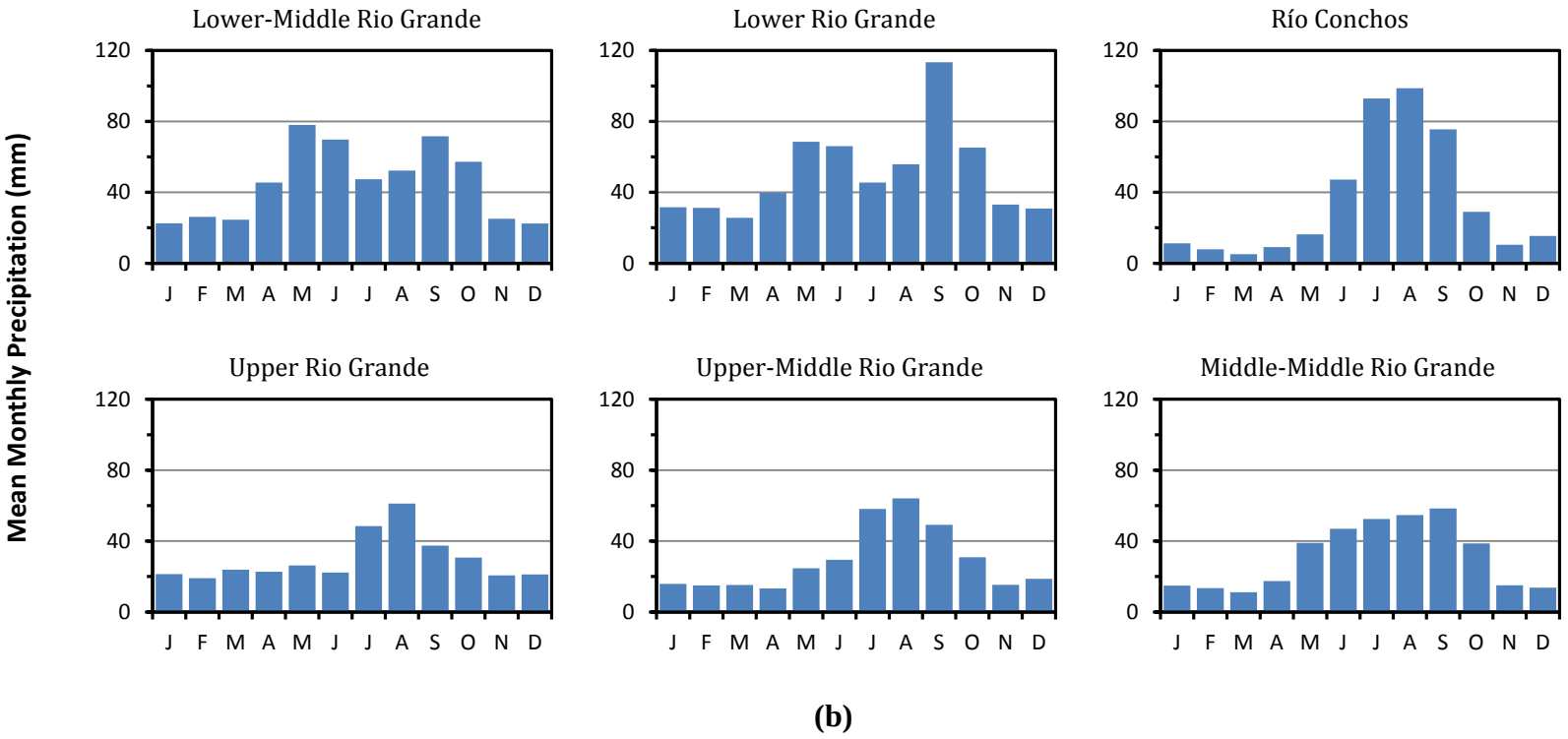

(b)

Figure 4 Continued.

2.7.1.2 Temporal Variation

Figure 5 shows the time series of average monthly precipitation from all stations within each region, smoothed with a centered 13-month moving average window to accentuate yearly variations. Precipitation from Mexican stations in Lower RG is shown in a separate plot. The top panel of the figure shows the duration of PDO and ENSO in their respective phases. Yearly standardized anomaly, which is the anomaly for a particular year divided by the standard deviation of the series, was calculated for each station. A positive (negative) standardized anomaly indicates higher (lower) than average precipitation. The patterns give a visual picture of the time, duration, and spatial extent of deficits and excesses in yearly precipitation across the basin. The standardized anomaly for the stations in the US, Mexico, and Río Conchos are shown separately in Figure 6.

Precipitation across the basin varies both spatially (Figure 4) and temporally. The standardized anomaly plot shows that precipitation is generally around the long term mean interspersed with drought spells, and a few extremely wet years, often spreading across the whole watershed. There have been more periods of rainfall deficits than excesses between 1935 and 2008. The most critical drought event started in 1951 and lasted up to 1956. In the semi-arid upper half portion of the basin, the drought started earlier, in 1942, right after an exceptionally wet year (1941). This event, commonly termed as the drought of the 1950s, affected a large extent of the conterminous US and is the most severe drought on record for the watershed. It coincides with the cold phases of both ENSO and PDO. ENSO actually oscillated mostly between La Niña and neutral conditions between May 1942 and February 1957 (Figure 3), the longest period in which the index remained in these phases. PDO shifted into its cold phase in November 1947 and remained mainly in this phase for up to February 1957. Another significant period of rainfall deficit started in 1962 and lasted up to 1965. It is associated with a drought that affected most of the northeast US [*Namais*, 1966; 1967] and coincides with cold PDO and mostly neutral ENSO with La Niña conditions between May 1964 and February 1965.

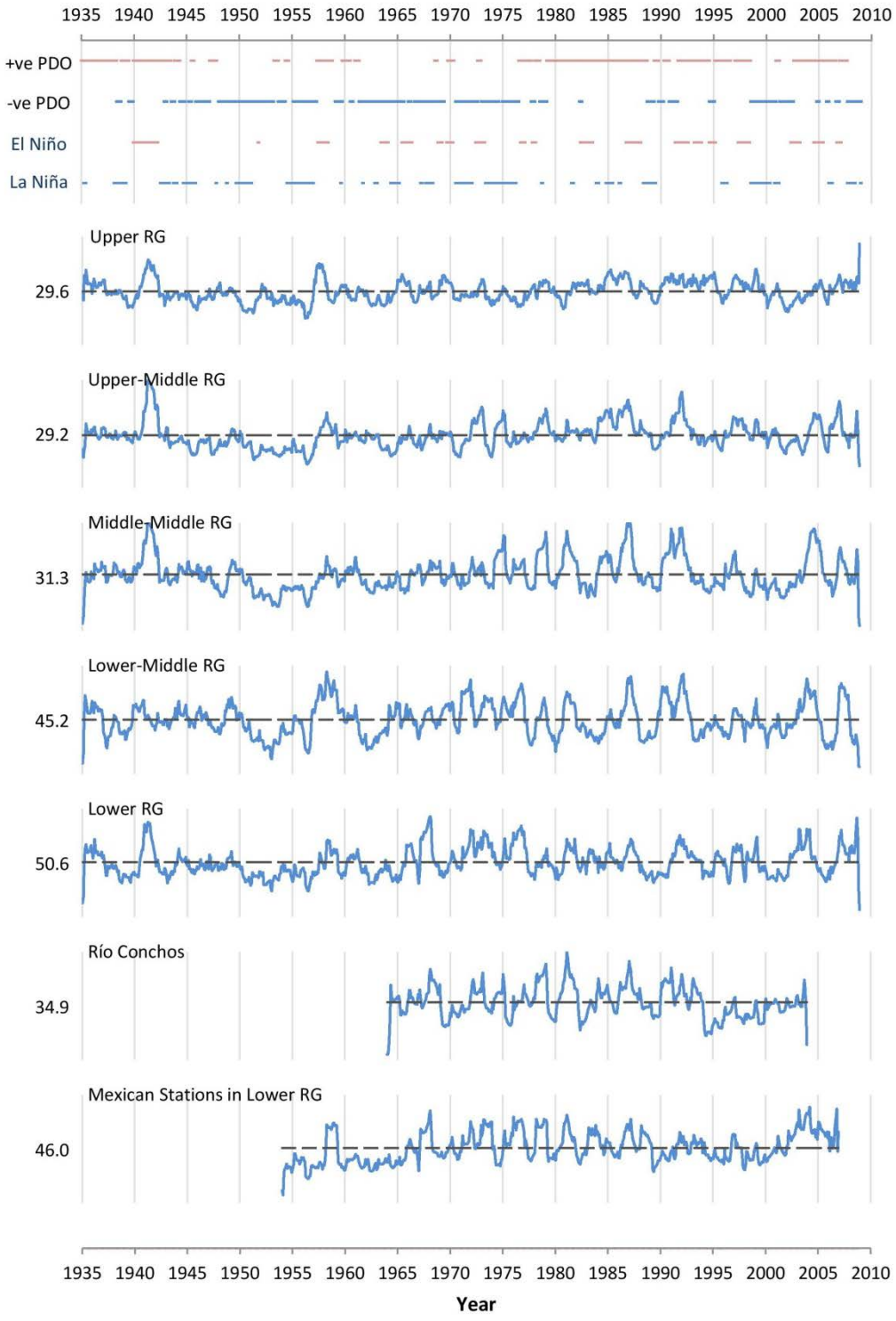

Figure 5. Smoothed series of average monthly gauged precipitation (mm/month) for each region. The broken horizontal line is the long-term average. The scales of the ordinates are arbitrary to illustrate variability. The top panel shows the phases of PDO and ENSO.

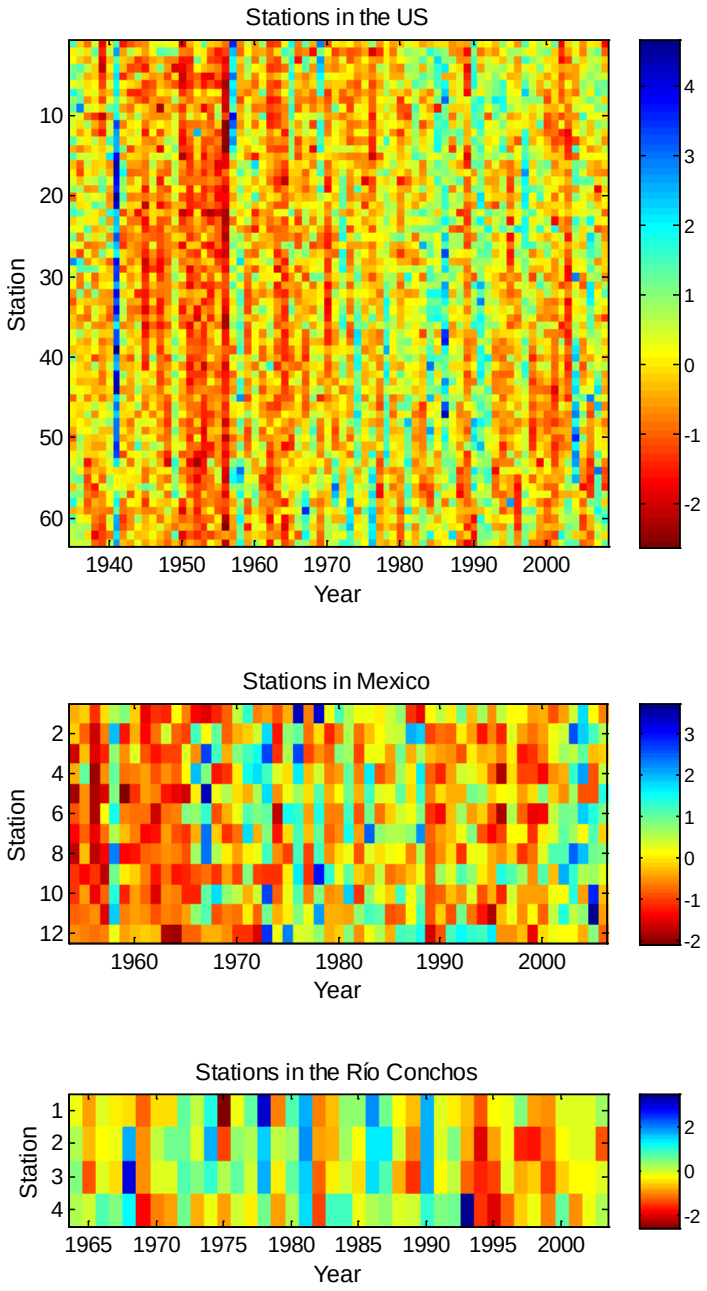

Figure 6. Time series of standardized anomaly for stations in the US, Mexico, and Río Conchos (Stations are latitudinally arranged with numbers corresponding to Figure 2).

The 1976-1988 and 1991-1994 periods were that of normal and above normal precipitation across the watershed, with a few dry patches. Meteorological conditions prevailing were

influenced by warm PDO (which started in July 1976) reinforcing multi-year El Niños (see Table 1). Year 1989, however, was a dry year across the whole basin, sandwiched between two wet periods. This lack of precipitation was influenced by negative ENSO (1988-1989 La Niña) and a weak PDO oscillating mostly between ±0.5°C. Given that the 1988-1989 La Niña is one of the strongest (see Table 2), and is not reinforced (dampened) by a negative (positive) PDO, its influence on water availability is worth investigating further.

The 2002-2004 drought is the second longest and most severe the region has experienced in recent record. It started earlier in the lower central arid portion and then propagated across the basin. Interestingly, this event did not coincide with La Niña conditions, but rather with neutral ENSO shifting into El Niño conditions, while PDO was in its cold phase until mid-2002 and shifted into its warm phase thereafter. Such dry conditions are not uncommon in the southwest as neutral ENSO with cold PDO can result in nearly as dry conditions as La Niña with cold PDO [*Goodrich*, 2004; *Quiring and Goodrich*, 2008]. The impact of such combination of the two indices on water availability will be further examined.

2.7.2 ENSO EVENTS

2.7.2.1 Definition of El Niño and La Niña

The definition for El Niño has evolved over time; different investigations use different indices and criteria, thus producing dissimilar lists of events. For long, there was no specific definition for La Niña despite an ongoing debate in the scientific community; they were defined in the context of the El Niño phenomenon [*O'Brien*, 2002]. *Trenberth* [1997] analyzed El Niño conditions between 1950 and 1997 using both Niño 3 and Niño 3.4 indices, relative to a base period climatology of 1950-1979, and suggested that an ENSO event is deemed to occur when the Niño 3.4 index is above (or below) ±0.4°C for at least six months. In 2003 the National Oceanic and Atmospheric Administration (NOAA) issued an official operational definition for El Niño and La Niña. The definition was endorsed by both Canada and Mexico in 2005 (North American countries reach consensus on El Niño definition available at http://www.noaanews.noaa.gov/stories2005/s2394.htm) and has been adopted by the World

Meteorological Organization Region IV [*Larkin and Harrison*, 2005]. Accordingly, an El Niño (La Niña) is defined as:

> A phenomenon in the equatorial Pacific Ocean characterized by a positive (negative) sea surface temperature departure from normal (for the 1971-2000 base period) in the Niño 3.4 region greater than or equal in magnitude to 0.5 degrees C, averaged over three consecutive months.

Neutral condition is when the index is between ±0.5°C. Figure 3 shows a plot of the Niño 3.4 index for 1935 to 2008, overlain with a centered 3-month moving average, which smoothens out variations in SST not associated with ENSO, and the ±0.5°C thresholds. The base period climatology for the IRI dataset is 1951-1980 [*Kaplan et al.*, 1998] and was adjusted to 1971-2000 to satisfy the above definition. During that period, El Niño occurred 21% of the time and La Niña 27% of the time, that is, the Pacific was either active in one of the two conditions or neutral about half the time.

2.7.2.2 Comparison of ENSO Events (1979 – 2008)

Table 1 gives the start, end, and duration of El Niño and La Niña events occurring since 1979. The braces indicate coupled events where the average SSTA remained in one phase. NOAA's definition, unlike *Trenberth's* [1997], does not specify a minimum period over which the average index has to be above (or below) the threshold to be deemed a significant event, thus smaller periods of one to three months are also included in the list. We note that between 1979 and 2008, El Niños generally lasted longer than La Niñas, and there were more months above the +0.5°C threshold, resulting in El Niños 26.4% of the time, as opposed to 21.1% for La Niñas. A higher frequency of El Niños since 1976 has been associated with decadal changes in the climate in the Pacific Ocean accentuated by recent climatic changes [*Kumar et al.*, 1994; *Trenberth*, 1990]. The two often called major El Niños (1991-1995 and 2002-2005) and major La Niñas (1983-1986 and 1998-2001) occurred between 1979 and 2008.

The onset of ENSO event is not consistent; El Niño events typically begin between May and September and La Niña events begin between July and October, except for the 1988 event which started earlier, in May, and the 2005 event evolved later, in December. The time

interval between El Niño events ranged between 15 and 47 months with an average of 33 months when coupled events are counted as one. In the case of La Niña events, the interval was normally around 26 months, except when the two major El Niño events occurred, leading to a gap of 75 and 57 months, respectively. The time interval between phase shifts varies from as short as one month (1997-1998 El Niño to 1998-2001 La Niña) to neutral conditions lingering for up to 23 months (1988-1989 La Niña to 1991-1995 El Niño).

Table 1. El Niño and La Niña events between 1979-2008 following NOAA's definition. Braces indicated coupled events.

El Niño event			La Niña event		
Begin	**End**	**Duration**	**Begin**	**End**	**Duration**
May 1982	June 1983	14	July 1981	August 1981	2
September 1986	January 1988	17	November 1983	January 1984	3
May 1991	July 1992	15	October 1984	May 1985	8
May 1993	July 1993	5	January 1986	February 1986	2
October 1993	October 1993	1	May 1988	June 1989	14
August 1994	February 1995	7	October 1995	March 1996	6
May 1997	May 1998	13	July 1998	April 2000	22
May 2002	February 2003	10	October 2000	February 2001	5
July 2004	January 2005	7	December 2005	March 2006	4
May 2005	May 2005	1	September 2007	May 2008	9
September 2006	January 2007	5			

Not all El Niños (La Niñas) are the same; some events last for only a few months while others may persist for two or more calendar years. Figure 7 compares the recent strongest El Niño and La Niña events. El Niños (La Niñas) tend to peak (trough) between November and February, except for the 1986-1988 event which peaked earlier in September. The strongest El Niño has a higher Niño 3.4 index value compared to the lowest index value for the strongest La Niña. Two El Niños with maximum SSTA above +2°C were noted, while La Niñas'

maxima were within −1 and −2°C. The reason for this lies mainly in the depth of the thermocline, which is shallower on the easternmost part of the Pacific basin, and it is therefore harder for the cold tongue to get colder, thus explaining why El Niños tend to be stronger than La Niñas [*Neelin*, 2010].

All these differences make it difficult to rank El Niños (La Niñas). It is hard to define the criteria to be used for such ranking; should it be (i) the duration above (or below) the defined threshold, (ii) the maximum (or minimum) SST recorded, or (iii) the total duration of the event in the phase of interest [*Wolter and Timlin*, 1998]? M. Glantz (The El Niño Olympics, or the Search for the El Niño of the Century, 1998, from Fragilecologies blog, http://fragilecologies.com/blog/?p=226) argues that a number of socio economic criteria, such as global spread of impacts, costs of devastation, or even public perception and media coverage, should also be considered. These criteria, however, are too complex and not totally objective and will thus not be considered in this study. Table 2 ranks the three strongest ENSO events, using the Niño 3.4 index, following *Wolter and Timlin* [1998], and intensity – a new metric which incorporates both SSTA and duration. ENSO intensity is the sum of monthly indices above (or below) the ±0.5°C threshold divided by the corresponding number of months. For combined events, the months where the index is within the neutral range are excluded.

Duration and Maximum/Minimum SSTA

The ranking reveals some interesting results regarding the individuality of ENSO events. In both El Niños and La Niñas, the list of the three strongest events using duration above the threshold is very different from that using the maximum (or minimum), implying that events persisting for long periods do not necessarily exhibit large deviations from the mean. The 1991-1995 event, for example, started in January 1990 and persisted until July 1995 [*Trenberth and Hoar*, 1996], and is the longest El Niño on record, with a combined total of 28 months above the +0.5°C threshold, but does not show up within the list of events with maximum temperature or intensity. *Allan and D'Arrigo* [1999], examining palaeoclimatic records of ENSO infer that such events are not unusual. El Niños persisting for three years or longer may occur around four to five times per century. On the other hand, instrumental

records analyzed by *Trenberth and Hoar* [1996] indicate that this event is unlikely the result of natural decadal-timescale variation but is rather influenced by global warming. The 1997-1998 El Niño, which developed earlier than the scientific community expected, is also noteworthy and has been dubbed "the climate event of the century" [*Changnon and Bell*, 2000]. Unlike the 1991-1995 event, it lasted only 13 months but was still one of the strongest on record with a peak SSTA of 2.56°C, closely rivaling the 1982-1983 event [*Kiladis and Diaz*, 1986]. By contrast the 1990-1995 event had a peak temperature of only 1.71°C occurring within the first third of the event. This super El Niño, just like the one in 1982-1983, had a dramatic impact on global weather variability causing the second worst drought in Australia and devastating floods across the western United States, with record precipitation in California. Western Pacific Islands, Central America and Mexico experienced severe droughts. It ended abruptly in the middle of 1998 when a mass of cold water under-rode the warm surface waters causing one of the longest and strongest La Niña ever recorded.

The 1998-2001 La Niña started in June 1998 and lingered till May 2001, with a combined total of 27 months below the −0.5°C threshold. The SSTA reached a minimum of −1.50°C in December 1998 and appeared to decay thereafter but resurged with a lower SSTA of −1.76°C in January 2000. The 1988-1989 La Niña, the second longest since 1979, reached a lower SSTA of −2.03°C in November 1988, and is one of the lowest on record.

When the total duration the index remains in the positive or negative phase is considered, the same El Niños are ranked, but a slight difference is noted in the order of La Niñas. The 1983-1986 event, even though has fewer months below the threshold, takes longer to decay, and hence supersedes the 1988-1989 event.

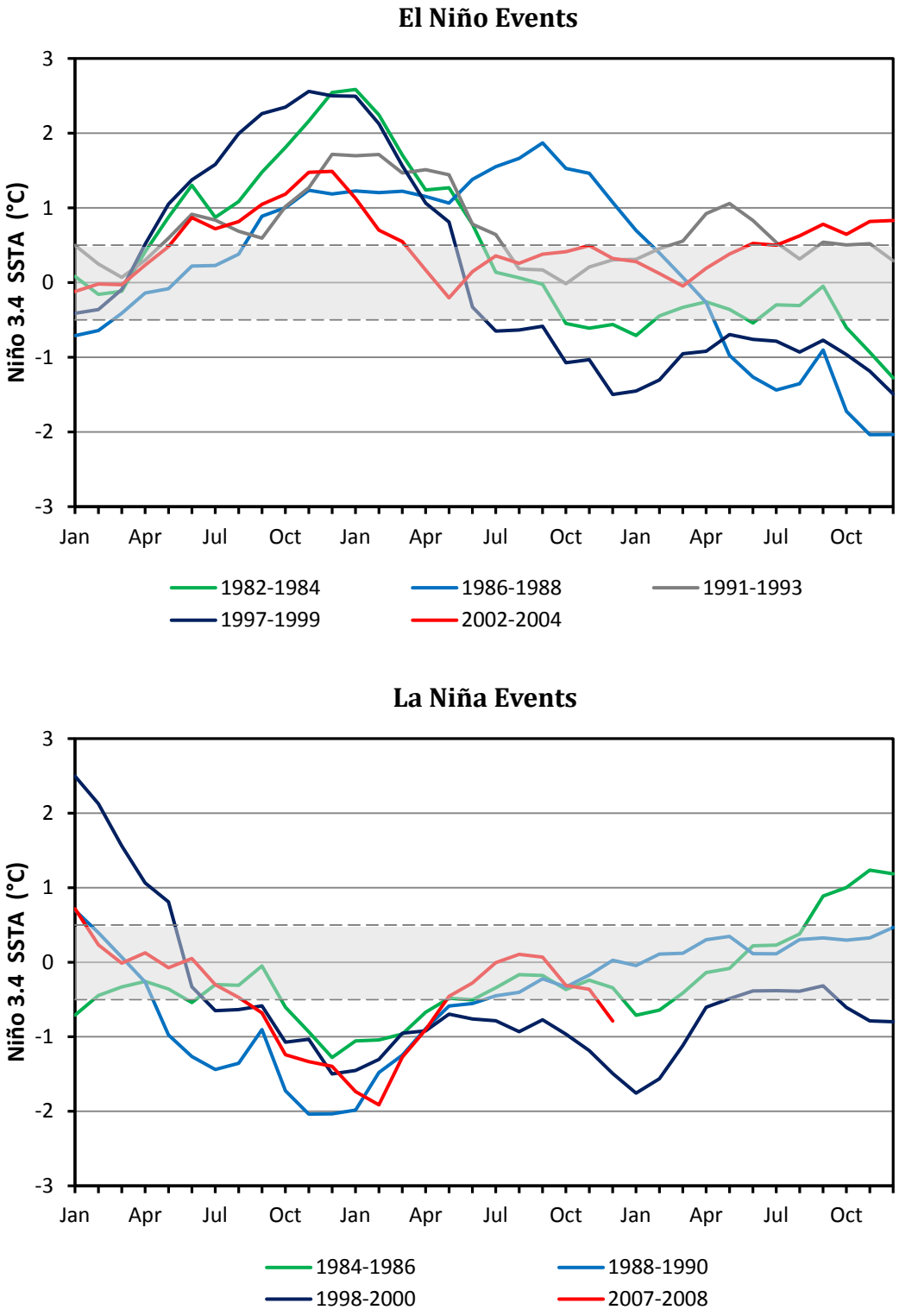

Figure 7. Comparison of major El Niño and La Niña events between 1979 and 2008 (transparent gray band shows ±0.5°C neutral range).

ENSO Intensity

ENSO intensity shuffles the ranking of El Niños based on maximum SSTA recorded. The 1997-1998 event, with an intensity of 1.325, surpasses the 1982-1983 event, even though the latter has the highest temperature among recent episodes. In the case of La Niña, the list based on intensity agrees with that based on temperature, but not with the one based on duration. The 2007-2008 La Niña, being a short event, does not feature in the list based on duration but has the second lowest temperature and intensity. It is also important to note that La Niñas have much higher intensities than El Niños as they generally have shorter durations.

Table 2. The three strongest ENSO events since 1979 based on different ranking criteria.

Criteria	El Niño event	La Niña event
Duration above (or below) the defined threshold	1991-1995	1998-2001
	2002-2005	1988-1989
	1986-1988	1983-1986
Maximum (or minimum) temperature recorded	1982-1983	1988-1989
	1997-1998	2007-2008
	1986-1988	1998-2001
Total duration of event in the positive (or negative) phase	January 1990-July1995	June 1998-May 2001
	April 2002-September 2005	August 1983-May 1986
	June 1986-February 1988	April 1988-October 1989
ENSO intensity	1997-1998 *(1.325)*	1988-1989 *(-1.820)*
	1982-1983 *(1.068)*	2007-2008 *(-1.715)*
	1986-1988 *(0.759)*	1998-2001 *(-1.482)*

The numbers in bracket are the intensity for associated event.

The effect of ENSO on water availability, based on the criteria discussed above, will be examined to ascertain if SSTA, duration, or intensity have different impacts. Note that in subsequent sections, ENSO events will be referred to as labeled in the legend of Figure 7.

2.7.3 CLIMATE TELECONNECTION AND PRECIPITATION

Precipitation is the main determinant of water availability. To assess the relationship and spatial influence of climate variability on the precipitation in RG, climate indices were correlated with the average seasonal precipitation for each rainfall station. Kriging plots [*Delhomme*, 1978] for correlations with PDO (Figure 8), and ENSO indices () were constructed for winter (DJF), spring (MAM), summer (JJA), and fall (SON). The Pearson correlation coefficient, ρ_{xy}, forms the basis of the statistical test of independence. The null hypothesis is that the seasonal average precipitation is independent and identically distributed (iid) normal random variable not dependent on the indices. The magnitude and sign of the correlation coefficient are thus indicative of the existence, strength, and nature of any association [*Redmond and Koch*, 1991]. The correlation significance (*p*-value) for each station was also computed and is given (inset maps) along with the kriging plots. The *p*-value is the probability, if the test statistics is distributed as assumed in the null hypothesis, of observing a test statistic as extreme, or more, than the one actually observed, i.e., how unlikely it may be due to chance. The *p*-values are stratified as follows: less than or equal to 0.01%, 0.1%, 1%, 1–5%, and greater than 5%.

2.7.3.1 PDO

The PDO series between 1935 and 2008 has almost equal number of cold and warm years, thus prevents any bias that may result from the dominance of either phase over the other [*Kurtzman and Scanlon*, 2007]. The correlation structure is different for each season and varies considerably across the basin (Figure 8). The highest correlations are in winter and spring. In winter, a statistically significant positive correlation, ranging between 0.3 and 0.5, is observed in the lower RG region, especially in Mexico, at the mouth of the basin. This correlation structure shifts diametrically in the spring, with the northern semi-arid regions exhibiting higher correlation, while those in the lower half, from the Río Conchos downwards,

are statistically insignificant. The stations in the Río Conchos do not show any statistically significant correlation with PDO, except for one station in winter, at the mouth of this sub-basin. Summer precipitation, across the whole basin, exhibits no significant correlation with PDO, while negligible correlation is observed in some sections of the basin in the fall. Hence, it is noted that despite relatively low correlation, PDO does have an influence on the winter and spring conditions in the southern and northern parts of the basin respectively. Therefore, knowledge of the state of PDO is essential for water resources planning.

2.7.3.2 ENSO: Niño 3.4, MEI, and EMI

The seasonal kriging plots for Niño 3.4, MEI and EMI are given in Figure 9. All three indices exhibit the same general seasonal correlation structure, but overall the correlation of EMI with precipitation is the weakest.

Just like for PDO the correlation structure is different for each season and varies across the basin. A positive, statistically significant correlation, ranging between 0.3 and 0.7, was observed for winter and spring across the whole basin, except for the Upper RG region which exhibits a negative correlation with ENSO. This negative correlation at the head of basin, in the Rockies, is consistent with the findings of *Smith and O'Brien* [2001] and *Patten et al.* [2003] on snowfall pattern in the US. In spring the highest correlation region is the Upper-Middle RG. From a water management perspective this finding is important as higher snowfall at the headwaters, during La Niña conditions, may offset reduced precipitation in New Mexico. In summer and fall a negative correlation, even though not statistically significant, is observed, especially in the lower half of the basin.

The correlation between EMI and precipitation is not statistically representative in the basin and may therefore not be useful for water management purposes. The correlation structures of Niño 3.4 and MEI are similar; therefore despite MEI's appeal as a more inclusive ENSO index, we shall adhere to NOAA's operational definition of El Niño and La Niña, as discussed in section 2.7.2.1 above, for the remainder of the dissertation.

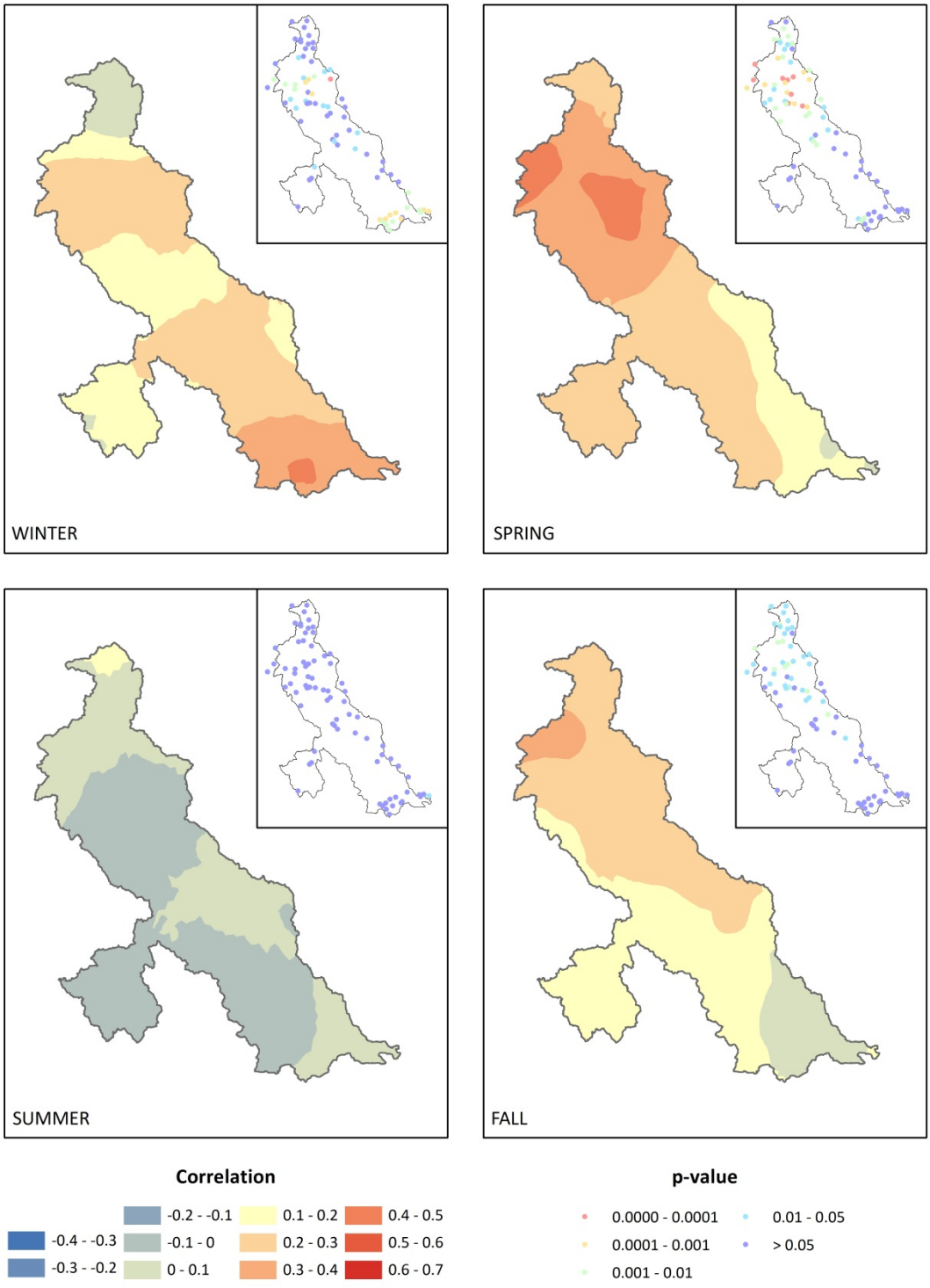

Figure 8. Plots of seasonal correlation coefficients between PDO and precipitation anomaly. Inset gives the *p*-values for the regression coefficients.

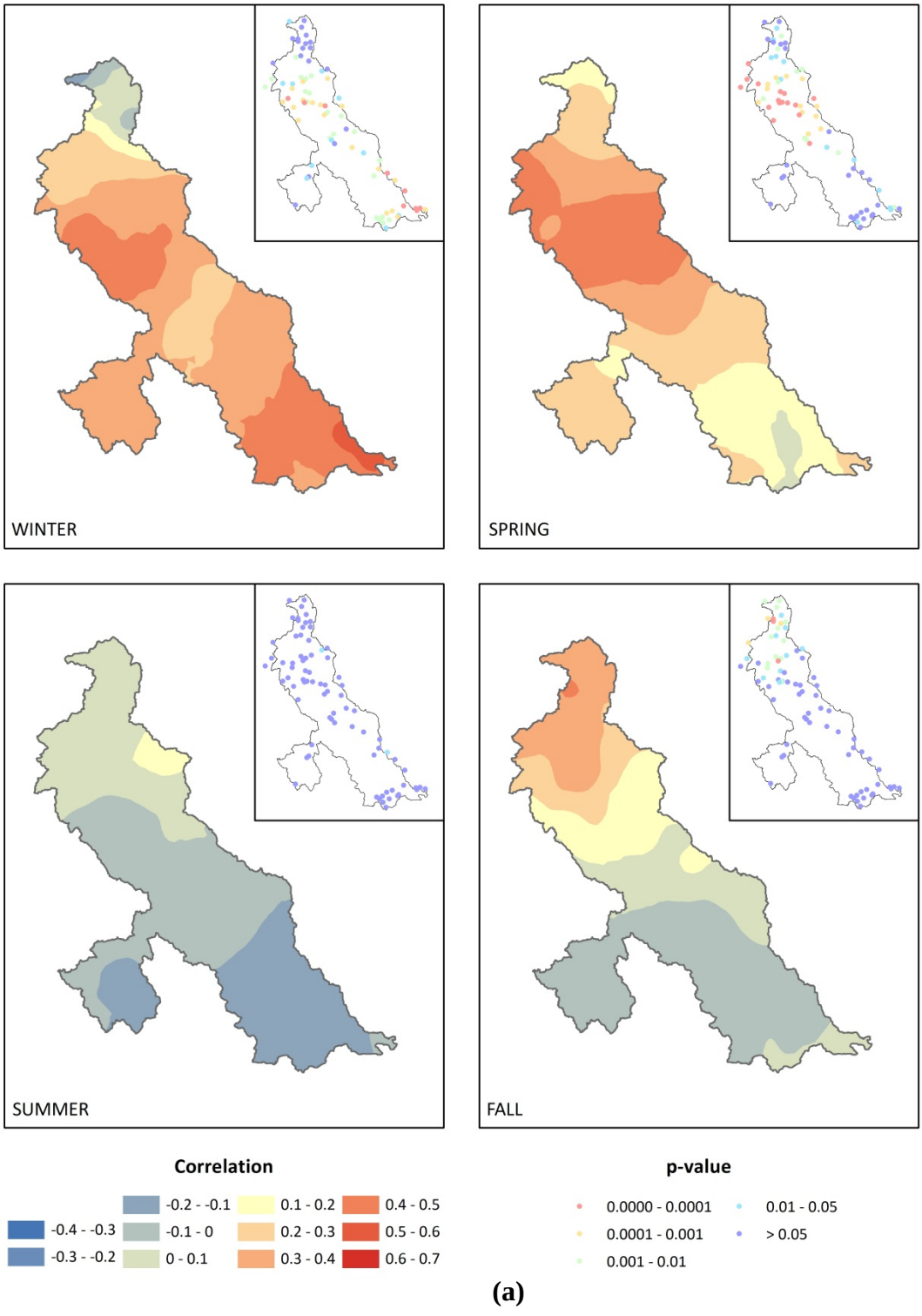

Figure 9. Plots of seasonal correlation coefficients between (a) Niño 3.4, (b) MEI, and (c) EMI and precipitation anomaly. Inset gives the *p*-values for the regression coefficients.

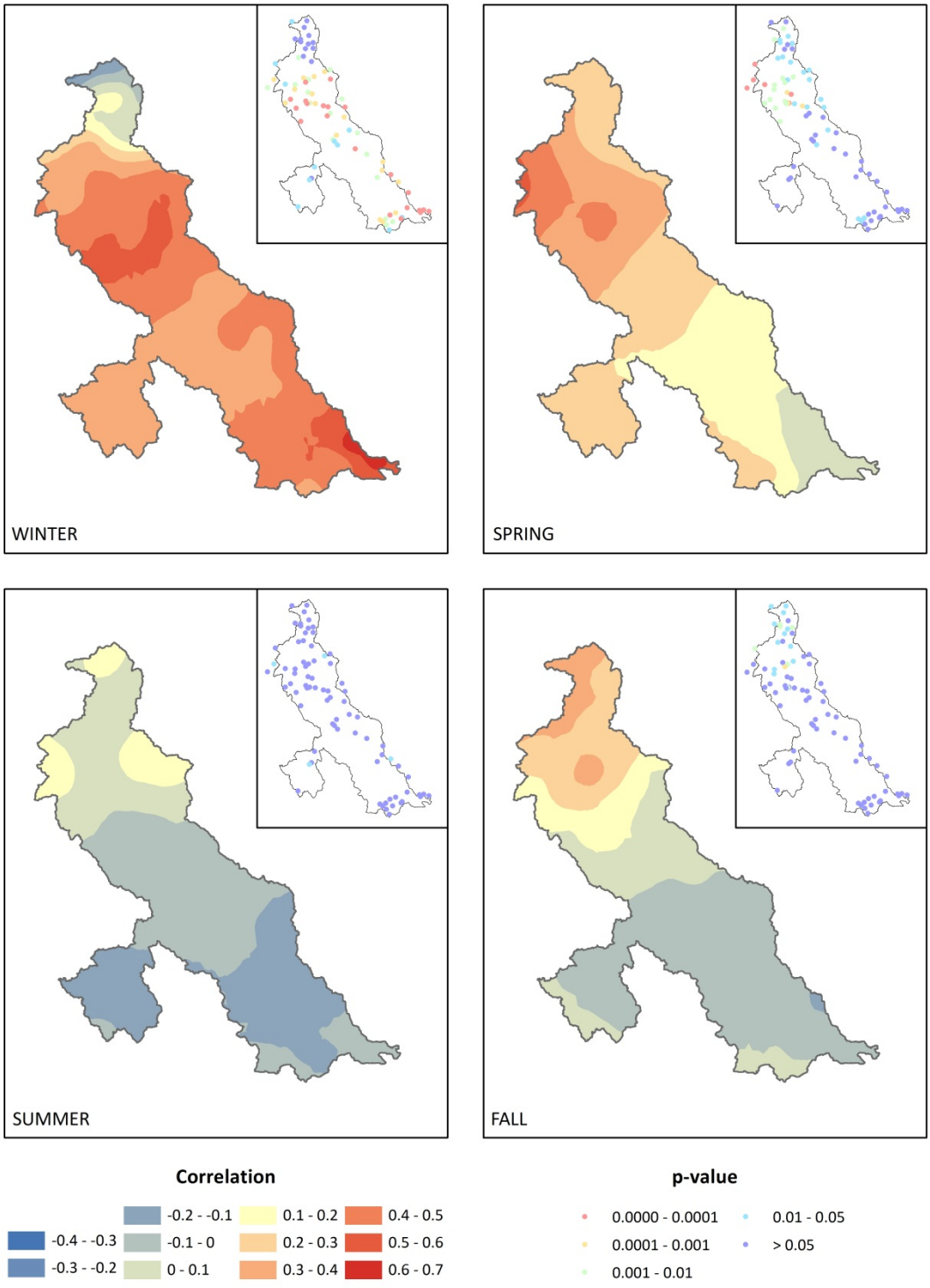

(b)

Figure 9 Continued.

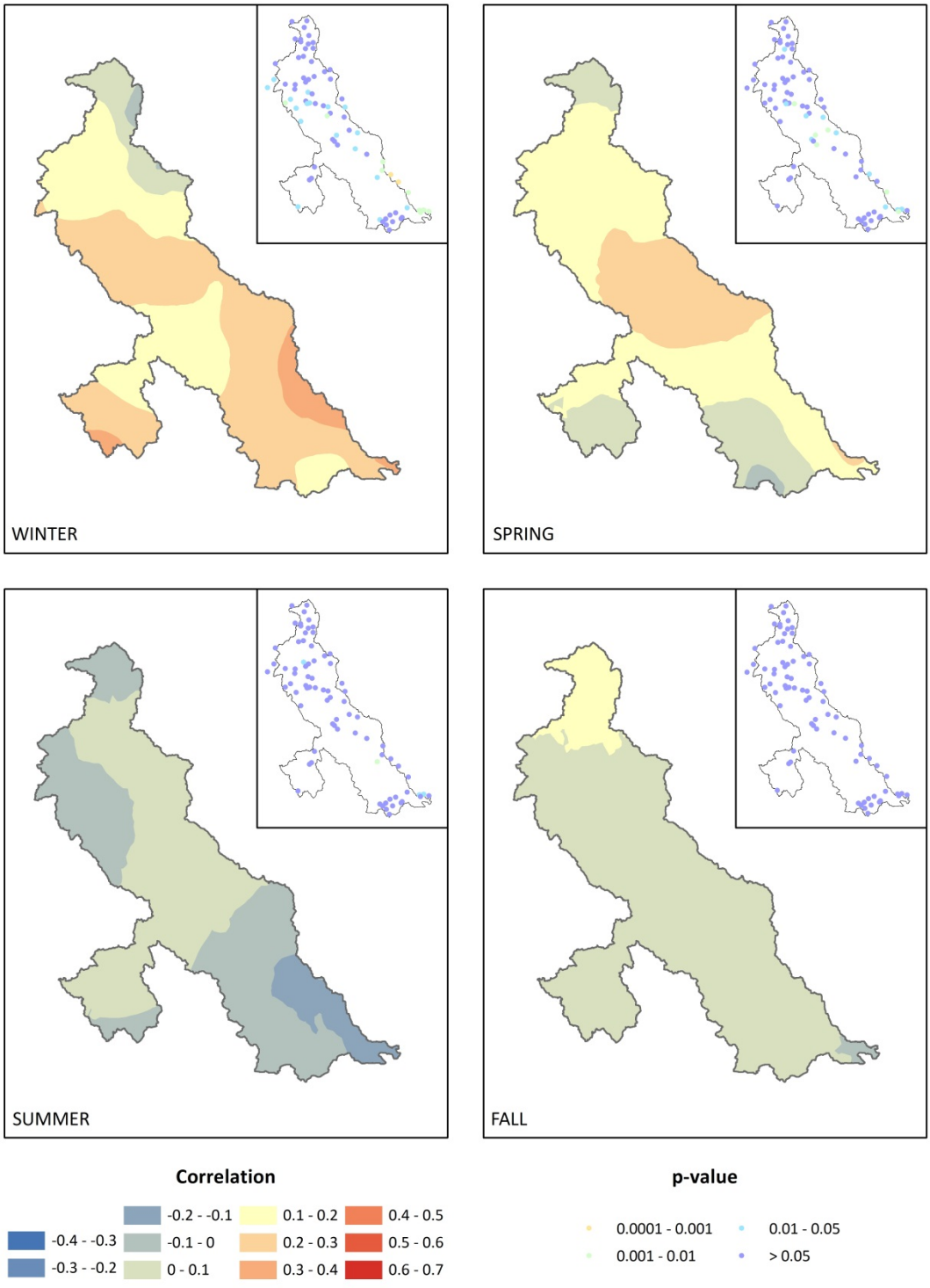

(c)

Figure 9 Continued.

2.8 CONCLUSIONS

In this study, it was found that the correlation between PDO and three ENSO indices, namely Niño 3.4, MEI, and EMI, with gauged precipitation respectively shows that both ENSO and PDO have a strong influence on the winter and spring precipitation in the basin. The overall correlation is positive, except for the Upper RG region which includes the headwaters in the San Juan range in the Rocky Mountains in southern Colorado. Therefore, higher snowfall during La Niña conditions may help in maintaining flow in the river and offset the lack of water due to precipitation reduction in arid/semi-arid New Mexico.

The correlation between the Niño 3.4 and MEI indices with precipitation are similar, since they are closely related. The temporal structure and influence of EMI is different and is not strongly correlated with precipitation in the basin.

An examination of the major El Niño and La Niña events by classifying them using four criteria (duration above defined threshold, maximum or minimum SSTA, duration in phase of interest, and intensity). ENSO events are not equivalent, some events have short duration but high intensity, while others lingers for several years with lower SSTA.

3 UNDERSTANDING CHANGES IN WATER AVAILABILITY UNDER THE INFLUENCE OF LARGE-SCALE CIRCULATION PATTERNS USING A LAND SURFACE MODEL*

3.1 OVERVIEW

Water availability plays an important role in the socio-economic development of a region. It is however, subject to the influence of large-scale circulation patterns, resulting in periodic excesses and deficits. An assessment of the degree of correlation between climate indices and water availability, and the quantification of changes with respect to major climate events is important for long-term water resources planning and management, especially in transboundary basins as it can help in conflict avoidance. In this study, following the assessment of the correlation of the Pacific Decadal Oscillation (PDO) and El Niño-Southern Oscillation (ENSO) with gauged precipitation in RG discussed in section 2, the changes in water availability using runoff generated from the Noah land surface model are quantified. Both spatial and temporal variations are noted, with winter and spring being most influenced by conditions in the Pacific Ocean. Negative correlation is observed at the headwaters and positive correlation across the rest of the basin. The influence of individual ENSO events, classified using four different criteria, is also examined. El Niños (La Niñas) generally cause an increase (decrease) in runoff, but the pattern is not consistent; the percentage change in water availability varies across events. Further, positive PDO enhances the effect of El Niño and dampens that of La Niña, but during neutral/transitioning PDO, La Niña dominates meteorological conditions. Long El Niños have more influence on water availability than short duration high intensity events. We also note that the percentage increase during El Niños significantly offsets the drought-causing effect of La Niñas.

* Part of this section is reprinted with permission from "Understanding changes in water availability in the Rio Grande/Río Bravo del Norte basin under the influence of large-scale circulation indices using the Noah land surface model" by C. P. Khedun, A. K. Mishra, J. D. Bolten, H. K. Beaudoing, R. A. Kaiser, J. R. Giardino, and V. P. Singh, 2012, *J. Geophys. Res.*, 117(D5), D05104, doi: 10.1029/2011jd016590, Copyright 2012 American Geophysical Union.

3.2 INTRODUCTION

In the previous section, the correlation between large-scale circulation patterns and gauged precipitation was effected to explore the spatial and temporal influence of ENSO and PDO separately on the basin. The correlation structure of precipitation with two canonical ENSO indices (Niño 3.4 and the Multi-ENSO index (MEI)) were compared to that of the El Niño Modoki index (EMI) to determine which index shows maximum correlation and is best suited for water management within the basin.

The degree of association between hydrologic variables and climate patterns give only qualitative information and has limited use in water management. Water planning and management is multidimensional and include factors such as demand and priority, and is constrained by availability. The first two factors are influenced by demographic changes and economic considerations and can be addressed through policies. The last factor is driven by large-scale climate variations and cannot be attended locally.

In this section the influence of large-scale climate indices, namely ENSO and PDO, on the water availability within the Rio Grande/Río Bravo del Norte basin (RG) is investigated. Streamflow is often used as a measure of surface water availability, but in large basins, stream gage records are not a realistic representation of actual flow as they are affected by dams, diversions, return flows, reduction in base flows by excessive groundwater pumping, and urbanization [*Legates et al.*, 2005], thus obscuring climate influences. Runoff can be used as a proxy for surface water availability.

Runoff is not linearly related to precipitation, but affected by natural processes and subjected to other meteorological variations, such as temperature, evapotranspiration, wind speed, etc. which are also influenced by remote climate teleconnections. A land surface model (LSM), but with land-use-land-cover constant, is used to generate runoff as it incorporates all necessary factors in the process. The basin is divided into six sub-regions and the temporal variations in water availability with respect to climate indices are examined. The percentage change in water availability in each sub-region, with respect to individual El Niño and La Niña events and coincident PDO phases is then examined.

3.3 LAND SURFACE MODELING

The hydrologic cycle is governed by both local processes and large-scale ocean-atmosphere interactions. On the local scale the land surface exerts a non-negligible influence on the atmospheric boundary layer through momentum, energy, and water fluxes. These processes occur over large spatial and temporal scales and influence both the weather and the global climate system. The interaction between land surfaces and the atmosphere can be broadly classified into two types: that affecting the physical climate system and that impacting the biogeochemical cycles. The physical system involves the exchanges of radiation, sensible heat, latent heat, and momentum, and has an immediate impact on the wind regime, precipitation, skin temperature, and soil moisture. The biogeochemical cycles involve the exchanges of gases which affect the radiative transfer characteristics and consequently the energy budget of the planet [*Sellers*, 1991].

Hence, incorporating the state and exchanges of water, energy, and carbon improves agricultural, water resources, and disaster modeling and management. Land surface models (LSMs) compute terrestrial water, energy, momentum, and bio-geochemical exchange processes by solving the governing equations of the soil-vegetation-snowpack medium [*Peters-Lidard et al.*, 2007]. A number of LSMs have been developed over the last 30 years and are constantly being refined as our understanding of the physics underlying earth system processes improves, and computing capabilities increase. Four LSMs, namely Mosaic, Noah, the Variable Infiltration Capacity (VIC), and Sacramento models, were evaluated over the Continental United States (CONUS) as part of the North American Land Data Assimilation System (NLDAS) project [*Mitchell et al.*, 2004]. *Lohmann et al.* [2004] evaluated these models for their performance in partitioning water balance terms (evapotranspiration, runoff, and storage change) across four different quadrants over CONUS, and their ability to reproduce streamflow in small- to medium-sized catchments at different timescales (daily, monthly, and annual). At the continental scale the results varied significantly in the wet eastern US but were generally in agreement over the drier western region. The Mosaic and Sacramento models underestimated runoff, and VIC produced more runoff, while Noah's predictions fell in between. In small- to medium-sized catchments, the models showed similar bias gradient in the east, increasing from north to south. VIC, for example, produced the right

annual runoff in the northeast US but more runoff towards the south. Noah predicted less runoff in the northeast US, more in the south, and the right runoff in the middle.

Of the four models, Noah showed the lowest regional bias. *Lohmann et al.* [2004] further speculated that the high runoff produced by the models in the southwestern US may be attributed to farming and irrigation which is not included within the NLDAS setup. Seasonal analysis showed that Noah produced correct runoff in a number of basins for the cold season with the same north-south annual bias. Both VIC and Noah produced soil moisture anomalies close to observed values. However, in the Little River Experimental Watershed, *Sahoo et al.* [2008] found that Noah produced higher soil moisture, which, as a result of the model physics governing partitioning, produced less surface and subsurface runoff. Nevertheless, *Lohmann et al.* [2004] found that the Sacramento and Noah reproduced daily streamflow better, with Noah having the highest overall score based on the Nash-Sutcliff efficiency. The study also evaluated the model performance over nine large basins in the US. The Rio Grande was not included, but the sizes of the basins examined are comparable. There was disagreement between modeled and measured runoff in high and less regulated basins. In high regulated basis, which comprise a number of dams and reservoirs, smaller seasonal signals were observed, whereas in less regulated ones, seasonality was closely captured. This confirms that the models were actually effectively reproducing seasonal variations, which is being dampened by engineering infrastructures in the highly regulated basins, thus lending credence in using an LSM in modeling the Rio Grande which has a large number of dams, diversions, and reservoirs.

3.3.1 NOAH LSM

Previous studies investigating the effect of climate on streamflow have generally used models which, to a large extent, ignore the effect of local and remote atmospheric phenomenon. Since the objectives of this study is to pay due consideration to the influence of remote meteorological variables on water availability, we chose the Noah LSM, developed for coupling with weather prediction and climate models. Noah LSM's [*Chen et al.*, 1996; *Koren et al.*, 1999] legacy extends into modeling efforts carried in the 1980s [*Mahrt and Ek*, 1984; *Mahrt and Pan*, 1984; *Pan and Mahrt*, 1987] and has been further refined in the 1990s under

the GEWEX/GCIP/GAPP Program Office of NOAA/OGP, led by the National Centers for Environmental Prediction (NCEP) and benefitting from the collaboration of investigators from both public and private institutions. Noah has been a candidate in major off-line land surface experiments, such as Project for Intercomparison of Land-surface Parameterization Schemes [PIPLS; *Henderson-Sellers et al.*, 1996] and the Global Soil Wetness Project [GSWP; *Dirmeyer et al.*, 1999] among others. It has been validated in both coupled and uncoupled modes [*Mitchell*, 2005] and is implemented in the MM5 modeling system (http://www.mmm.ucar.edu/mm5/mm5-home.html).

The community Noah LSM is a stand-alone 1-D column model that can simulate soil moisture (both liquid and frozen), soil temperature, skin temperature, snowpack depth, snowpack water equivalent, canopy water content, and water and energy flux terms of the surface water and energy balance [*Mitchell*, 2005]. The model has a snow layer and a canopy layer. The soil profile extends to a depth of 2 m divided into four layers from the ground surface to the bottom: 0-0.1 m, 0.1-0.4 m, 0.4-1 m, and 1-2 m. The root zone is limited to the upper 1 m of soil, and the lower 1 m layer acts as a reservoir with gravity drainage at the bottom [*Chen and Dudhia*, 2001]. The volumetric soil moisture content obeys the law of conservation of mass and is determined using the diffusive form of Richard's equation which is derived from Darcy's law under the assumption of rigid, isotropic, homogeneous, and one-dimensional vertical flow. The surface skin temperature is determined by applying a single linearized surface energy balance equation following *Mahrt and Ek* [1984]. The ground heat flux is governed by the diffusion equation for soil temperature.

The governing equations for the physical processes of the soil-vegetation-snowpack medium are solved by applying a finite difference spatial discretization and the Crank-Nicolson time integration scheme. The total evaporation, in the absence of snow, is the sum of direct evaporation from the topmost soil layer, evaporation of precipitation intercepted by plant canopy, and transpiration from canopy of vegetation. The direct evaporation from the soil layer follows *Mahfouf and Noilhan* [1991] and the potential evaporation is calculated using Penman-based energy balance and includes a stability-dependent aerodynamic resistance after *Mahrt and Ek* [1984]. The wet canopy evaporation follows *Noilhan and Planton* [1989] and

Jacquemin and Noilhan [1990]. The model adopts a gravitational free-drainage subsurface scheme, and surface runoff is the excess after infiltration [*Schaake et al.*, 1996]. A complete description of the model physics and order in which computations are carried out is available in *Chen and Dudhia* [2001] and *Grunmann* [2005].

The model has one snow layer and simulates snow accumulation, sublimation, melting, and heat exchange at snow-atmosphere and snow-soil interfaces. Precipitation is deemed snow, if the temperature of the lowest atmospheric layer is below 0°C. *Lohmann et al.* [2004] points out that one notable difference between Noah and other LSMs considered in the NLDAS project is the earlier onset of runoff in snowmelt season when compared to other models and observed values. This may make Noah a less likely candidate for streamflow studies in snow dominated watersheds. In Noah snow can either sublimate or melt as there is no horizontal transport. *Sheffield et al.* [2003] and *Pan et al.* [2003] evaluated the four LSMs considered in the NLDAS project for snow cover extent and simulated snow water equivalent. Systematic low biases were observed in the snow cover extent and snow water equivalent in the simulations for all four models and larger discrepancies were observed at higher elevations. Noah consistently underestimates the snow cover extent at all elevations. This under-prediction is partly explained by its higher snow water equivalent threshold for large snow cover values as compared to other models. Noah also tends to melt snow earlier, which is due to the low albedo values in each snow covered grid, which leads to higher available energy at the surface creating a positive feedback mechanism which enhances snowmelt and sublimation.

Hogue et al. [2005] evaluated the transferability of calibrated parameters in Noah between two semi-arid sites in the southern US for evaluating model performance under different climatic conditions these regions are subjected to. They found that generally Noah accurately simulated sensible heat, ground heat, and ground temperature. However discrepancies were noted during brief periods of moist air influx responsible for monsoon or during El Niño. When compared against other LSMs Noah reproduced streamflow with high accuracy, with the smallest bias in both evaporation and runoff with respect to observed annual water budget [*Mitchell et al.*, 2004].

Thus, based on extensive evaluation and comparison and despite some of its limitations, Noah seems the best suited LSM for the hydrological modeling of RG for purposes of this study. This study also provides an opportunity to test the validity of Noah outside the southern US border, while still within NLDAS-2 domain, and may thus supplement previous findings

3.3.2 LAND INFORMATION SYSTEM

Noah LSM has been run within NASA Goddard Space Flight Center's (GSFC) Land Information System (LIS; http://lis.gsfc.nasa.gov/). LIS, designed as a problem solving environment for hydrologic modeling applications, is an integrated high-performance land surface modeling and data assimilation framework [*Kumar et al.*, 2006] which evolved from the Global Land Data Assimilation System [GLDAS; *Rodell et al.*, 2004] and the North America Land Data Assimilation System [NLDAS; *Mitchell et al.*, 2004]. It "has been developed as an observation-driven land surface component of an Earth system model to advance our understanding of terrestrial water, energy and carbon cycles by incorporating unique NASA Earth observing system (EOS)-era observations into a near-real-time modeling capability at the 1 km scale of the observations … a challenge that was impossible prior to the development of LIS" [*Peters-Lidard et al.*, 2007].

LIS comprises an ensemble of community LSMs (e.g., Noah LSM, VIC, Community Land Model (CLM), Mosaic, Hyssib, Catchment, etc.) that normally runs as stand-alone, uncoupled from atmospheric models, using observationally based precipitation, radiation, and other meteorological inputs, along with a number of surface parameters, such as topography, vegetation, and soils. The LSMs simulate energy and water states, such as snow pack and soil moisture, soil and skin temperatures, and fluxes at the land surface, such as evaporation, transpiration, and runoff. Simulating these variables at high spatial and temporal resolution is computationally intensive, given the high density of data involved and the large number of simulation runs required. LIS uses state-of-the-art scalable high performance computing and communication technologies, designed as an object oriented framework, that facilitates the use of existing features for the development of new applications, and with abstract interfaces that allows the incorporation of new features [*Kumar et al.*, 2008]. It follows earth system

modeling standards and conventions, such as the Earth System Modeling Framework (ESMF) and Assistance for Land Modeling Activities (ALMA).

LIS has unique global water and energy cycle modeling and prediction capabilities that can benefit the study of weather extremes, such as floods and droughts [*Peters-Lidard et al.*, 2007]. It is being used in a number of areas encompassing satellite mission support, scientific research, and decision-support, e.g., in the global estimates of soil moisture by NOAA; water resource management and planning by the US Bureau of Reclamation and Mississippi Research Consortium; and agricultural management, flood and drought prediction, military mobility, and trafficability by the US Corps of Engineers and US Air Force Weather Agency [*Kumar et al.*, 2008].

3.3.3 FORCING DATA AND PARAMETERS FOR LSM

The North American Land Data Assimilation System – Phase 2 (NLDAS-2) forcing data was used to run the Noah LSM. NLDAS-2 has a 1/8° latitude/longitude resolution over a domain covering the conterminous United States, part of Canada and Mexico (125°W–67°W, 25°N–53°N), thus allowing the modeling of both the US and Mexican portion of the Rio Grande. In numerical weather prediction models, forcing errors accumulate in the surface and energy stores leading to incorrect surface water and energy partitioning and related processes. Radiation and precipitation are critical components in land surface modeling, and their accuracy has a significant impact on the ability of LSMs to produce realistic simulations of land surface processes. Thus, NLDAS aims to utilize data that that has been quality controlled and free from model bias. It incorporates both measured and modeled data from multiple sources: gauged precipitation measurements, satellite data, radar precipitation measurements, and output from numerical prediction models. NLDAS has been run retrospectively starting in January 1979, and provide hourly measurements in near real-time. The dataset include *u* and *v* wind components at 10 m above the surface, air temperature and specific humidity at 2 m above the surface, surface pressure, surface downward longwave and shortwave radiation, and total and convective fraction of precipitation, convective available potential energy, and potential evaporation. The hourly observation-based shortwave radiation field is a product

from the University of Maryland (UMD) and the National Environmental Satellite Data and Information Service (NESDIS), derived from NOAA's Geostationary Operational Environmental Satellites and interpolated from 1/2° to NLDAS grid size [*Pinker et al.*, 2003] and supplemented with EDAS/Eta data. The UMD-NESDIS product is valid at 15 minutes after the hour and is temporally interpolated to match NLDAS time conventions [*Cosgrove et al.*, 2003].

The precipitation field in NLDAS utilizes the NCEP Climate Prediction Center (CPC) reprocessed daily gauged analyses that have been subjected to orographic adjustment based on the Parameter-elevation Regressions on Independent Slopes Model [PRISM; *Daly et al.*, 1994] climatology. The reprocessed data set has approximately 13,000 daily gauge reports by combining real-time reports with non-real-time reports obtained from the National Weather Service's (NWS) COOP Network. The unified gauged precipitation is interpolated to the 1/8° NLDAS grid, and temporally disaggregated at hourly timescale using either the NWS Doppler radar-based (WSR-88D) precipitation, which has a 4 km spatial coverage, or the 8 km NOAA CPC Morphing Technique (CMORPH) hourly precipitation analyses [*Joyce et al.*, 2004]. This product uses hourly multiagency gauge data for bias correction and has been mosaicked over CONUS by NCEP/EMC [*Baldwin and Mitchell*, 1997]. The radar network is limited at the US borders with Canada and Mexico, and around 13% of CONUS are not covered. These gaps are first filled with nearest neighbor mosaicked data from within a 2° radius, and if the latter is not available, CMORPH data are used instead. In Mexico, which is outside the radar covering range, CMORPH data is used. CMORPH is not available before 2002, and CPC hourly data is used and if it is not available, the North American Regional Reanalysis [NARR; *Mesinger et al.*, 2006] data is used instead.

The NLDAS dataset has been extensively compared, tested, and validated for snow cover and snow water equivalent [*Pan et al.*, 2003; *Sheffield et al.*, 2003], soil moisture [*Schaake et al.*, 2004], and streamflow and water balance [*Lohmann et al.*, 2004]. It has also been evaluated against the Atmospheric Measurement Program/cloud and radiation testbed, the Surface Radiation observation data, and the Oklahoma Mesonet which is a quality controlled dataset

from a dense network of over 100 meteorological stations with meteorological measurements every 5 minutes [*Luo et al.*, 2003; *Robock et al.*, 2003].

Noah also requires a set of parameters defining soil, vegetation, and topography for each grid. We use Zobler's assessment of Food and Agriculture Organization (FAO) Soil Units [*Zobler*, 1986] which gives sand, silt, and clay fractions. The land cover is from the University of Maryland's (UMD) 1 km spatial resolution global land cover product [*Hansen et al.*, 2000]. It contains 14 different classes (11 vegetation types, bare ground, urban/built up area, and water). The model also requires information on the quarterly and maximum albedo, monthly greenness fraction, and bottom temperature without elevation corrections.

3.4 RESULTS AND DISCUSSIONS

3.4.1 RUNOFF AND WATER AVAILABILITY

Noah or LIS does not have a routing scheme; runoff is generated at 1/8° pixel level (Figure 10). Further, since the basin is divided into sub-regions rather than sub-basins, and because RG has a number of endorheic sub-basins, area-averaged runoff (AAR) is a better representation of regional water availability [*Shukla and Wood*, 2008].

$$AAR = \frac{\sum_{i=1}^{n} r_i}{\sum_{i=1}^{n} a_i} \quad \textbf{(2)}$$

where r is the pixel runoff at the temporal scale of interest, a is the area of the corresponding pixel, and n is the number of pixel in the sub-region considered.

Before assessing changes in water availability, we evaluated NLDAS-2 and runoff from Noah LSM against observations to assess the validity of our approach.

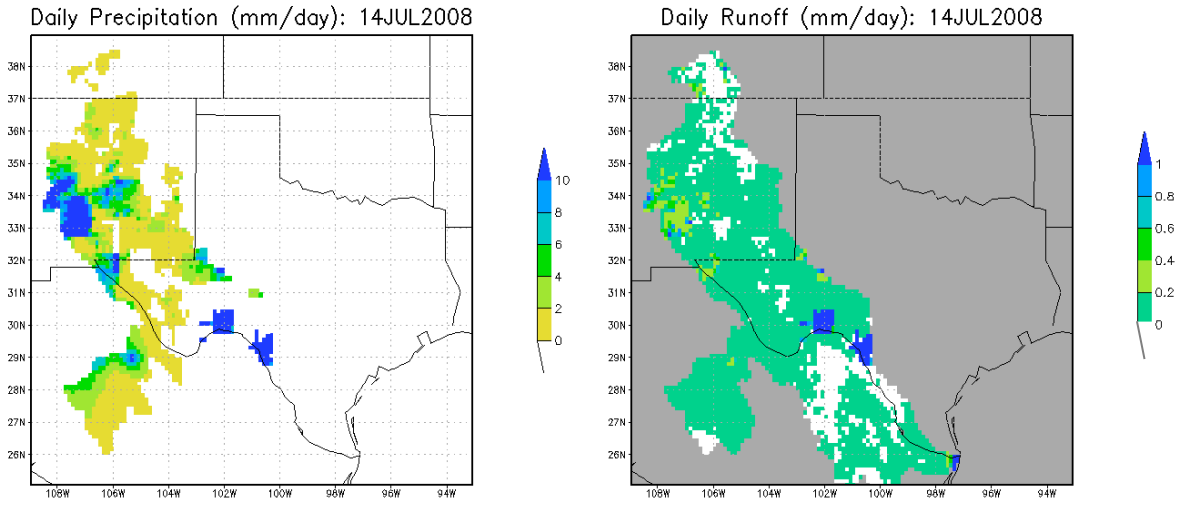

Figure 10. A snapshot of the model run showing daily precipitation and runoff within the catchment.

3.4.1.1 Model Validation

Precipitation

The precipitation field in NLDAS-2 is derived from a number of sources whose coverage near the US borders and beyond is often limited. The product has been extensively validated over CONUS but has not received the same treatment beyond the US borders. Given that RG is a transboundary basin, extending into Mexico, and that the density and length of precipitation record in Mexico is low, it is important to verify the adequacy of NLDAS-2 over the Mexican portion of the basin. We selected three of the six sub-regions within the basin, one in the US and two in Mexico, for validation. The Upper-Middle RG has a dense rain gauge network, with 31 stations; it is found almost entirely within the state of New Mexico and therefore benefits from the high quality products used in generating NLDAS-2. The two regions in Mexico are the Río Conchos and the Lower RG. Río Conchos, located entirely within Mexico, is an important sub-basin, but has only four viable stations aligned along the major axis of the catchment. The major portion of Lower RG is located within Mexico, and has 5 stations along

the US border and 11 stations in Mexico. We therefore compared the NLDAS-2 precipitation field with the observations from the Mexican stations.

The precipitation field in NLDAS does not agree very well with station observations at the hourly timescale, but as the data is aggregated over longer timescales the correlation increases [*Luo et al.*, 2003]. This is because NLDAS-2 precipitation is generated from multiple sources and averaged over the domain of interest. We compared precipitation at the monthly scale. Figure 11 shows the scatter plots of the area-averaged monthly precipitation (similar to AAR) derived from the NLDAS-2 precipitation field (M) against average monthly observed precipitation from gauges (O) within each sub-region. The data length differs, as shown by the total number of data points (N) in each plot. The relative bias, root mean square deviation (RMSD), and correlation coefficient (ρ) are given for each region, along with the identity (1:1) line.

$$Relative\ Bias = \frac{\bar{M} - \bar{O}}{\bar{O}} \quad \textbf{(3)}$$

$$RMSD = \sqrt{\frac{\sum_{i=1}^{N}(M_i - O_i)^2}{N}} \quad \textbf{(4)}$$

All three regions have very high ρ values implying that the precipitation field in NLDAS-2, at the monthly timescale, over the entire RG basin is in good agreement with observations. A small consistent bias is noted towards observations, similar to the findings reported by *Luo et al.* [2003]. The RMSD values for the Río Conchos and Lower RG are greater than that for the Upper-Middle RG by a factor of three. This can be attributed to the fact that the Upper-Middle RG has a dense network uniformly spread over the whole region, while in Mexico the density and spread is limited. Also, most stations in Mexico did not have a continuous series but have been reconstructed from observations available from adjoining sites.

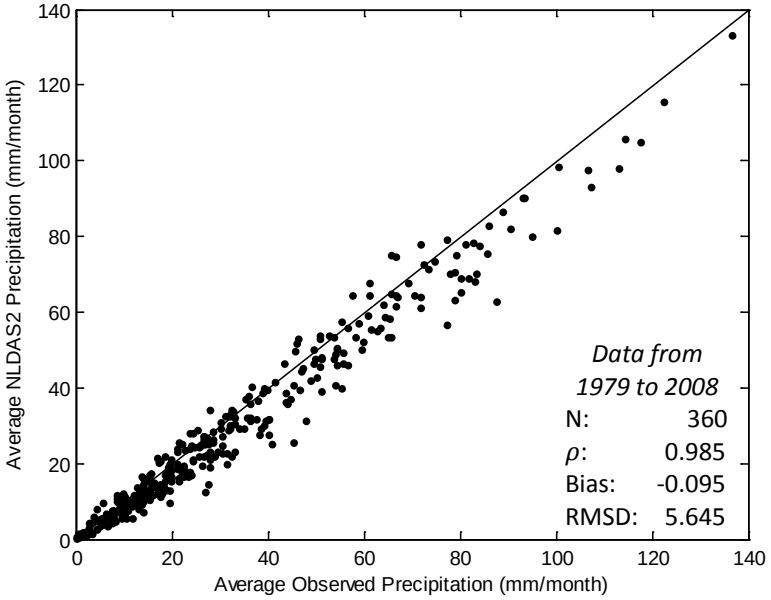

(a)

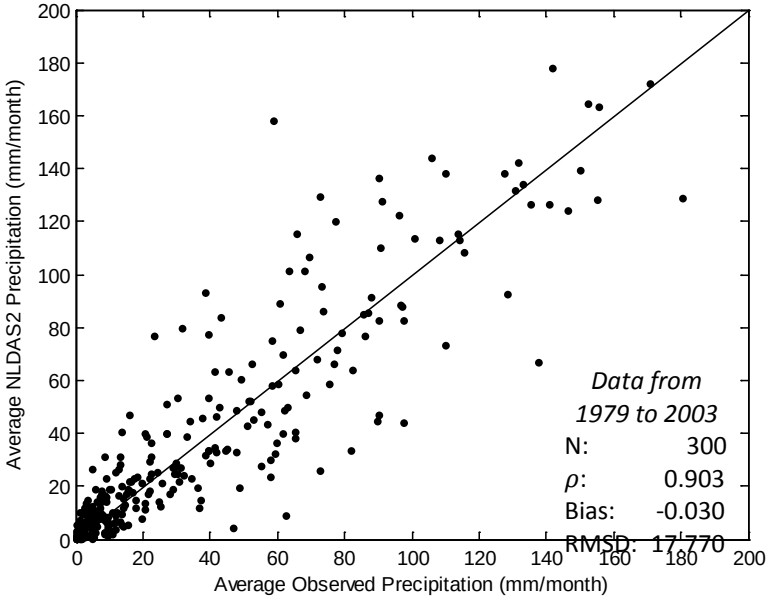

(b)

Figure 11. Scatter plot of area-averaged monthly NLDAS-2 precipitation and observed precipitation for the (a) Upper-Middle RG, (b) Río Conchos, and (c) Lower RG region (Mexican stations only).

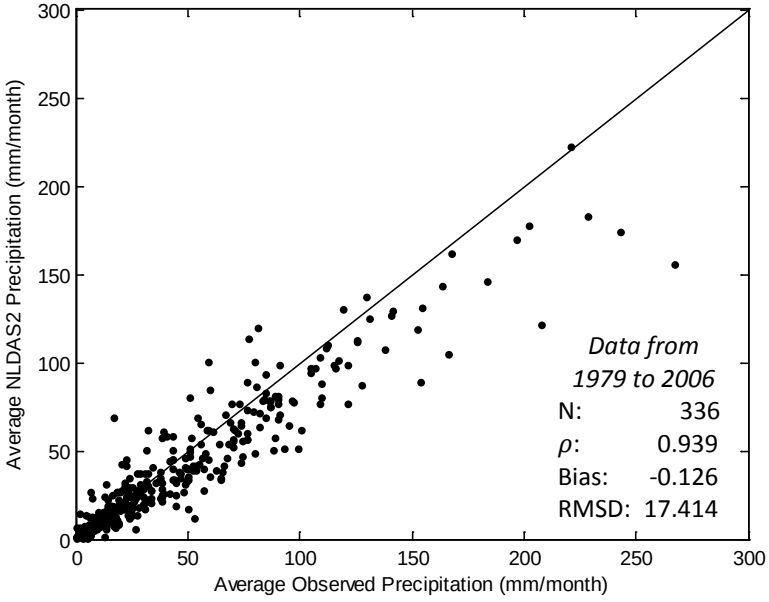

(c)

Figure 11 Continued.

Runoff

In order to assess the representativeness of the modeled runoff we compared AAR of the Río Conchos, which is a closed sub-basin, unlike the other sub-regions, to measured values at Ojinaga, which is located at the confluence of the Río Conchos with RG. Historical mean daily discharge data for RG at Ojinaga is available from the International Boundary and Water Commission (IBWC). This dataset, as can be expected, incorporates land-use-land-cover changes, the effect of dams, diversions, and other infrastructural changes. A dataset of naturalized monthly flow, extending up to 2000, for the Río Conchos at Ojinaga is also available [*Sandoval-Solis et al.*, 2010]. The naturalization process utilized streamflow recorded at gaging stations and adjusted to remove the effect of reservoir storage and evaporation, water supply diversions, and return flows from surface and groundwater, so that the resulting series is as close to flow unimpaired by engineering infrastructures. However the influence of land-use-land-cover changes, infiltration, surface storage-flow, subsurface

storage-flow, and evapotranspiration cannot be adequately accounted for [*Wurbs*, 2006]. Noah accounts for evaporation, infiltration, and other hydrological parameters; but land-use-land-cover was kept constant to minimize extraneous noise that may interfere with the climate teleconnection signals. Figure 12a gives the plot of AAR, naturalized, and observed time series of monthly streamflow in the Río Conchos. Prior to any inference, it is important to point out that none of these three series are accurate representation of flow in the basin; each have different intrinsic limitations. Figure 12b gives a 12-month-sliding-window correlation plot for the period January 1998 to December 2000, which includes the period for which Noah was validated by *Lohmann et al.* [2004], thereby giving a benchmark for comparison. Each value in the graph is the Pearson correlation coefficient for 12 consecutive months starting from the month in which it is plotted. This process allows us to compare the consistency in the correlation across different seasons.

It can be noted that Noah faithfully captures the monthly variations in runoff in the basin. Surprisingly, however, the correlation between AAR and the measured flow is consistently higher than with naturalized flow. This may be a function of the naturalization procedure, where evapotranspiration and other hydrologic process cannot be amply determined given their complexity. Another notable feature of the running correlation is the periodic variation in the correlation values. The correlation is generally between 0.85 and 0.95 except for certain short intervals, which may be attributed to reservoir operation and diversions affecting the recorded flow. *Lohmann et al.* [2004] reported a correlation of 0.954 for the Nehalem River in Oregon which is a much smaller watershed (1,727 km^2) compared to the Río Conchos (64,000 km^2). In the larger snow dominated Wind River in Wyoming (4,897 km^2), a very low correlation of 0.117 was obtained which was due to a difference in the timing of snowmelt in Noah. The highest correlation across the series is generally noted in the fall and winter and this can be explained by multiple factors: the timing of snowmelt [*Pan et al.*, 2003; *Sheffield et al.*, 2003], the influence of the North American Monsoon [*Hogue et al.*, 2005], and the influence of engineering infrastructures, such as dams, return flows, and unmetered diversions for agricultural purposes within the basin. Given that summer and early fall are the wettest months for the region (Figure 4), streamflow may initially be stored in the reservoirs and any

excess thereafter is released once the reservoirs have reached capacity and hence recorded at the downstream stream gauge as values closest to the natural variations.

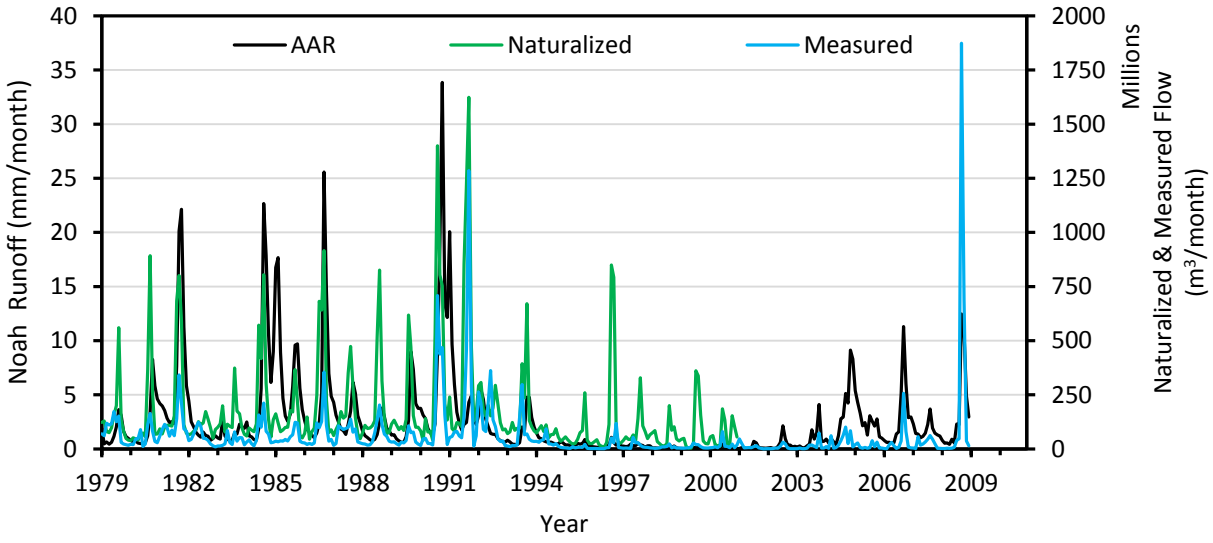

(a)

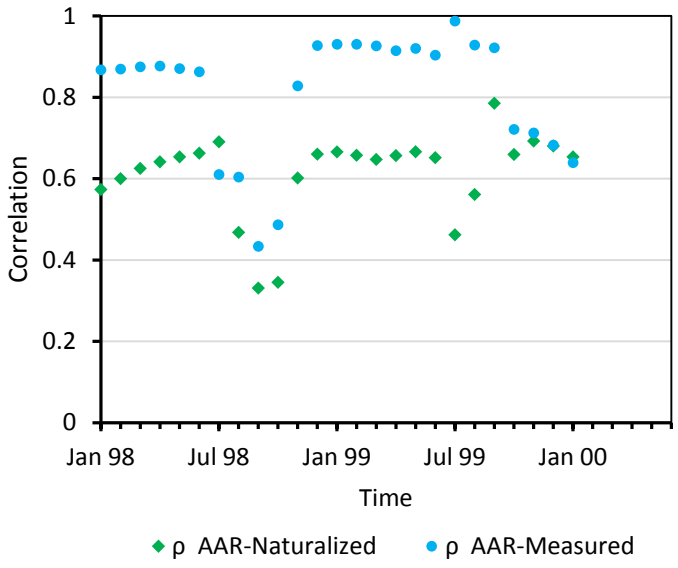

(b)

Figure 12. (a) Modeled, naturalized, and measured streamflow in the Río Conchos sub-basin, (b) sliding-window correlation.

3.4.1.2 Temporal Pattern – Climate Indices, Precipitation, and Water Availability

Continuous wavelet transform allows the study of the temporal structure of precipitation and runoff across the basin and make inferences on the influence of climate variability patterns. Wavelet transform decomposes a signal in terms of some elementary functions derived from a "mother wavelet" using a sliding window function whose radius increases in space (i.e., decreasing in frequency), allowing the low-frequency content of the signal to be resolved [*Rivera et al.*, 2004]. A number of mother wavelets are commonly used, and can be grouped into continuous and orthogonal wavelets; each having intrinsic advantages for specific applications. We chose the Morlet wavelet, which consists of a plane wave modified by a Gaussian envelope, as it is the most widely used continuous wavelet in geophysical applications. Its complex structure allows the detection of both time-dependent amplitude and phase for different frequencies in the time series [*Lau and Weng*, 1995].

Kumar and Foufoula-Georgiou [1997] discussed the applications of wavelet to geophysical processes. *Torrence and Compo* [1998] reported on the application of wavelet, including a comparison to the widowed Fourier transform, to climate analysis using ENSO series. *Labat et al.* [2001] showed how wavelet can be appropriately employed in rainfall-runoff analysis.

The continuous wavelet power spectrum of AAR from each section of the basin is given in Figure 13b and can be compared against those of the four climate indices considered in this study (Figure 13a). The time spans for the plots of climate indices are the same as for runoff, i.e., 1979 to 2008. We used the MATLAB® based software package developed by *Grinsted et al.* [2004] (available from http://www.pol.ac.uk/home/research/waveletcoherence/) for generating the wavelet plots. The statistical significance of the peaks in the wavelet spectrum was tested using Monte Carlo methods against a lag-1 autoregressive red noise background; peaks with greater than 95% confidence are designated by thick black contours in the figures. However, regions out of these 95% confidence level areas should not be construed as the product of noise only. Natural processes are also present in these regions, albeit having a lower bearing on the power spectrum, and information on the influence of climate teleconnections can still be garnered from them [*Anctil and Coulibaly*, 2004].

PDO has a cycle of about 20 to 30 years, which is not apparent in this wavelet power spectrum, as it is limited to 1979 to 2008 only. During this time span, the index was mostly positive until 1995 after which it oscillated with a period of three and a half years in each phase (Figure 3). This cycle is visible in the continuous wavelet power spectrum. ENSO has a much shorter wavelength, with a recurrence pattern of 3 to 6 years and every event normally lasts for around a year. Significant power in this band is observed throughout the entire record in the wavelet power spectrum of both Niño 3.4 and MEI, along with weaker significant power in the 1.5 to 2 year band associated with secondary variations in the indices while in a particular phase. Niño 3.4 and MEI have very similar power spectrum as they are highly correlated (ρ = 0.92). The plot for EMI is different from the latter indices as it has a different mode and evolves with a different frequency [*Ashok et al.*, 2007].

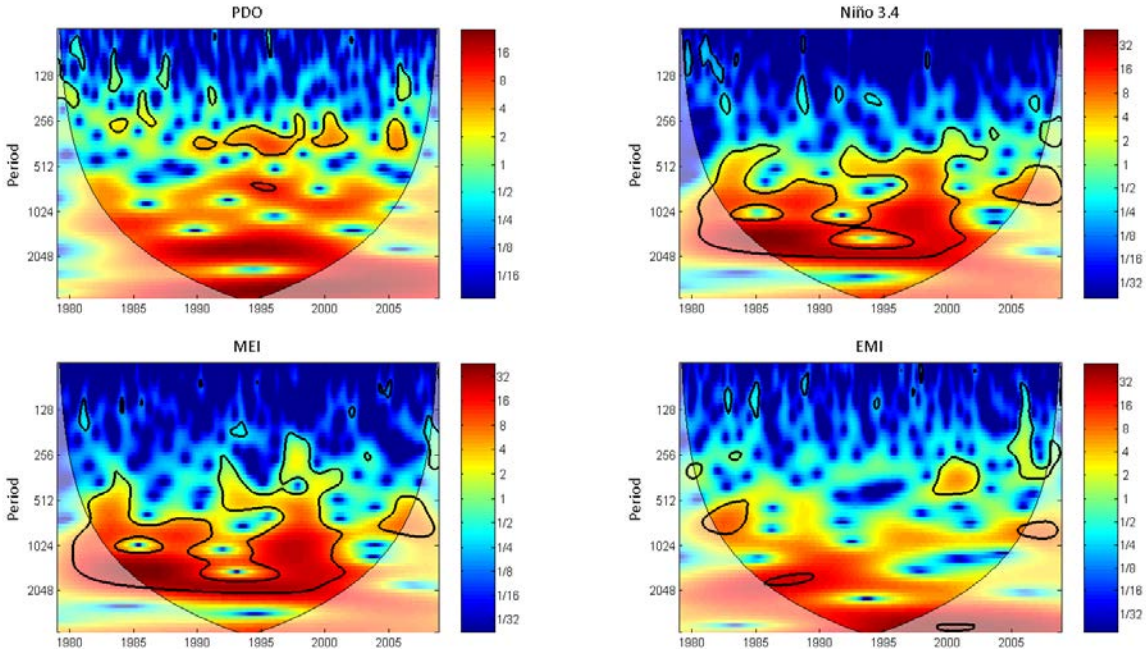

(a)

Figure 13. Continuous wavelet power spectrum of (a) climate indices and (b) AAR for each region. Period is in days. The thick black contours designate the 5% significance level against red noise and the thin black line demarcate the cone of influence beyond which, shown in a lighter shade, the image may be distorted since the data is not padded at the edges.

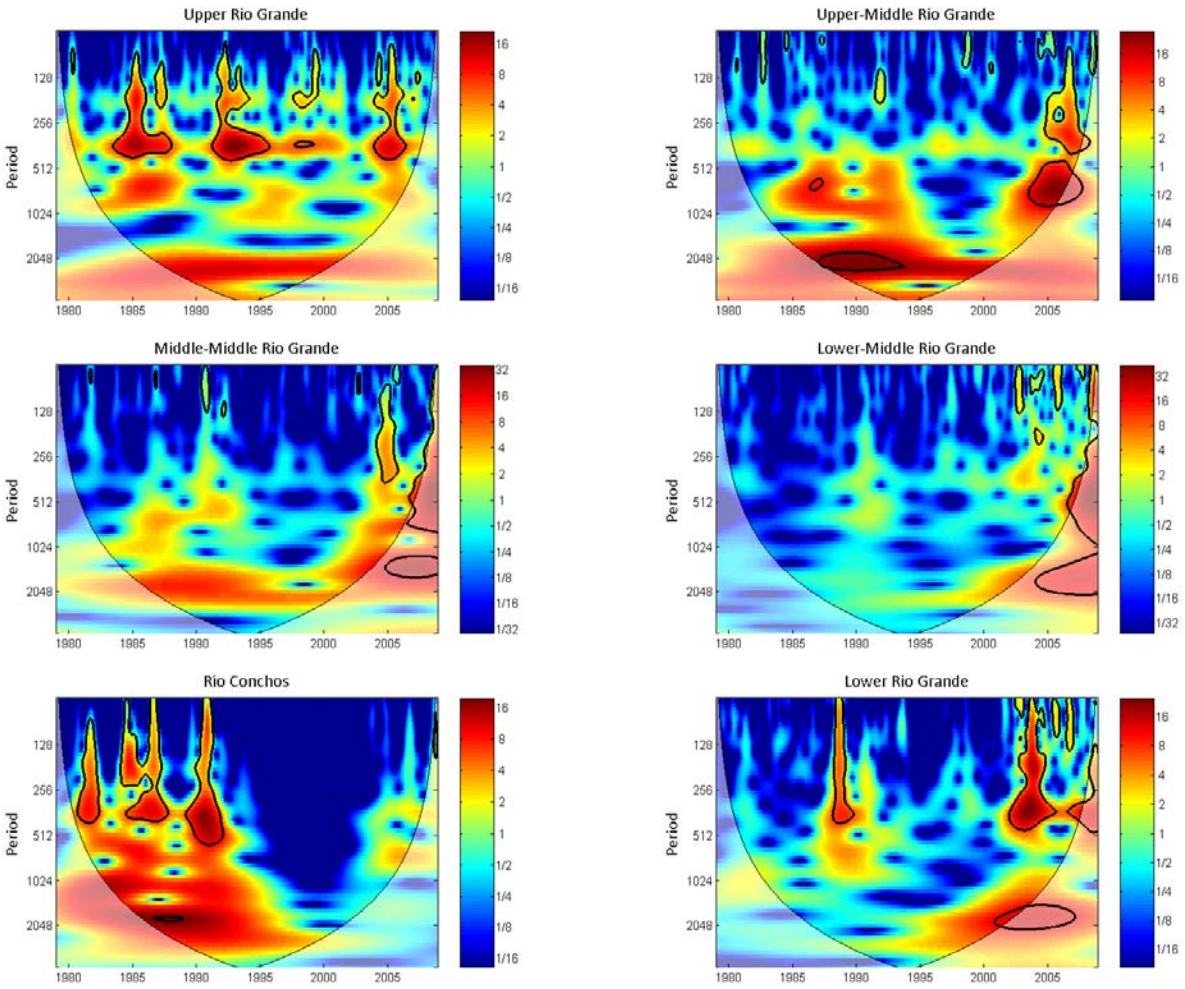

(b)

Figure 13 Continued.

Variations at both ENSO and PDO frequencies are apparent in the wavelet power spectrum of AAR. Significant powers in the smaller period (higher frequency) band are the result of seasonal variations. It is worth pointing out that the continuous wavelet power spectra of both the averaged gauged precipitation and the first principal component of gauged precipitation for each sub-region (not shown here) exhibited variations similar to ENSO and PDO frequencies, further supporting the correlations established in section 2.7.2. The fact that the influence of climate variability was more apparent in precipitation than in streamflow is because runoff is not a first order response of precipitation but is filtered by the watershed characteristics

[*Legates et al.*, 2005]. Looking closer at each spectrum we note that in the Upper RG region significant power at the 5% significance level is exhibited within the high frequency band, coincident with the pattern exhibited by the PDO spectrum but ENSO related patterns were not significant at the 5% level. In the Upper-Middle RG region, however, variations at the ENSO frequencies are clearly evident in most part of the spectrum except for the period 1995 to 2003. In the Middle-Middle RG region, the spectrum exhibited variations in the ENSO frequencies even though not statistically significant throughout. The spectrum for the Lower-Middle RG region was devoid of statistically significant powers as can be expected, because the correlation of ENSO indices with precipitation is consistently lower than in its two adjoining regions (Figure 9). In the Lower RG region variations at ENSO frequencies is visible in the second half of the series. It should be noted that this region is close to the Gulf of Mexico and subjected to oceanic influences and hurricanes whose effects are embedded in the model outputs. In the Río Conchos, variations at ENSO frequencies are evident in the first half of the series but completely absent in the second part when the basin was subjected to an exceptional drought.

3.4.2 Effects of Large-scale Circulation Patterns on Water Availability

After having established the spatial correlation of precipitation with large scale climate indices and investigated the sensitivity of runoff to PDO and ENSO using continuous wavelet transform, we now discuss the changes in water availability with respect to major El Niño and La Niña events. We also determine if there is any lag in runoff relative to ENSO.

3.4.2.1 Lag Correlation

To investigate the lag between individual ENSO events and runoff in RG we considered an 18-month long series encompassing each event. Most events peaked in early winter; therefore the series considered extended from March before to August after the peak. The 1986-1988 El Niño peaked earlier in September and thus the range considered was from December before to May after the peak. Table 3 gives monthly lag correlation coefficients of AAR of the whole RG basin relative to the Niño 3.4 index. The lag is defined by the month having maximum statistically significant correlation. A positive lag indicates that the index led runoff. Lags

ranging between 0 to 3 months were observed for AAR of the whole basin with respect to most El Niños and La Niñas. It is interesting to note that for some events a negative correlation was observed despite the fact that there is an overall dominant positive correlation between ENSO and runoff in the basin.

Table 3. Lag correlation of Niño 3.4 index with Noah runoff for the whole of the basin.

Lag (months)	El Niño Event					La Niña Event			
	1982-1984	**1986-1988**	**1991-1993**	**1997-1999**	**2002-2004**	**1984-1986**	**1988-1990**	**1998-2000**	**2007-2008**
-6	0.332	0.464	-0.375	0.659	-0.409	-0.004	-0.047	-0.790	-0.319
-5	0.237	0.555	-0.276	0.542	-0.073	-0.175	-0.217	-0.681	-0.322
-4	0.120	0.628	-0.182	0.432	0.193	-0.261	-0.453	-0.428	-0.202
-3	-0.144	0.669	-0.091	0.332	0.351	-0.323	-0.539	-0.102	-0.056
-2	-0.272	0.668	0.051	0.272	0.551	-0.324	-0.508	0.299	0.058
-1	-0.226	0.627	0.283	0.102	0.562	-0.228	-0.415	0.426	0.329
0	-0.350	0.562	0.597	-0.185	0.456	-0.300	-0.102	0.354	0.649
+1	-0.509	0.293	0.707	-0.370	0.210	-0.355	-0.086	0.311	0.675
+2	-0.384	0.085	0.730	-0.485	-0.094	-0.471	-0.077	0.251	0.614
+3	0.031	-0.093	0.622	-0.453	-0.187	-0.339	0.069	0.121	0.450
+4	0.002	-0.223	0.405	-0.287	-0.242	-0.074	0.266	-0.021	0.178
+5	-0.019	-0.294	0.151	-0.289	-0.145	0.180	0.511	-0.054	-0.148
+6	-0.025	-0.322	-0.040	-0.262	-0.276	0.213	0.649	0.010	-0.431

Shaded values are statistically significant at $p < 0.05$

Lag correlation was also computed for each sub-region and the consolidated result of the statistically significant correlations is shown in Figure 14. For the 1998-2000 La Niña, which is bimodal, the lags shown are with respect to the second dip as it has a lower SSTA. In the Upper RG the lag is 3 to 4 months. In the Middle-Middle RG a consistent lag of 1 to 4 months

is observed relative to most El Niño events and in the Rio Conchos a lag of 0 to 5 months is observed relative to three of the four La Niñas considered. This result is consistent with the findings of *Chen and Kumar* [2002] who used a large-area basin-scale LSM to investigate the relationship among terrestrial hydrologic processes with ENSO over North America and *Kumar and Hoerling* [2003] who compared and confirmed the observed lag in zonal mean tropical thermal anomalies with respect to east Pacific SST using an atmospheric GCM.

Lag (months)	Upper RG		Upper-Middle RG		Middle-Middle RG		Lower-Middle RG		Lower RG		Río Conchos	
-6	△▲		▲	▼	▲△	▼		▼	△		△	▽
-5	▲		△	▽	△△			▽		▼	△	▽
-4	△△	▽	△	▽	△△	▽	△			▽	▲	▽▽
-3		▽▼	△▲	▽	△		▲		△	▽	△	▽▽
-2	▲	▽	△		▲		△		△△	▽	△	▽▼
-1	△	▽	△		△		△		▲△		△	▽▽
0			△	▼▽	△	▽▽		▼	△▲	▽	▲	▼
+1			▲	▽▼	△△△	▼	△	▽		▽	△	▽▽
+2	△	▽	△	▽▽	△▲▲	▽	▲			▼		▽▼
+3	▲▲	▽		▽▽	△△△		△			▽	△▲	▽▽
+4	△△	▼		▼		▼	▲			▼	△△	▽
+5		▽		▽								▼▽▽
+6								▼		▼	▲	▽

Legend

(filled triangles are for maximum statistically significant correlations)

Symbols	El Niño Event	Symbols	La Niña Event
△ ▲	1982-1984	▽ ▼	1984-1986
△ ▲	1986-1988	▽ ▼	1988-1990
△ ▲	1991-1993	▽ ▼	1998-2000
△ ▲	1997-1999	▽ ▼	2007-2008
△ ▲	2002-2004		

Figure 14. Lag correlation for each section of the basin.

3.4.2.2 Changes in Water Availability

In order to assess the effects of ENSO events on water availability, the seasonal percentage change with respect to the long term average in AAR, for each sub-region and for the whole basin was computed (Figure 15). ENSO events typically peak around November and since the lag between ENSO and runoff was found to be generally between 0 month to a season, water availability in winter and spring are expected to be most influenced. Note, however, that the 1986-1988 El Niño and 1998-2000 La Niña do not fit the general trend. The 1986-1988 El Niño lingered for a year before reaching its peak temperature and the 1998-2000 La Niña was bi-modal, with two distinct troughs, over a 27-month period.

The first thing we note is that even though there is a general tendency for an increase (decrease) in runoff during El Niños (La Niñas), some events actually caused a decrease (increase) in water availability.

PDO generally enhances ENSO events [*Kurtzman and Scanlon*, 2007], therefore we also consider the phases of PDO for corresponding major El Niño and La Niña events in our discussion. Table 4 gives the coincident phases of PDO with respect to the ENSO events considered. We note that some El Niños (La Niñas) were strengthened by positive (negative) PDO, while others coincided with weak or transitioning PDO.

Table 4. PDO phase for major ENSO events.

El Niño Event	PDO Phase	La Niña Event	PDO Phase
1982-1984	Weak but overall +	1984-1986	+
1986-1988	+	1988-1990	Transitioning (+ to –)
1991-1993	Transitioning (– to +)	1998-2000	Transitioning (+ to –)
1997-1999	Transitioning (+ to –)	2007-2008	–
2002-2004	+		

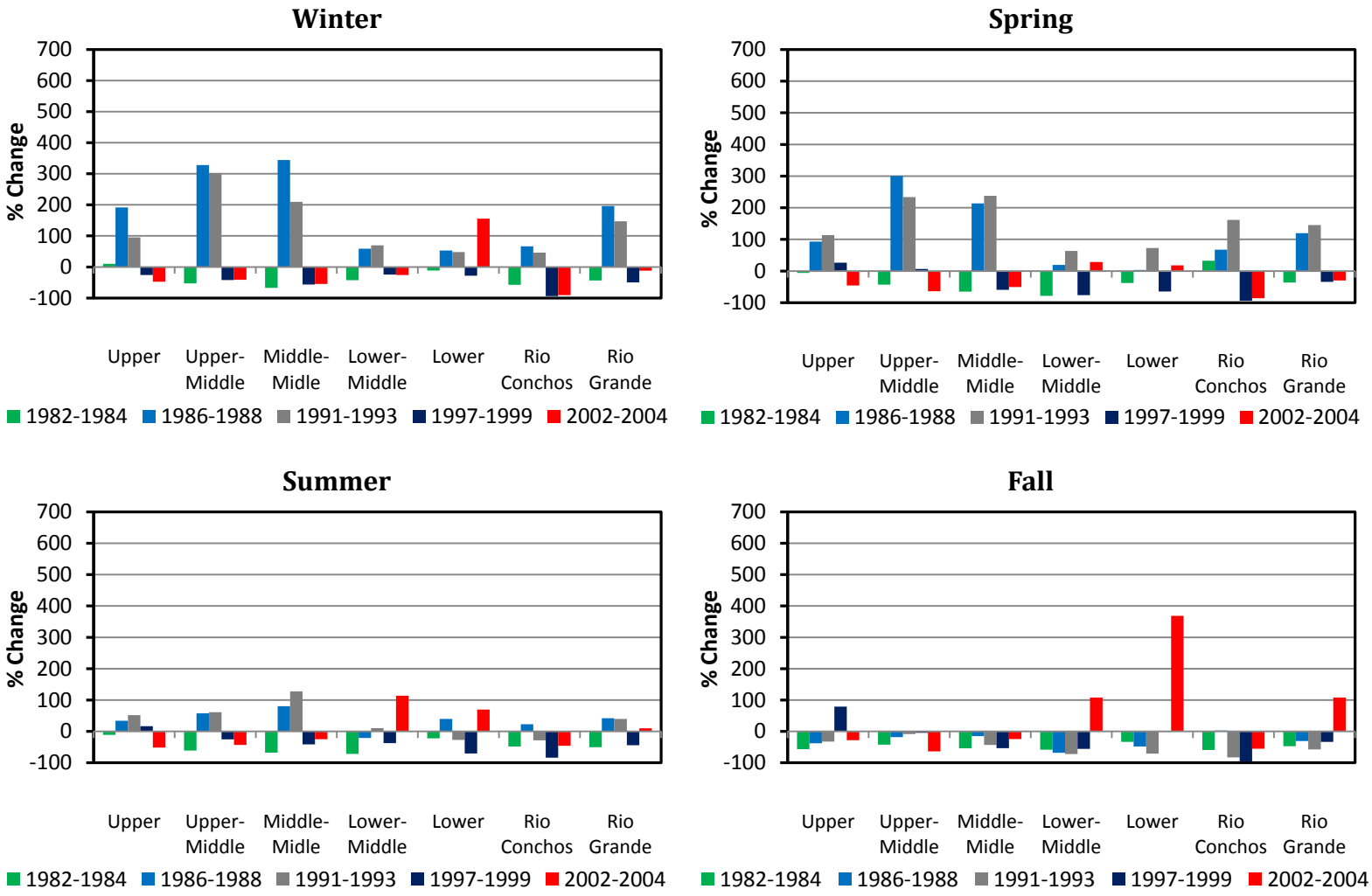

(a)

Figure 15. Percentage change in water availability during (a) El Niño and (b) La Niña events.

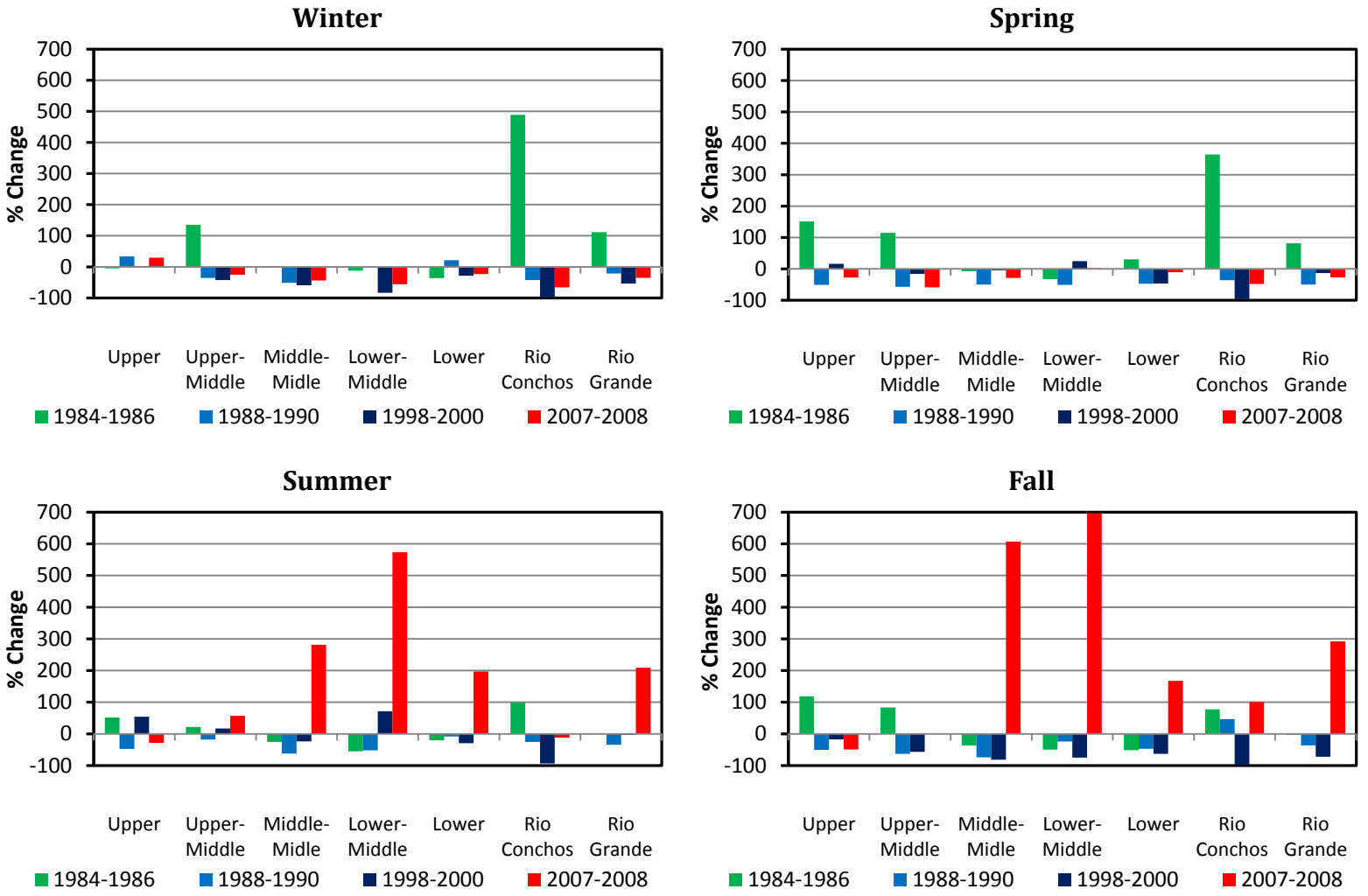

(b)

Figure 15 Continued.

El Niño and PDO

The 1986-1988 El Niño, even though was the third strongest event since 1979 (Table 2), brought the highest percentage increase in runoff for the whole basin (196%), with the upper half of the basin gaining between 190 to 350% more runoff in winter. The lower half, including Río Conchos experienced a more modest increase of around 60%. The same pattern, but with lower percentages, persisted in spring and summer. The event was enhanced by a strong positive PDO – both events evolved synchronously and peaked in August 1987 (Figure 3).

The 1991-1993 El Niño coincided with a PDO transitioning into its positive phase. It triggered the same pattern in runoff but with slightly lower percentages (average of 147% for the whole basin). The Río Conchos benefitted from the highest increase in runoff in spring during that event, compared to all other El Niños. This event had the longest duration above the ±0.5°C threshold among the El Niños considered, but was not within the top three in terms of maximum temperature recorded. It had three peaks; the two following the first one, however, have lower SSTAs. The second peak coincided with positive PDO and the third one coincided with a temporary shift in the phase of PDO to negative. Interestingly, the percentage change in AAR was negative across the basin during both the second and third peaks.

The 1982-1984, 1997-1999, and 2002-2004 El Niños did not generate higher runoff in the basin, but rather a decrease in water availability. AAR was lower by 50% over the whole basin and over 90% in the Río Conchos sub-basin. The 1982-1984 and 1997-1999 events were two of the strongest El Niños on record, based on ENSO intensity and maximum temperature recorded. They both coincided with weak PDO; the 1982-1984 event starts when PDO was in its positive phase but peaked when the latter was almost neutral, oscillating between phases. The 1997-1999 event coincided with a PDO decaying from its positive to negative phase.

La Niña and PDO

AAR in the basin was normally lower than the long term average during La Niña winters and springs, except for the 1984-1986 event. The three events (1988-1990, 1998-2000, and 2007-

2008) that caused a decrease in water availability occurred when PDO was either in its negative phase or transitioning from positive to negative. Given that the 1998-2000 event is the longest La Niña since 1979 (27 months) and is bimodal, with the second dip, occurring in January 2000, having a lower SSTA and coinciding with negative PDO, we also computed the change in water availability following the second dip (not shown in Figure 15). A decrease in AAR was noted across all sub-regions, except for winter in Upper RG (increase of 6%) which exhibits negative correlation with ENSO. The total decrease in AAR for the whole basin was nearly 60% for year 2000.

The 1984-1986 La Niña coincided with a positive PDO and was the only event that caused an increase in water availability. An exceptionally large increase is noted in the Río Conchos in both winter and spring, which translated in an increase for the whole basin. These results are consistent with the analysis of multiyear droughts in the past three centuries by *Cole et al.* [2002] who showed that persistent negative PDO enhances the impact of La Niña related droughts, while oscillating PDO produced moderate and/or localized droughts, and a positive PDO would suppress drought despite persistent La Niña conditions.

Based on the above observations, we note that PDO has an important influence on water availability in the basin. A positive PDO enhances the effect of El Niño and dampens the negative effect of La Niña. When PDO is in a neutral/transition phase, La Niña dominates climatic conditions and reduces water availability. El Niños lingering for long periods have more influence on water availability than short duration high intensity events. Finally it is interesting to note that the percentage increase during El Niños significantly offsets the drought-causing effect of La Niñas. This finding should not be discounted in long-term water resources planning.

3.5 CONCLUSIONS

Local meteorological and hydrological variables, and hence water availability, are influenced by large-scale climate indices. In this section the influence of ENSO and PDO on the water availability in RG was investigated by first establishing the spatial and temporal variation of the correlation between climate indices and gauged precipitation across the basin and then

determining percentage changes in water availability as derived from an LSM instead of using streamflow which is constantly impacted by activities in the basin masking climate influences.

Runoff across the basin was generated using the Noah LSM and AAR was used as a proxy for water availability. The basin was divided into six sub-regions for analysis purposes. Continuous wavelet power spectrum shows the extent of influence of ENSO and PDO on runoff. Variations at both ENSO and PDO frequencies are apparent in the wavelet power spectrum of AAR for each region.

The influence of individual ENSO events, five El Niños and four La Niñas between 1979 and 2008 and corresponding phases of PDO, on water availability in the basin was investigated. Lags ranging between 0 to 3 months were observed between runoff and ENSO events. A general increase (decrease) in runoff during El Niños (La Niñas) was noted but some individual events actually caused a decrease (increase) in water availability. El Niños lingering for long periods have more influence on water availability than short duration high intensity events. The upper-middle section of the basin records a higher increase in winter water availability during El Niño events (200-300%) while the lower half, including the Río Conchos, experiences a more modest change.

PDO has an important influence on water availability. A positive PDO enhances the effect of El Niño and dampens the negative effect of La Niña. When it is in its neutral/transition phase, La Niña dominates climatic conditions and reduces water availability.

The percentage increase during El Niños significantly offsets the decrease registered during La Niñas. This finding is important for water resources planning.

The study extends the discussion between the influence of large-scale circulation patterns and local meteorological and hydrological conditions by quantifying the seasonal percentage changes in water availability, which is more tangible information for water resources planning. Climate change may alter the frequency and intensity of ENSO events and may cause droughts that are more extreme and/or of longer duration than on record. The current results, while not intended for prediction purposes, may help in the long-term sustainable water planning and management within the basin for both the United States and Mexico.

Finally, the methodology presented in this section is not limited to the watershed scale but can be applied to larger continental scale to assess the need and effectiveness of interstate water transfers.

4 WATER DEFICIT DURATION AND SEVERITY ANALYSIS BASED ON RUNOFF DERIVED FROM THE NOAH LAND SURFACE MODEL*

4.1 OVERVIEW

The identification and prediction of drought events depend on the integrity of the dataset employed. Streamflow is a good indicator of surface water availability and has dominated the literature on frequency analysis of hydrological droughts and water management. However, gauged measurements are impaired by climate and land use changes, especially in large, modified watersheds. Hence, their use in drought prediction is limited, as they may violate the assumption of stationarity, unless a naturalized observation series is obtained. In this section land surface model generated runoff of the Rio Grande/Río Bravo del Norte basin (RG) is used. Land use land cover is kept constant so that changes are due to climatological variations. The river treads across several climatic zones; therefore the basin is divided into different regions for analysis. Using statistical theory of runs, water deficit duration and severity and drought inter-arrival time are extracted from three-month standardized runoff index series for each region and for the whole basin. Copulas are used to develop joint distribution functions of water deficit duration and severity. Nine copulas, two from the extreme value family and seven from the one-parameter families of the Archimedean copulas are tested. Different copulas are deemed suitable for each region as they are subject to different climatologic conditions, which affect the nature of deficit events, especially at the extremes. Conditional probability models of duration and severity are developed and compared for two regions – one experiencing alpine climate at the headwaters and one in the semi-arid portion of the basin. Further, conditional probabilities derived from model runoff are compared with that based on observed precipitation. Finally, univariate and conditional return periods based on duration

* Part of this section is reprinted with permission from "Water deficit duration and severity analysis based on runoff derived from the Noah land surface model" by C. P. Khedun, H. Chowdhary, A. K. Mishra, J. R. Giardino, and V. P. Singh, 2012, *J. Hydrol. Eng.*, doi: 10.1061/(ASCE)HE.1943-5584.0000637, in press, Copyright 2012 American Society of Civil Engineers.

and severity are computed for the basin and their significance in long-term water resources planning is discussed.

4.2 INTRODUCTION

Droughts have catastrophic impacts across a wide range of sectors: domestic water supply, agriculture, economy, ecology, health, etc. Proper assessment of droughts is central to water management. Early identification and prediction can help mitigate the negative impacts of a drought. A number of indices have been developed and are currently in use for characterizing droughts. These indices can be based on either only one meteorological variable or a set of variables, ranging from precipitation, temperature, vegetation conditions, streamflow, etc. [*Mishra and Singh*, 2010]. Each index has its advantages and drawbacks and may be best suited for a particular application. One major challenge in computing these indices, however, is the integrity of the original datasets. Precipitation, the most important hydrologic variable, is not significantly affected by anthropogenic changes, if we discount climate change, but other local variables, such as soil moisture and streamflow are greatly influenced by land use land cover changes.

Streamflow is an important measure of surface water availability and has dominated the literature on frequency analysis of hydrological droughts and water management. It is a good indicator of variability as it incorporates meteorological forcings, even though not as a first order response but filtered by watershed characteristics. However, gauged measurements, especially in large, modified catchments, do not accurately reflect changes in water availability as they are affected by dams, diversions, return flows, reduction of base flows by excessive groundwater pumping, and urbanization [*Legates et al.,* 2005]. Hence, their use in drought prediction is limited, as they may violate the assumption of stationarity, unless a naturalized observation series is obtained.

In this study a land surface model (LSM), with land use land cover kept constant, is used to generate runoff in the Rio Grande/Río Bravo del Norte basin. It is a transboundary basin and is vital for the economy of both the United States and Mexico. It is ‘heavily engineered’ on both sides of the border and the flow is over allocated, such that in periods of extreme droughts the

river does not reach the Gulf of Mexico. Thirty years of runoff data is generated for the basin using Noah LSM; standardized runoff index is computed from which the duration and associated severity of water deficits are extracted and a copulas are employed to analyze the bivariate characteristics of water deficit duration and severity in different parts of the basin.

Nine copulas, two from the extreme value family and seven from the one-parameter families of the Archimedean copulas, are considered in order to assess which ones are most suited to model the dataset. Joint probabilities of water deficit duration and severity, conditional probability distribution charts of severity given a threshold duration and of duration given a threshold drought severity, and conditional return periods of severity and duration are presented.

4.3 DATA AND METHDOLOGY

4.3.1 RUNOFF MODELING

Runoff data used in this section is derived from the hydrological modeling of the basin using Noah LSM, discussed in section 3.3. The LSM was run retrospectively for a period of 30 years (1 January 1979 to 31 December 2008) at a time step of 30 minutes and output files are written for every 3 hours. The three-hourly modeled runoff outputs, at the pixel scale, was spatially and temporally aggregated to produce monthly area-averaged runoff (AAR) series (section 3.4.1) for each of the six sub-regions in the basin and for the basin as a whole.

4.3.2 STANDARDIZED RUNOFF INDEX

Of all the indices developed for drought assessment, the standardized precipitation index (SPI) [*McKee et al.*, 1993] is perhaps the simplest one as it is based solely on recorded precipitation. *Guttman* [1999] notes that the motivation was to have an index that can be compared across different climatic regions. It is designed to be a spatially invariant quantity that can be computed to give precipitation excesses and deficits at multiple timescales. It gives a better representation of abnormal wetness and dryness than the Palmer Drought Severity Index (PDSI) for example, and can provide an early warning of drought as compared to other indices

that utilize soil moisture because runoff and reservoir storage respond faster to a storm event than soil moisture, thus making it a suitable index for use by the water management community.

The standardized runoff index (SRI) is a natural extension of SPI. It has more appeal as it is not limited to one water quantity determinant only but incorporates both hydrologic and meteorological processes that influence the volume and timing of streamflow [*Shukla and Wood*, 2008]. SRI is calculated following the same procedure as SPI from the simulated AAR.

Different averaging periods can be considered to determine a set of time scales of 2-, 3-, 6-,…, 36-month periods depending on the SRI of interest. In this study, a three-month SRI [hereafter referred to as SRI(3)] was used in order to preserve seasonal variations. *McKee et al.* [1993] utilized a gamma distribution for fitting precipitation data series, but other distributions may be more appropriate depending on the geographic location which determine precipitation patterns, and the degree of temporal aggregation which may affect the statistical characteristics (especially skewness and kurtosis) of the AAR series [*Shukla and Wood*, 2008]. *Guttman* [1999] explains that the use of different probability distributions will lead to different values. In order to maintain a baseline for comparison across the basin, the gamma distribution was chosen for each region and for the whole basin. The gamma function is not defined for values equal to zero, but AAR may contain zeros, though at a much lesser frequency than precipitation; therefore to circumvent the presence of zeros in the dataset, a mixed distribution [$H(x) = q + (1 - q)G(x)$] was employed, where q is the probability of zeros and $G(x)$ is the distribution function estimated from non-zero values. The resulting CDF was then transformed to the standard normal distribution with mean zero and variance one, which gave the values of SRI. Normalizing allowed for a consistent representation of wet and dry periods. A positive SRI value indicates a wetter than normal period and a negative value shows a water deficit. *McKee et al.* [1993] proposed four arbitrary thresholds (0, −1, −1.5, and −2) for defining the severity of a drought. In the case of SRI, the same thresholds may be used, but for simplicity, in this study, water deficit is defined for SRI < 0. A water deficit period begins when SRI first falls below zero and ends when SRI value becomes positive. Thus, using the statistical theory of runs for analyzing sequential time series, run-lengths and run-sum were used to extract

water deficit durations and associated severities (deficit volume), respectively, from the SRI series. The inter-arrival times, which are the durations of SRI > 0 between successive water deficit events, were similarly obtained.

4.3.3 Univariate Water Deficit Duration and Severity Model

Drought duration normally follows an exponential distribution and severity follows a gamma distribution [*Shiau and Modarres*, 2009] as given below:

$$f_D(d|\lambda) = \frac{1}{\lambda} e^{-d/\lambda} \qquad 0 \le d < \infty, \qquad \lambda > 0 \tag{5}$$

$$f_S(s|\alpha,\beta) = \frac{1}{\beta^{\alpha}\Gamma(\alpha)} s^{\alpha-1} e^{-s/\beta} \qquad 0 < s < \infty, \qquad \alpha,\beta > 0 \tag{6}$$

where d is the duration, s is the severity, λ is the parameter for the exponential distribution, and α and β are the shape and scale parameters of the gamma distribution, respectively. These parameters are estimated for (i) each of the six regions, and (ii) the whole basin, using the maximum likelihood estimate.

4.3.4 Copulas

Drought severity-duration frequency analyses have relied on the conventional bivariate and multivariate frequency distributions. The limitation of this approach is that the marginals have to be from the same distribution family and at times have to be restricted in their mutual association. Moreover, the dependence structure of most conventional bivariate distributions is based on the Pearson correlation coefficient which is limited to representing linear association [*Kotz et al.*, 2000; *Yue et al.*, 2001]. Although water deficit duration and severity in this study follow exponential and gamma distributions, respectively, and could thus be considered gamma distributed, in general they could come from different marginal distributions. Copulas offer a viable alternative as marginals from different families can be combined into a joint distribution. The concept, developed by *Sklar* [1959], states that the joint distribution of any randomly distributed variables (X, Y) may be written as

$$H(x,y) = C[F(x), G(y)] \qquad x, y \in R \tag{7}$$

where $F(x)$ and $G(y)$ are the marginal probability distributions and $C = [0,1] \times [0,1] \rightarrow [0,1]^2$, the mapping function is the copula. This implies that a valid probabilistic model for (X, Y) may be obtained when the three components, $F, G,$ and C, are from the following parametric families:

$$F(x;\boldsymbol{\delta}), \qquad G(y;\boldsymbol{\eta}), \qquad C(u,v;\boldsymbol{\theta}) \tag{8}$$

where $\boldsymbol{\delta}$ and $\boldsymbol{\eta}$ are parameter vectors of the marginal distributions and $\boldsymbol{\theta}$ is the parameter vector for the dependence structure. u and v are the quantiles of the uniformly distributed variables $U = F(X)$ and $V = G(Y)$, respectively [*Chowdhary et al.*, 2011]. A number of copula families are available and are categorized into four classes: Archimedean, extreme value, elliptical, and other miscellaneous classes. A comprehensive treatment of copulas and their application to geoscience is available in *Nelsen* [2006], *Salvadori et al.* [2007], and *Genest and Favre* [2007]. In hydrology, the Archimedean family has been widely adopted for its ease of construction and wide range of choices for the strength of dependence. The general form of the Archimedean family is

$$\begin{aligned} \phi[H(x,y)] &= \phi\{C[F(x), G(y)]\} \\ &= \phi[F(x)] + \phi[G(y)] \end{aligned} \tag{9}$$

where the generator of the copula $\phi(t)$ is a continuous strictly decreasing mapping function from $[0,1]$ to $[0,\infty]$ such that $\phi(1) = 0$. The joint probability function for a bivariate random variable (X, Y) can be expressed as

$$\begin{aligned} H(x,y) &= C[F(x), G(y)] \\ &= \phi^{[-1]}\{\phi[F(x)] + \phi[G(y)]\} \\ &= C(u,v) = \phi^{[-1]}\{\phi(u) + \phi(v)\} \end{aligned} \tag{10}$$

Note that $U = F(X)$ and $V = G(Y)$ are uniformly distributed probability integral transform variates. The function $\phi^{[-1]}(t)$: $[0, \infty] \rightarrow [0,1]$ is the pseudo-inverse of the generating function, continuous and non-increasing on $[0, \infty]$ and strictly decreasing on $[0, \phi(0)]$ and is given by

$$\phi^{[-1]}(t) = \begin{cases} \phi^{-1}(t), & \forall\ 0 \leq t \leq \phi(0) \\ 0, & \forall\ \phi(0) \leq t < \infty \end{cases} \quad \textbf{(11)}$$

The generator is termed 'strict' and the resulting copula a strict copula when $\phi(0) = \infty$. The generating function $\phi(t)$ contains the dependence parameter θ.

4.3.4.1 Copula Parameter Estimation

The copula dependence structure can be estimated using methods, such as the moment-like method (MOM), the canonical or maximum pseudo-likelihood (MPL) method, or the exact maximum likelihood (EML) method. In this study the MPL method was used in which the dependence structure was kept independent of the marginal and was represented non-parametrically by their respective scaled ranks, and the dependence parameter was obtained by maximizing the likelihood function. The log-likelihood function, assuming C_θ is absolutely continuous with density c_θ, is of the form

$$\begin{aligned} l(\theta) &= \sum_{i=1}^{n} log\left[c_\theta\left(\tilde{F}(x_i), \tilde{G}(y_i)\right)\right] \\ &= \sum_{i=1}^{n} \log\left[c_\theta\left(\frac{R_i}{n+1}, \frac{S_i}{n+1}\right)\right] \end{aligned} \quad \textbf{(12)}$$

where $\tilde{F}(x) = R_i/(n+1)$ and $\tilde{G}(x) = S_i/(n+1)$ are non-parametric marginal probabilities solely based on ranks, i.e., this method gives the maximum likelihood estimate of θ only [*Chowdhary et al.*, 2011].

4.3.5 CONDITIONAL DISTRIBUTION FOR DROUGHT DURATION AND SEVERITY

Once a copula is chosen and the dependence parameter θ obtained, the conditional distribution can be derived. Following *Shiau* [2006], the probability that duration and severity exceed a certain threshold can be expressed as

$$\begin{aligned} P(D \geq d, S \geq s) &= 1 - F_D(d) - F_S(s) + F_{D,S}(d,s) \\ &= 1 - F_D(d) - F_S(s) + \mathrm{C}\big(F_D(d), F_S(s)\big) \end{aligned} \quad \textbf{(13)}$$

where $F_D(d)$ and $F_S(s)$ are the cumulative duration and severity frequency distributions, respectively. The conditional drought severity distributions given a drought duration exceeding a certain threshold d', and the conditional drought duration given that drought severity exceeds a certain threshold s', are

$$P(S \leq s | D \geq d') = \frac{F_S(s) - C\big(F_D(d'), F_S(s)\big)}{1 - F_D(d')} \quad \textbf{(14)}$$

$$P(D \leq d | S \geq s') = \frac{F_D(d) - C\big(F_D(d), F_S(s')\big)}{1 - F_S(s')} \quad \textbf{(15)}$$

respectively.

4.3.6 RETURN PERIODS

The concept of a return period is usually associated with the design and operation of hydrological structures, but can also be applied to long-term water planning and management. Return periods for water deficit events with severity or duration greater than or equal to a certain value is given as [*Shiau and Shen*, 2001]

$$T_S = \frac{E(L)}{1 - F_S(s)} \quad \textbf{(16)}$$

$$T_D = \frac{E(L)}{1 - F_D(d)} \quad \textbf{(17)}$$

where L is the drought inter-arrival time and $E(L)$ is the expected drought inter-arrival time. T_S and T_D are the return period defined by severity and duration, respectively. *Shiau* [2003] categorized return periods of bivariate distributed hydrologic events as joint and conditional return periods. Two cases of joint water deficit duration and severity return periods were proposed: return period for $D \geq d$ and $S \geq s$ (Eq. 18) and return period for $D \geq d$ or $S \geq s$ (Eq. 19).

$$T_{DS} = \frac{E(L)}{1 - F_D(d) - F_S(s) + \mathrm{C}\big(F_D(d), F_S(s)\big)} \quad \textbf{(18)}$$

$$T'_{DS} = \frac{E(L)}{1 - \mathrm{C}\big(F_D(d), F_S(s)\big)} \quad \textbf{(19)}$$

Further water deficit duration and severity return periods can also be defined as conditional, that is return period of water deficit duration given severity exceeding a certain threshold (Eq. 20) and of severity given drought duration exceeding a threshold (Eq. 21).

$$T_{D|S \geq s} = \frac{E(L)}{[1 - F_S(s)]\big[1 - F_D(d) - F_S(s) + \mathrm{C}\big(F_D(d), F_S(s)\big)\big]} \quad \textbf{(20)}$$

$$T_{S|D \geq d} = \frac{E(L)}{[1 - F_D(d)]\big[1 - F_D(d) - F_S(s) + \mathrm{C}\big(F_D(d), F_S(s)\big)\big]} \quad \textbf{(21)}$$

4.4 RESULTS AND DISCUSSION

4.4.1 WATER DEFICIT DURATION AND SEVERITY

SRI(3) was computed for each region and for the whole basin, from which water deficit durations and severities and inter-arrival times were extracted. Figure 16 shows the plot of

SRI(3) superimposed over AAR anomalies for the whole basin and for each region. The basic statistics for AAR, deficit durations and severities, and inter-arrival times for each region and for the whole basin are given in Table 5. The severity values reported in the table are absolute values.

The Río Conchos and Middle-Middle RG regions have the least number of water deficit events, but have two of the longest events lasting 97 and 50 months respectively, thus explaining the lower number of events. These two regions span across the semi-arid portion of the basin and are subjected to high rainfall variability (Figure 4). The North American Monsoon is responsible for most of the precipitation in this region and is subjected to meteorological conditions in the Pacific, mainly the El Niño Southern Oscillation.

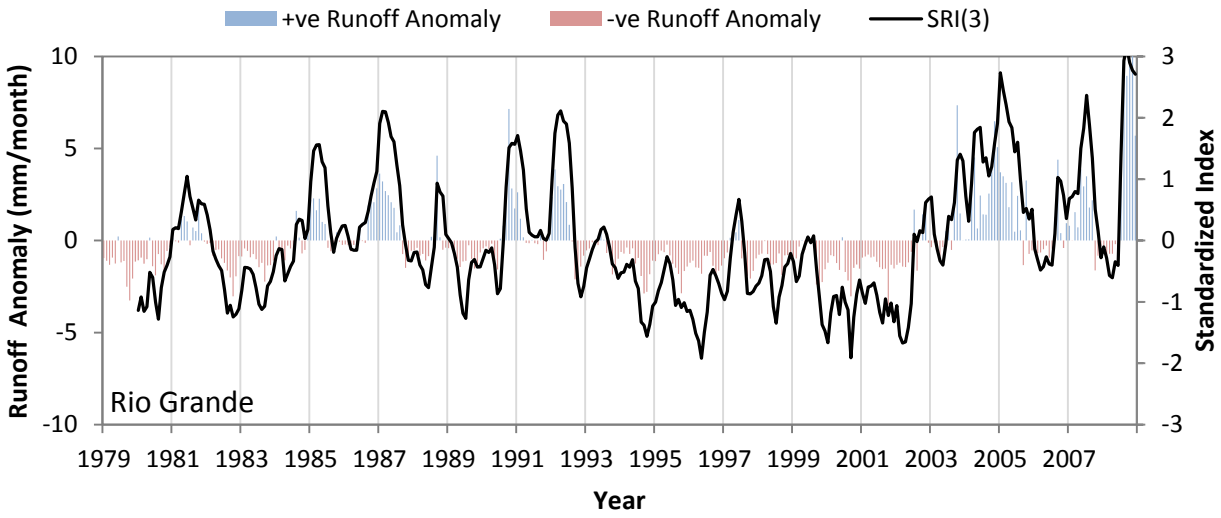

(a)

Figure 16. AAR anomaly overlain with SRI(3) for (a) the whole Rio Grande (RG) Basin and (b) each region.

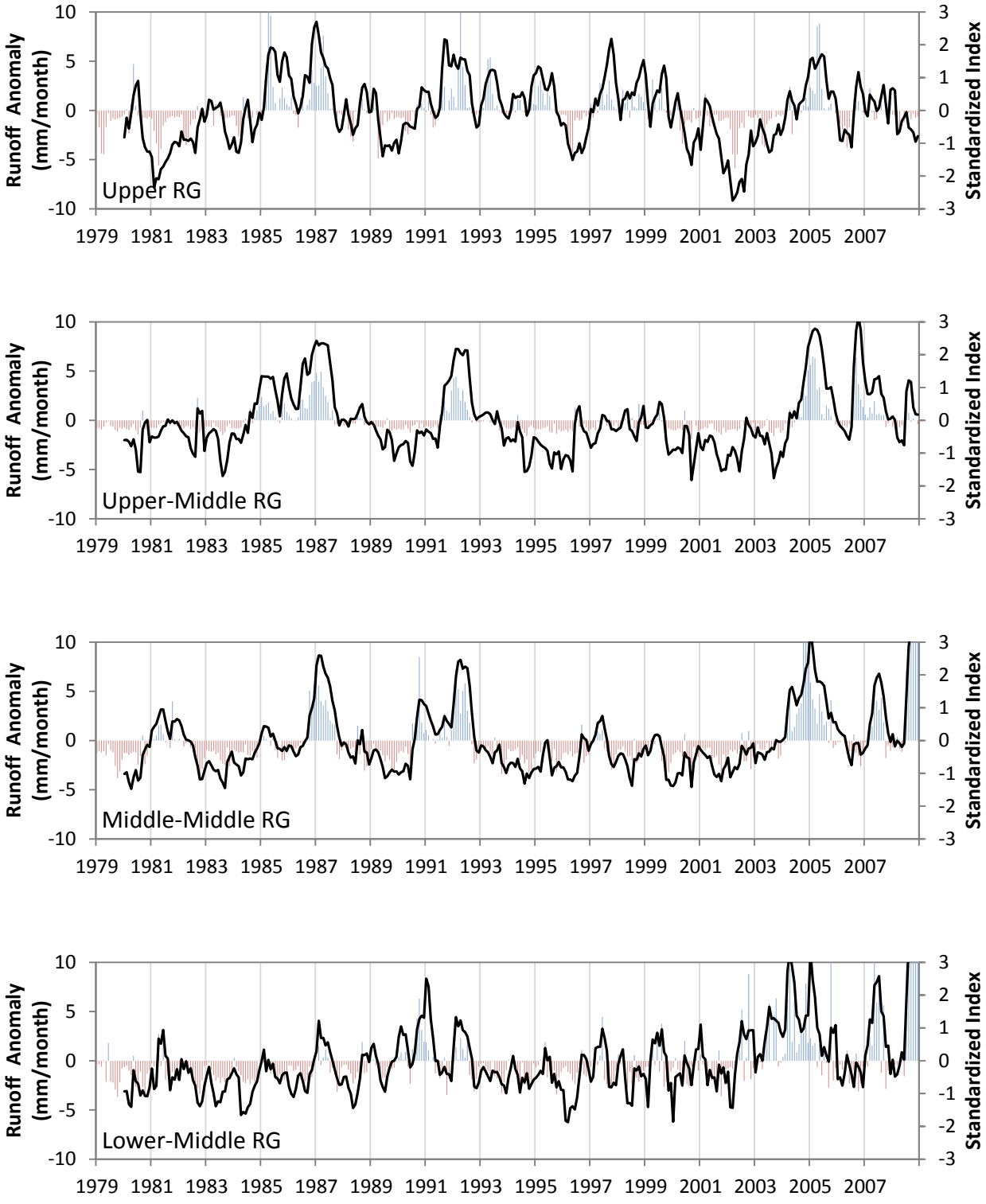

Figure 16 Continued.

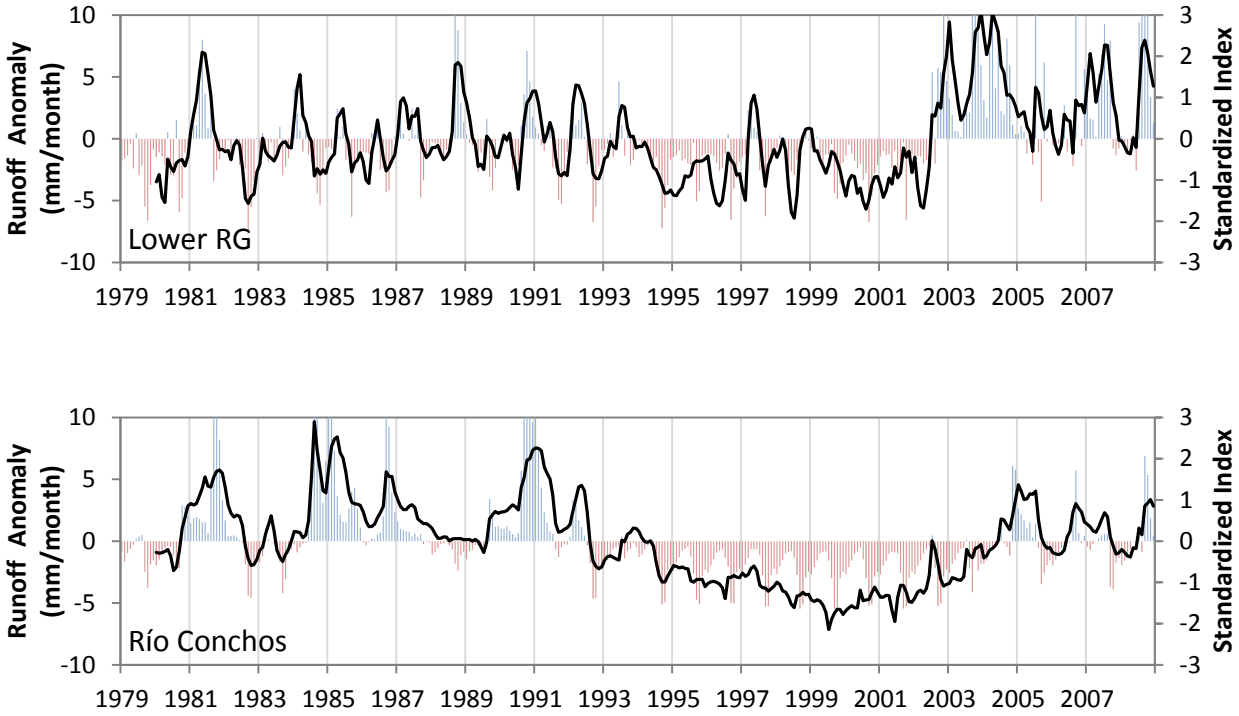

(b)

Figure 16 Continued.

Interestingly, for the period considered, the Upper RG has the highest number of events and the smallest total water deficit durations, resulting in the lowest mean water deficit duration. The mean water deficit duration for the basin as a whole was 13.6 months and that Upper RG, Upper-Middle RG, Lower-Middle RG, and Lower RG were below the mean while that for Middle-Middle RG and the Río Conchos sub-basin were above the mean. The Río Conchos also endures the harshest severity and the Lower-Middle RG has the lowest severity despite having the second highest number of events. The mean severity for the whole basin was 9.28, and again that for the different regions, except for Río Conchos, was lower. The mean inter-arrival time for the whole basin was 10 months, and the highest inter-arrival time was 65 months, in the Río Conchos.

Table 5. Statistics for AAR and SRI(3) for each region and the whole basin.

	Upper RG	Upper-Middle RG	Middle-Middle RG	Lower-Middle RG	Lower RG	Río Conchos	Rio Grande
AAR (mm/month)							
Mean	2.565	1.484	2.521	2.149	3.719	2.563	2.387
Standard deviation	2.721	1.433	3.480	3.795	5.001	4.144	2.134
SRI(3)							
No. of events	25	16	14	24	21	10	14
Duration (months)							
Total	163	200	210	194	197	166	190
Mean	6.52	12.50	15.00	8.08	9.38	16.60	13.57
Standard deviation	8.37	11.96	14.41	7.86	11.08	28.86	13.65
Skewness	2.10	1.08	1.21	1.91	2.20	2.93	1.05
Minimum	1	1	1	1	1	1	1
Maximum	33	35	50	35	41	97	43

Table 5 Continued.

	Upper RG	Upper-Middle RG	Middle-Middle RG	Lower-Middle RG	Lower RG	Río Conchos	Rio Grande
Severity							
Total	133.94	128.00	124.59	120.90	130.11	139.69	129.85
Mean	5.36	8.00	8.90	5.04	6.20	13.97	9.28
Standard deviation	10.18	10.36	10.51	6.26	10.27	35.34	13.15
Skewness	2.62	1.47	1.12	2.31	2.58	3.11	1.62
Minimum	0.02	0.11	0.04	0.03	0.03	0.02	0.02
Maximum	40.60	31.89	33.20	27.77	37.73	114.04	38.01
Inter-arrival Time (months)							
Minimum	1	1	1	1	1	1	1
Maximum	17	39	28	31	35	65	30
Mean	6.72	8.25	8.57	5.46	6.33	16.70	10.00

Note: Severity values are absolute

Figure 17 gives a scatter plot of severity of water deficits versus duration. The deficit durations can be roughly classified into three categories: events lasting up to 12 months, events lasting between 12 and 24 months, and multi-year events. The majority of events, around 70%, had durations less or equal to 12 months and around 15% had durations between 12 and 24 months. One exceptional event in the Río Conchos lasted 97 months with an associated severity of 114 (shown in the inset plot in Figure 17). There is a high dependence between duration and severity in the basin and in the six regions; Pearson ρ above 0.95 and Kendall τ ranging between 0.83 (Lower RG) and 0.96 (whole basin) was found.

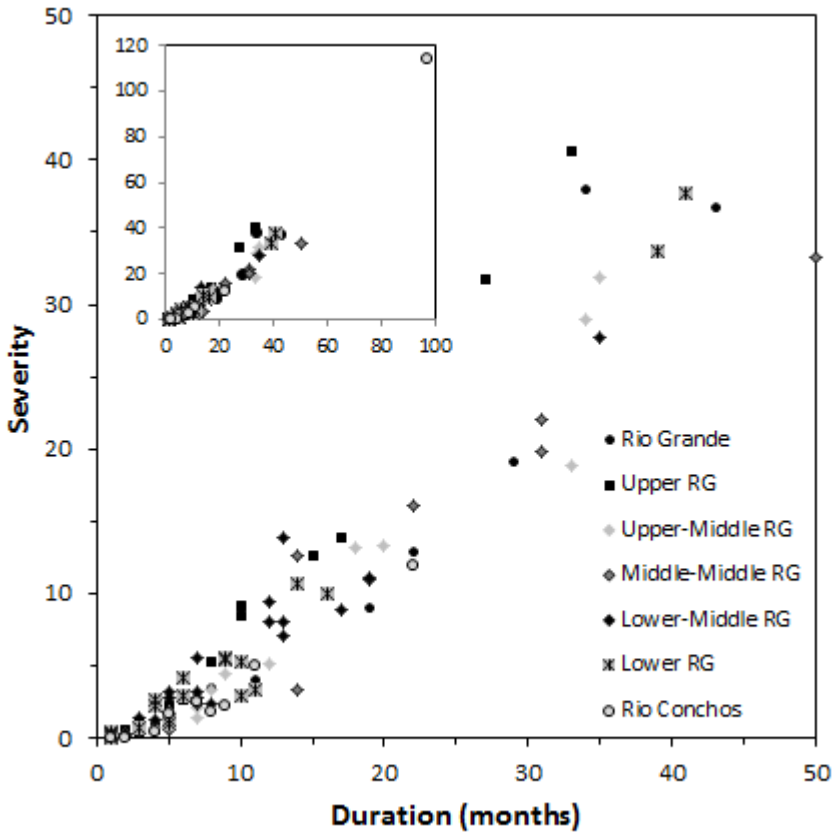

Figure 17. Scatter plot of severity versus duration for the whole basin and for each region (inset shows an exceptional drought event in the Río Conchos).

The exponential and gamma distributions were fitted to the duration and severity series for each region and for the whole basin, respectively. Figure 18 illustrates the exponential and gamma model fitted to the observed duration and severity histograms for the Lower-Middle RG region. The statistical parameters for each region and for the basin are given in Table 6.

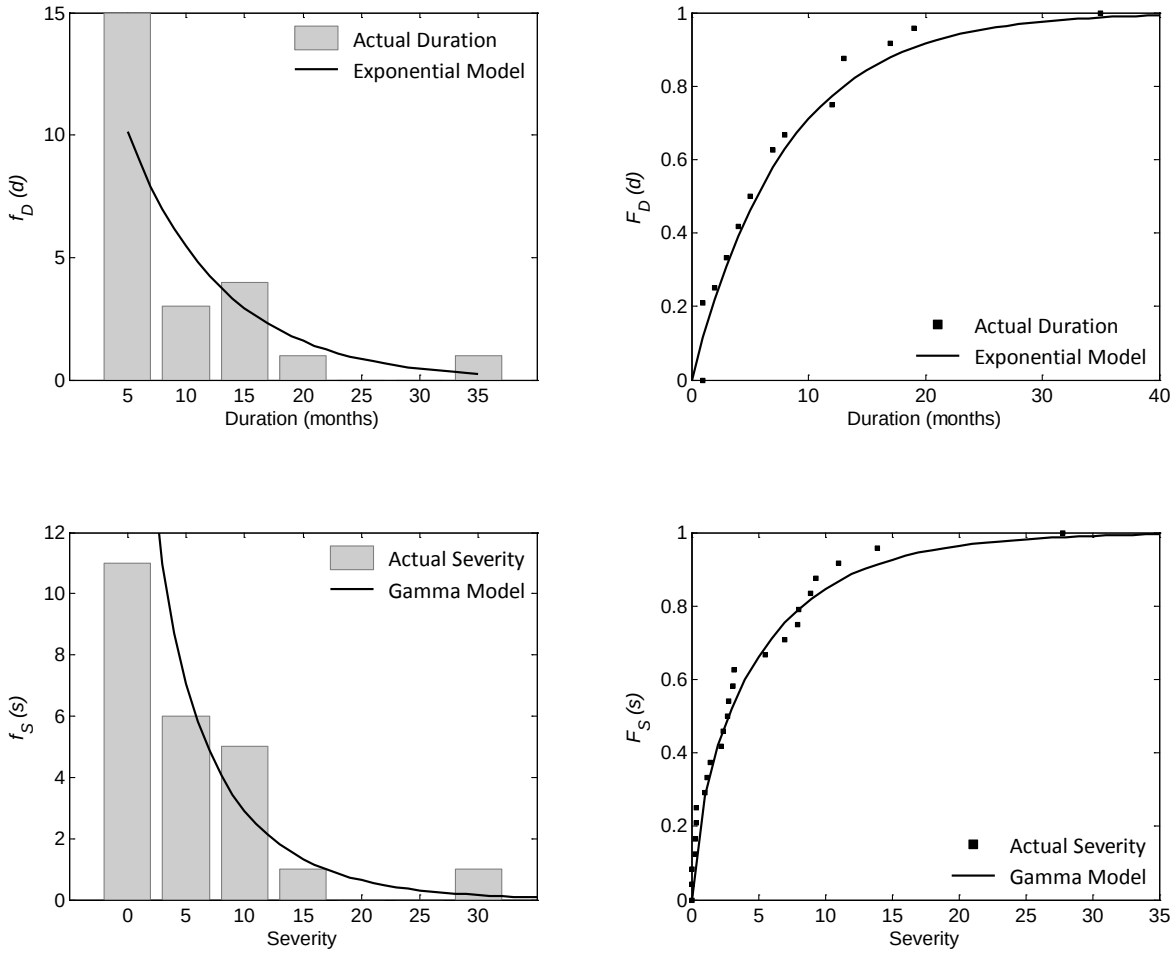

Figure 18. Observed duration with exponential fit and observed severity with gamma fit for Lower-Middle RG.

Table 6. Parameters for exponential and gamma distribution fitted to observed duration and severity respectively.

		Upper RG	Upper-Middle RG	Middle-Middle RG	Lower-Middle RG	Lower RG	Río Conchos	Rio Grande
Duration	λ	6.520	12.500	15.000	8.083	9.381	16.600	13.571
Severity	α	0.387	0.575	0.461	0.641	0.531	0.302	0.421
	β	13.837	13.915	19.320	7.855	11.668	46.240	22.060

4.4.2 COPULA PARAMETER ESTIMATION AND SELECTION

The scatterplot (Figure 17) and high association values between water deficit duration and severity indicate that a positive relationship exists between the two variables. Considering features of copulas to allow for non-linear association through rank-based parameters and to allow different marginals, in general copulas are considered a viable alternative for obtaining joint distribution in this study. For each region and for the whole basin, nine copulas were tested – two from the extreme value family [Galambos (GLM) and Gumbel-Hougaard (GH)] and seven from the one-parameter families of the Archimedean copulas: Clayton (CLT), Frank (FRK), Genest-Ghoudi (GG), Yager (YGR), and N12, N13, and N14 from Table 4.1 of *Nelsen* [2006]. The probability function, parameter space, generating function, and relationship of non-parametric dependence measure for each copula are given in Table 7.

The dependence parameter for each copula considered was obtained using the MPL method. The maximized log-likelihood (LL_{max}), point estimates of theta ($\hat{\theta}$) and associated lower and upper interval estimates having a coverage probability of 0.95 (LCL and UCL) along with standard errors, root mean square errors (RMSE), mean absolute errors (MN-A-ERR), and Kendall tau values were computed for each region and for the whole basin. Based on the values of LL_{max} and error statistics, it was noted that different copulas appeared viable for each region and often more than one copula appeared suitable for each region in the basin.

Table 7. Probability function, parameter space, generating function, and relationship of non-parametric dependence measure with association parameter for the copulas considered in this study.

Copula	$C_\theta(u,v)$	**Parameter Space**	**Generator** $\phi(t)$	**Kendall's** τ
Clayton	$\left[\max\left(u^{-\theta}+v^{-\theta}-1,0\right)\right]^{-1/\theta}$	$[-1,\infty)\backslash\{0\}$	$\frac{1}{\theta}\left(t^{-\theta}-1\right)$	$\theta/(\theta+2)$
Frank	$-\frac{1}{\theta}\ln\left[1+\frac{\left(e^{-\theta u}-1\right)\left(e^{-\theta v}-1\right)}{\left(e^{-\theta}-1\right)}\right]$	$(-\infty,\infty)\backslash\{0\}$	$-\ln\frac{e^{-\theta t}-1}{e^{-\theta}-1}$	$1+\frac{4}{\theta}[D_1(\theta)-1]$ $D_1(\theta)=\frac{1}{\theta}\int_0^\theta \frac{t^k}{\exp(t-1)}dt$
Genest-Ghoudi (GG)	$\left\{\max\left(1-\left[\left(1-u^{1/\theta}\right)^\theta+\left(1-v^{1/\theta}\right)^\theta\right]^{1/\theta},0\right)\right\}^\theta$	$[1,\infty)$	$\left(1-t^{1/\theta}\right)^\theta$	$(2\theta-3)/(2\theta-1)$
Gumbel-Houggard (GH)[#]	$\exp\left\{-\left[(-\ln u)^\theta+(-\ln v)^\theta\right]^{1/\theta}\right\}$	$[1,\infty)$	$(-\ln t)^\theta$	$1-1/\theta$
Galambos	$uv\exp\left\{\left[(-\ln u)^{-\theta}+(-\ln v)^{-\theta}\right]^{-1/\theta}\right\}$	$[1,\infty)$	n.a.	n.a.

Table 7 Continued.

Copula	$C_\theta(u,v)$	Parameter Space	Generator $\phi(t)$	Kendall's τ
N12*	$\left\{1+\left[(u^{-1}-1)^\theta+(v^{-1}-1)^\theta\right]^{1/\theta}\right\}^{-1}$	$[1,\infty)$	$\left(\frac{1}{t}-1\right)^\theta$	$1-2/(3\theta)$
N13*	$\exp\left\{1-\left[(1-\ln u)^\theta+(1-\ln v)^\theta-1\right]^{1/\theta}\right\}$	$(0,\infty)$	$(1-\ln t)^\theta-1$	n.a.
N14*	$\left\{1+\left[\left(u^{-1/\theta}-1\right)^\theta+\left(v^{-1/\theta}-1\right)^\theta\right]^{1/\theta}\right\}^{-\theta}$	$[1,\infty)$	$\left(t^{-1/\theta}-1\right)^\theta$	$1-2/(1+2\theta)$
Yager	$\max\left(1-\left[(1-u)^\theta+(1-v)^\theta\right]^{1/\theta},0\right)$	$[1,\infty)$	$(1-t)^\theta$	$1-2/\theta$

[#] GH is both an Archimedean and an extreme value copula

[*] Table 4.1 of *Nelsen* [2006]

Graphical and analytical methods were used in conjunction to select the most appropriate copula for each case. Most copulas exhibit similar form in their central part but differ significantly in the tails where extreme values are located; given that each region is subject to different climatologic conditions, affecting the nature of water deficit events, the same copula cannot be assumed suitable for all cases. A complete description of the analysis is available in [*Khedun et al.*, 2012a].

The YGR copula was deemed the most viable for Upper RG and Upper-Middle RG, while GG, GH, and YGR were suitable for Middle-Middle RG. For Lower RG, GH was a suitable copula. N12 and CLT copulas had the highest LL_{max} and were therefore appropriate for the Río Conchos and the whole of the basin respectively.

4.4.3 JOINT CDF OF DURATION AND SEVERITY

Using the chosen copula models, joint probability functions for water deficit duration and severity were computed for each region and for the basin. The resulting contour plot, in the domain of original variables, for the Lower-Middle RG is shown in Figure 19.

Such copula-based drought joint deficit duration and severity analysis can yield important information for water management purposes. It allows a water planner to assess the non-exceedance probability of a deficit event with a certain duration and severity occurring simultaneously, i.e. $P(D \leq d, S \leq s)$. This information cannot be garnered from unvariate analysis [*Shiau,* 2006]. For example, the probability of different categories of droughts, based on threshold severities, lasting for specific durations can be identified and necessary operational contingency plans can be developed and implemented when such situation arises.

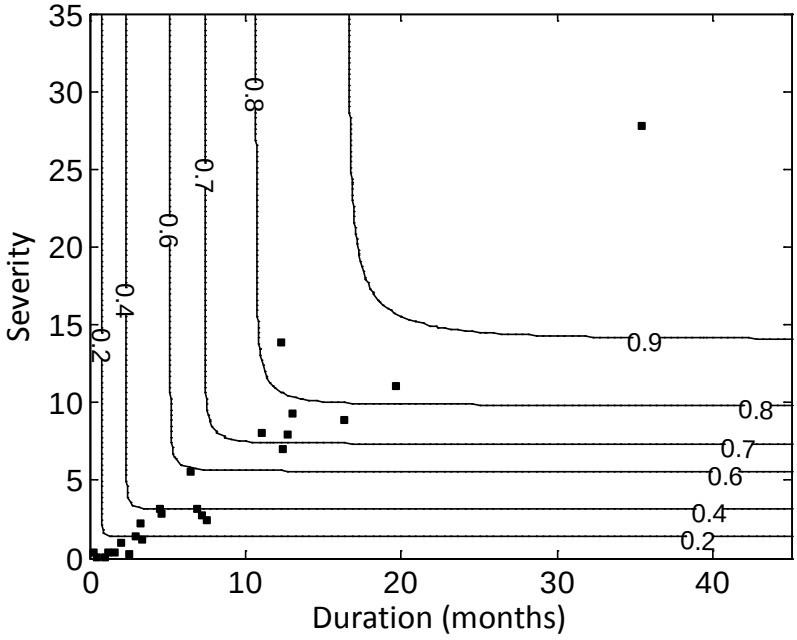

Figure 19. Contours of joint probabilities of severity versus duration for Lower-Middle RG.

4.4.4 CONDITIONAL PROBABILITY OF WATER DEFICIT DURATION AND SEVERITY

Bayesian decision making is indispensable in both short-term water resources management and long-term planning. Conditional probability models permit the estimation of the probability of an upcoming hydrological drought of a certain duration given a particular severity value or vice-versa. Figure 20 shows the conditional probability distribution of severity given duration exceeding a threshold d' for the whole basin, and in the Upper RG and Lower-Middle RG. Similarly Figure 21 gives the conditional probability of the duration given severity exceeds a certain threshold s'. Upper RG and Lower-Middle RG are chosen for further discussion because they have almost the same number of events and mean duration and severity, but are located in two climatologically different regions.

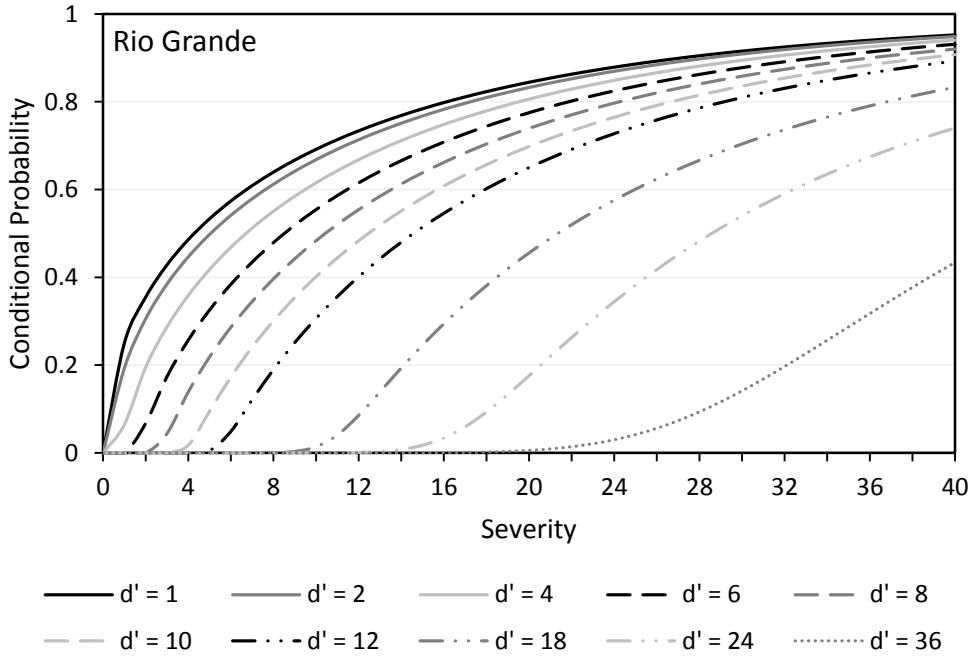

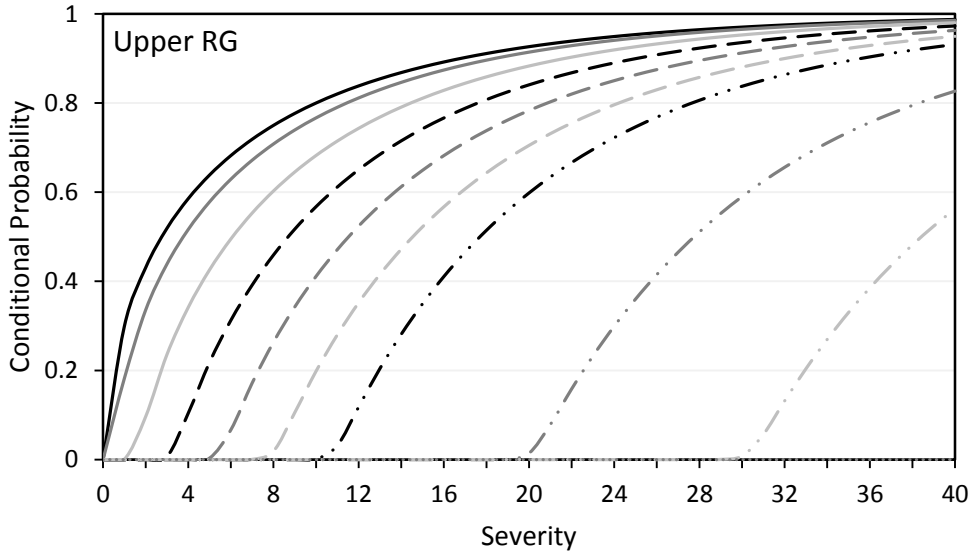

Figure 20. Conditional distribution of water deficit severity given that duration exceeds $\boldsymbol{d'}$month(s).

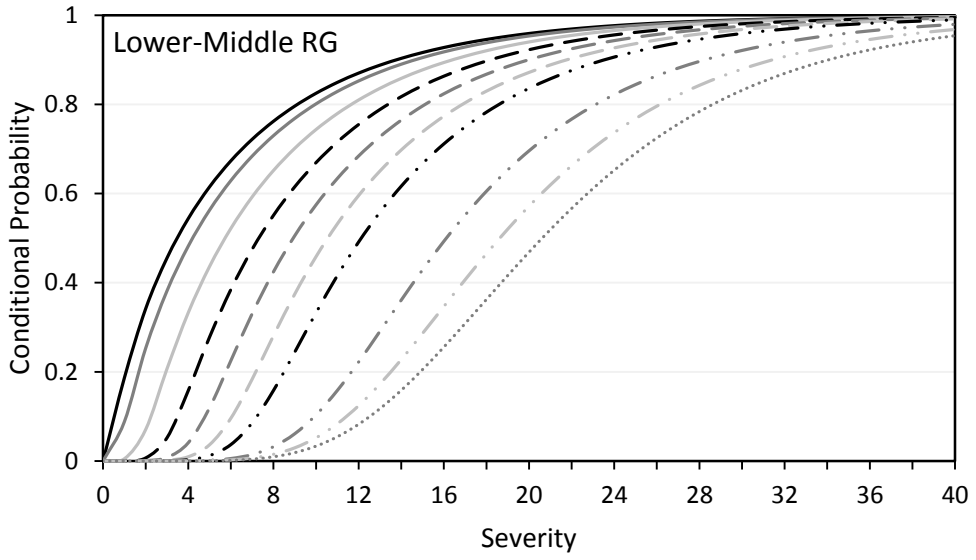

Figure 20 Continued.

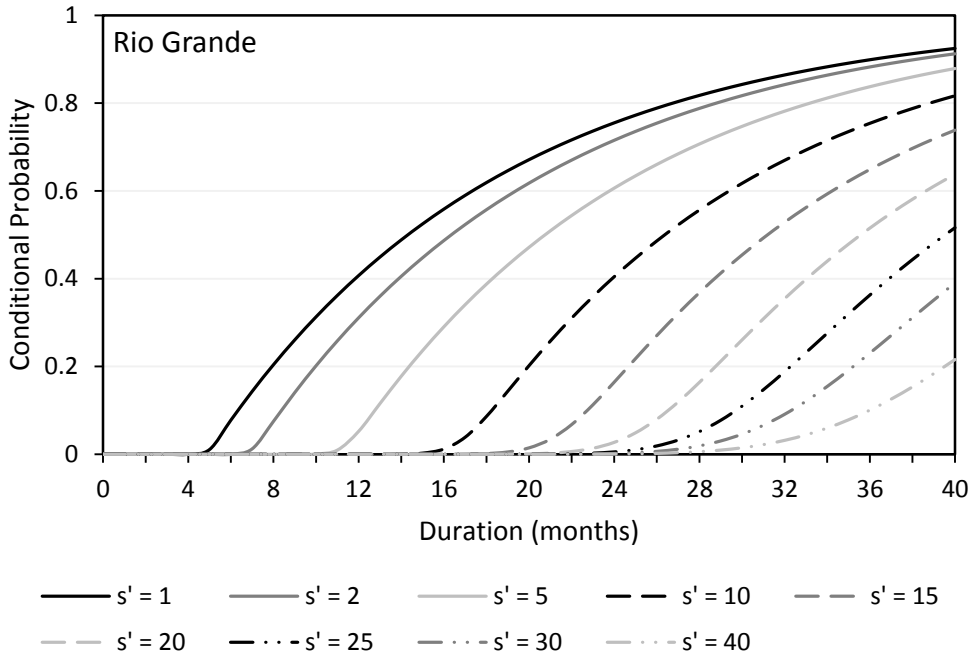

Figure 21. Conditional distribution of water duration given that severity exceeds s'.

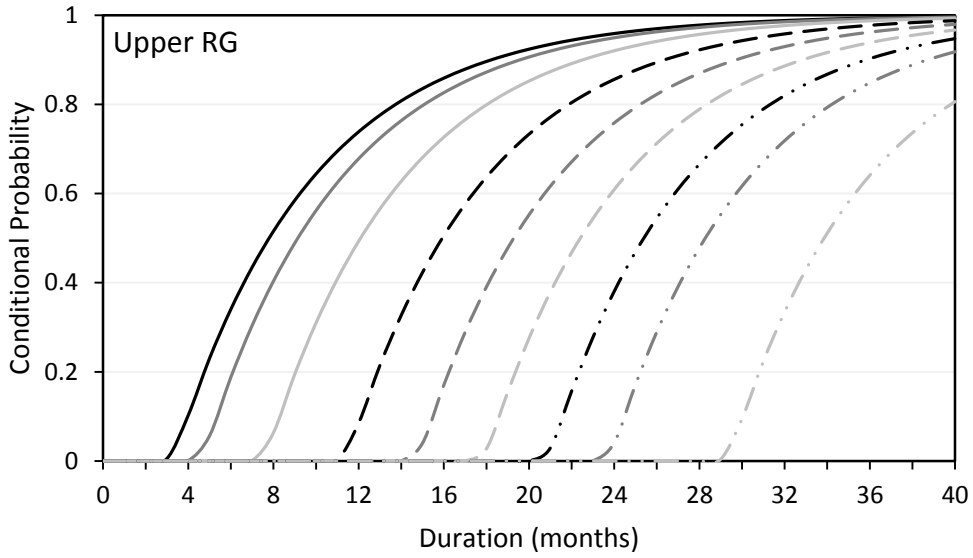

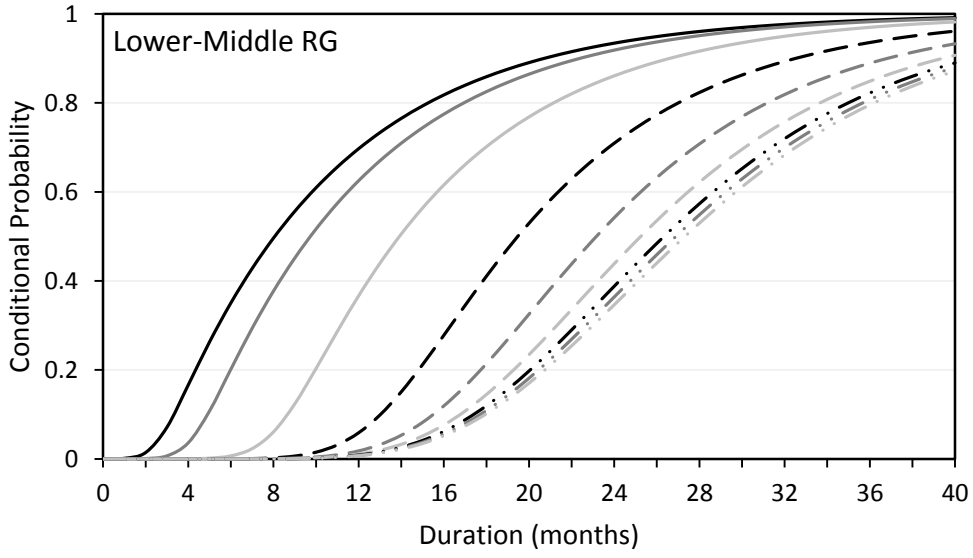

Figure 21 Continued.

The conditional models for the three cases were different; the probability of low severity given short duration events were relatively similar (e.g., the probability for $s \leq 2$ given $d' \geq 1$

month was 0.430 for Upper RG, 0.341 for Lower-Middle RG, and 0.355 in RG), but for high severity given long duration events, the probabilities were considerably different. The conditional probability of a water deficit event with $s \leq 12$ given $d' \geq 12$ months was 0.118 for Upper RG, but was 0.491 for Lower-Middle RG, and 0.401 in RG. A similar trend was observed for short duration given low severity (e.g., the probability for $d \leq 5$ months given $s' \geq 1$ was 0.230 for Upper RG and 0.263 for Lower RG) as opposed to long duration given high severity events. The conditional probability of a water deficit event with $d \leq 24$ months given $s' \geq 15$ was 0.758 for Upper RG, but was 0.542 for Lower-Middle RG.

This divergence can be explained by the dissimilar climatic conditions prevailing in each region, which also influenced the choice of copulas. The Upper RG (Figure 2) is alpine and subjected to less variation in precipitation and generally experiences minor droughts of short duration (except on two occasions as shown in Figure 16), whereas the Lower-Middle RG is located in a semi-arid region and endures longer water deficit events which cumulatively results in high severities. The combined effect of the varying climatic conditions across RG is reflected in the conditional plots for the whole basin. The disparities in the conditional models, shown in Figure 21, are again due to differences in climate regimes. An interesting point to note in the Lower-Middle RG is the bunched high s' curves, indicating that long duration events may quickly cumulate into very high severities, which is typical of arid/semi-arid regions.

4.4.4.1 Comparison between SRI and SPI Derived Conditional Probabilities

In this section, conditional probabilities of duration and severities between SRI(3), derived from Noah LSM generated runoff, and SPI(3), based on gauged precipitation are compared. Deficits in SPI is indicative of meteorological droughts, which are associated with a sustained, extended deficiency in precipitation while deficits in SRI would represent hydrological droughts, usually initiated by a prolonged period of rainfall deficit resulting in the reduction of surface and subsurface flow. It may be further accentuated by land use land cover changes. In this exercise, runoff from the Noah LSM includes both surface and subsurface flow with land use land cover assumed constant during the modeling period.

To ensure a suitable baseline for comparison, the precipitation field in NLDAS-2 was first validated against observed precipitation. NLDAS-2 precipitation is a combination of reprocessed daily gauged analyses that have been subjected to orographic adjustment and temporally disaggregated to hourly timescale using either the NWS Doppler radar-based precipitation or NOAA CPC Morphing Technique (CMORPH) hourly precipitation analyses [*Joyce et al.*, 2004]. In places with limited radar coverage, such as Mexico, gaps are filled with CMORPH and North American Regional Reanalysis data [NARR; *Mesinger et al.*, 2006].

A dataset of 79 precipitation stations (63 in the US and 16 in Mexico) were compiled for the Rio Grande basin (section 2). For multiple reasons, the spatial density of precipitation stations is not uniform across the basin. The Lower-Middle RG region has one of the least densities of stations (3 in the US and 1 in Mexico) and thus represents the ideal setting for assessing the effectiveness of model derived conditional water deficit duration and severity probabilities and how it can be used as an alternative for planning purposes when adequate observation data is not available. Figure 22 gives a scatter plot of monthly area-averaged NLDAS-2 precipitation data against averaged observed precipitation from the US stations for Lower-Middle RG. The period of comparison is January 1979 to December 2008. A relatively high correlation, with a small negative bias towards observation, which is typical of NLDAS-2 [*Luo et al.*, 2003], is noted.

The observed precipitation dataset ranges from 1935 to 2008. SPI(3) was computed and using the theory of runs, rainfall deficit [SPI(3) < 0] durations and severities were extracted. Ninety six rainfall deficit events with duration ranging from 1 to 20 months, with a mean of 4.43 months, were noted. For the period 1979 to 2008, 35 deficit events ranging from 1 to 20 months with a mean of 4.94 months were recorded. A Pearson ρ of 0.90 and Kendall τ of 0.75 were found between duration and severity. The duration and severity follow exponential and gamma distributions respectively, just like for SRI(3). Following the copula fitting procedure adopted for SRI(3), it was found that GLM was the most appropriate copula for rainfall deficit events in Lower-Middle RG. Figure 23 shows the conditional probability of severity given duration d' and duration given severity s' for modeled runoff and averaged observed precipitation for three cases representing the quartiles of rainfall deficit durations and

severities. The conditional probabilities for both severity given duration and duration given severity derived from observed precipitation were found to be different for precipitation and runoff. This is because the two hydrologic variables are not linearly connected, that is runoff is not a linear translation of observed precipitation. For example, the conditional probability of having a water deficit event with a severity $s \leq 6$ given duration $d' \geq 3.5$ months was 0.551, while that of having a rainfall deficit with the same conditions was 0.582 (Figure 23a); and the conditional probability of having a water deficit event with a duration $d \leq 6$ months given a severity $s' \geq 2$ was 0.201, while that of having a rainfall deficit with the same conditions was 0.491 (Figure 23b).

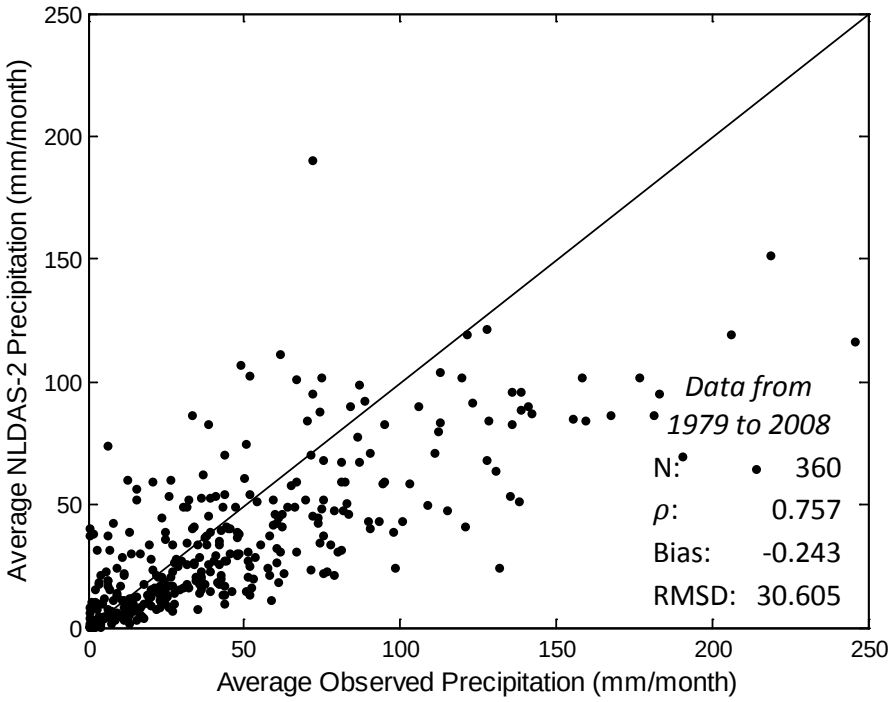

Figure 22. Scatter plot of monthly area-averaged monthly NLDAS-2 precipitation and averaged observed precipitation for Lower-Middle RG.

The higher conditional probability of non-exceedance based on SPI(3) curves indicates lesser chances of experiencing droughts of a certain level, as compared to SRI(3) based curves. In other words, given that the drought severity (or duration) exceeds a certain level, there would

be less likelihood for meteorological droughts to prolong beyond a certain duration (or have greater severity than a certain level), as compared to hydrological droughts.

Since SPI(3) and SRI(3) based severities refer to different attributes of drought phenomenon, the aforementioned assertion is to be considered in qualitative terms only. Further, for application purposes, the information garnered from the model and observation should not be viewed as mutually exclusive, but should be used in tandem for water planning and management. In regions where ground based observation is not adequate, the model generated information may be employed.

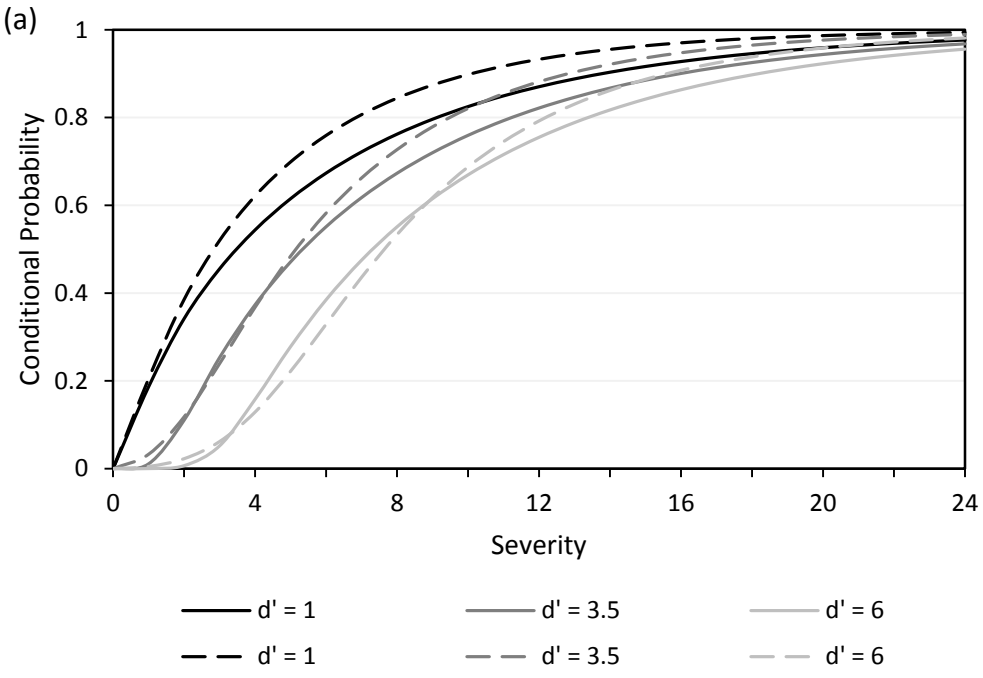

Figure 23. Comparison of conditional probability of (a) severity given duration $\boldsymbol{d'}$ and (b) duration given severity $\boldsymbol{s'}$ for Noah LSM runoff (solid line) and averaged observed precipitation (dashed line) in Lower-Middle RG.

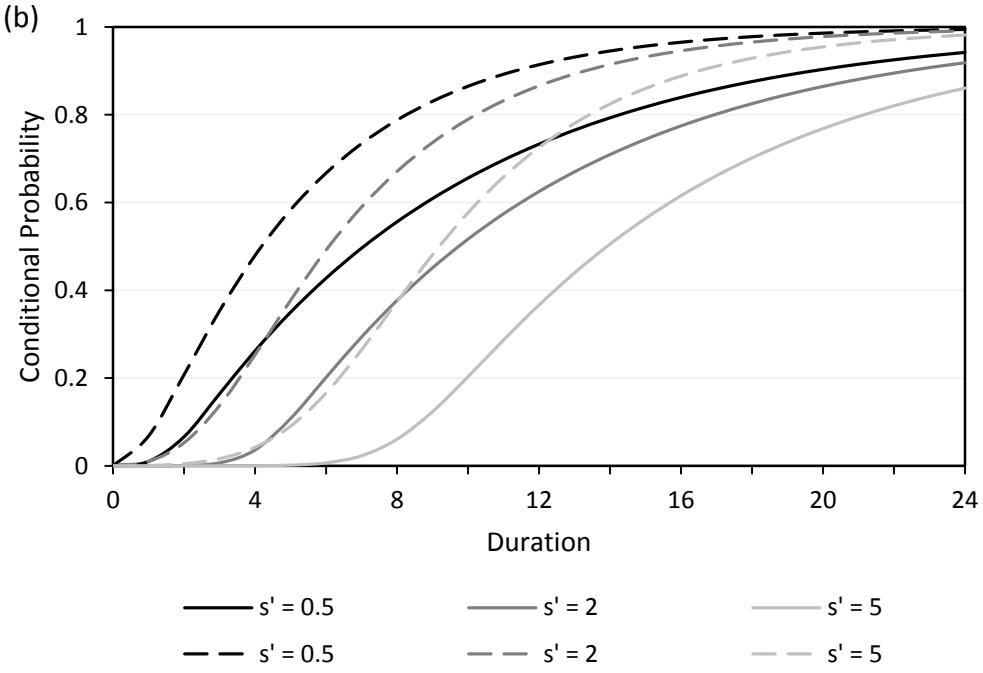

Figure 23 Continued.

4.4.5 RETURN PERIODS

The water deficit durations (Table 8) and severities (Table 9) for different return periods ranging between 2 to 100 years were calculated. The mean observed water deficit duration for the whole basin is 13.6 months, and mean severity is 9.3. Based on the computed results, the return period for mean water deficit duration is less than 5 years, and that for mean severity is less than 2 years. Given that water deficit events are bivariate characterized by duration and severity, joint and conditional return periods provide more information than univariate return periods. The conditional return period, for the whole basin, of water deficit duration given severity exceeding a certain value is shown in Figure 24 and that of severity duration exceeding a certain threshold is shown in Figure 25. The return period for a water deficit event in the basin of duration 12 months and severity exceeding 10 was 5.5 years and that of severity 10 given duration exceeding12 months was 3.8 years. The return period of deficit events with durations less than 2 years and severities exceeding values between 1 and 15 was less than 20

years, but that of long duration high severity events increased rapidly. In the case of return periods for severity given duration exceeding a certain threshold a sharp increase in return periods for severities above 12 was noted.

Table 8. Water deficit durations (months) for different return periods.

Return period (years)	Upper RG	Upper-Middle RG	Middle-Middle RG	Lower-Middle RG	Lower RG	Río Conchos	Rio Grande
2	5.78	7.55	7.27	7.47	7.82	0.63	5.44
5	14.08	17.35	19.26	13.55	16.04	13.59	17.82
10	21.28	25.42	29.62	18.36	22.76	31.31	29.05
20	28.95	33.80	40.61	23.28	29.73	52.69	41.16
50	39.56	45.19	55.75	29.90	39.22	84.31	58.02
100	47.85	53.97	67.52	34.98	46.53	109.86	71.22

Table 9. Water deficit severities for different return periods.

Return period (years)	Upper RG	Upper-Middle RG	Middle-Middle RG	Lower-Middle RG	Lower RG	Río Conchos	Rio Grande
2	8.30	13.35	15.44	11.97	12.50	6.02	11.88
5	14.27	24.80	29.19	19.38	21.09	21.23	24.32
10	18.79	33.47	39.59	24.98	27.60	32.74	33.72
20	23.31	42.13	49.98	30.58	34.10	44.24	43.13
50	29.29	53.58	63.73	37.99	42.69	59.45	55.56
100	33.81	62.25	74.12	43.59	49.20	70.96	64.97

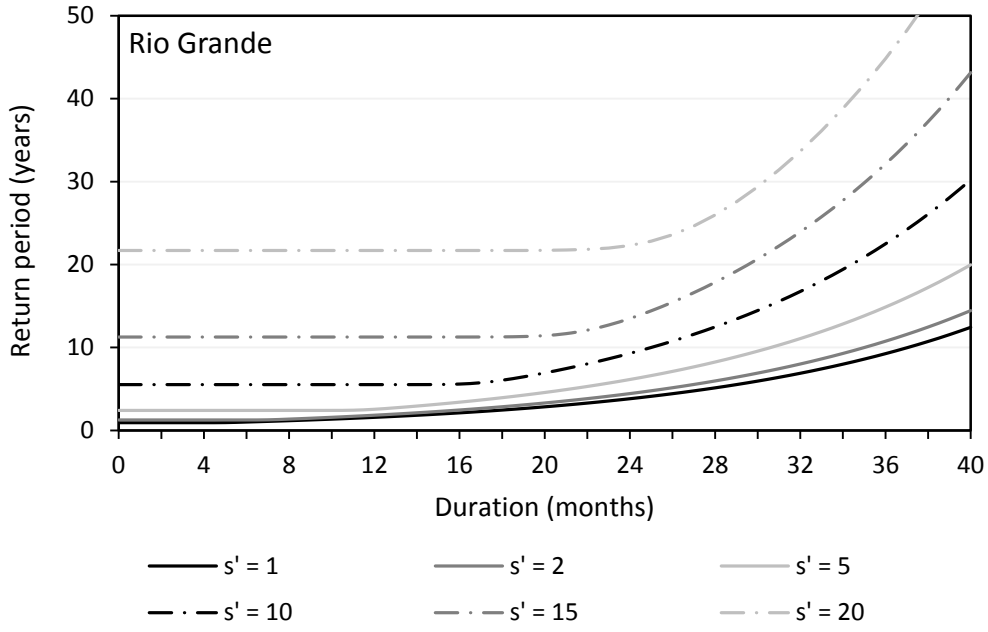

Figure 24. Conditional return period of water deficit duration given that severity exceeds s' for RG.

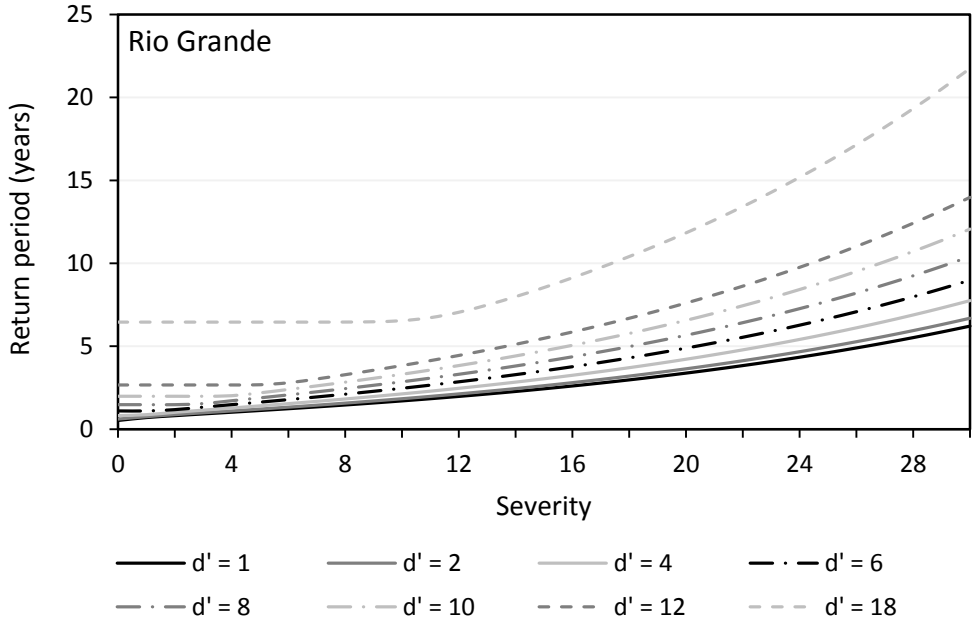

Figure 25. Conditional return period of water deficit severity given that duration exceeds d' months for RG.

4.5 CONCLUSIONS

The early identification of droughts is essential for water management purposes as it can limit the social, financial, and public health burden that may result from such extreme hydrological events. A number of indices have been developed for drought identification, but each has intrinsic limitations. Streamflow is an important indicator of changes in water availability, but gauged values are impaired by land use changes in heavily modified catchments. In this study, runoff was derived for RG using a land surface model, keeping land use land cover constant, such that changes are due to climatological variations. RG is divided into 6 regions and different marginal distributions were fitted to the duration and severity, respectively, and copulas are employed in bivariate water deficit analysis. The following conclusions can be drawn from this study:

1. Water deficit duration and severity are derived from SRI(3) series and exponential and gamma distributions are found to adequately model duration and severity, respectively.

2. Given that RG is a large basin subjected to different climatological conditions across its course, it is divided into sub-regions and nine copulas are tested on each region using graphical assessment and analytical goodness-of-fit tests. It is found that given that water deficit duration and severity characteristics varied across regions, different copulas are deemed suitable.

3. The conditional probability models for severity given a threshold duration and duration given a threshold severity are different. Comparing two climatologically distinct regions (Upper RG and Lower-Middle RG) it is found that the conditional probability of minor events are almost similar but that for long duration high severity events are very different, reflecting the nature of deficit events in these regions.

4. The conditional probabilities of water deficit durations and severities, based on modeled runoffs, are compared with conditional probabilities of rainfall deficit duration and severities, based on observed data in Lower-Middle RG, and it is found that the latter is consistently higher.

5. Modeled derived water deficit conditional probabilities can be used in tandem with observation driven conditional probabilities for long term water planning and management. Further, model derived information may be used in regions having limited ground observation data.

Return periods based on duration and severity separately, and conditional return periods of duration given a threshold severity and severity given a threshold duration are constructed and can be employed along with joint probability plots in the estimation risks in long-term water resources planning.

5 PROBABILISTIC PREDICTION OF PRECIPITATION USING LARGE-SCALE CIRCULATION INDICES AS PRECURSORS – EFFECT OF INTERDECADAL MODULATION

5.1 OVERVIEW

The influence of two large-scale circulation patterns [El Niño Southern Oscillation (ENSO) and Pacific Decadal Oscillation (PDO)] on precipitation and water availability has been explored in the previous sections. In this section, a simple model is proposed for the probabilistic prediction of precipitation, based on the state of ENSO and PDO. The study area is the state of Texas, US, which, by virtue of its size and geographical location, spans a wide range of climatic regions. The state is divided into ten climate divisions, and the precipitation pattern in each division follows different probability distributions. The climatic regimes which trigger this difference in probability distribution are discussed. The correlation between ENSO and PDO and precipitation anomaly in each climate division is established. Copula is used to model the dependence structure between the large-scale climate indices and precipitation. Ten copulas, from the elliptical and Archimedean families, were evaluated. Three of the copulas considered were two-parameter copulas, which can capture more than one type of dependence. Maximum pseudo-likelihood method, which ensures that the selected copula is independent of the marginal, was used for fitting. Different copulas were found to be suitable for different climate divisions. Lower tail dependence, which is associated with La Niña conditions and negative precipitation anomaly, was found to be the determining factor guiding copula selection. Two models, a bivariate, using ENSO and precipitation, and a trivariate, using ENSO, PDO, and precipitation, were constructed and compared. Using the most appropriate copula, precipitation anomalies, in three distinctly different climate divisions, were simulated using both models. The statistics of the simulated values agreed well with the observations. Finally, precipitation anomalies were predicted using the two models. The trivariate model was found to perform better, especially in predicting values in the lower quadrant, which are negative precipitation anomalies associated with La Niña and negative PDO.

5.2 INTRODUCTION

Texas cycles through short- and long-duration droughts, interspersed with periods of above average precipitation. Precipitation, or the lack thereof, has often been linked to conditions in the Pacific Ocean. The state of the El Niño Southern Oscillation (ENSO) is a major determinant: El Niño often leads to above average conditions, and La Niña has been associated with major droughts in the state. Further, the Pacific Decadal Oscillation (PDO) has also been shown to affect local climate conditions. *Özger et al.* [2009], for example, using two Niño indices and a PDO index, showed that there is a robust relationship between the large-scale climate circulation pattern and the Palmer Drought Severity Index (PDSI) in Texas. The correlation structure was not uniform across the state; the semi-arid regions exhibited higher correlation than the sub-tropic regions.

Gershunov and Barnett [1998a] note that PDO modulates the effect of ENSO; El Niño (La Niña) during the positive (negative) phase of PDO, leads to stronger climate responses, than when they are evolving in opposite phases. *McCabe and Dettinger* [1999] state that precipitation prediction skill, in North America can be enhanced when information on both ENSO and PDO is considered.

In this section, a simple model is developed to (i) assess how well ENSO conditions alone can predict precipitation, and (ii) if considering the state of PDO improves precipitation prediction in the state of Texas. Given that ENSO, PDO, and precipitation assume different marginal behaviors, copulas [*Sklar*, 1959] are used to model the dependence structure between the large-scale climate patterns and precipitation. *Maity and Nagesh Kumar* [2008] used a bivariate copula model to capture the dependence between two climate variables (ENSO and the Equatorial Indian Ocean Oscillation (EQUINOO)) combined into a joint index, and the Indian Summer Monsoon. Their model was able to predict rainfall at one station with a high degree of confidence.

In this section, the correlation between ENSO and PDO on precipitation in the ten climate divisions in Texas is first assessed separately. The interdecadal modulation of ENSO by PDO and its effect on precipitation is then examined. Marginals are then fitted to the climate indices

data and to precipitation anomalies in each climate division. The choice of marginals, with respect to basic statistical characteristics of precipitation is discussed. Bivariate copula models for ENSO and precipitation, and trivariate models for ENSO, PDO, and precipitation, are developed and compared. The choice of copulas is discussed in light of the dependence structure. The selected copula is then used to simulate and predict precipitation in three climate divisions: 5, which is semi-arid, 8, located in the wettest region, and 7 in the middle-eastern part of the state.

5.3 STUDY AREA: TEXAS

Texas is the second largest, with a total land and inland water area of 691,146 km^2, and the second most populous state (25.67 million in 2012), in the United States. Of the 50 states, it registered the largest population growth between 2000 and 2010, and the population is further projected to increase by 82% to 43.6 million by 2060. Lack of water, however, can lead to serious social, economic, and environmental consequences across the state. The drought of the 1950s, once considered the drought of record, caused an estimated annual loss of $3.5 billion (adjusted to 2008 dollars) [*Texas Water Development Board*, 2012]. Recently, in 2011, the state suffered the worst single year drought and harshest drought in recorded history. Economic losses to the agricultural sector alone have been evaluated at $7.62 billion, making it the costliest drought on record [*Fannin*, 2012].

5.3.1 CLIMATE OF TEXAS

Texas extends from latitude 25°50′N to 36°30′N and from longitude 93°31′W to 106°38′W. It has a mean elevation of 519 m; the highest point is the Guadalupe Peak (2,668 m), on the far western part of the state, and the lowest point is the Gulf of Mexico (sea level), which forms the southeastern boundary. By virtue of its size and geographical location, Texas spans a wide range of climatic regions with a multitude of microclimates. The eastern third of the state is classified as subtropical humid and the middle third as subtropical subhumid and subtropical steppe, while the western region is subtropical arid and the north western panhandle area is continental steppe (Figure 26).

On the Köppen-Geiger climate classification system (not shown here), the eastern half of the state is warm temperate, fully humid, with hot summer (Cfa) while the western half is mostly cold arid steppe (BSk). The far western tip is arid desert (BWk) and eastern lower edge, running along the border with Mexico, is arid steppe, with hot arid temperatures (BSh).

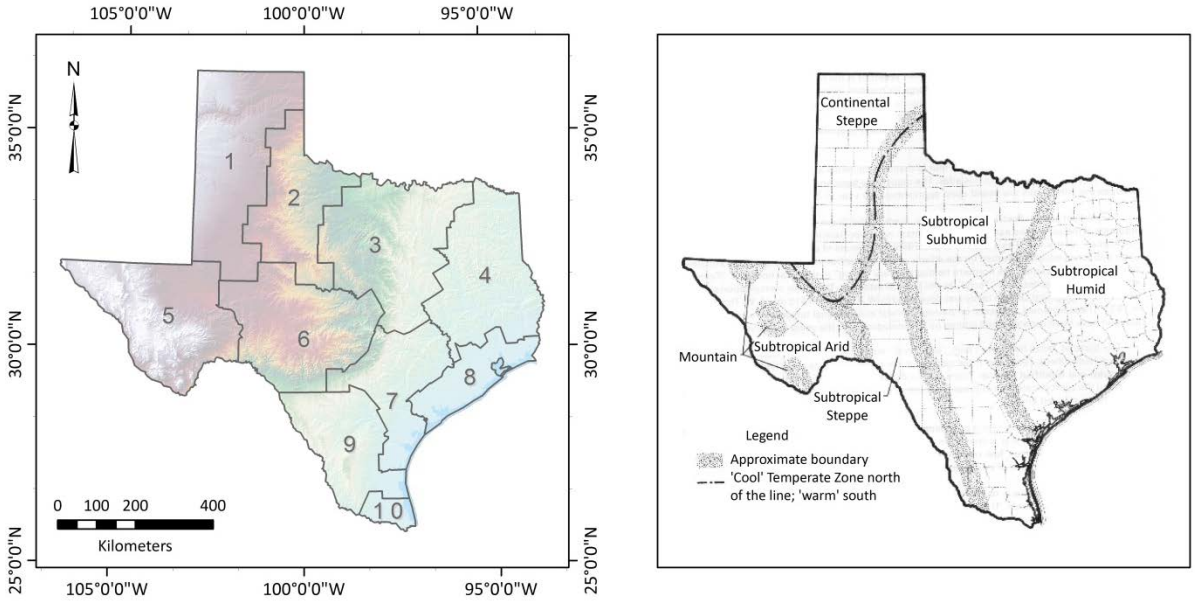

1. High Plains	2. Low Rolling Plains	3. North Central	4. East Texas	5. Trans Pecos
6. Edwards Plateau	7. South Central	8. Upper Coast	9. Southern	10. Lower Valley

Figure 26. Climate divisions and climate regions of Texas (adapted from [*Larkin and Bomar*, 1983]).

5.3.1.1 Climate Divisions

The number and areal extent of climate divisions in the state of Texas has undergone several iterations; in 1904, the state had seven climatic divisions, which was reduced to three in 1936, and in 1951, the state was divided into the current 10 climatic regions (Figure 26) [*Griffiths et al.*, 1990]. One limitation of the current climate division is that it does not always reflect homogeneous climate regions, but has geographical boundaries that match county boundaries.

Furthermore, they are not of equal area; climate division 1 is the largest, covering nearly 15% of the state, and division 10 is the smallest and covers just over 1%.

5.3.1.2 Precipitation, Temperature, and Evaporation Patterns

The climate of Texas is influenced by its topography and regional characteristics [*Nielsen-Gammon*, 2009]. Three large geographical features, the Rocky Mountains, the central and eastern North American continent, and the Gulf of Mexico, influence the state's climate. The Rocky Mountains provide a barrier to winds moving from east to west or vice versa; hence winds from north or south are prevalent in Texas, except in the Far West region lying in the Cordillera. The central and eastern North American continent and the Gulf of Mexico, on the other hand, provide a barrier-free pathway for moisture transport into Texas. Cold air masses originating from the eastern side of the North American Cordillera flows southward into Texas. The Gulf of Mexico provides both a source of moisture and regulates the temperature as its surface temperatures do not vary considerably on a daily or seasonal basis as do land surface temperatures. Moisture is transported by the Caribbean low-level jet, which carries moisture from the Caribbean Sea and Atlantic Ocean into the Gulf of Mexico where the air picks additional moisture and is transported inland by the Great Plains low-level jet [*Mo et al.*, 2005]. The eastern Trans-Pecos and Panhandle regions receive moisture from the eastern Pacific Ocean and from land-recycled moisture as well.

Average annual precipitation in the state decreases longitudinally from east (1,535 mm at Beaumont) to west (247 mm at El Paso) at a rate of 100 mm/°longitude. Average annual temperature increases from about 11°C in the northern Panhandle of Texas (climate division 1) to about 20°C in the Lower Rio Grande Valley. Lowest temperatures are generally recorded in January, where a sharp north (−6.7°C) – south (10°C) gradient exist, and highest temperatures are recorded in July (~33.3°C across the whole state) [*Nielsen-Gammon*, 2009]. Average annual gross lake evaporation increases from the east (< 1,270 mm) to west (> 1,905 mm) [*Texas Water Development Board*, 2012].

Figure 27 is a violin plot of monthly precipitation in each climate division. A violin plot is a boxplot combined with kernel density plots, added on each side of the boxplot, to show the

probability distribution of the dataset. Moving from west to east/southeast across the state, along with an increase in the median value, more dispersion and skewness is noted in the monthly precipitation. Furthermore, the probability of months with zero precipitation is highest for climate divisions 1 and 5 and lowest for divisions 4 and 8.

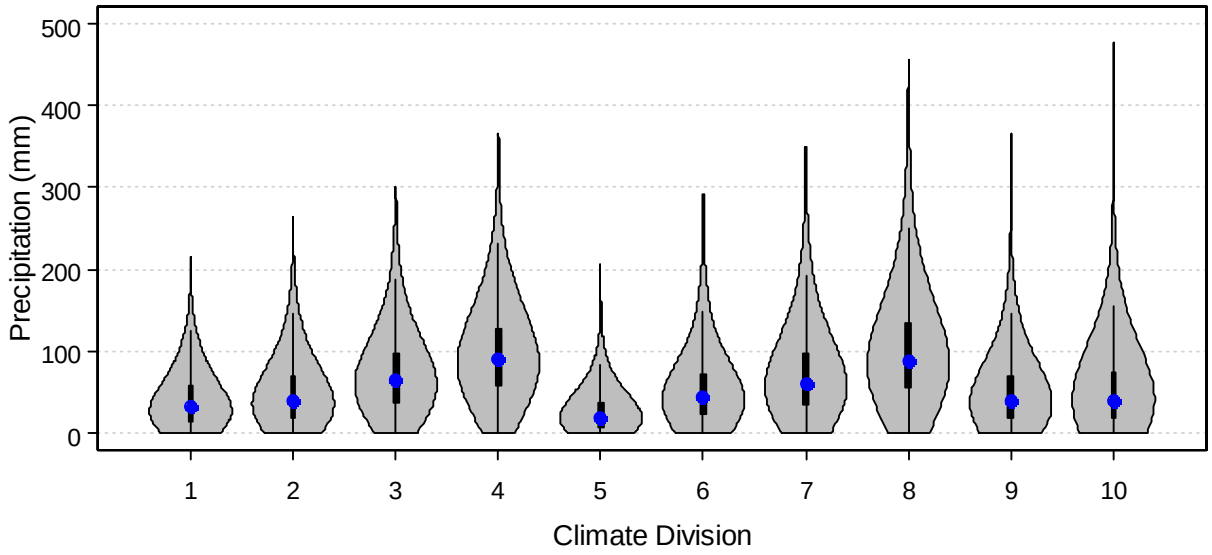

Figure 27. Violin plots of monthly precipitation in each climate division in Texas. Thick black line and blue dot shows the 25th and 75th percentile range and median respectively, and thin black line shows the 5th and 95th percentile range.

Monthly mean precipitation for each month in each climate division, along with that for the whole state, is given in Figure 28. Texas has a very distinct bimodal precipitation pattern; in fact precipitation patterns in climate divisions located in the subtropical subhumid and subtropical steppe part of the state (2, 3, 6, 7, and 9) are bimodal, prompting a bimodal pattern for the state. May is the wettest month followed by September. Climate divisions 1 and 5, located in the continental steppe and subtropical arid zones, respectively, have a unimodal precipitation pattern; November^{0} – April^{+} is the dry season and May^{0} – October^{0} is the wet season. Wet season rainfall represents 75% of annual precipitation. High precipitation in July and August is the consequence of the North American Monsoon (NAM), which can

dramatically change the landscape of the arid southwestern US. NAM is triggered by differential warming between land and the Pacific Ocean, causing the monsoon ridge to migrate north and result in a shift in wind direction from southwesterly to more southeasterly, marking the onset of NAM. Precipitation is due to low level moisture surges, carried from the Gulf of California, and slow upper-level moisture from the Gulf of Mexico. Interannual variability in the monsoon rainfall is not strongly associated with ENSO [*Adams and Comrie*, 1997]. However, El Niño (La Niña) occurring concurrently with high (low) phase of the North Pacific oscillation causes a weaker (stronger) and southward (northward) displaced monsoon ridge. Such condition delays (advances) the onset of NAM and below (above) average early summer precipitation is recorded [*Castro et al.*, 2001]. Climate division 1 also benefits from NAM, but May and June precipitations are the highest due to the West Texas Dryline [*Nielsen-Gammon*, 2009]. The dryline is a result of collision between warm dry air from the desert west and moisture laden air from the Gulf of Mexico, causing severe thunderstorm on the east of the dryline. The dryline disappears in the summer as the jet stream weakens and the monsoon system arises.

The eastern, coastal, climate divisions 4, 8, and 10 have almost uniform monthly mean precipitation, fueled by a constant supply of moisture from the Gulf of Mexico and occasional hurricanes in the summer, which can bring considerable amount of rainfall in a short period of time.

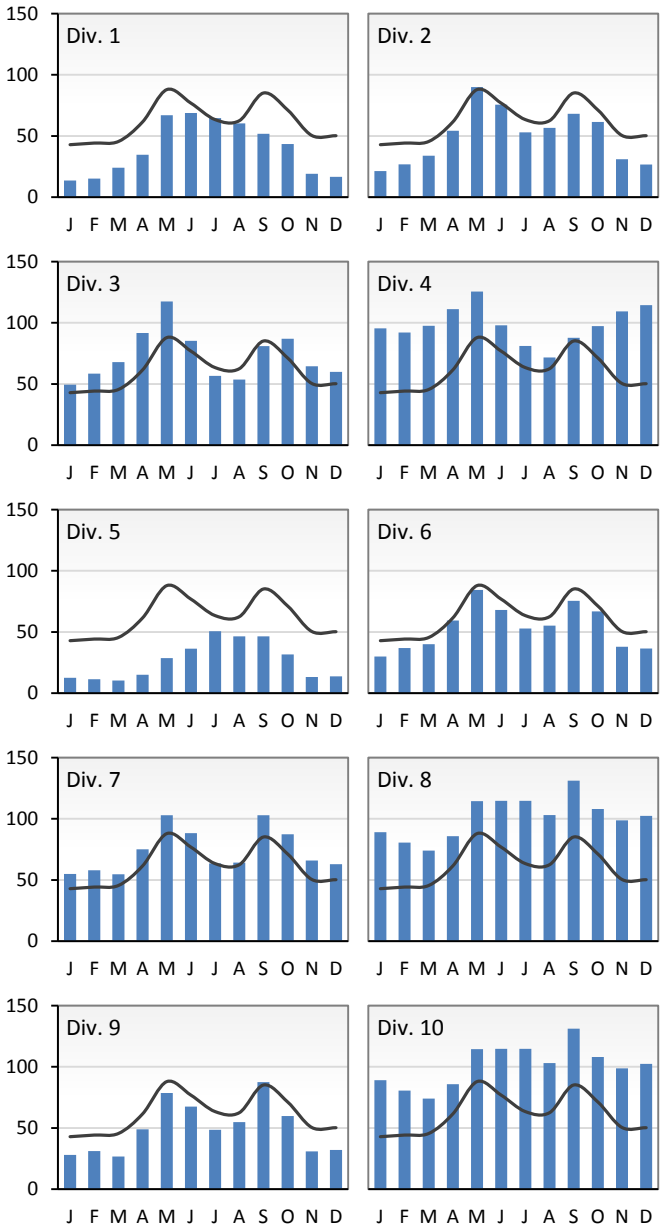

Figure 28. Monthly mean precipitation for each month (in mm) in each climate division based on data for 1900 to 2011. Solid black line represents the mean monthly precipitation for the whole state.

5.4 DATA

5.4.1 PRECIPITATION

Sparse weather records, in Texas, exist from as early as 1836, but statewide weather records began in 1895. The time period considered in this study is January 1900 to March 2012. Monthly mean precipitation data for each of the ten climate divisions in Texas was obtained from the National Climatic Data Center (NCDC). The monthly values are equal-weighted averages from stations reporting both temperature and precipitation within a division. Equal weightage minimizes any bias that may result from changes in the number of stations included over time [*Guttman and Quayle*, 1996]. Figure 29 gives a plot of monthly precipitation for each division, smoothed with a 13-month centered moving average window, around the long-term means for the dataset.

5.4.2 CLIMATE INDICES

5.4.2.1 Southern Oscillation Index (SOI)

The El Niño Southern Oscillation (ENSO) is a coupled ocean-atmosphere phenomenon associated with changes in the sea surface temperature in the tropical Pacific and major shifts in the Intertropical Convergence Zone over the Pacific Ocean. The Southern Oscillation is the atmospheric component, pertaining to the large-scale fluctuation in atmospheric mass between the Indian and Pacific Oceans in the tropics and sub-tropics [*Trenberth*, 1984]. SOI combines the fluctuations in atmospheric pressure between Tahiti (17.5°S 149.6°W) and Darwin, Australia (12.4°S 130.9°E) into one series. Monthly SOI data (standardized Tahiti - standardized Darwin), derived following *Trenberth* [1984], was obtained from the National Center for Atmospheric Research (NCAR) Climate & Global Dynamics (CGD) climate analysis section. *Trenberth's* [1984] standardization maximizes the signal to noise ratio. SOI is preferred to other ENSO indices (e.g. Niño indices) for this study as they exhibit slightly higher correlations with precipitation in Texas.

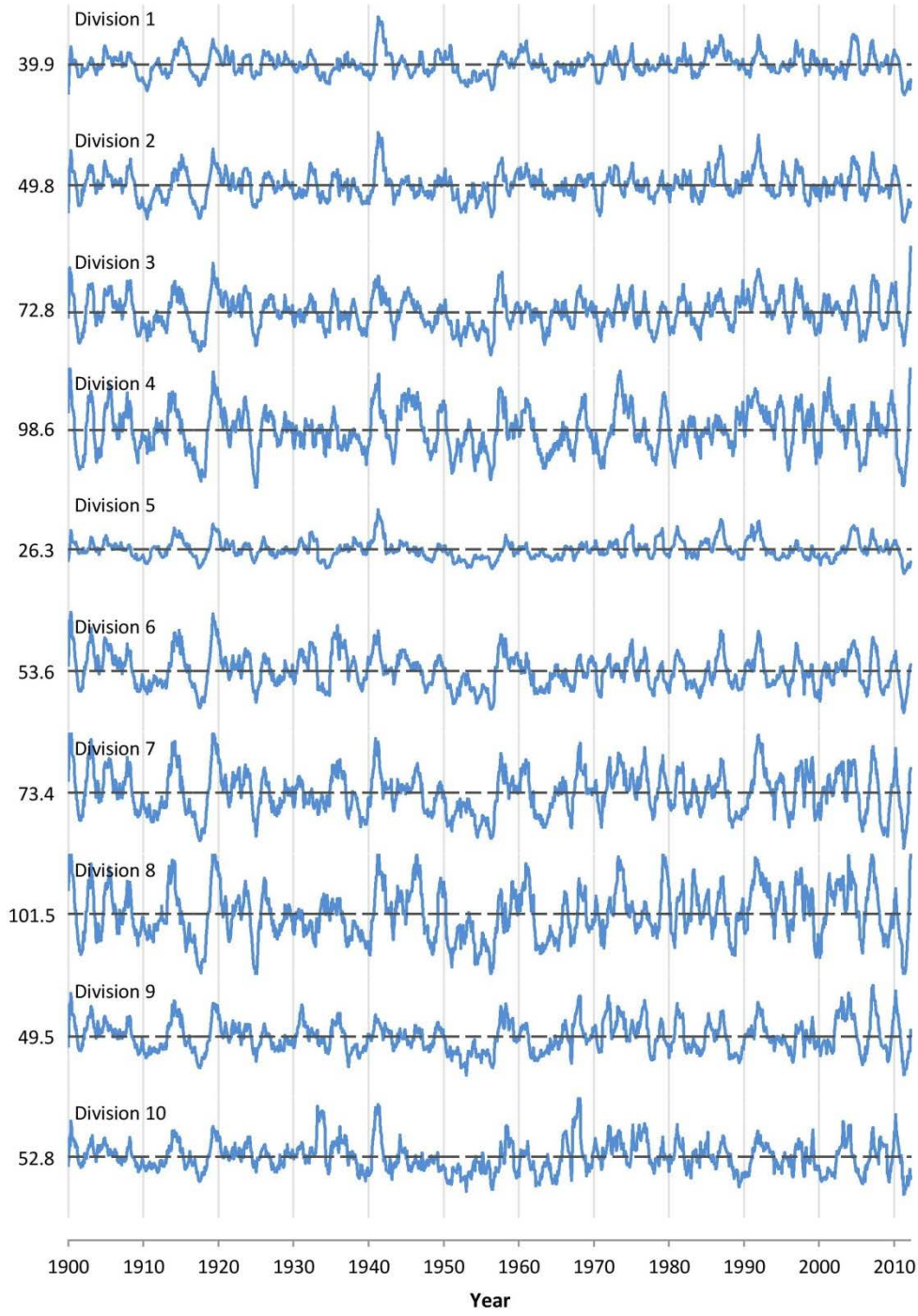

Figure 29. Time series of monthly precipitation for each climate division. The time series has been smoothed with a 13-month centered running mean filter. The dotted line represents the means for the dataset (mm). The time series were not padded at the ends.

The correlation between SOI and precipitation in the southern United States is generally negative. Negative correlations, however, affect the types of copulas that can be employed in this study, as some copulas, e.g. the Archimedean copula families, exist in the positive dependence space. Rotated versions of these copulas can be used to cover negative dependence, but would nearly double the number of copulas to be included in the analysis. To circumvent this hurdle, we created a negative SOI series (NSOI) by multiplying the SOI values by −1. A plot of monthly NSOI values is shown in Figure 30. El Niño and La Niña events are associated with extremes in the NSOI series. Unlike with the Niño 3.4 index (North American countries reach consensus on El Niño definition available at http://www.noaanews.noaa.gov/stories2005/s2394.htm), there is no established definition for ENSO events based on SOI. *Ropelewski and Jones* [1987] suggested that ENSO events can be identified using a five-month running mean of NSOI values, with El Niño (La Niña) defined when the running mean value is above +0.5 (below −0.5) standard deviations for five months or longer. *Kiladis and van Loon* [1988], on the other hand, suggested that ENSO events be defined when both SST is at least 0.5°C above mean for three seasons and SOI is negative and below −1 for the same duration. The plot in Figure 30 shows a five-month running mean and the ±0.5 and ±1 thresholds overlain on monthly NSOI indices.

5.4.2.2 Pacific Decadal Oscillation (PDO)

Monthly PDO indices for the study period were obtained from the Joint Institute for the Study of the Atmosphere and Ocean (JISAO). The PDO index is the leading principal component from an un-rotated empirical orthogonal analysis of monthly residuals of the North Pacific Ocean SSTA, poleward of 20°N [*Mantua et al.*, 1997]. The residuals are the difference between observed anomalies and monthly mean global average SSTA; hence the index is not affected by global warming trends.

Figure 30 gives a plot of the monthly PDO indices. The series was smoothed with a centered 13-month moving average filter to highlight multi-decadal frequencies. Positive (negative) values indicate warm (cold) phases of PDO. Between January 1900 and March 2012, 51.4% of the record was warm months and 48.4% was cold months. There has been two full PDO cycles in the last century: cool phases lasting from 1890 to 1924 and from 1947 to 1976, and warm

phases lasting from 1925 to 1946 and from 1977 to 1998 [*Mantua and Hare*, 2002; *Minobe*, 1997]. From 1998, the PDO has been in a short 4 year cold phase, until 2002, a warm phase lasting from 2002 to 2007, and is currently in a cold phase.

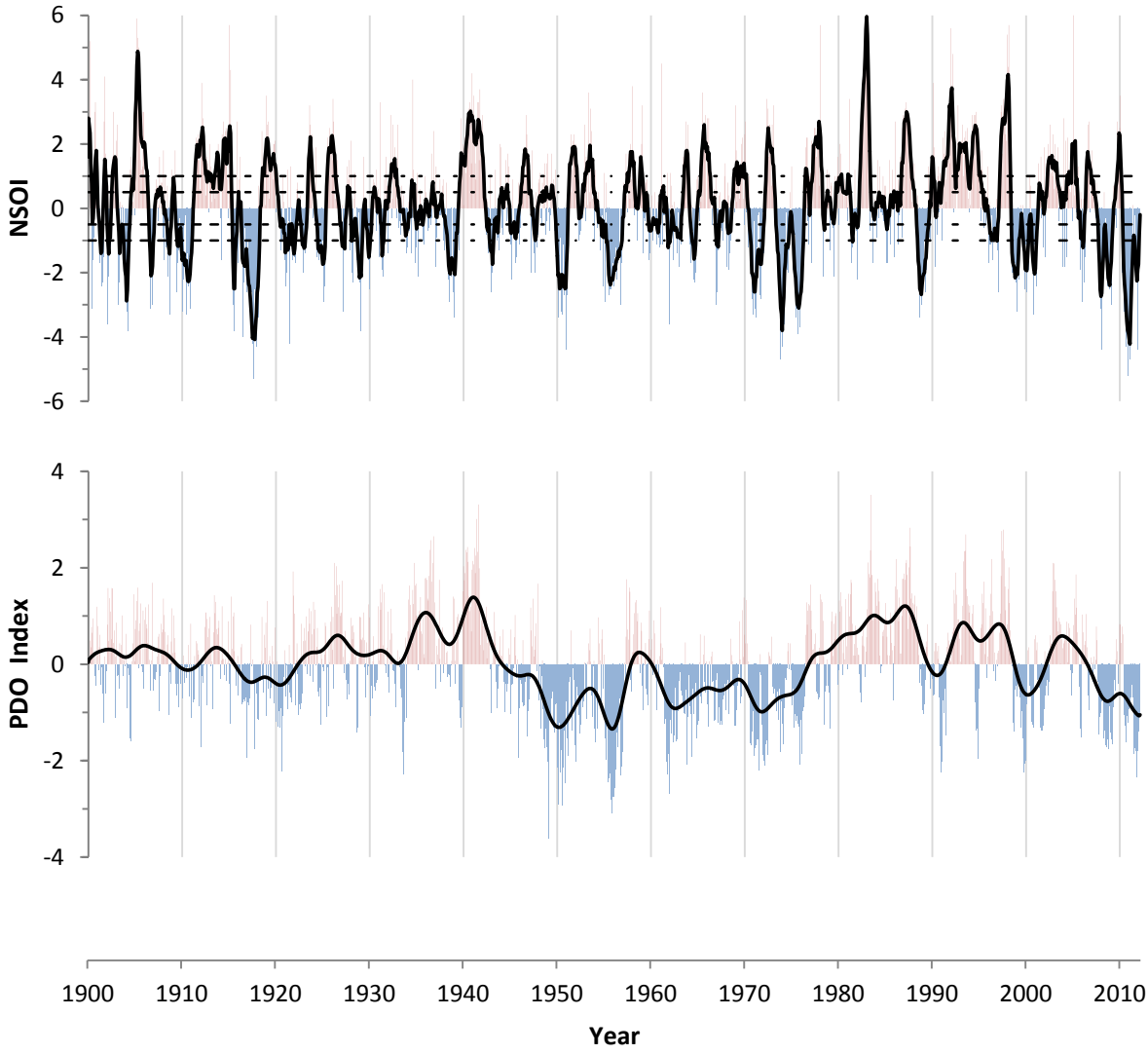

Figure 30. Time series of monthly NSOI and PDO indices. The NSOI series is overlain with a 5-month centered running mean filter and ± 0.5 and ± 1 thresholds. The PDO series is smoothed with 10 passes of a 13-month centered running mean filter.

5.5 METHODOLOGY

5.5.1 MARGINAL DISTRIBUTION SELECTION

Marginals were chosen from a suite of theoretical distributions commonly used in hydrology. A combination of graphical assessment, Q-Q plots, and formal goodness-of-fit techniques were used to compare observed sample distributions with theoretical distributions in the selection of the best fitting marginal.

The Kolmogorov-Smirnov (K-S) test is a common goodness-of-fit technique. It compares the empirical distribution function with the theoretical one. It is very convenient as it does not depend on the underlying cumulative distribution being tested, and is an exact test. One major limitation of the K-S test, however, is that the distribution has to be fully specified, i.e. location, scale, and shape parameters cannot be estimated from the data sample. Because of this limitation, the Anderson-Darling test is often preferred. It is a modified version of the K-S test and gives more weight to the tails. Unfortunately, the test is not available for all distributions [*NIST/SEMATECH*, 2012] and therefore cannot be used as a common comparison baseline for the suite of theoretical distributions tested.

We opted for the chi-square goodness-of-fit test in order to discriminate between theoretical distributions. The chi-square goodness-of-fit test verifies the null hypothesis that the data follows the specified distribution. The test statistics is given by:

$$\chi^2 = \sum_{i=1}^{k} \frac{(O_i - E_i)^2}{E_i} \qquad \textbf{(22)}$$

where O_i is observed frequency for bin i, E_i is the expected frequency for bin i and k is the total number of bins based on Sturges' formula ($k = \log_2 N + 1$). $E_i = N\big(F(Y_u) - F(Y_l)\big)$, where F is the cumulative distribution function for the distribution under test, Y_u and Y_l are, respectively, the upper and lower limits for class i, and N is the sample size. The test statistic is distributed as a χ^2 random variable with $k - p - 1$ degrees of freedom, p being the number

of estimated parameters. The test fails to reject the null hypothesis when χ^2 is less than the chi-square critical value with $k - p - 1$ degrees of freedom and significance level α.

5.5.2 COPULA SELECTION

Simulating and predicting the influence of large scale circulation phenomena on precipitation requires multidimensional modeling of random variables. Multidimensional analyses have traditionally been expressed using classical multivariate families which assume that the marginals describing the behavior of the individual random variables are from the same family as the multivariate distributions. Moreover, the dependence structure of most conventional multivariate distributions directly or indirectly assumes linear correlation given through Pearson's product-moment correlation coefficient (e.g. bivariate gamma distributions discussed by *Yue et al.* [2001]). Copula, which is due to *Sklar* [1959], skirts these constraints and allows univariate margins and dependence structure to be modeled independently.

A copula is a multivariate distribution with all univariate margins being standard uniform $[U(0,1)]$. *Joe* [1997] explains that for an m-variate distribution $F \in \mathcal{F}(F_1, \dots, F_m)$, with j^{th} univariate margin F_j, there exists a copula $C\colon [0,1]^m \rightarrow [0,1]$ that satisfies

$$F(x) = C[F_1(x_1), \dots, F_m(x_m)], \quad x \in \Re^m \tag{23}$$

If F is a continuous m-variate distribution function with univariate margins $F_1, \dots, F_m$, and quantile functions $F_1^{-1}, \dots, F_m^{-m}$, then

$$C(\boldsymbol{u}) = F[F_1^{-1}(u_1), \dots, F_m^{-m}(u_m)] \tag{24}$$

is unique; otherwise C is uniquely determined on $\text{Ran}F_1 \times \dots \times \text{Ran}F_m$, where $\text{Ran}F_j = F_j([-\infty, \infty])$ is the range of F_j.

Copula C is 'independent' of the univariate margins:

$$G(\boldsymbol{y}) = C[G_1(y_1), \dots, G_m(y_m)] \quad \textbf{(25)}$$

is a distribution function if $G_1, \dots, G_m$ are all univariate distributions. The copula can be parametrized by a single value $\boldsymbol{\theta}$, or can be multi-parameter.

Copulas are generally classified into four classes: Archimedean, extreme value, elliptical, and other miscellaneous class. In this study, bivariate and trivariate cases of two copulas from the elliptical class (Gaussian and Student's t with different degrees of freedom) and eight from the Archimedean class (Clayton, Gumbel, Frank, Joe, BB1, BB6, BB7, and BB8) were considered. BB1, BB6, BB7, and BB8 are from the two-parameter families. The two-parameter families of copula can be particularly useful in capturing more than one type of dependence, e.g. one parameter for upper tail and lower tail dependence each, or one parameter for concordance while the other captures the lower tail dependence [*Joe*, 1997].

5.5.2.1 Elliptical Copula

Gaussian (Normal) Copula

The Gaussian copula, derived from a multivariate Gaussian distribution, is perhaps the most popular copula. It can be expressed as

$$C(u_1, \dots, u_m) = \boldsymbol{\Phi}_{\Sigma}[\Phi^{-1}(u_1), \dots, \Phi^{-1}(u_m)] \quad \textbf{(26)}$$

where Φ is the distribution function of a standard normal variable $N(0,1)$ and Σ is the correlation matrix with $m(m-1)/2$ parameters satisfying the positive semidefiniteness constraint. $\boldsymbol{\Phi}_{\Sigma}$ is the m-variate standard normal distribution with mean 0 and covariance matrix Σ, i.e. $\boldsymbol{\Phi}_{\Sigma} \sim N_m(0, \Sigma)$ [*SAS/ETS*, 2011].

Student's t Copula

The Student's t copula can be written as

$$C_{\Theta}(u_1, \dots, u_m) = \mathbf{t}_{\nu,\Sigma}[t_{\nu}^{-1}(u_1), \dots, t_{\nu}^{-1}(u_m)] \quad \textbf{(27)}$$

where $\Theta = \{(\nu, \Sigma): \nu \in (1, \infty), \Sigma \in \mathbb{R}^{m \times m}\}$ and t_ν is the univariate t distribution with ν degrees of freedom. $\mathbf{t}_{\nu,\Sigma}$ is the multivariate Student's t distribution with correlation matrix Σ and ν degrees of freedom [*SAS/ETS*, 2011].

5.5.2.2 Archimedean Copulas

The Archimedean family is the most popular copula family employed in hydrological analyses because of its ease of construction and wide range of choices for the strength of dependence. The general form of the Archimedean family is

$$C(u_1, \dots, u_m) = \phi^{-1}[\phi(u_1) + \cdots + \phi(u_m)] \quad \textbf{(28)}$$

where $\phi: [0,1] \rightarrow [0, \infty)$ is a strict Archimedean copula generator function and its inverse ϕ^{-1} is completely monotonic on $[0, \infty)$. The generator is a decreasing function and is termed strict, and the resulting copula a strict copula, when $\phi(0) = \infty$ and $\phi(1) = 0$ [*SAS/ETS*, 2011]. The dependence parameter θ is embedded in the generating function ϕ.

5.5.2.3 Copula Parameter Estimation

The copula parameter can be estimated via several methods: the exact maximum likelihood method, the moment-like method, which is based on the inversion of the non-parametric dependence measure (e.g. Kendall's tau), and the maximum pseudo-likelihood method. The first method can be used if the marginal distributions are already uniform. The last two methods require that the observations, $\boldsymbol{x}_i = (x_{i1}, \dots, x_{im})^{\top}, i = 1, \dots, n$, are transformed into pseudo-observations, $\widehat{\boldsymbol{u}}_i = (\hat{u}_{i1}, \dots, \hat{u}_{im})$, $i = 1, \dots, n$, i.e. in the unit hypercube. $\hat{u}_{ij} = (1/(n+1))\text{rank}\,(x_{ij})$, where $\text{rank}(x_{ij})$ is the rank, in ascending order between $i = 1, \dots, n$. Non-parametrically ranking the joint variates through their respective scale ranks ensures that the dependence structure is determined independently of the marginals [*Genest and Favre*, 2007]. In this study the maximum pseudo-likelihood method is used. For a copula

$C(u_1, \dots, u_m; \theta)$, with density $c(u_1, \dots, u_m; \theta)$, the parameter θ can be estimated by maximum likelihood:

$$\hat{\theta} = \arg\max_{\theta \in \Theta} \sum_{i=1}^{n} \log c(\hat{u}_{i1}, \dots, \hat{u}_{im}; \theta) \quad \textbf{(29)}$$

5.5.2.4 Goodness-of-fit Tests

A combination of graphical and formal goodness-of-fit tests was employed to select the most suitable copula. A scatter plot of observed data (the support of the empirical copula C_m) overlapped upon a set of random samples generated from copula C_{θ_m} is an efficient way of visually comparing the effectiveness of the fitted copula in capturing the dependence structure in the empirical dataset. *Genest and Favre* [2007] suggest that in order to avoid any arbitrariness due to sampling variability, a large sample generated from $C_{\theta_m}$is preferred to smaller samples, which may not display the whole range of the distribution. Too large samples, however, may obscure the actual frequency of occurrence [*Chowdhary et al.*, 2011].

Genest et al. [2009] provide a review of formal goodness-of-fit tests for copulas. Two tests, the Cramér-von Mises and Kolmogorov-Smirnov tests, were used to test the adequacy of copula models and differentiate between the suitability of each copula in capturing the dependence structure. The expressions for the Cramér-von Mises and Kolmogorov-Smirnov are respectively given as [*Genest et al.*, 2006]

$$\begin{aligned} S_n &= \int_0^1 |\mathrm{K}_n(w)|^2 k_{\theta_n}(w)\, dw \\ &= \frac{n}{3} + n \sum_{j=1}^{n-1} K_n^2\left(\frac{j}{n}\right)\left[K_{\theta_n}\left(\frac{j+1}{n}\right) - K_{\theta_n}\left(\frac{j}{n}\right)\right] \\ &\quad - n \sum_{j=1}^{n-1} K_n\left(\frac{j}{n}\right)\left[K_{\theta_n}^2\left(\frac{j+1}{n}\right) - K_{\theta_n}^2\left(\frac{j}{n}\right)\right] \end{aligned} \quad \textbf{(30)}$$

and

$$\mathcal{T}_n = \sup_{0 \le w \le 1} |\mathrm{K}_n(w)| = \sqrt{n} \max_{i=0,1;0 \le j \le n-1} \left\{ \left| K_n\left(\frac{j}{n}\right) - K_{\theta_n}\left(\frac{j+1}{n}\right) \right| \right\} \quad \textbf{(31)}$$

where $\mathrm{K}_n(w) = \sqrt{n}\{\mathrm{K}_n(w) - \mathrm{K}_{\theta_n}(w)\}$

These tests can be employed for any type of copulas. The p-values associated with test statistics were computed by bootstrapping. A stepwise methodology is provided by *Genest and Favre* [2007].

5.6 RESULTS AND DISCUSSION

5.6.1 TEMPORAL CHANGES IN PRECIPITATION AND MAJOR EVENTS

Figure 29 shows the time series of monthly precipitation, from January 1900 to March 2012, in each climate division, smoothed with a 13-month centered running mean filter, around the long-term average precipitation. Precipitation is rarely around the long term mean, rather Texas cycles between successive short- and long-term droughts interspersed with periods of significantly above average rainfall. The Dust Bowl drought of the 1930s is one of the most devastating natural disasters the US has faced. Weather patterns were influenced by a combination of La Niña and warmer than normal conditions in the tropical Atlantic Ocean, which suppressed the supply of moisture carried inland from the Gulf of Mexico [*Schubert et al.*, 2004]. The drought extended from northern Mexico to the Canadian prairies. Notwithstanding socio-economic considerations and based solely on precipitation deficit, the Dust Bowl drought is not the worst drought in the state of Texas. In fact, precipitation in most part of state hovered around the long term average and was even above average in some climate divisions. The most glaring precipitation deficit episode spanning all climate divisions occurred in 1914 and lasted until 1918. This event coincides with La Niña conditions and a cold PDO (Figure 30). Another important drought event prior to the Dust Bowl occurred in 1924-1925. The eastern part of the state was most affected, with climate divisions 4, 7, and 8

suffering the highest precipitation deficit. NSOI was in a negative phase in 1924 and shifted into positive in the beginning of 1925, while PDO oscillated between positive and negative.

The most important drought in Texas, often dubbed the drought of record, occurred in the 1950s. The drop in precipitation in the early 1950s was particularly noticeable, as it followed a decade of above average precipitation, driven by El Niño and warm PDO, across the whole state. Subsequently PDO gradually transitioned into its negative phase and by 1948 was predominantly negative and remained so, with two noticeable peaks around 1950 and 1956, for the following 10 years. Two strong La Niña events, interrupted by weak positive NSOI episodes, occurred in 1950 and 1955-1956, coincident with the troughs in the PDO cycle. In some climate divisions, the 1950 drought appears as two or three distinct droughts with short wet spells. It was nonetheless the longest and most widespread drought and has since been deemed the baseline, or worst case scenario, for the state's water plans. Another significant event, with two droughts occurring, back-to-back, occurred between 1962 and 1967. The first drought started in 1962, and precipitation briefly neared average in 1964 to be followed by another drought event and was subsequently broken by a wet spell towards the end of 1967. It is interesting to note that PDO was negative for the duration of this drought event and the first wet spell, in 1966, coincides with a short El Niño, but the second event that officially broke the drought coincides with a transitioning or neutral ENSO. A short duration high severity drought occurred in 1970-1971, coincident with a La Niña, seriously affecting agriculture and cattle. The 1971 to around 1990 period is very different from the rest of the record. It represents the wettest ten to twenty years; precipitation was generally around the long-term mean with numerous above average peaks. The 1990 to 2010 period was marked by several short and long-term droughts punctuated by wet years [*Nielsen-Gammon*, 2011].

2011 was an exceptional year in the recorded history of Texas; the state faced a drought of unprecedented intensity. The drought started in September 2010, following a relatively wet year favored by El Niño conditions. The later El Niño coincides with a brief period of positive PDO. By the middle of 2010 both NSOI and PDO had shifted into their negative phases and remained so until March 2012, the last data point in the dataset. Both indices exhibited bimodality and evolved synchronously; NSOI exhibited its first trough in December 2010,

with a minimum index value of −5.2 (lowest NSOI value registered is −5.3 in August 1917), and appeared to decay by June 2011, but resurged and a second dip, with a minimum index value of −4.4 (fourth lowest NSOI value), was recorded in December 2011. During this period, precipitation across the state was minimal. October 2010 to September 2011 were the driest 12 consecutive months on record, where Texas received only 297 mm of rainfall, which represents only 40% of the state average annual total (741 mm) and is 64 mm less than the 12-month record set during the 1950s drought [*Nielsen-Gammon*, 2011]. Summer temperatures in 2011 were exceptionally high; June-August temperature across the state was 2.5°F higher than previous summers and 5°F above the long-term average [*Nielsen-Gammon*, 2011], thus further contributing to the lack of water in the state. *Hansen et al.* [2012] argues this event was most likely enhanced by global warming, as the likelihood of such extreme anomalies is otherwise very small.

Atlantic hurricanes generally bring abundant rainfall in a very short period of time in the summer and fall, often resulting in major flooding, especially in the eastern part of the state. While El Niño (La Niña) tends to favor and increase (decrease) in precipitation, it also suppresses (enhances) Atlantic hurricane formation [*Pielke and Landsea*, 1999].

5.6.2 Climate Teleconnection and Precipitation

Comparison of precipitation patterns in the ten climate divisions against time series for NSOI and PDO shows that major precipitation events (both droughts and above average anomalies) are often prompted by fluctuations in ocean temperature in the Pacific Ocean. *Ropelewski and Halpert* [1986] found a consistent relationship between ENSO and October^{0} – March^{+} precipitation patterns in the Gulf and Mexican area. October^{0} – March^{+} has also been identified as the season exhibiting highest correlation with SST or atmospheric pressure fluctuations in the Pacific Ocean by others [e.g. *Kurtzman and Scanlon*, 2007; *Redmond and Koch*, 1991]. Incidentally, October is the beginning of the hydrological year in Texas, thus the water year is split into two 6-month periods which will henceforth be referred to as the cold (October^{0} – March^{+}) and warm (April^{0} – September^{0}) seasons. The influence of ENSO and

PDO on warm season precipitation is not as distinct as that on cold season precipitation, and will therefore not be considered further.

Figure 31 shows boxplots of the cold season average precipitation distribution for each climate division. The east to west negative gradient in monthly precipitation mean is also present in the cold season average precipitation. One notable difference, however, is between climate divisions 4 and 8, which have almost the same interquartile range for monthly precipitation but visibly different ranges and medians for cold season average precipitation.

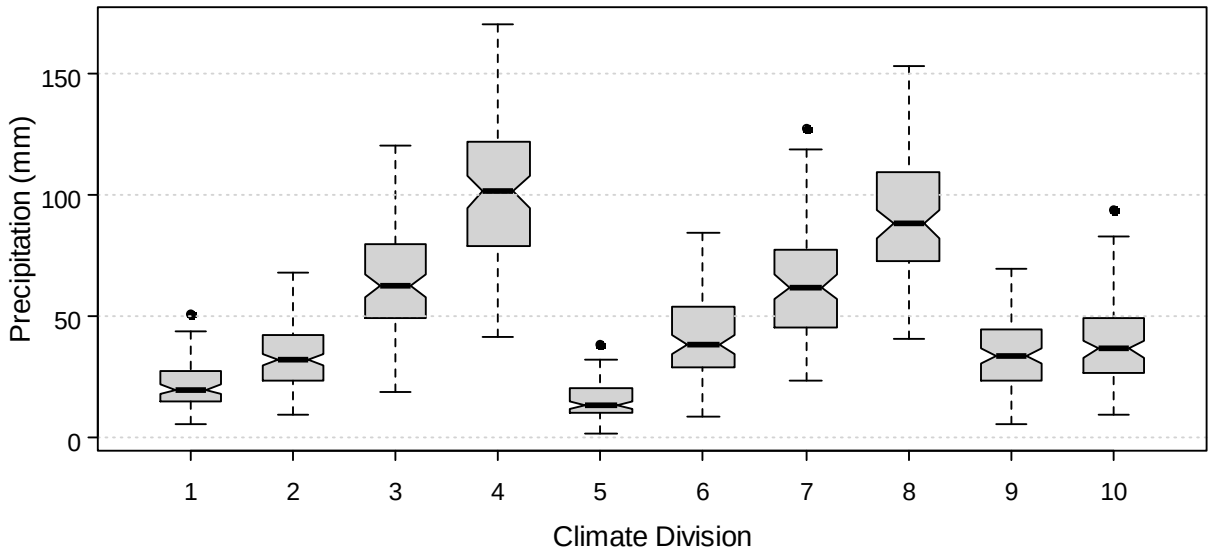

Figure 31. Boxplots of cold season (October^0 – March$^+$) average precipitation in each climate division in Texas.

Redmond and Koch [1991] explored the relationship between SOI and precipitation in the western US, hypothesizing that since events in the Pacific are teleconnected to remote precipitation or temperature events, a time lag would separate each event, and found an optimum lag of 4 months, i.e. highest correlation was obtained between June^0 – November^0 average of monthly SOI and October^0 – March$^+$ average of monthly precipitation. *Kurtzman and Scanlon* [2007] chose to truncate the SOI averaging period to June^0 – September^0, in order to have an index that is available at the beginning of the hydrologic year. June^0 – September^0

and June^0 – November^0 averages of monthly SOI values have a very high correlation (r^2 = 0.969 for the period 1900 to 2011).

Using an atmospheric general circulation model, *Kumar and Hoerling* [2003] explored and confirmed that a lag of a season exists between the peaks of the Niño 3.4 SST anomalies and zonal mean rainfall anomalies. This lag is convenient for water planning and management, as by preceding the start of the hydrologic year, it forewarns possible changes in precipitation anomalies. Given that ENSO events normally peak from November onward [*Khedun et al.*, 2012b] and major precipitation events in the US happen after the peak, we opt to adhere to June^0 – November^0 averages of monthly NSOI as the forewarning index. Further, since June^0 – September^0 and June^0 – November^0 averages of monthly SOI are highly correlated, predictions can be made on the former and reevaluated and updated after two months into the water year.

Figure 32 shows the correlation patterns between June^0 – November^0 average NSOI and cold season average precipitation anomalies, and cold season average PDO indices with cold season average precipitation anomalies. The Pearson correlation coefficient, ρ_{xy}, forms the basis of the statistical test of independence. The null hypothesis is that the average precipitation anomalies are independent and identically distributed (iid) normal random variables, not dependent on the indices. The magnitude and sign of the correlation coefficient thus indicate the existence, strength, and nature of any association [*Redmond and Koch*, 1991]. The correlation significance (*p*-value) for each climate division was also computed and is given in the inset maps.

A statistically significant positive correlation between both June^0 – November^0 average NSOI and cold season PDO, and cold season precipitation anomalies is noted. The correlation structure for NSOI is consistently above 0.4, except for climate division 1, across the whole state. The correlation structure for PDO reveals two regions. Climate regions 1 to 4 and 8, covering the top half of the state, have a lower correlation, ranging between 0.237 (division 4) and 0.387 (division 2), while the lower south-western half of the state has a correlation of greater than 0.4. Climate division 8 has the highest correlation with NSOI (0.535) but is included in the region exhibiting lower correlation with PDO.

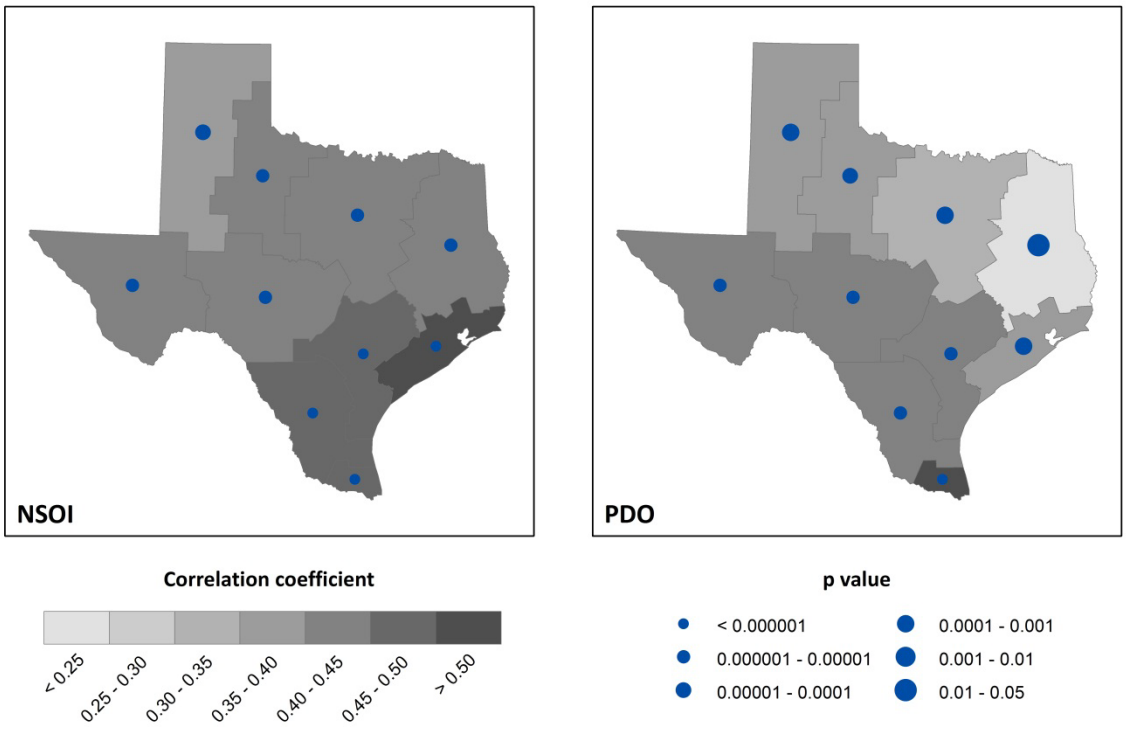

Figure 32. Plots of correlation coefficients between June^0 – November^0 average NSOI and cold season (October^0 – March$^+$) average precipitation anomalies and cold season average PDO index and cold season average precipitation anomalies.

5.6.2.1 Interdecadal Modulation of ENSO's Impacts

The effects of ENSO and PDO on precipitation patterns are not independent; in fact PDO modulates the effect of ENSO, leading to stronger climate responses when El Niño (La Niña) is coincident with the positive (negative) phase of PDO. When the indices are evolving in opposite phases (i.e. El Niño and negative PDO or La Niña and positive PDO), climate signals may be weaker, spatially incoherent, and unstable [*Gershunov and Barnett*, 1998a].

Table 10 presents the number and percentage of times the June^0 – November^0 average NSOI and cold season average PDO index are in different states. El Niño (La Niña) events are deemed stronger when NSOI is greater (less) than +1 (−1) and moderate when the index is between +0.5 and +1 (−0.5 and −1) (based on K. Redmond, Classification of El Niño and La Niña Winters, available at http://www.wrcc.dri.edu/enso/ensodef.html). For the period of

record, there is a slightly higher number of stronger El Niño than La Niña events. Also, the ratio of moderate to stronger events is about 1:3, which indicates that the index rarely hovers between ±0.5 and ±1. In fact, once initiated, it eventually develops into a significant El Niño (La Niña) event. The record is split into a combined total of 54 years of stronger El Niño or La Niña, and 58 neutral years, implying that ENSO was either active in one of the two conditions or neutral about half the time.

Cold season average PDO has almost equal number of positive and negative cases. When the state of NSOI and PDO are considered together, an equal number of El Niño coincident with positive PDO, and La Niña with negative PDO, are recorded. Also, the number of El Niño (La Niña) during positive (negative) PDO is higher than when they are in counter phase. Finally, more (less) El Niño (La Niña) events during negative (positive) PDO is noted.

In order to verify the occurrence of positive (negative) precipitation anomalies occurring during El Niño (La Niña) events, and corresponding PDO phases, cold season average precipitation anomalies are plotted against June^0 – November^0 average NSOI (Figure 33a). Climate division 8 is chosen for illustration, as it is unique in that it has the highest correlation with NSOI and falls with the region having relatively lower correlation with PDO. The dotted lines represent the ±1 thresholds above (below) which strong El Niño (La Niña) conditions are felt. Positive (negative) precipitation anomalies occurring during El Niño (La Niña) are identified and plotted against cold season PDO (Figure 33b). It can be clearly seen that El Niño (La Niña) brings above (below) average precipitation, and there is no distinct pattern during the neutral phase of NSOI. 21% of the 112 years of data are in the El Niño-positive anomaly region 18% and are in the La Niña-negative anomaly region. When the precipitation events are transposed on the PDO plot, the overall precipitation pattern is no longer as distinct, which explains the lower correlation. It is nonetheless clear that there is a higher frequency of above (below) average precipitation when the indices are evolving concurrently than in opposite phases.

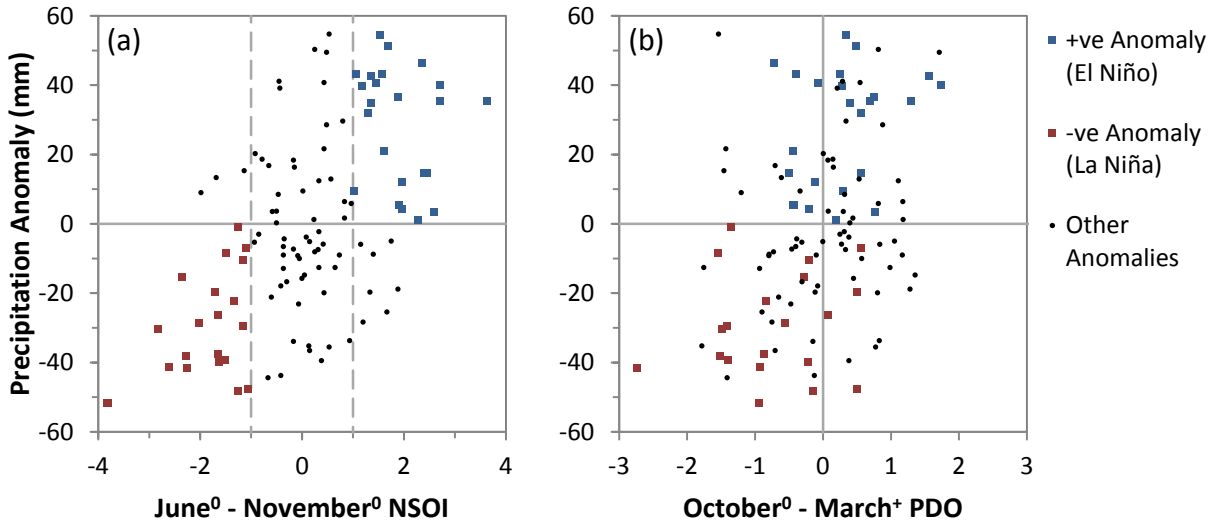

Figure 33. Scatter plot of cold season (October^0 – March$^+$) average precipitation anomalies versus (a) June^0 – November^0 average NSOI and (b) cold season average PDO indices for climate division 8. Positive (negative) anomalies during El Niño (La Niña) events are shown in blue (red).

The amount and percentage change in precipitation for each climate division, given different phases of NSOI and PDO, were computed (Table 11). Results confirm the hypothesized interdecadal modulation of ENSO impacts, and also reveal that the percentage changes in precipitation anomalies are not uniform across the state. Considering NSOI only, an increase ranging between 15.8% (division 4) and 25.9% (division 1) is registered during El Niño events, and a decrease ranging between −18.4% (division 4) and −34.9% is recorded during La Niña events. A more modest increase (decrease) is noted when PDO is positive (negative). When El Niño (La Niña) occurs concurrently with positive (negative) PDO, the change in precipitation is considerably greater. El Niño events during negative PDO causes a small increase in precipitation, while La Niña events during positive PDO still result in considerable rainfall deficits, implying that irrespective of the phase of PDO, La Niña events can often have adverse effects on water resources in the state. Spatially, the wetter eastern climate divisions are less affected than the drier western climate divisions. This may be due to their proximity with the coast and the effect of hurricanes, whose frequency has an inverse relationship with NSOI.

Table 10. Number and percentage of time the June^{0} – November^{0} average NSOI and cold season (October^{0} – March^{+}) average PDO index are in different phases.

Case	Number of Events	Percentage
NSOI > +1 (Stronger El Niño)	31	27.7
+0.5 < NSOI < +1 (Moderate El Niño)	10	8.9
−0.5 < NSOI > +0.5	40	35.7
−1 < NSOI > +1	58	51.8
−1 < NSOI < −0.5 (Moderate La Niña)	8	7.1
NSOI < −1 (Stronger La Niña)	23	20.5
PDO > 0	58	52.7
PDO < 0	53	47.3
NSOI > +1 and PDO > 0	19	17.0
NSOI < −1 and PDO < 0	19	17.0
NSOI > +1 and PDO < 0	12	10.7
NSOI < −1 and PDO > 0	4	3.6

Table 11. Amount (mm) and percentage change (*in italics*) in cold season (October^{0} – March^{+}) average precipitation for different phases of June^{0} – November^{0} average NSOI and cold season average PDO index.

Case	Climate Divisions									
	1	**2**	**3**	**4**	**5**	**6**	**7**	**8**	**9**	**10**
NSOI > 1	5.613	7.709	11.836	16.035	3.548	9.062	15.003	19.706	7.397	8.390
	25.9	*22.9*	*18.0*	*15.8*	*23.2*	*22.0*	*23.4*	*21.3*	*21.4*	*21.7*
NSOI < −1	−5.669	−11.395	−16.824	−18.554	−5.438	−14.440	−18.231	−23.763	−10.743	−11.179
	−25.6	*−34.1*	*−26.3*	*−18.4*	*−35.2*	*−34.9*	*−28.5*	*−25.8*	*−30.9*	*−28.8*
PDO > 0	3.202	4.752	7.420	6.804	2.806	7.178	9.195	10.346	5.419	6.118
	14.3	*14.1*	*11.2*	*6.6*	*18.3*	*17.4*	*14.3*	*11.1*	*15.7*	*15.8*
PDO < 0	−3.267	−4.774	−7.131	−6.451	−3.053	−7.684	−9.956	−11.067	−6.304	−7.564
	−14.6	*−14.3*	*−11.3*	*−6.5*	*−19.7*	*−18.6*	*−15.6*	*−12.1*	*−18.1*	*−19.5*
NSOI > 1 and PDO > 0	7.470	10.100	17.760	21.542	6.099	14.485	22.654	26.612	11.062	13.428
	34.4	*30.1*	*27.2*	*21.2*	*39.7*	*35.1*	*35.3*	*28.8*	*31.9*	*34.7*
NSOI < −1 and PDO < 0	−5.976	−12.040	−17.071	−18.517	−6.021	−15.039	−18.225	−23.466	−10.889	−11.415
	−27.0	*−36.0*	*−26.7*	*−18.4*	*−39.0*	*−36.4*	*−28.5*	*−25.5*	*−31.3*	*−29.5*
NSOI > 1 and PDO < 0	2.672	3.924	2.458	7.315	−0.492	0.475	2.889	8.771	1.595	0.412
	12.5	*11.7*	*3.5*	*7.1*	*−3.1*	*1.2*	*4.5*	*9.4*	*4.7*	*1.1*
NSOI < −1 and PDO > 0	−4.211	−8.332	−15.650	−18.731	−2.665	−11.597	−18.260	−25.173	−10.054	−10.062
	−18.9	*−24.9*	*−24.5*	*−18.6*	*−17.2*	*−28.1*	*−28.6*	*−27.4*	*−28.9*	*−26.0*

5.6.3 MARGINAL SELECTION

5.6.3.1 NSOI and PDO

Marginals for the June^0 – November^0 average NSOI and the October^0 – March$^+$ average PDO indices were selected from over 25 theoretical distributions. Based on their chi-square statistics, it was found that NSOI and PDO can be appropriately modeled by a GEV (Generalized Extreme Value) and a Weibull distribution, respectively. The probability density function of the GEV is given by

$$f(x) = \begin{cases} \frac{1}{\sigma}\exp\left(-(1+\xi z)^{-1/\xi}\right)(1+\xi z)^{-1-1/\xi}, & \xi \neq 0 \\ \frac{1}{\sigma}\exp\left(-z-\exp(-z)\right), & \xi = 0 \end{cases} \quad \textbf{(32)}$$

in the following domain: $1+\xi\frac{(x-\mu)}{\sigma} > 0$ for $\xi \neq 0$ and $-\infty \leq x \leq +\infty$ for $\xi = 0$. $z \equiv \frac{x-\mu}{\sigma}$, and ξ, σ, and μ are the shape, scale and location parameters, respectively.

For $\gamma \leq x \leq +\infty$, the 3-parameter Weibull is given as

$$f(x) = \frac{\alpha}{\beta}\left(\frac{x-\gamma}{\beta}\right)^{\alpha-1}\exp\left(-\left(\frac{x-\gamma}{\beta}\right)^{\alpha}\right) \quad \textbf{(33)}$$

where α, β, and γ are, respectively, the shape, scale, and location parameters.

The maximum likelihood estimates of the parameters for the GEV are $\hat{\xi} = -0.314$, $\hat{\sigma} = 1.382$, and $\hat{\mu} = -0.320$; and for the Weibull are $\hat{\alpha} = 5.992$, $\hat{\beta} = 4.699$, and $\hat{\gamma} = -4.405$. Figure 34 shows the histograms of June^0 – November^0 average NSOI and October^0 – March$^+$ average PDO values with their respective marginal models and Q-Q plots.

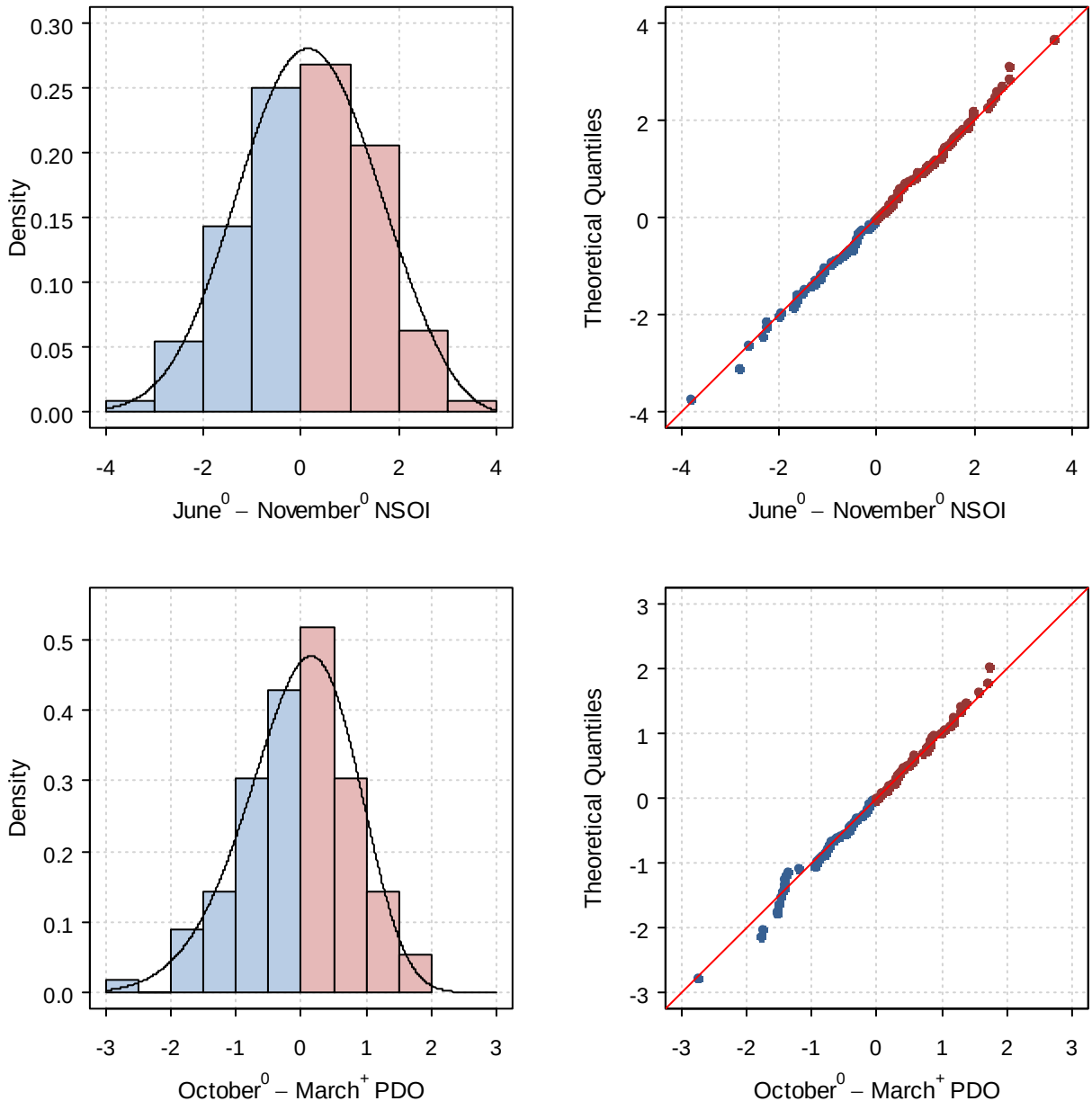

Figure 34. Histograms and Q-Q plots of June^0 – November^0 average NSOI and October^0 – March$^+$ average PDO indices. NSOI follows GEV and PDO follows Weibull. Negative (positive) values are show in blue (red).

5.6.3.2 Cold Season Average Precipitation

Marginal distributions for cold season average precipitation anomaly for each climate division were selected from the same suite of probability distributions used for NSOI and PDO. Table

12 gives the selected model, associated maximum likelihood estimates of its parameters, chi-square statistic, and *p*-value for each climate division. Figure 35 is a plot of the histogram of the cold season average precipitation anomaly and selected marginal model for each climate division.

Table 12. Marginal distribution, parameters, chi-square statistic, and *p*-value for cold season (October^{0} – March^{+}) average precipitation anomaly for each climate division.

Climate Division	Distribution	Parameters	Chi-square	*p*-value
1	Weibull	$\hat{\alpha} = 1.852$ $\hat{\beta} = 19.333$ $\hat{\gamma} = -17.151$	4.025	0.673
2	Normal	$\hat{\sigma} = 13.476$ $\hat{\mu} = 0.0182$	2.058	0.914
3	Gamma	$\hat{\alpha} = 48.082$ $\hat{\beta} = 3.184$ $\hat{\gamma} = -152.930$	2.426	0.877
4	GEV	$\hat{\xi} = -0.308$ $\hat{\sigma} = 27.995$ $\hat{\mu} = -9.331$	3.372	0.761
5	Weibull	$\hat{\alpha} = 2.118$ $\hat{\beta} = 16.335$ $\hat{\gamma} = -14.469$	8.176	0.225
6	Lognormal	$\hat{\sigma} = 0.238$ $\hat{\mu} = 4.277$ $\hat{\gamma} = -74.070$	0.632	0.996
7	Lognormal	$\hat{\sigma} = 0.207$ $\hat{\mu} = 4.730$ $\hat{\gamma} = -115.660$	3.309	0.769

Table 12 Continued.

Climate Division	Distribution	Parameters	Chi-square	p-value
8	GEV	$\hat{\xi} = -0.180$ $\hat{\sigma} = 26.470$ $\hat{\mu} = -11.137$	4.225	0.646
9	GEV	$\hat{\xi} = -0.150$ $\hat{\sigma} = 13.170$ $\hat{\mu} = -5.902$	2.195	0.901
10	GEV	$\hat{\xi} = -0.073$ $\hat{\sigma} = 12.995$ $\hat{\mu} = -6.635$	0.611	0.996

Note:

Gamma: $f(x) = \frac{(x-\gamma)^{\alpha-1}}{\beta^{\alpha}\Gamma(\alpha)}\exp(-(x-\gamma)/\beta)$ where α, β, γ and are the shape, scale, and location parameters, respectively

GEV: $f(x) = \begin{cases} \frac{1}{\sigma}\exp\left(-(1+\xi z)^{-1/\xi}\right)(1+\xi z)^{-1-1/\xi}, & \xi \neq 0 \\ \frac{1}{\sigma}\exp\left(-z-\exp(-z)\right), & \xi = 0 \end{cases}$ where $z \equiv \frac{x-\mu}{\sigma}$, and ξ, σ, and μ are the shape, scale and location parameters, respectively

Lognormal: $f(x) = \frac{\exp\left(-\frac{1}{2}\left(\frac{\ln(x-\gamma)-\mu}{\sigma}\right)^2\right)}{(x-\gamma)\sigma\sqrt{2\pi}}$ where σ, μ, and γ are the scale and location parameters respectively

Normal: $f(x) = \frac{\exp\left(-\frac{1}{2}\left(\frac{x-\mu}{\sigma}\right)^2\right)}{\sigma\sqrt{2\pi}}$ where σ and μ are the scale and location parameters respectively

Weibull: $f(x) = \frac{\alpha}{\beta}\left(\frac{x-\gamma}{\beta}\right)^{\alpha-1}\exp\left(-\left(\frac{x-\gamma}{\beta}\right)^{\alpha}\right)$ where α, β, and γ are the shape, scale, and location parameters, respectively

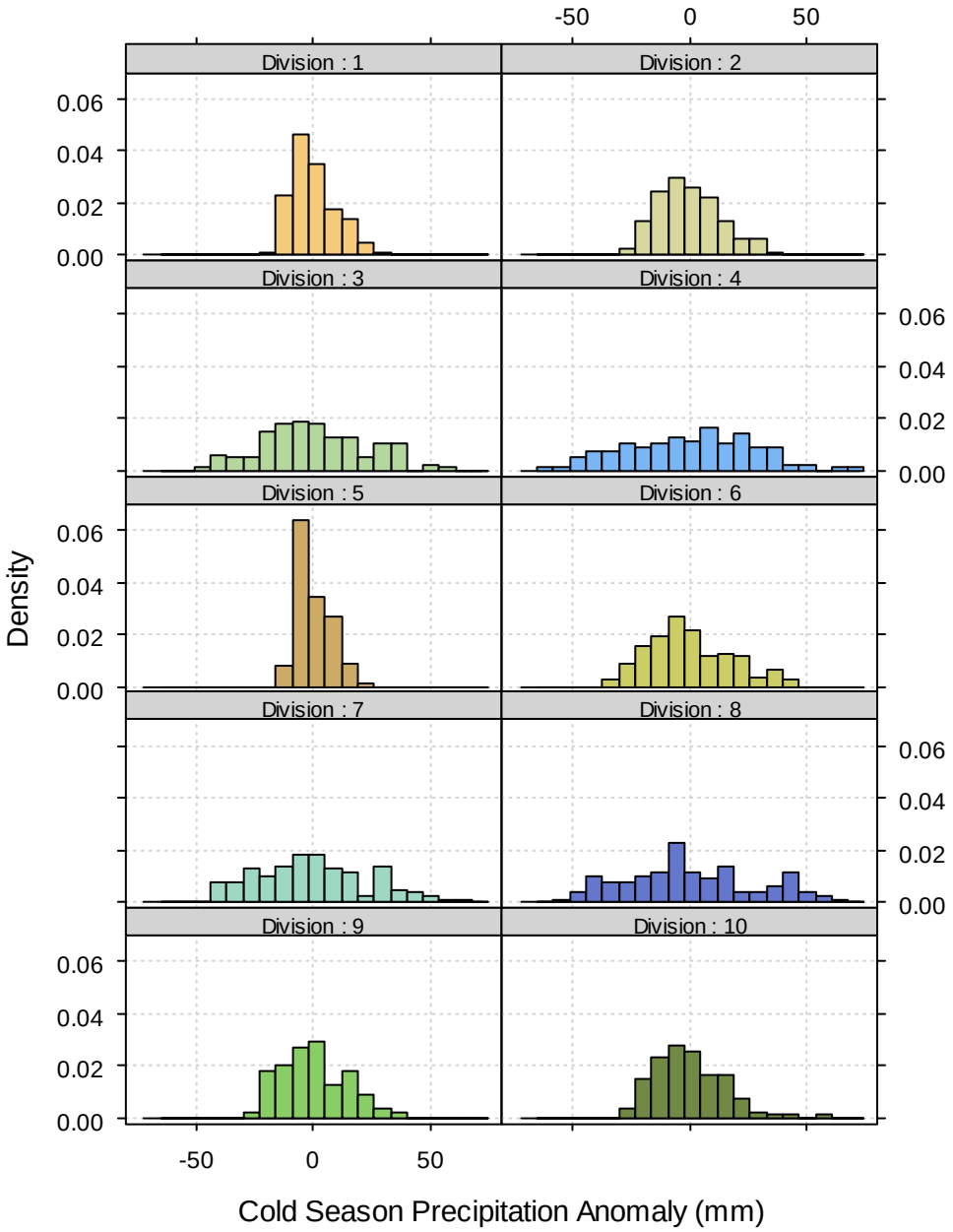

Figure 35. (a) Histogram of cold season (October^{0} – March^{+}) average precipitation anomaly and (b) plot of selected marginal distribution, for each climate division.

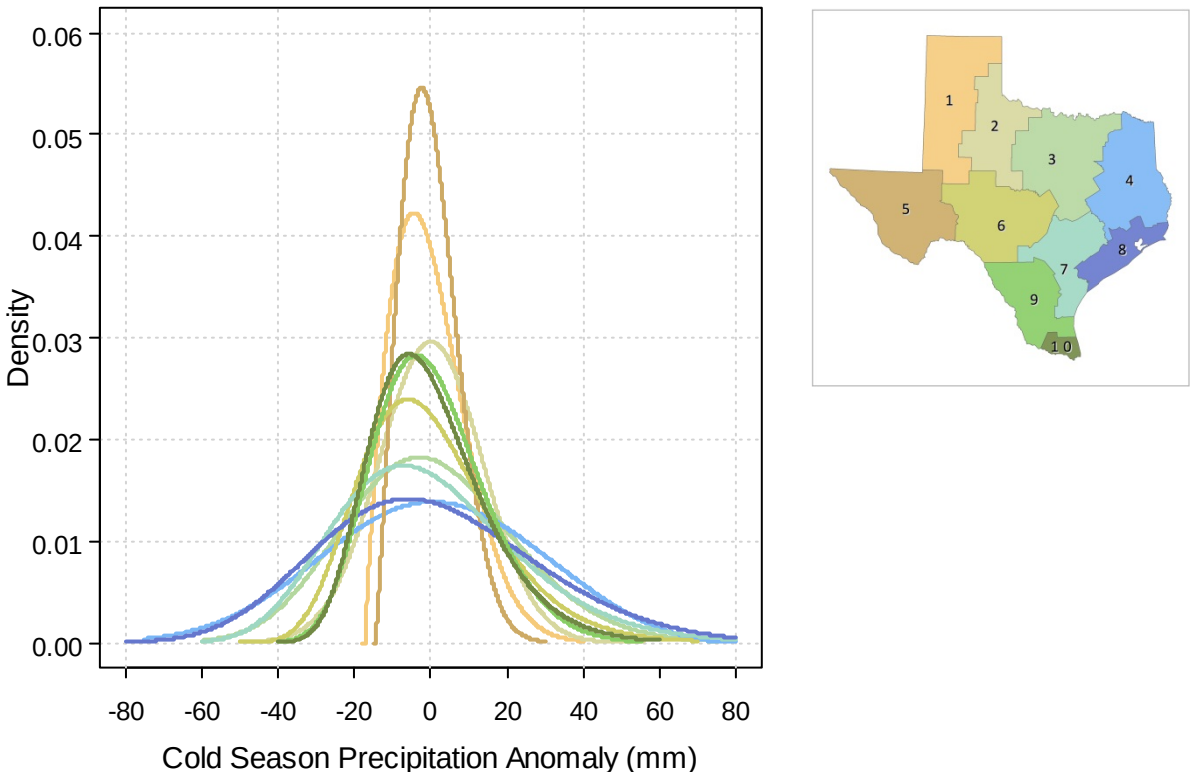

Figure 35 Continued.

It is interesting to note that the selected marginals vary with climatic conditions prevailing in each region. As evidenced by the plot of the marginal distributions and the statistics in Table 13, cold season average precipitation in all climate divisions, except 4, are positively skewed, with the median value being lower than the mean, implying that precipitation is generally below normal, which is typical for the southern US. Cold season precipitation pattern in both the western arid climate divisions 1 and 5, and eastern climate divisions 4, 8, 9, and 10, follows extreme value distributions. Western climate divisions follow shifted Weibull distributions (a.k.a. the Extreme Value Type III), while eastern climate divisions follow the GEV distribution. Note that the Weibull distribution is a special case of GEV, for which the shape parameter $\xi < 0$. The standard deviations of cold season average precipitation anomaly for climate divisions 1 and 5 ($\sigma_{1,5}$), and consequently the shape parameters of the fitted distributions, are relatively smaller compared to that of climate divisions 4 and 8, since precipitation, during the cold season, is minimal in west Texas when NAM, the major source

of moisture for the region, is not active. Also, the distributions for 1 and 5 are more peaked, supported by higher kurtosis values in the data, implying less variability in the cold season precipitation across the years.

Table 13. Statistics of cold season (October^{0} – March^{+}) average precipitation anomaly for each climate division.

Climate Division	Minimum (mm)	Maximum (mm)	Mean (mm)	Median (mm)	Standard Deviation	Skewness	Kurtosis
1	-16.508	29.212	0.010	-1.967	9.689	0.709	2.899
2	-23.889	34.234	0.018	-1.389	13.476	0.447	2.610
3	-45.718	55.671	0.177	-1.903	22.132	0.183	2.557
4	-59.636	69.312	0.103	0.372	27.326	0.016	2.436
5	-13.820	22.841	-0.020	-2.114	7.240	0.618	2.841
6	-32.763	43.310	-0.010	-2.855	17.723	0.456	2.571
7	-40.728	63.624	0.032	-1.824	23.927	0.355	2.483
8	-51.589	61.441	0.074	-4.133	27.802	0.239	2.248
9	-28.787	35.221	-0.019	-0.974	14.181	0.359	2.522
10	-29.408	55.216	-0.013	-2.040	15.199	0.754	3.812

The range of average precipitation in the east is much wider, as indicated by the large standard deviation (3 to 4 times $\sigma_{1,5}$), and the fitted distribution becomes broader. This is due to their proximity to the Gulf of Mexico, which is a perennial source of moisture. Climate division 4, which registers the highest average cold season precipitation, is far enough north to be affected by wintertime disturbances and has enough moisture for precipitation when the disturbances arrive [*Nielsen-Gammon,* 2009]. Climate divisions 6 and 7, in the lower central part of the state, follow lognormal distribution, while climate divisions 2 and 3, in the upper

central portion, follows normal and gamma distributions respectively. The standard deviations of climate divisions 3 and 7, which are further east, are larger and the probability of months without rainfall is relatively low, again due to the influence of the Gulf of Mexico.

5.6.4 COPULA SELECTION

In this section the copula selection procedure is discussed. The bivariate case between June^0 – November^0 average NSOI and cold season average precipitation anomaly for climate division 8 is used for illustration purposes.

5.6.4.1 Copula Parameter Estimation

Precipitation anomalies exhibit a positive association between NSOI (and PDO) in Texas Figure 32). Note that SOI was converted to NSOI to ensure positive association and thus reduce the number of potential copulas. For climate division 8, the sample estimates of the Pearson correlation coefficient, Kendall's tau, and Spearman's rho were 0.535, 0.354, and 0.511, respectively with corresponding *p*-values of 1.216e-09, 3.442e-08, and 8.894e-09. The association between the two variables is further explored graphically through Kendall's plot (K-plot) and chi-plots (Figure 36). A K-plot is equivalent to a QQ-plot, but where data points falling on $y = x$ diagonal indicate that u_1 and u_2 are independent and points above (below) the diagonal line indicate positive (negative) dependence. Chi-plots [*Fisher and Switzer*, 2001] are based on the chi-square statistics for independence in a two-way table [*Genest and Favre*, 2007] and λ_i is a measure of the distance of the points $(u_{1,i}, u_{2,i})$ from the center of the data, defined by its median $(\widetilde{u_1}, \widetilde{u_2})$. In case of no relationship between the two variables, 95% of the data points should fall within the two control lines. Both the K- and chi-plots suggest significant positive dependence. Further, the chi-plots for the lower and upper tails (where lower (upper) tail is defined for those $u_{1,i}$ and $u_{2,i}$ values that are smaller (larger) than their respective means), suggest that the data exhibit both lower and upper tail dependence. Moreover, stronger lower than upper tail dependence is also visible from the plots, which implies that the influence of ENSO during La Niña is more apparent than during El Niño.

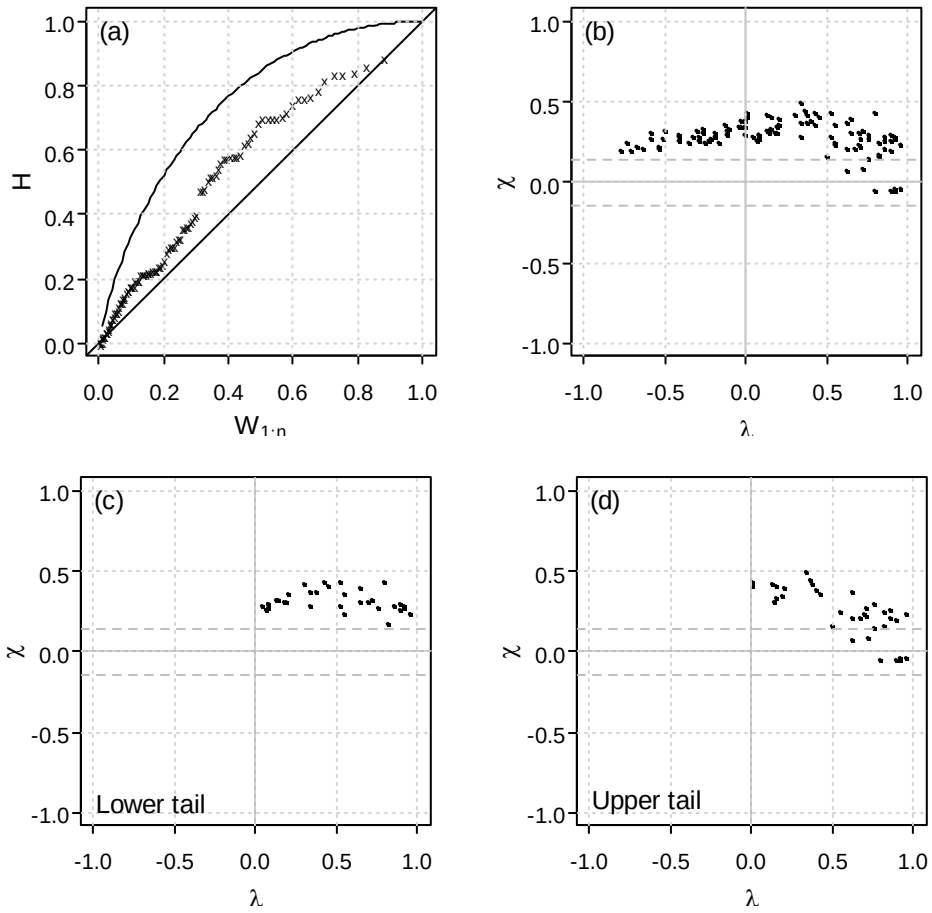

Figure 36. Dependence between June^0 – November^0 average NSOI and cold season average precipitation anomaly for climate division 8 illustrated through (a) Kendall's plot and (b, c, and d) chi-plots.

Based on information garnered from the correlation coefficients and graphically illustrated dependence structure, sets of one- and two-parameter copulas were chosen as potential candidates for modeling the relationship between June^0 – November^0 average NSOI and cold season average precipitation anomalies. The probability function, generating function, parameter space, lower and upper tail dependence, and relationship of non-parametric dependence measure for the bivariate form of each copula are given in Table 14 [*Schepsmeier and Brechmann*, 2012].

Table 14. Probability function, generating function, parameter space, lower and upper tail dependence, and relationship of non-parametric dependence measure with association parameter for bivariate form of the ten copulas used in this study.

Copula	Generator	Parameter Space	Kendall's τ	Tail Dependence	
				Lower (λ_L)	Upper (λ_U)
Elliptical Copula					
Gaussian		$\rho \in (-1,1)$	$\frac{2}{\pi}\arcsin(\rho)$	0	0
Student t		$\rho \in (-1,1)$ $\nu > 2$	$\frac{2}{\pi}\arcsin(\rho)$	$2t_{\nu+1}\left(-\sqrt{\nu+1}\sqrt{\frac{1-\rho}{1+\rho}}\right)$	
Archimedean Copula					
Clayton	$\frac{1}{\theta}\left(t^{-\theta}-1\right)$	$\theta > 0$	$\frac{\theta}{\theta+2}$	$2^{-1/\theta}$	0
Gumbel	$(-\log t)^{\theta}$	$\theta \geq 0$	$1-\frac{1}{\theta}$	0	$2-2^{1/\theta}$
Frank[a]	$-\log\left[\frac{e^{-\theta t}-1}{e^{-\theta}-1}\right]$	$\theta \in \mathbb{R}\backslash\{0\}$	$1-\frac{4}{\theta}+4\frac{D_1(\theta)}{\theta}$	0	0
Joe	$-\log\left[1-(1-t)^{\theta}\right]$	$\theta > 1$	$1-\frac{4}{\theta^2}\int_0^1 t\log(t)\,(1-t)^{\frac{2(1-\theta)}{\theta}}\,dt$	0	$2-2^{1/\theta}$
BB 1	$\left(t^{-\theta}-1\right)^{\delta}$	$\theta > 1$ $\delta \geq 1$	$1-\frac{2}{\delta(\theta+2)}$	$2-2^{-1/(\theta\delta)}$	$2-2^{-1/\delta}$

Table 14 Continued.

Copula	Generator	Parameter Space	Kendall's τ	Tail Dependence	
				Lower (λ_L)	Upper (λ_U)
BB 6	$\left(-\log\left[1-(1-t)^{\theta}\right]\right)^{\delta}$	$\theta \geq 1$ $\delta \geq 1$	$1+4\int_0^1 \left(-\log\left(-(1-t)^{\theta}+1\right)\times \frac{\left(1-t-(1-t)^{-\theta}+t(1-t)^{-\theta}\right)}{\delta\theta}\right)dt$	0	$2-2^{-1/(\theta\delta)}$
BB7[b]	$\left[1-(1-t)^{\theta}\right]^{-\delta}-1$	$\theta \geq 1$ $\delta > 0$	$1-\frac{2}{\delta(2-\theta)}+\frac{4}{\theta^2\delta}B\left(\frac{2-\theta}{\theta},\delta+2\right)$	$2^{-1/\delta}$	$2-2^{1/\theta}$
BB 8	$-\log\left[\frac{1-(1-\delta t)^{\theta}}{1-(1-\delta)^{\theta}}\right]$	$\theta \geq 1$ $0 < \delta \leq 1$	$1+4\int_0^1 \left(-\log\left(\frac{(1-t\delta)^{\theta}-1}{(1-\delta)^{\theta}-1}\right)\times \frac{\left(1-t\delta-(1-t\delta)^{-\theta}+t\delta(1-t\delta)^{-\theta}\right)}{\delta\theta}\right)d$	0	0[c]

[a] $D_1(\theta)=\int_0^{\theta}\frac{c/\theta}{exp(x)-1}dx$ (Debey function); [b] $B(x,y)=\int_0^1 t^{x+1}(t-1)^{y-1}\,dt$ (Beta function); [c] $2-2^{1/\theta}$ if $\delta=1$, otherwise 0

The dependence parameter(s) for each copula was determined using the maximum pseudo-likelihood method, which ensures that the dependent structure is determined independently of the margins. The corresponding Kendall's tau values, maximized log-likelihood values (LL_{max}) and Akaike and Bayesian Information Criteria (expressions for AIC and BIC, respectively, are given as footnotes to Table 15) were also computed.

5.6.4.2 Goodness-of-fit Tests

For each copula considered, two formal goodness-of-fit tests were performed: Cramér-von Mises and Kolmogorov-Smirnov. Table 15 gives the test statistics and associated *p*-values, computed using bootstrapping based on random samples of size 1,000, except for the Gaussian copulas, where computational constraints limited the sample size to 100. At 5% significance level, four copulas (Gumbel, Frank, BB 6, and BB 8) can be rejected as viable models. Based on AIC and BIC, the Gaussian, Student t, and Clayton copulas appear to be most suited to model the dependence structure between June^0 – November^0 average NSOI and cold season average precipitation anomaly in climate division 8. Note that since for large degrees of freedom, the Student t copula tends to a Gaussian copula, only the latter and Clayton copulas will be analyzed further.

Figure 37 allows a visual comparison of the observed data with random samples generated from the Gaussian and Clayton copulas. Positive (negative) precipitation anomalies occurring during El Niño (La Niña) are identified as in Figure 33a. Note that the extreme lower left data point is associated with the 1917 drought, where the June^0 – November^0 average NSOI was −3.82 and associated cold season average precipitation anomaly was −51.59 mm, i.e. coordinates (−3.82, −51.59). By contrast, the recent 2011 drought has coordinates (−2.62, −41.43).

The spread of the two copulas are visibly different; even though they both envelop the observed data, they exhibit different tail behaviors. Lower and upper tail dependence in the Gaussian copula is weak, whereas the Clayton copula exhibits strong lower tail and weak upper tail dependence. The relationship between June^0 – November^0 average NSOI and cold season average precipitation anomaly does exhibit some degree of lower tail dependence,

especially when the major drought events are considered [1917 (−3.82, −51.59), 1950 (−2.28, −38.04), 1975 (−2.83, −30.42), 2011 (−2.62, −41.43)], a feature which, graphically, makes Clayton a more attractive copula. However, based on analytical goodness-of-fit results, the Gaussian copula is deemed most suited for this climate division.

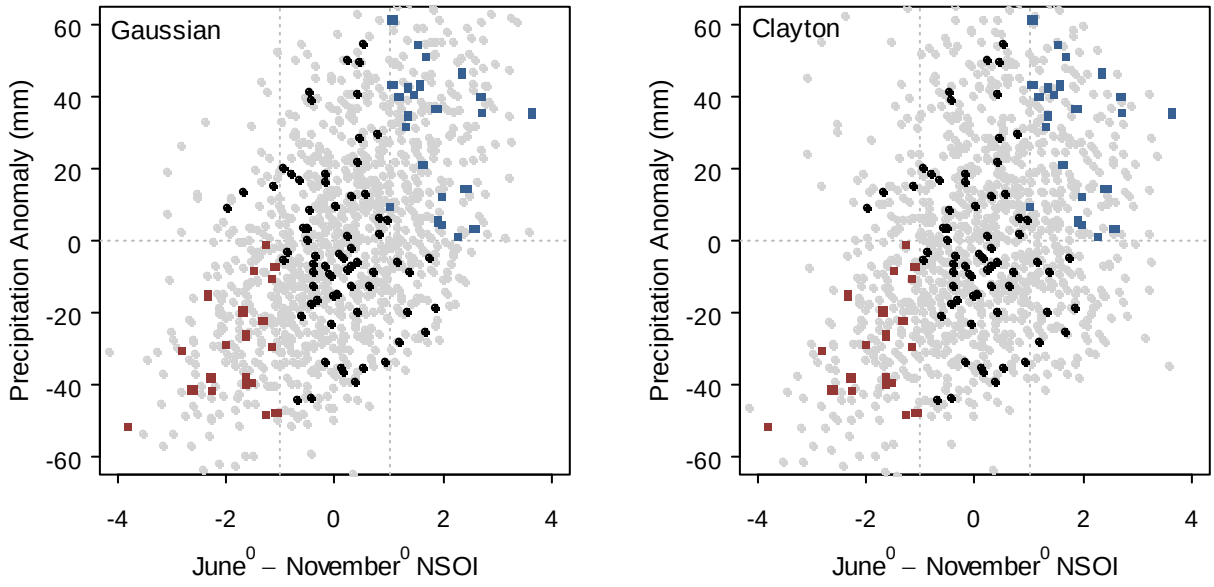

Figure 37. Comparison of observed data with 1,000 random samples generated from the Gaussian and Clayton copula (solid light gray dots). Observed positive (negative) anomalies during El Niño (La Niña) events are shown in blue (red) and other events are shown in solid black dots.

Table 15. Parameter(s), Kendall's tau, AIC, BIC, and Cramér-von Mises and Kolmogorov-Smirnov goodness-of-fit statistics, along with their respective *p*-values, for each copula for climate division 8.

Copula	$\widehat{\boldsymbol{\theta}}$	$\widehat{\boldsymbol{\delta}}$	$\boldsymbol{\tau}$	$\mathbf{LL_{max}}$	**AIC**[1]	**BIC**[2]	$\mathcal{S}_n$ **statistic**	$\mathcal{S}_n$ p	$\mathcal{T}_n$ **statistic**	$\mathcal{T}_n$ p
Gaussian	0.553		0.373	18.545	−35.091	−32.372	0.097	0.230	0.671	0.500
Student t	0.544		0.366	18.046	−34.092	−31.374	0.084	0.370	0.607	0.580
Clayton	0.922		0.315	17.809	−33.618	−30.899	0.123	0.187	0.849	0.206
Gumbel	1.444		0.307	12.596	−23.192	−20.474	0.223	0.009	1.027	0.028
Frank	3.511		0.350	16.329	−30.657	−27.939	0.140	0.050	0.727	0.263
Joe	1.510		0.223	7.587	−13.173	−10.455	0.715	0.981	1.698	0.925
BB 1	0.753	1.094	0.336	18.041	−32.083	−26.646	0.096	0.263	0.728	0.367
BB 6	1.001	1.443	0.307	12.588	−21.175	−15.738	0.223	0.015	1.028	0.035
BB7	1.055	0.896	0.323	17.838	−31.676	−26.239	0.112	0.191	0.809	0.236
BB 8	6.000	0.460	0.331	15.465	−26.930	−21.493	0.177	0.024	0.890	0.090

[1] $AIC = -2\sum_{i=1}^{N} ln[c(u,v|\boldsymbol{\theta},\boldsymbol{\delta})] + 2k$ and [2] $BIC = -2\sum_{i=1}^{N} ln[c(u,v|\boldsymbol{\theta},\boldsymbol{\delta})] + ln(N)k$ where N is the length of the observations and k is the number of copula parameters; τ = Kendall's tau; LL_{max} = maximum log-likelihood; $\mathcal{S}_n$ statistic = Cramér-von Mises statistics; $\mathcal{S}_n$ p = p-value for Cramér-von Mises goodness-of-fit test; $\mathcal{T}_n$ statistic = Kolmogorov-Smirnov statistics; $\mathcal{T}_n$ p = p-value for Kolmogorov-Smirnov goodness-of-fit test.

5.6.4.3 NSOI and Precipitation Anomaly

Following the steps illustrated in sections 5.6.4.1 and 5.6.4.2, copulas were fitted to all ten climate divisions in the state. Table 16 gives the most suited copula and associated parameter and goodness-of-fit statistics for each climate division.

Table 16. Parameter(s) and Cramér-von Mises and Kolmogorov-Smirnov goodness-of-fit statistics, along with their respective *p*-values, for the copula selected for modeling the dependence between June^0 – November^0 average NSOI and cold season average precipitation anomaly for each climate division.

Climate Division	Copula	$\widehat{\theta}$	S_n statistic	S_n p	T_n statistic	T_n p
1	Gaussian	0.399	0.056	0.800	0.573	0.860
2	Clayton	0.814	0.054	0.756	0.626	0.714
3	Clayton	0.785	0.054	0.739	0.556	0.852
4	Gaussian	0.456	0.062	0.640	0.755	0.350
5	Frank	2.733	0.058	0.588	0.633	0.582
6	Clayton	0.806	0.065	0.610	0.774	0.345
7	Clayton	0.918	0.083	0.423	0.757	0.378
8	Gaussian	0.553	0.097	0.230	0.671	0.500
9	Clayton	0.824	0.159	0.064	0.908	0.114
10	Gaussian	0.530	0.061	0.530	0.586	0.720

Most copulas exhibit similar forms in their central part but differ significantly in the tails, where extreme values are located. Given that each climate division is subject to different climatologic conditions and subject to a number of small- and large-scale meteorological regimes, the degree of dependence with NSOI varies, hence the difference in the selected

copula. It is important to note that since the maximum pseudo-likelihood method was used for the copula selection, the chosen copula is independent of the marginals and solely due to the dependence structure.

Cold season precipitation in the western part of the state, as shown in section 5.6.3.2, is minimal and not highly variable, given the limited sources of moisture. Further, the correlation of cold season average precipitation with June^0 – November^0 average NSOI is relatively small. The most suited copula for modeling the dependence in climate divisions 1 and 5 are Gaussian and Frank respectively. The difference between the Gaussian and Frank copulas is in the intermediate area where the Frank copula exhibits a stronger dependence, but at the tails, the Gaussian copula tends to be stronger. The Gaussian is also the chosen copula for climate divisions 4, 8, and 10, which are located on the wettest part of the state. Despite strong correlation between NSOI and precipitation for these climate divisions, there is no distinct tail dependence, which leads us to infer that other meteorological effects, most likely a result of their proximity to the Gulf of Mexico, may tend to mask drought events that may be due to La Niña.

The copula deemed suitable for modeling the dependence between NSOI and precipitation in climate divisions 2, 3, 6, 7, and 9, located in the central part of the state, is Clayton. Clayton's $\theta \to 0$ indicates that the marginals are independent, and as $\theta \to \infty$, the copula attains the Fréchet upper bound. It does not, however, attain the Fréchet lower bound. The Clayton copula exhibits a strong lower tail dependence, but a relatively weak upper tail dependence, which implies that there is a strong association between negative NSOI (La Niña) and precipitation conditions, while the association between positive NSOI (El Niño) may be either weaker or obscured by local meteorological conditions.

Finally, it is surprising to note that two parameter copulas, considered in this study because of their ability in capturing more than one type of dependence, were not selected in any of the 10 climate divisions.

5.6.4.4 PDO and Precipitation Anomaly

The same set of copulas considered for NSOI and precipitation anomaly were considered to model the dependence structure between cold season average PDO and cold season average precipitation anomaly. The Gaussian copula dominates the dependence structure between PDO and precipitation across the state. Note that due to the relatively high variability in precipitation, attributed partly to the influence of ENSO and partly to local meteorological factors, the correlation between PDO and precipitation is lower than with NSOI. Further, PDO has a long cycle of about 20 to 30 years and hence its influence can be qualified as more subtle, which explains the absence of strong tail dependence (both upper and lower) and the choice of Gaussian as the most appropriate copula.

5.6.4.5 NSOI, PDO, and Precipitation Anomaly

For the subsequent section, three climate divisions, 5 located in arid west, 7 in the middle-eastern part, and 8 representing the wettest region in the state, are chosen for further analysis, simulation, and prediction of cold season average precipitation anomalies, using the state of NSOI and PDO as precursors.

In this section, the most appropriate copula for modeling the dependence between both large-scale circulation patterns, June^0 – November^0 average NSOI and cold season average PDO, and cold season average precipitation anomaly is discussed. From the results of the bivariate analysis, three copulas (Clayton, Frank, and Gaussian) are chosen for modeling the predictor and dependent variables. The parameter estimates, goodness-of-fit statistic, and *p*-value for each are given in Table 17. The Clayton copula does not fare well (very low *p*-values) in all three climate divisions, implying that there is no distinct lower tail dependence. Based on the maximum log likelihood values, which is equivalent to comparing AIC, since all three copulas are single parameter, the Gaussian copula seems most suitable for modeling the three variables. Given that the Gaussian copula is chosen over the Frank copula indicates that there is some dependence at the tails.

Table 17. Parameter and Cramér-von Mises goodness-of-fit statistic along with its *p*-value, for the Clayton, Frank, and Gaussian copulas modeling the dependence between June^0 – November^0 average NSOI, cold season average PDO, and cold season average precipitation anomaly for climate divisions 5, 7, and 8.

Climate Division	**5**	**7**	**8**
Clayton copula			
Parameter (std. error)	0.598 (0.098)	0.713 (0.129)	0.680 (0.109)
Maximum log likelihood	24.178	30.708	28.624
S_n statistic	0.095	0.066	0.075
S_n p	0.003	0.042	0.015
Frank copula			
Parameter	2.712 (0.426)	2.850 (0.443)	2.773 (0.409)
Maximum log likelihood	26.033	27.327	26.255
S_n statistic	0.046	0.045	0.053
S_n p	0.110	0.153	0.054
Gaussian copula[a]			
ρ_1	0.491 (0.079)	0.491 (0.080)	0.490 (0.076)
ρ_2	0.435 (0.080)	0.518 (0.068)	0.554 (0.080)
ρ_3	0.449 (0.075)	0.435 (0.093)	0.356 (0.073)
Maximum log likelihood	28.921	32.578	32.989
S_n statistic	0.028	0.029	0.032
S_n p	0.363	0.372	0.261

[a] Position of ρs in an unstructured Gaussian matrix

$$\begin{array}{c} \\ NSOI \\ PDO \\ Pcp \end{array} \begin{array}{c} \begin{array}{ccc} NSOI & PDO & Pcp \end{array} \\ \begin{pmatrix} 1 & \rho_1 & \rho_2 \\ \rho_1 & 1 & \rho_3 \\ \rho_2 & \rho_3 & 1 \end{pmatrix} \end{array}$$

5.6.5 SIMULATION

For the three climate divisions (5, 7, and 8), representing three varying climate regimes and dependence with NSOI and PDO, random values are generated from the chosen copula to assess how the model simulates the precipitation for different cases or ranges of NSOI and PDO. The bivariate case, between NSOI and precipitation anomaly is first considered, and the influence of PDO, in a trivariate model, in then discussed.

Embrechts et al. [2003] provide an effective algorithm for the generation of random variates for an m-variate distribution, such that $U_1, \dots, U_m$ have joint distribution function C. For k-dimensional margins of C, let $C_k(u_1, \dots, u_k) = C(u_1, \dots, u_k, 1, \dots, 1)$ with $k = 2, \dots, m-1$, and $C_1(u_1) = u_1$ and $C_m(u_1, \dots, u_m) = C(u_1, \dots, u_m)$. The conditional distribution of U_k given $U_1, \dots, U_{k-1}$, is given by

$$\begin{aligned} C_k(u_k|u_1, \dots, u_{k-1}) &= \mathbb{P}\{U_k \leq u_k | U_1 = u_1, \dots, U_{k-1} = u_{k-1}\} \\ &= \frac{\partial^{k-1} C_k(u_1, \dots, u_k)}{\partial u_1 \dots \partial u_{k-1}} \Big/ \frac{\partial^{k-1} C_{k-1}(u_1, \dots, u_{k-1})}{\partial u_1 \dots \partial u_{k-1}} \end{aligned} \quad \textbf{(34)}$$

assuming that both numerator and denominator exist and the denominator is not zero. This algorithm can be used to simulate the whole range of the joint distribution, or for the prediction of the range of response variables given an explanatory value.

5.6.5.1 Bivariate Simulation: NSOI and Precipitation Anomaly

Figure 38 shows boxplots of both observed values and that simulated from the selected copula for different NSOI ranges for climate divisions 5, 7, and 8. Notched boxplots are preferred as they visually depict the significance between the observed values and simulated data. Non-overlapping notches indicate that the medians are significantly different at a 95% confidence level. The size of the notch around each median (M) is calculated as $M \pm Cs$, where C is a constant chosen to be 1.7 and $s = 1.25R/1.35\sqrt{N}$ is the Gaussian-based asymptotic approximate of the standard deviation of the median with R being the interquartile range and N the number of observations in each group [*McGill et al.*, 1978]. The basic statistics of the observed and simulated values, for the same NSOI ranges, are given in Table 18.

When the whole range of NSOI is considered (−4 < NSOI < 4), the interquartile ranges of both the observed and simulated data overlap and the medians are not significantly different. The medians in all cases are lower than the means, indicating a higher probability of precipitation deficit, which is typical for the state. The skewness and kurtosis of the simulated values agree fairly well with the observations. When specific ranges of NSOI is considered, we note that there is better agreement for negative than positive NSOI ranges, implying the copula is modeling values in the lower quadrant more efficiently. For climate divisions 7 and 8, the ranges and medians of the simulated values is often lower than those derived from observations, especially for 1 < NSOI < 2.

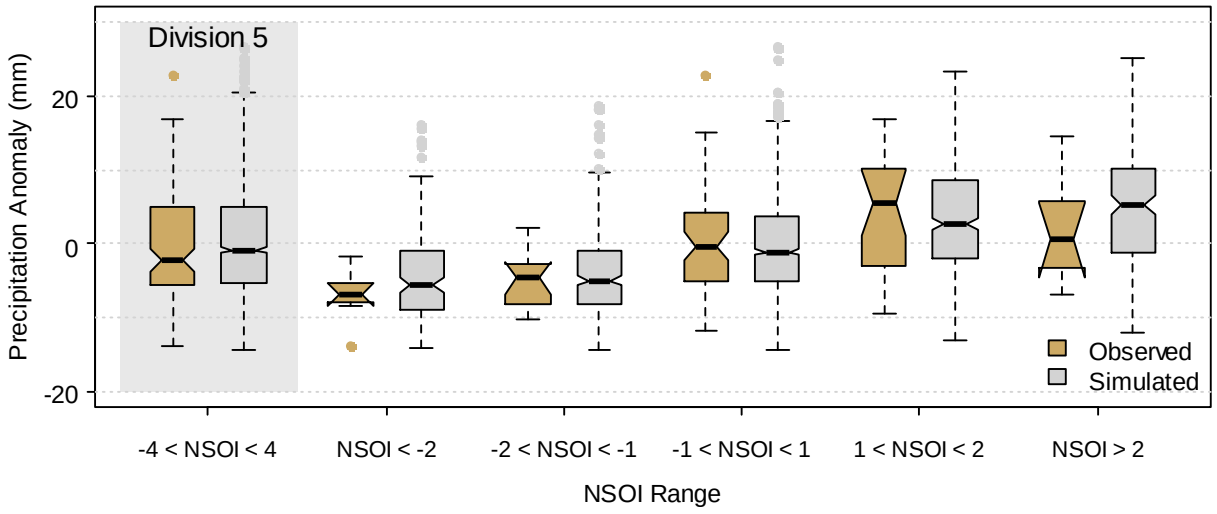

Figure 38. Boxplots of observed and simulated cold season precipitation anomalies for different NSOI ranges for climate divisions 5, 7, and 8. Boxplot with light gray background is for complete NSOI range.

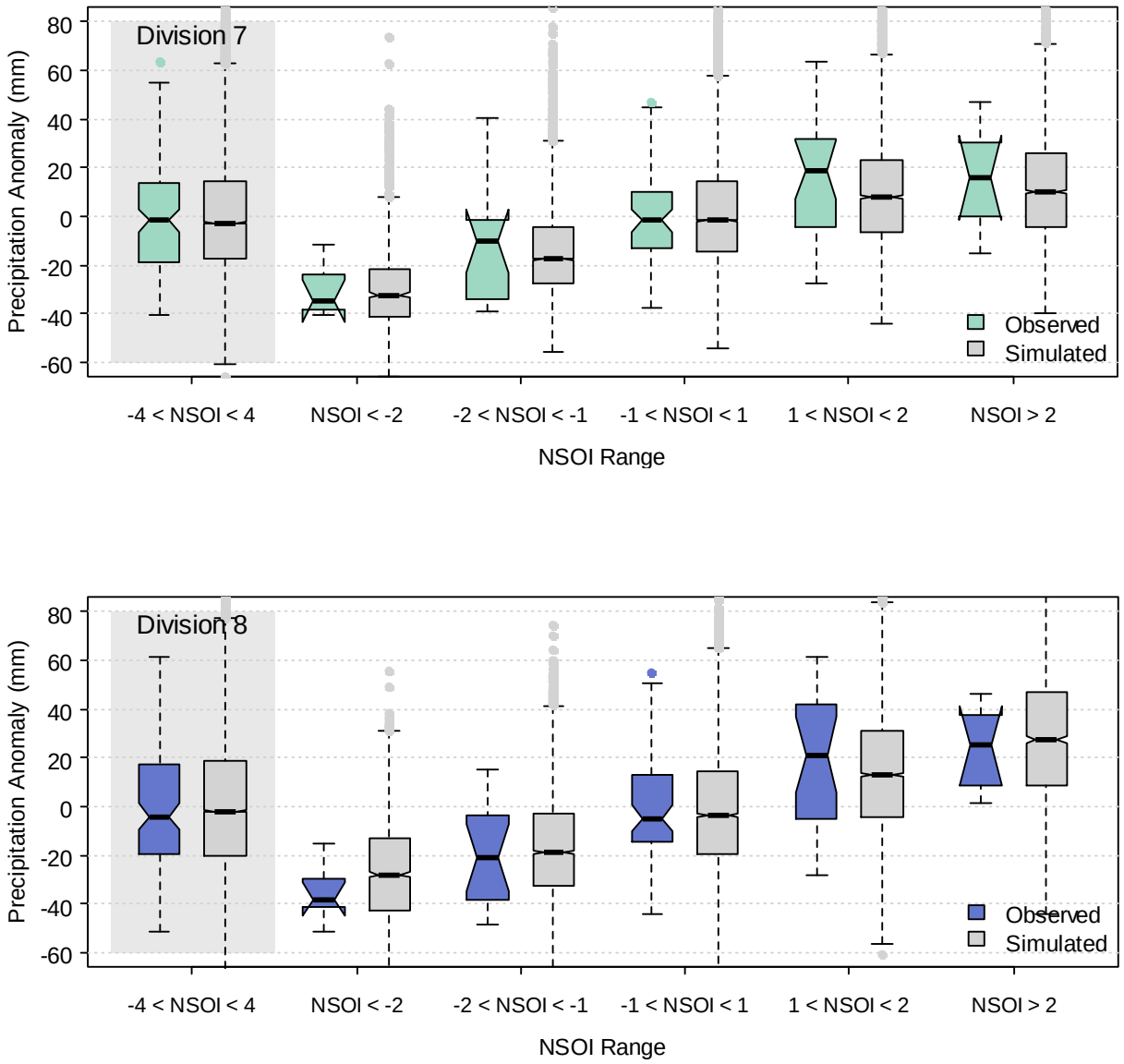

Figure 38 Continued.

Table 18. Statistics of observed and simulated cold season precipitation anomalies for different NSOI ranges for climate divisions 5, 7, and 8.

NSOI Range	-4 < NSOI < 4		NSOI < -2		-2 < NSOI < -1		-1 < NSOI < 1		1 < NSOI < 2		NSOI > 2	
	Obs.	***Sim.***	***Obs.***	***Sim.***	***Obs.***	***Sim.***	***Obs.***	***Sim.***	***Obs.***	***Sim.***	***Obs.***	***Sim.***
Climate Division 5												
Mean	-0.020	0.112	-6.951	-4.106	-4.776	-3.884	0.222	-0.411	4.187	3.551	1.713	4.737
Standard deviation	7.240	7.354	3.714	6.468	3.807	5.899	6.921	6.761	7.735	7.427	6.965	7.389
Median	-2.115	-0.827	-6.790	-5.478	-4.590	-4.942	-0.380	-1.084	5.570	2.580	0.615	5.266
25^{th} percentile	-5.463	-5.369	-7.855	-8.816	-8.135	-8.177	-4.783	-5.133	-3.065	-1.905	-3.235	-1.055
75^{th} percentile	5.060	4.956	-5.335	-0.969	-2.698	-0.955	4.075	3.630	10.080	8.583	5.255	10.132
Skewness	0.618	0.594	-0.604	1.121	0.253	1.079	0.794	0.579	-0.360	0.529	0.615	-0.003
Kurtosis	2.841	3.100	3.089	3.916	2.137	4.483	3.691	3.249	1.905	3.249	2.463	2.526
Climate Division 7												
Mean	0.032	0.068	-30.144	-29.071	-13.018	-13.842	-0.728	1.665	14.865	10.234	15.400	11.914
Standard deviation	23.927	24.324	10.774	17.943	22.453	19.871	19.549	22.381	25.403	22.733	21.474	22.521
Median	-1.825	-2.630	-34.760	-32.253	-10.100	-17.754	-1.675	-1.754	18.880	7.568	15.615	10.078
25^{th} percentile	-18.123	-17.236	-38.020	-41.338	-33.973	-27.761	-12.828	-14.533	-4.155	-6.283	6.315	-4.684
75^{th} percentile	13.418	14.705	-23.770	-21.592	-2.388	-4.191	10.028	14.451	31.980	22.908	29.600	25.725
Skewness	0.355	0.664	0.689	1.380	0.640	1.244	0.487	0.889	-0.033	0.774	-0.229	0.643
Kurtosis	2.483	3.799	2.029	5.939	2.880	5.270	2.885	4.301	2.096	4.162	2.042	3.725

Table 18 Continued.

NSOI Range	-4 < NSOI < 4		NSOI < -2		-2 < NSOI < -1		-1 < NSOI < 1		1 < NSOI < 2		NSOI > 2	
	Obs.	***Sim.***	***Obs.***	***Sim.***	***Obs.***	***Sim.***	***Obs.***	***Sim.***	***Obs.***	***Sim.***	***Obs.***	***Sim.***
Climate Division 8												
Mean	0.075	0.108	-35.291	-26.956	-18.720	-17.077	-0.965	-1.839	18.257	14.209	23.871	27.958
Standard deviation	27.802	28.374	11.667	22.018	21.145	22.366	23.844	24.752	27.884	25.719	17.559	27.089
Median	-4.135	-2.057	-38.040	-28.055	-20.875	-18.734	-4.770	-3.672	20.970	12.906	24.970	27.522
25^{th} percentile	-19.660	-20.199	-41.495	-42.489	-38.083	-32.837	-14.325	-19.581	-5.485	-4.342	11.708	8.250
75^{th} percentile	17.173	18.681	-29.555	-13.223	-5.488	-3.118	12.755	14.187	41.630	30.870	36.713	46.774
Skewness	0.239	0.342	0.403	0.333	0.187	0.401	0.379	0.343	-0.213	0.249	-0.092	0.106
Kurtosis	2.248	2.957	2.471	3.073	1.816	3.216	2.823	3.029	1.714	2.888	1.426	2.633

5.6.5.2 Trivariate Simulation: NSOI, PDO, and Precipitation Anomaly

Figure 39 shows the boxplots of observed and simulated values for different NSOI and PDO ranges for climate divisions 5, 7, and 8. The basic statistics for the different cases shown are given in Table 19. When the whole range of NSOI is considered, irrespective of the state of PDO, the interquartile ranges of both the observed and simulated data overlap and the medians are not significantly different. The basic statistics of observed and simulated data agree fairly well on the whole. When the data is stratified into cases when PDO is negative and positive, depicted with a light blue and light red background, respectively, an interesting trend emerges. Inclusion of PDO in the model generally improves the simulation results, especially for the cases when PDO is negative. Better agreement in the observations and simulation is noted in the lower quadrant, that is negative precipitation anomaly due to La Niña and negative PDO, but no significant improvement can be seen in the upper quadrant (positive precipitation anomaly during El Niño coincident with positive PDO).

These results highlight the importance of including PDO in the probabilistic prediction of precipitation. While ENSO, being a strong large-scale circulation pattern modulating climatic conditions over the whole planet, is an important determinant of precipitation conditions, it does not fully explain the variability between El Niño (La Niña) events [*Khedun et al.*, 2012b]. Knowledge of the state of the PDO can greatly improve our expectation of precipitation conditions. La Niña coincident with negative PDO have been shown to increase drought severities, while positive PDO may lead to above average precipitation, despite negative ENSO conditions [*Cole et al.,* 2002]. The trivatiate copula model does fairly well in simulating conditions when the PDO is negative, but not as well when PDO is positive, especially when both NSOI and PDO are positive. This is due to the limitation of this simplistic model in simulating the complex local and remote drivers of precipitation. During a drought, once dry conditions are initiated, the ground loses soil moisture, which can further intensify local conditions, by raising the ground temperature and creating a high pressure system, which may suppress rainfall. On the other hand, even low rainfall event can increase soil moisture which evaporates back and increases humidity level in the atmosphere, along with evaporation from surface waters in lakes and rivers, and in this case moisture from the

Gulf of Mexico. When temperature and other meteorological conditions are conducive, this leads to more precipitation. These local conditions may not be influenced by large-scale climate phenomenon, hence the high variability in the upper quadrant of the dataset, which the copula model is unable to capture; hence the lower mean and median in the simulated values as opposed to the observed data.

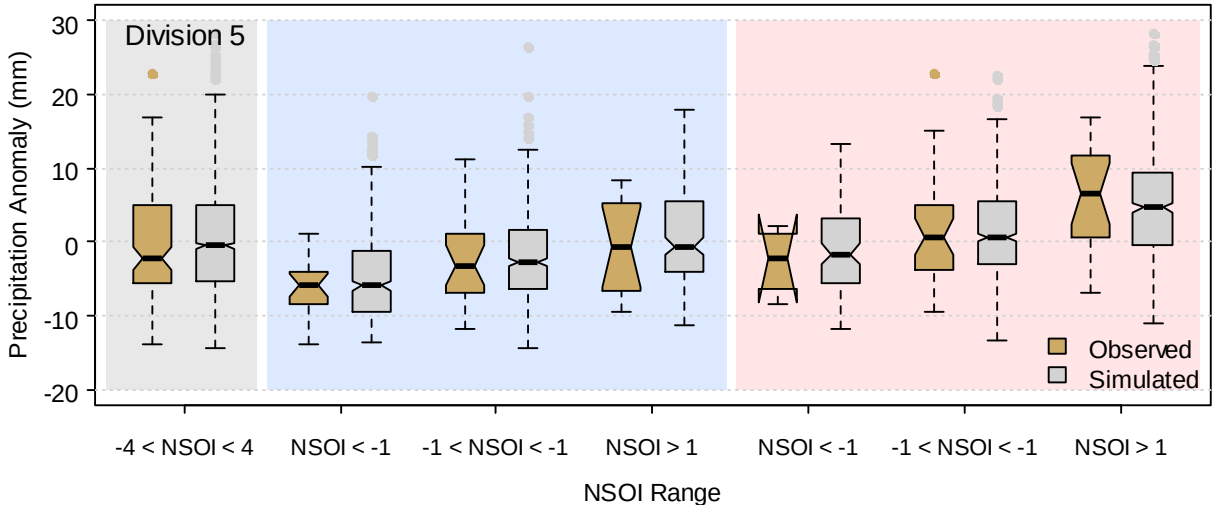

Figure 39. Boxplots of observed and simulated cold season precipitation anomalies for different NSOI and PDO ranges for climate divisions 5, 7, and 8. Boxplot with light gray background is for complete NSOI and PDO ranges while light blue (red) is for different NSOI ranges and negative (positive) PDO.

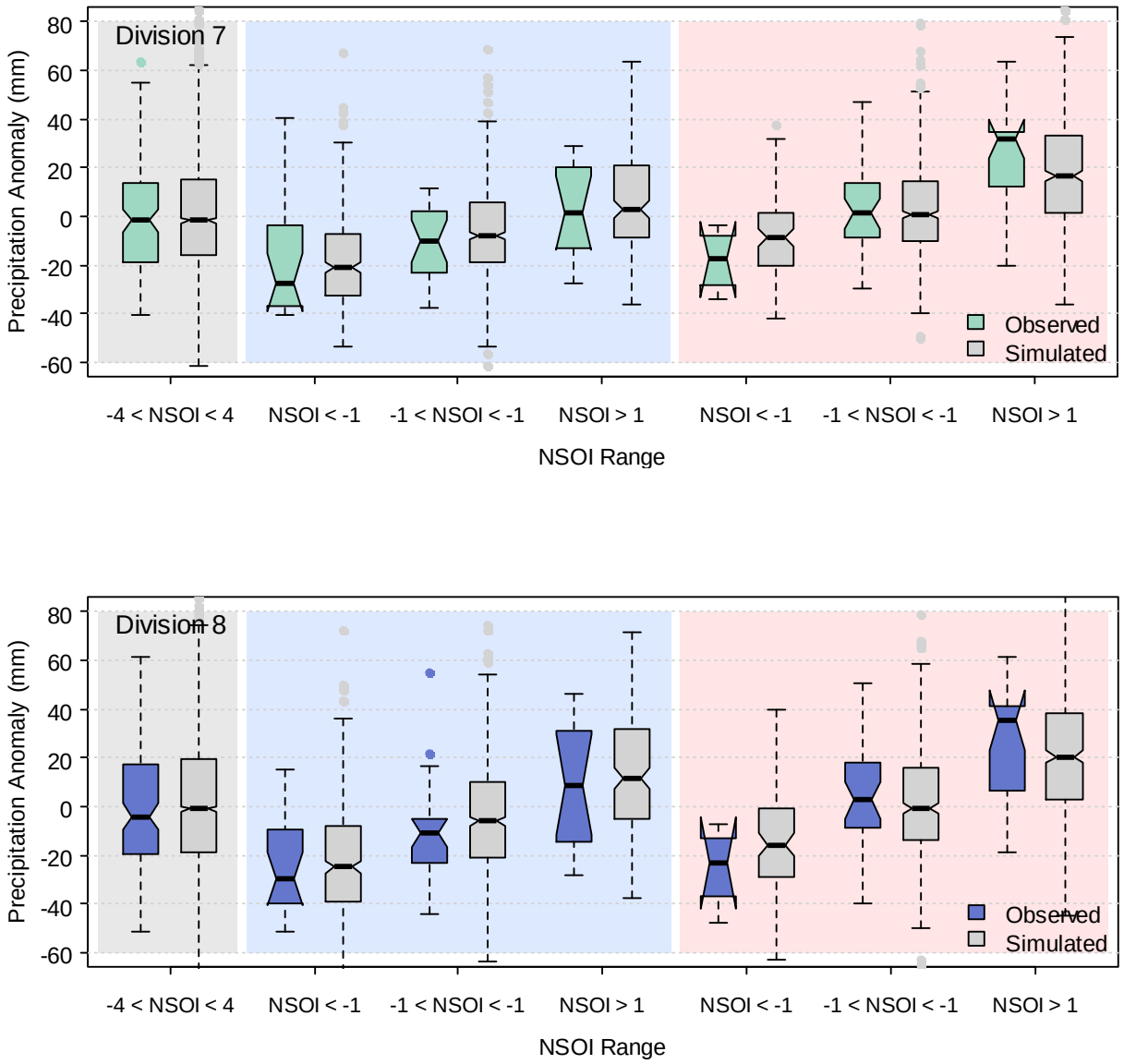

Figure 39 Continued.

Table 19. Statistics of observed and simulated cold season precipitation anomalies for different NSOI and PDO ranges for climate divisions 5, 7, and 8.

NSOI Range	-4 < NSOI < 4		Negative PDO					
			NSOI < -1		-1 < NSOI < -1		NSOI > 1	
	Obs.	*Sim.*	*Obs.*	*Sim.*	*Obs.*	*Sim.*	*Obs.*	*Sim.*
Climate Division 5								
Mean	-0.020	0.092	-6.022	-4.765	-1.888	-2.049	-0.492	0.550
Standard deviation	7.240	7.094	3.501	5.941	6.010	6.081	6.718	6.174
Median	-2.115	-0.521	-5.860	-5.921	-3.190	-2.811	-0.760	-0.540
25^{th} percentile	-5.463	-5.200	-8.275	-9.433	-6.468	-6.453	-6.313	-3.943
75^{th} percentile	5.060	4.890	-3.910	-1.301	1.100	1.620	4.805	5.547
Skewness	0.618	0.481	-0.146	0.838	0.545	0.590	0.072	0.447
Kurtosis	2.841	3.037	3.032	3.613	2.595	3.364	1.373	2.560
Climate Division 7								
Mean	0.032	0.344	-18.225	-18.556	-9.822	-6.007	2.888	6.794
Standard deviation	23.927	23.862	22.597	19.344	14.460	19.122	19.480	21.450
Median	-1.825	-1.782	-27.390	-21.044	-10.145	-8.037	1.180	2.495
25^{th} percentile	-18.123	-16.259	-37.025	-32.641	-22.253	-19.106	-9.903	-8.718
75^{th} percentile	13.418	15.288	-3.880	-7.075	1.613	5.552	19.588	21.241
Skewness	0.355	0.554	0.961	0.727	-0.120	0.403	-0.194	0.718
Kurtosis	2.483	3.658	3.210	3.834	1.909	3.212	1.726	4.082

Table 19 Continued.

NSOI Range	-4 < NSOI < 4		Negative PDO					
			NSOI < -1		-1 < NSOI < -1		NSOI > 1	
	Obs.	***Sim.***	***Obs.***	***Sim.***	***Obs.***	***Sim.***	***Obs.***	***Sim.***
Climate Division 8								
Mean	0.075	0.476	-23.466	-22.694	-11.179	-4.468	8.771	13.958
Standard deviation	27.802	28.001	21.055	23.752	22.883	23.537	26.147	24.835
Median	-4.135	-1.038	-29.490	-24.932	-10.925	-6.148	8.735	11.660
25^{th} percentile	-19.660	-18.746	-39.590	-39.347	-22.643	-20.687	-11.530	-4.903
75^{th} percentile	17.173	19.112	-9.425	-8.139	-5.638	10.029	25.913	31.998
Skewness	0.239	0.250	0.585	0.480	0.959	0.258	0.047	0.246
Kurtosis	2.248	2.981	2.081	3.382	4.405	3.046	1.806	2.688

NSOI Range	-4 < NSOI < 4		Positive PDO					
			NSOI < -1		-1 < NSOI < -1		NSOI > 1	
	Obs.	***Sim.***	***Obs.***	***Sim.***	***Obs.***	***Sim.***	***Obs.***	***Sim.***
Climate Division 5								
Mean	-0.020	0.092	-2.665	-1.150	1.445	1.299	6.100	4.958
Standard deviation	7.240	7.094	4.670	5.956	7.271	6.357	6.977	6.914
Median	-2.115	-0.521	-2.200	-1.663	0.740	0.650	6.590	4.722
25^{th} percentile	-5.463	-5.200	-5.405	-5.471	-3.490	-2.992	0.615	-0.284
75^{th} percentile	5.060	4.890	0.540	2.994	4.838	5.401	11.750	9.519
Skewness	0.618	0.481	-0.236	0.329	0.839	0.404	-0.346	0.380
Kurtosis	2.841	3.037	1.522	2.425	3.738	2.959	1.972	3.112

Table 19 Continued.

NSOI Range	-4 < NSOI < 4		Positive PDO					
			NSOI < -1		-1 < NSOI < -1		NSOI > 1	
	Obs.	***Sim.***	***Obs.***	***Sim.***	***Obs.***	***Sim.***	***Obs.***	***Sim.***
Climate Division 7								
Mean	0.032	0.344	-18.258	-7.661	4.297	2.929	22.654	18.523
Standard deviation	23.927	23.862	12.854	18.051	20.431	20.223	24.013	23.555
Median	-1.825	-1.782	-17.675	-8.900	1.100	0.793	31.750	16.729
25^{th} percentile	-18.123	-16.259	-25.453	-19.986	-8.378	-10.176	12.190	1.312
75^{th} percentile	13.418	15.288	-10.480	1.718	13.753	14.697	34.480	33.125
Skewness	0.355	0.554	-0.125	0.296	0.392	0.511	-0.359	0.635
Kurtosis	2.483	3.658	1.642	2.480	2.536	3.483	2.257	3.804
Climate Division 8								
Mean	0.075	0.476	-25.175	-14.297	5.144	1.122	26.612	21.340
Standard deviation	27.802	28.001	17.041	23.607	22.949	22.929	23.081	25.813
Median	-4.135	-1.038	-22.975	-15.772	2.575	-0.760	35.320	20.504
25^{th} percentile	-19.660	-18.746	-31.675	-28.773	-8.640	-13.959	6.470	2.774
75^{th} percentile	17.173	19.112	-16.475	-0.971	17.840	15.864	41.315	38.254
Skewness	0.239	0.250	-0.414	0.168	0.202	0.260	-0.469	0.247
Kurtosis	2.248	2.981	1.945	2.352	2.628	2.993	2.046	2.933

5.6.6 PREDICTION

In this section we discuss the possibility of using the copula models demonstrated in the previous sections for the prediction of precipitation anomalies, given the state of NSOI and PDO. The prediction capabilities of the bivariate case, that is NSOI and precipitation anomaly, will be compared against the trivariate model, which incorporates PDO, for climate divisions 5, 7, and 8. They experience very different climate regimes and the cold season average precipitation anomaly follows different marginal distributions.

The 112 year long dataset was divided into two sets; one for constructing the model and the other for validation. The modeling set contained 70% of the data and the remaining 30% was used for validation. The following procedure was adopted for the selection of the validation dataset. The June^0 – November^0 average NSOI, cold season average PDO, and cold season average precipitation anomalies (for all three climate divisions) matrix was stratified based on NSOI values followed by PDO values, and representative samples were randomly selected from each stratum. This procedure ensured that the overall dependence structure was not impaired, while enough data points are obtained in each case. Thus, the models remained unbiased, as it would be when the whole dataset is used for cold season precipitation prediction. Further, extracting the validation data once, and not repeating the procedure separately for each climate division, allows comparison of the model performance across different climate conditions.

Copulas were fitted to the modeling data, from the same set of copulas considered above and following the same procedure described in section 5.6.4. Again, note that the maximum pseudo-likelihood method was used, which ensures that the copula selected is independent of the marginals and due to the dependence structure only. Once the most appropriate copula is selected, the predictor, conditioned upon the explanatory variable, was obtained using Eq. 34. The result is in the unit hypercube domain and was back transformed, using the fitted marginal, to obtain the cold season average precipitation anomaly.

The predicted values against observed values for the bivariate and trivariate case, for all three climate divisions, are shown as scatterplots in Figure 40. The coefficient of correlation

between the predicted and observed values for the bivariate case was 0.66, 0.69, and 0.60 for climate divisions 5, 7, and 8, respectively. When PDO was included, the correlation dropped slightly to 0.58, 0.60 and 0.42. This drop in correlation was expected given the high variability in precipitation due to local meteorological conditions, as illustrated with simulations, especially when both the NSOI and PDO were positive. Interestingly, though, the correlation between observed and predicted values in the lower quadrant, that is, when both NSOI and PDO were negative was significantly improved in the trivariate model. Correlation increased from 0.26, 0.45, and 0.35 to 0.65, 0.53, and 0.71 for climate divisions 5, 7, and 8 respectively. This result is in accord with the improved simulation ranges when PDO was negative.

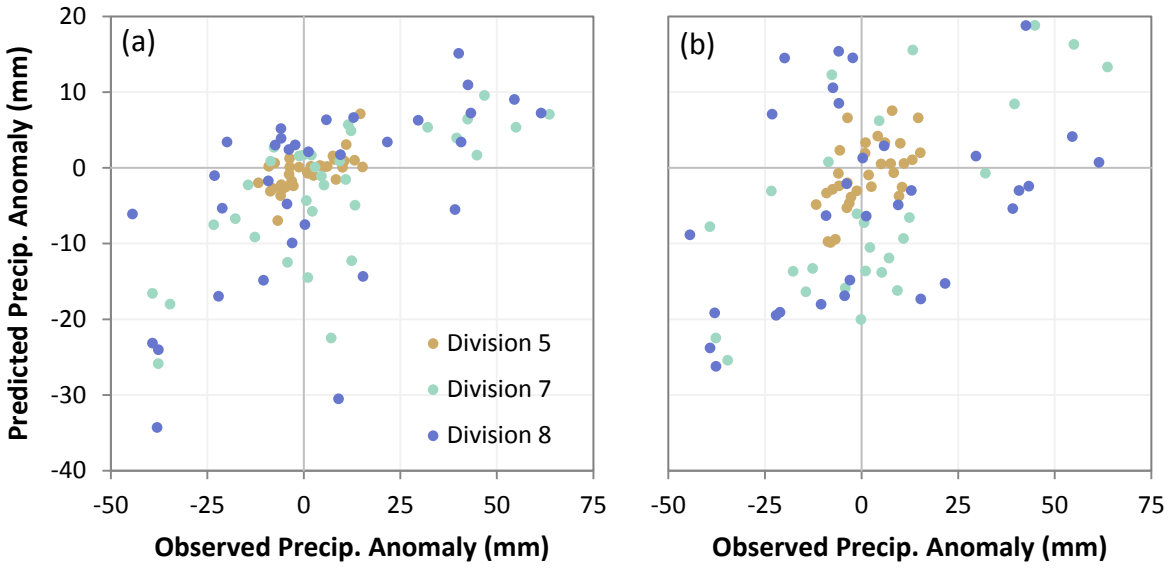

Figure 40. Scatter plot of predicted versus observed predicted cold season average rainfall anomaly for (a) NSOI and precipitation anomaly model and (b) NSOI, PDO, and precipitation anomaly model.

5.7 CONCLUSIONS

Precipitation in the state is influenced by large-scale circulation patterns in the Pacific Ocean. A statistically significant correlation between both June^{0} – November^{0} average NSOI, and cold season (October^{0} – March^{+}) average PDO, with cold season average precipitation is found. The spatial correlation patterns for the two indices, across the 10 different climate divisions, are not identical and higher correlation with NSOI is recorded, than with PDO. Nonetheless, the effect of PDO can be significant. It has been known to modulate the effect of ENSO, leading to stronger response when they are coincident than when they are out of phase.

A simple model is developed to assess how well ENSO conditions alone can predict precipitation and if knowing the state of PDO improves the prediction. Copula is used to model the bivariate dependence between NSOI and precipitation anomaly and the trivariate dependence between NSOI, PDO, and precipitation anomaly. Ten copulas, from the elliptical and Archimedean families, are evaluated. Three of the copulas considered are two-parameter copulas, as they can capture more than one type of dependence. The copulas are fitted using the maximum pseudo-likelihood method which ensures that the selected copula is independent of the marginals. Different copulas are found to be suitable for different climate divisions. The choice of copula is strongly driven by the lower tail dependence; which is associated with La Niña conditions and negative precipitation anomaly.

Using the chosen copula, precipitation is simulated from the bivariate and trivariate models for three different climate divisions: 5, which is semi-arid, 8, located in the wettest region, and 7 in the middle-eastern part of the state. When the whole range of NSOI and PDO are considered, both the bivariate and trivariate models generate results having almost the same interquartile ranges and basic statistics as observations. When the data were stratified into different NSOI cases, in the bivariate model, better agreement in the negative NSOI range than in the positive range was noted. It is also found that the inclusion of PDO, in the trivariate model, generally improves the simulation results, and even better agreement between observations and simulations, in the lower quadrant, which represents negative precipitation anomaly due to La Niña and negative PDO, is observed.

Finally, the record was divided into two sets, one for modeling and one for testing the prediction capability of the bivariate and trivariate models. Relatively good correlation between the predicted values and the observations are noted using the bivariate model. The coefficient of correlation between observed values and predicted values in the trivariate model is slightly less than with the bivariate model. However, significant improvement is noted in the prediction of negative precipitation anomalies.

The proposed model can be effectively used in predicting negative average cold season precipitation anomalies based on the state of June^0 – November^0 average NSOI and the state of PDO. Further, given that June^0 – September^0 average NSOI and June^0 – November^0 average NSOI are strongly correlated, the former can be used as a forewarning index prior to the start of the hydrologic year.

6 CONCLUSIONS

An understanding of the influence of large-scale circulation patterns on local hydrological and meteorological variables, especially precipitation, is crucial for short- and long-term water resources planning and management. In this dissertation the influence of two major climate teleconnection patterns, namely the El Niño Southern Oscillation (ENSO) and the Pacific Decadal Oscillation (PDO) was studied. The state of Texas, US, and the Rio Grande (RG), a transboundary basin straddling three states in the US and five states in Mexico were used as study area.

Three ENSO indices (Niño 3.4, Multi-ENSO Index (MEI), and El Niño Modoki (EMI)), and one PDO index were used. Statistically significant positive correlation between the indices and gauged precipitation for most of RG was found for winter and spring, while summer and fall precipitation showed negligible correlation. At the headwaters, a negative correlation was found, which means that higher snowfall during La Niña conditions may help in maintaining flow in the river and offset the lack of water which may result due to precipitation deficit in the arid/semi-arid New Mexico region.

The spatial correlation structure and strength of Niño 3.4 and MEI indices with precipitation were similar, while the correlation of EMI with precipitation was weaker. Given that the operational definition of NOAA for El Niño and La Niña in North America is based on the Niño 3.4 index, the latter should be the *de facto* index for water resources planning exercises, even though MEI, being a more inclusive ENSO index, has more appeal.

Using NOAA's definition, recent El Niño and La Niña events were identified and compared using four metrics: duration above or below the defined threshold of ±0.5°C, maximum or minimum SSTA recorded, duration in the phase of interest, and intensity. It was found that not all ENSO events are created equal; some events have short duration but high intensity, while others lingers for several years with lower SSTA.

For water resources management purposes, information on the degree and strength of correlation of these indices with precipitation is useful to a certain extent only. Quantification of changes in flow is more useful for planning. Given that RG is heavily engineered, gauged flows is not reliable, as it incorporates both the effect of land use land cover changes and climate variability. Flow in the basin, was therefore reconstructed from a land surface model (LSM) and area-averaged runoff (AAR) was used as a proxy for water availability. The basin was divided into six sub-regions for analysis purposes, and the influences of recent major ENSO events were analyzed individually.

A general increase (decrease) in runoff during El Niños (La Niñas) was noted but some events actually caused a decrease (increase) in water availability. The percentage increase during El Niños significantly offsets the decrease registered during La Niñas. Long El Niños had more influence on water availability than short duration high intensity events. PDO was also found to have an important influence on water availability. A positive PDO was seen to enhance the effect of El Niño and dampen the negative effect of La Niña. When it was in its neutral/transition phase, La Niña was seen to dominate climatic conditions and reduce water availability.

Runoff generated from the LSM was used for water deficit duration and severity analysis. Three-month Standardized Runoff Index [SRI(3)] series were created from the AAR for each of the six regions. Water deficit duration and severity were respectively found to follow exponential and gamma probability distribution. Copulas were fitted, and different copulas were deemed suitable for each region as they are subject to different climatologic conditions, which affect the nature of deficit events, especially at the extremes. Conditional probability models of duration and severity were developed and compared. Further, conditional probabilities derived from model runoff were compared with that based on observed precipitation. It was found that model derived information can be effectively used in regions having limited ground observation data, or can be used in tandem with observation driven conditional probabilities for more efficient water resources planning and management.

Finally, a simple copula-based model was developed to assess how well ENSO conditions alone can predict precipitation, and if knowing the state of PDO improves the prediction. A

bivariate model, between NSOI and precipitation anomaly, and a trivariate model, incorporating PDO, were constructed and compared. Ten copulas, from the elliptical and Archimedean families, were evaluated. Three of the copulas considered were two-parameter copulas, as they can capture more than one type of dependence. Different copulas were found to be suitable for different climate regions. The choice of copula was strongly driven by the lower tail dependence; which is associated with La Niña conditions and negative precipitation anomaly.

Relatively good correlation between the predicted values and the observations were noted, using both the bivariate and trivariate models. The coefficient of correlation between observed values and predicted values in the trivariate model was slightly less than with the bivariate model. However, significant improvement was noted in the prediction of negative precipitation anomalies. The proposed model can thus be effectively used in predicting negative average cold season precipitation anomalies based on the state of June^0 – November^0 average NSOI and PDO, and can be used as a forewarning prior to the start of the hydrologic year.

The methodology developed and presented in this dissertation is not limited to the watershed scale or to the southern US. It can be extended and applied to larger continental scale for water resources planning and management, and to assess large-scale water projects, such as the need and effectiveness of interstate water transfers. It can also be used to guide policies and for formulating guidelines, especially in transboundary water management. Future studies should include the influence of climate change, particularly the effect global warming on the frequency, duration, and severity of ENSO and other large-scale circulation patterns, and their resulting effect on hydro-meteorological factors, and how they affect water resources management at the local level.

REFERENCES

Adams, D. K., and A. C. Comrie (1997), The North American monsoon, *Bull. Am. Meteorol. Soc.*, *78*(10), 2197-2213, doi: 10.1175/1520-0477(1997)078<2197:TNAM>2.0.CO;2.

Allan, R. J., and R. D. D'Arrigo (1999), 'Persistent' ENSO sequences: how unusual was the 1990-1995 El Niño?, *The Holocene*, *9*(1), 101-118, doi: 10.1191/095968399669125102.

Anctil, F., and P. Coulibaly (2004), Wavelet analysis of the interannual variability in southern Québec streamflow, *J. Clim.*, *17*(1), 163-173, doi: 10.1175/1520-0442(2004)017<0163:WAOTIV>2.0.CO;2.

Ashok, K., S. K. Behera, S. A. Rao, H. Weng, and T. Yamagata (2007), El Niño Modoki and its possible teleconnection, *J. Geophys. Res.*, *112*(C11), C11007, doi: 10.1029/2006jc003798.

Baker, W. L. (2003), Fires and climate in forested landscapes of the U.S. Rocky Mountains, in *Fire and Climatic Change in Temperate Ecosystems of the Western Americas*, edited by T. T. Veblen, W. L. Baker, G. Montenegro and T. W. Swetnam, pp. 120-157, Springer New York, N.Y., U.S.A.

Baldwin, M., and K. E. Mitchell (1997), The NCEP hourly multi-sensor U.S. precipitation analysis for operations and GCIP research, in *13th AMS Conference on Hydrology*, edited by American Meteorological Society, pp. 54-55, Boston, Mass., U.S.A.

Barlow, M., S. Nigam, and E. H. Berbery (2001), ENSO, Pacific decadal variability, and U.S. summertime precipitation, drought, and stream flow, *J. Clim.*, *14*(9), 2105-2128, doi: 10.1175/1520-0442(2001)014<2105:epdvau>2.0.co;2.

Barnston, A. G., M. Chelliah, and S. B. Goldenberg (1997), Documentation of a highly ENSO-related SST region in the equatorial Pacific: Research note, *Atmos. Ocean*, *35*(3), 367-383.

Bjerknes, J. (1969), Atmospheric teleconnections from the equatorial Pacific, *Mon. Weather Rev.*, *97*(3), 163-172, doi: 10.1175/1520-0493(1969)097<0163:ATFTEP>2.3.CO;2.

Castro, C. L., T. B. McKee, and R. A. Pielke, Sr. (2001), The relationship of the North American monsoon to tropical and North Pacific sea surface temperatures as revealed by observational analyses, *J. Clim.*, *14*(24), 4449-4473.

Changnon, S. A., and G. D. Bell (2000), *El Niño, 1997-1998: The Climate Event of the Century*, Oxford University Press, N.Y., U.S.A.

Chen, F., and J. Dudhia (2001), Coupling an advanced land surface–hydrology model with the Penn State–NCAR MM5 modeling system. Part I: Model implementation and sensitivity,

Mon. Weather Rev., *129*(4), 569-585, doi: 10.1175/1520-0493(2001)129<0569: CAALSH>2.0.CO;2.

Chen, F., K. Mitchell, J. Schaake, Y. Xue, H.-L. Pan, V. Koren, Q. Y. Duan, M. Ek, and A. Betts (1996), Modeling of land surface evaporation by four schemes and comparison with FIFE observations, *J. Geophys. Res.*, *101*(D3), 7251-7268, doi: 10.1029/95jd02165.

Chen, J., and P. Kumar (2002), Role of terrestrial hydrologic memory in modulating ENSO impacts in North America, *J. Clim.*, *15*(24), 3569-3585, doi: doi:10.1175/1520-0442(2003)015<3569:ROTHMI>2.0.CO;2.

Chowdhary, H., L. Escobar, and V. Singh (2011), Identification of suitable copulas for bivariate frequency analysis of flood peak and flood volume data, *Hydrol. Res.*, *42*(2–3), 193–216, doi: 10.2166/nh.2011.065.

Cole, J. E., J. T. Overpeck, and E. R. Cook (2002), Multiyear La Niña events and persistent drought in the contiguous United States, *Geophys. Res. Lett.*, *29*(13), 1647, doi: 10.1029/2001gl013561.

Cosgrove, B. A., D. Lohmann, K. E. Mitchell, P. R. Houser, E. F. Wood, et al. (2003), Real-time and retrospective forcing in the North American Land Data Assimilation System (NLDAS) project, *J. Geophys. Res.*, *108*(D22), 8842, doi: 10.1029/2002jd003118.

Dahm, C. N., R. J. Edwards, and F. P. Gelwick (2005), Gulf Coast rivers of the southwestern United States, in *Rivers of North America*, edited by C. B. Arthur and E. C. Colbert, pp. 180-228, Academic Press, Burlington, Mass., U.S.A.

Daly, C., R. P. Neilson, and D. L. Phillips (1994), A statistical-topographic model for mapping climatological precipitation over mountainous terrain, *J. Appl. Meteorol.*, *33*(2), 140-158, doi: 10.1175/1520-0450(1994)033<0140:ASTMFM>2.0.CO;2.

Delhomme, J. P. (1978), Kriging in the hydrosciences, *Adv. Water Resour.*, *1*(5), 251-266, doi: 10.1016/0309-1708(78)90039-8.

Dirmeyer, P. A., A. J. Dolman, and N. Sato (1999), The pilot phase of the Global Soil Wetness Project, *Bull. Am. Meteorol. Soc.*, *80*(5), 851-878, doi: doi:10.1175/1520-0477(1999)080<0851:TPPOTG>2.0.CO;2.

Dixon, P. G., G. B. Goodrich, and W. H. Cooke (2008), Using teleconnections to predict wildfires in Mississippi, *Mon. Weather Rev.*, *136*(7), 2804-2811, doi: 10.1175/2007MWR2297.1.

Embrechts, P., F. Lindskog, and A. McNeil (2003), Modelling dependence with copulas and applications to risk management, in *Handbook of Heavy Tailed Distributions in Finance*, edited by S. T. Rachev, Elsevier, Amsterdand, The Netherlands.

Fannin, B. (2012), Updated 2011 Texas agricultural drought losses total $7.62 billion, in *AgriLife Today*, edited, AgriLife Communications, College Station, Tex., U.SA. Accessed March 21, 2012. Available at http://agrilife.org/today/2012/03/21/updated-2011-texas-agricultural-drought-losses-total-7-62-billion/.

Fisher, N. I., and P. Switzer (2001), Graphical Assessment of Dependence: Is a Picture Worth 100 Tests?, *Am. Stat.*, *55*(3), 233-239.

Gedalof, Z., N. J. Mantua, and D. L. Peterson (2002), A multi-century perspective of variability in the Pacific Decadal Oscillation: New insights from tree rings and coral, *Geophys. Res. Lett.*, *29*(24), 2204, doi: 10.1029/2002gl015824.

Genest, C., and A.-C. Favre (2007), Everything you always wanted to know about copula modeling but were afraid to ask, *J. Hydrol. Eng.*, *12*(4), 347-368, doi: 10.1061/(asce)1084-0699(2007)12:4(347).

Genest, C., J.-F. Quessy, and B. Rémillard (2006), Goodness-of-fit procedures for copula models based on the probability integral transformation, *Scand. J. Statist.*, *33*(2), 337-366, doi: 10.1111/j.1467-9469.2006.00470.x.

Genest, C., B. Rémillard, and D. Beaudoin (2009), Goodness-of-fit tests for copulas: A review and a power study, *Insur. Math. Econ.*, *44*(2), 199-213, doi: 10.1016/j.insmatheco.2007.10.005.

Gershunov, A., and T. P. Barnett (1998a), Interdecadal modulation of ENSO teleconnections, *Bull. Am. Meteorol. Soc.*, *79*(12), 2715-2725.

Gershunov, A., and T. P. Barnett (1998b), ENSO influence on intraseasonal extreme rainfall and temperature frequencies in the contiguous United States: Observations and model results, *J. Clim.*, *11*(7), 1575-1586, doi: 10.1175/1520-0442(1998)011<1575:EIOIER>2.0.CO;2.

Goodrich, G. B. (2004), Influence of the Pacific Decadal Oscillation on Arizona winter precipitation during years of neutral ENSO, *Wea. Forecasting*, *19*(5), 950-953, doi: 10.1175/1520-0434(2004)019<0950:IOTPDO>2.0.CO;2.

Griffiths, J. F., J. W. Zeitler, L. L. Sedlar, D. L. Bjornson, and B. M. Bjornson (1990), A Decade of Texas Weather (1980-1989) *Rep.*, 88 pp, Office of the State Climatologist, Department of Meteorology, College of Geosciences, Texas A&M University, College Station, Tex., U.S.A.

Grinsted, A., J. C. Moore, and S. Jevrejeva (2004), Application of the cross wavelet transform and wavelet coherence to geophysical time series, *Nonlinear Process. Geophys.*, *11*(5-6), 561-566.

Grunmann, P. J. (2005), Variational Data Assimilation of Soil Moisture Information, PhD thesis, University of Maryland, College Park, Md., U.S.A.

Guttman, N. B. (1999), Accepting the Standardized Precipitation Index: A calculation algorithm, *J. Am. Water Resour. Assoc.*, *35*(2), 311-322, doi: 10.1111/j.1752-1688.1999.tb03592.x.

Guttman, N. B., and R. G. Quayle (1996), A historical perspective of U.S. climate divisions, *Bull. Am. Meteorol. Soc.*, *77*(2), 293-303, doi: 10.1175/1520-0477(1996)077<0293:ahpouc>2.0.co;2.

Hansen, J., M. Sato, and R. Ruedy (2012), Perception of climate change, *Proc. Nat. Acad. Sci. U.S.A.*, doi: 10.1073/pnas.1205276109.

Hansen, J., M. Sato, R. Ruedy, K. Lo, D. W. Lea, and M. Medina-Elizade (2006), Global temperature change, *Proc. Nat. Acad. Sci. U.S.A.*, *103*(39), 14288-14293.

Hansen, M. C., R. S. Defries, J. R. G. Townshend, and R. Sohlberg (2000), Global land cover classification at 1 km spatial resolution using a classification tree approach, *Int. J. Remote Sens.*, *21*(6), 1331-1364, doi: 10.1080/014311600210209.

Henderson-Sellers, A., K. McGuffie, and A. J. Pitman (1996), The Project for Intercomparison of Land-surface Parametrization Schemes (PILPS): 1992 to 1995, *Clim. Dyn.*, *12*(12), 849-859, doi: 10.1007/s003820050147.

Hessl, A. E., D. McKenzie, and R. Schellhaas (2004), Drought and Pacific Decadal Oscillation linked to fire occurrence in the inland Pacific Northwest, *Ecol. Appl.*, *14*(2), 425-442, doi: 10.1890/03-5019.

Higgins, R. W., Y. Yao, and X. L. Wang (1997), Influence of the North American Monsoon system on the U.S. summer precipitation regime, *J. Clim.*, *10*(10), 2600-2622, doi: 10.1175/1520-0442(1997)010<2600:IOTNAM>2.0.CO;2.

Hogue, T. S., L. Bastidas, H. Gupta, S. Sorooshian, K. Mitchell, and W. Emmerich (2005), Evaluation and transferability of the Noah land surface model in semiarid environments, *J. Hydrometeorol.*, *6*(1), 68-84.

International Boundary & Water Commission (1906), Convention between the United States and Mexico - Equitable Distribution of the Waters of the Rio Grande, edited, Washington D.C., U.S.A.

IPCC (2007), Climate Change 2007: Impacts, Adaptation and Vulnerability. Contribution of Working Group II to the Fourth Assessment Report of the Intergovernmental Panel on Climate Change *Rep.*, Cambridge, United Kingdom and New York, N.Y., U.S.A.

Jacquemin, B., and J. Noilhan (1990), Sensitivity study and validation of a land surface parameterization using the HAPEX-MOBILHY data set, *Bound.-Lay. Meteorol.*, *52*(1), 93-134, doi: 10.1007/bf00123180.

Joe, H. (1997), *Multivariate Models and Dependence Concepts*, Chapman & Hill, London, U.K.

Joyce, R. J., J. E. Janowiak, P. A. Arkin, and P. Xie (2004), CMORPH: A method that produces global precipitation estimates from passive microwave and infrared data at high spatial and temporal resolution, *J. Hydrometeorol.*, *5*(3), 487-503, doi: 10.1175/1525-7541(2004)005<0487:CAMTPG>2.0.CO;2.

Julian, P. R., and R. M. Chervin (1978), A study of the Southern Oscillation and Walker Circulation phenomenon, *Mon. Weather Rev.*, *106*(10), 1433-1451, doi: 10.1175/1520-0493(1978)106<1433:ASOTSO>2.0.CO;2.

Kahya, E., and J. A. Dracup (1993), U.S. streamflow patterns in relation to the El Niño/Southern Oscillation, *Water Resour. Res.*, *29*(8), 2491-2503, doi: 10.1029/93wr00744.

Kaplan, A., M. A. Cane, Y. Kushnir, A. C. Clement, M. B. Blumenthal, and B. Rajagopalan (1998), Analyses of global sea surface temperature 1856-1991, *J. Geophys. Res.*, *103*(C9), 18567-18589, doi: 10.1029/97jc01736.

Karl, T. R., and K. E. Trenberth (2003), Modern global climate change, *Science*, *302*(5651), 1719-1723, doi: 10.1126/science.1090228.

Karl, T. R., C.N. Williams, Jr., F. T. Quinlan, and T. A. Boden (1990), United States Historical Climatology Network (HCN) Serial Temperature and Precipitation Data *Rep.*, 389 pp, Environmental Science Division, Carbon Dioxide Information and Analysis Center, Oak Ridge National Laboratory, Oak Ridge, Tenn., U.S.A.

Khedun, C. P., H. Chowdhary, A. K. Mishra, J. R. Giardino, and V. P. Singh (2012a), Water deficit duration and severity analysis based on runoff derived from the Noah land surface model, *J. Hydrol. Eng.*, doi: 10.1061/(ASCE)HE.1943-5584.0000637, in press.

Khedun, C. P., A. K. Mishra, J. D. Bolten, H. K. Beaudoing, R. A. Kaiser, J. R. Giardino, and V. P. Singh (2012b), Understanding changes in water availability in the Rio Grande/Río Bravo del Norte basin under the influence of large-scale circulation indices using the Noah land surface model, *J. Geophys. Res.*, *117*(D5), D05104, doi: 10.1029/2011jd016590.

Kiladis, G. N., and H. F. Diaz (1986), An analysis of the 1877–78 ENSO episode and comparison with 1982–83, *Mon. Weather Rev.*, *114*(6), 1035-1047, doi: 10.1175/1520-0493(1986)114<1035:AAOTEE>2.0.CO;2.

Kiladis, G. N., and H. van Loon (1988), The Southern Oscillation. Part VII: Meteorological anomalies over the Indian and Pacific sectors associated with the extremes of the oscillation, *Mon. Weather Rev.*, *116*(1), 120-136, doi: 10.1175/1520-0493(1988)116<0120:tsopvm>2.0.co;2.

Kim, H.-M., Webster, Peter J., and J. A. Curry (2009), Impact of shifting patterns of Pacific Ocean warming on North Atlantic tropical cyclones, *Science*, *325*(5936), 77-80, doi: 10.1126/science.1174062.

Koren, V., J. Schaake, K. Mitchell, Q. Y. Duan, F. Chen, and J. M. Baker (1999), A parameterization of snowpack and frozen ground intended for NCEP weather and climate models, *J. Geophys. Res.*, *104*(D16), 19569-19585, doi: 10.1029/1999jd900232.

Kotz, S., N. Balakrishnan, and N. L. Johnson (2000), *Continuous Multivariate Distributions, Models and Applications*, John Wiley & Sons, N.Y., U.S.A.

Krishnan, R., and M. Sugi (2003), Pacific decadal oscillation and variability of the Indian summer monsoon rainfall, *Clim. Dyn.*, *21*(3), 233-242, doi: 10.1007/s00382-003-0330-8.

Kumar, A., and M. P. Hoerling (2003), The nature and causes for the delayed atmospheric response to El Niño, *J. Clim.*, *16*(9), 1391-1403, doi: 10.1175/1520-0442(2003)16<1391:TNACFT>2.0.CO;2.

Kumar, A., A. Leetmaa, and M. Ji (1994), Simulations of atmospheric variability induced by sea surface temperatures and implications for global warming, *Science*, *266*(5185), 632-634, doi: 10.1126/science.266.5185.632.

Kumar, P., and E. Foufoula-Georgiou (1997), Wavelet analysis for geophysical applications, *Rev. Geophys.*, *35*(4), 385-412, doi: 10.1029/97rg00427.

Kumar, S., C. Peters-Lidard, T. Yudong, R. Reichle, J. Geiger, C. Alonge, J. Eylander, and P. Houser (2008), An integrated hydrologic modeling and data assimilation framework, *Computer*, *41*(12), 52-59.

Kumar, S. V., C. D. Peters-Lidard, Y. Tian, P. R. Houser, J. Geiger, et al. (2006), Land Information System: An interoperable framework for high resolution land surface modeling, *Environ. Model. Software*, *21*(10), 1402-1415, doi: 10.1016/j.envsoft.2005.07.004.

Kunkel, K. E., and J. R. Angel (1999), Relationship of ENSO to snowfall and related cyclone activity in the contiguous United States, *J. Geophys. Res.*, *104*(D16), 19425-19434, doi: 10.1029/1999jd900010.

Kurtzman, D., and B. R. Scanlon (2007), El Niño-Southern Oscillation and Pacific Decadal Oscillation impacts on precipitation in the southern and central United States: Evaluation of spatial distribution and predictions, *Water Resour. Res.*, *43*(10), W10427, doi: 10.1029/2007wr005863.

Labat, D., R. Ababou, and A. Mangin (2001), Introduction of wavelet analyses to rainfall/runoffs relationship for a karstic basin: The case of Licq-Atherey karstic system (France), *Ground Water*, *39*(4), 605-615, doi: 10.1111/j.1745-6584.2001.tb02348.x.

Larkin, N. K., and D. E. Harrison (2005), On the definition of El Niño and associated seasonal average U.S. weather anomalies, *Geophys. Res. Lett.*, *32*(13), L13705, doi: 10.1029/2005gl022738.

Larkin, T. J., and G. W. Bomar (1983), Climatic Atlas of Texas *Rep.*, 157 pp, Texas Department of Water Resources, Austin, Tex., U.S.A.

Lau, K.-M., and H. Weng (1995), Climate signal detection using wavelet transform: How to make a time series sing, *Bull. Am. Meteorol. Soc.*, *76*(12), 2391-2402, doi: 10.1175/1520-0477(1995)076<2391:CSDUWT>2.0.CO;2.

Lee, T., and M. J. McPhaden (2010), Increasing intensity of El Niño in the central-equatorial Pacific, *Geophys. Res. Lett.*, *37*(14), L14603, doi: 10.1029/2010gl044007.

Legates, D. R., H. F. Lins, and G. J. McCabe (2005), Comments on "Evidence for global runoff increase related to climate warming" by Labat et al., *Adv. Water Resour.*, *28*(12), 1310-1315, doi: DOI: 10.1016/j.advwatres.2005.04.006.

Lohmann, D., K. E. Mitchell, P. R. Houser, E. F. Wood, J. C. Schaake, et al. (2004), Streamflow and water balance intercomparisons of four land surface models in the North American Land Data Assimilation System project, *J. Geophys. Res.*, *109*(D7), D07S91, doi: 10.1029/2003jd003517.

Luo, L., A. Robock, K. E. Mitchell, P. R. Houser, E. F. Wood, et al. (2003), Validation of the North American Land Data Assimilation System (NLDAS) retrospective forcing over the southern Great Plains, *J. Geophys. Res.*, *108*(D22), 8843, doi: 10.1029/2002jd003246.

Lyon, B. (2004), The strength of El Niño and the spatial extent of tropical drought, *Geophys. Res. Lett.*, *31*(21), L21204, doi: 10.1029/2004gl020901.

Macias Fauria, M., and E. A. Johnson (2006), Large-scale climatic patterns control large lightning fire occurrence in Canada and Alaska forest regions, *J. Geophys. Res.*, *111*(G4), G04008, doi: 10.1029/2006jg000181.

Macias Fauria, M., and E. A. Johnson (2008), Climate and wildfires in the North American boreal forest, *Phil. Trans. R. Soc. London, Ser. B*, *363*(1501), 2315-2327.

Mahfouf, J. F., and J. Noilhan (1991), Comparative study of various formulations of evaporations from bare soil using in situ data, *J. Appl. Meteorol.*, *30*(9), 1354-1365, doi: 10.1175/1520-0450(1991)030<1354:CSOVFO>2.0.CO;2.

Mahrt, L., and M. Ek (1984), The influence of atmospheric stability on potential evaporation, *J. Clim. Appl. Meteorol.*, *23*(2), 222-234, doi: 10.1175/1520-0450(1984)023<0222:TIOASO>2.0.CO;2.

Mahrt, L., and H. Pan (1984), A two-layer model of soil hydrology, *Bound.-Lay. Meteorol.*, *29*(1), 1-20, doi: 10.1007/bf00119116.

Maity, R., and D. Nagesh Kumar (2008), Probabilistic prediction of hydroclimatic variables with nonparametric quantification of uncertainty, *J. Geophys. Res.*, *113*(D14), D14105, doi: 10.1029/2008jd009856.

Malanson, G. P., D. G. Brown, D. R. Butler, D. M. Cairns, D. B. Fagre, and S. J. Walsh (2009), Ecotone dynamics: Invasibility of alpine tundra by tree species from the subalpine forest, in *The Changing Alpine Treeline: The Example of Glacier National Park, MT, USA*, edited by D. R. Butler, G. P. Malanson, S. J. Walsh and D. B. Fagre, Elsevier B.V., Amsterdam, The Netherlands.

Mantua, N., and S. Hare (2002), The Pacific Decadal Oscillation, *J. Oceanogr.*, *58*(1), 35-44, doi: 10.1023/a:1015820616384.

Mantua, N. J., S. R. Hare, Y. Zhang, J. M. Wallace, and R. C. Francis (1997), A Pacific interdecadal climate oscillation with impacts on salmon production, *Bull. Am. Meteorol. Soc.*, *78*(6), 1069-1079, doi: 10.1175/1520-0477(1997)078<1069:APICOW>2.0.CO;2.

McCabe, G. J., and M. D. Dettinger (1999), Decadal variations in the strength of ENSO teleconnections with precipitation in the western United States, *Int. J. Climatol.*, *19*(13), 1399-1410, doi: 10.1002/(sici)1097-0088(19991115)19:13<1399::aid-joc457>3.0.co;2-a.

McCabe, G. J., and M. D. Dettinger (2002), Primary modes and predictability of year-to-year snowpack variations in the western United States from teleconnections with Pacific Ocean climate, *J. Hydrometeorol.*, *3*(1), 13-25, doi: 10.1175/1525-7541(2002)003<0013:PMAPOY>2.0.CO;2.

McGill, R., J. W. Tukey, and W. A. Larsen (1978), Variations of box plots, *Am. Stat.*, *32*(1), 12-16.

McKee, T. B., N. J. Doesken, and J. Kleist (1993), The relationship of drought frequency and duration to time scales, in *Eighth Conference on Applied Climatology*, edited, Anaheim, Calif., U.S.A.

McRoberts, D. B., and J. W. Nielsen-Gammon (2011), A new homogenized climate division precipitation dataset for analysis of climate variability and climate change, *J. Appl. Meteorol.*, *50*(6), 1187-1199, doi: 10.1175/2010JAMC2626.1.

Mesinger, F., G. DiMego, E. Kalnay, K. Mitchell, P. C. Shafran, et al. (2006), North American Regional Reanalysis, *Bull. Am. Meteorol. Soc.*, *87*(3), 343-360, doi: doi:10.1175/BAMS-87-3-343.

Minobe, S. (1997), A 50-70 year climatic oscillation over the North Pacific and North America, *Geophys. Res. Lett.*, *24*(6), 683-686, doi: 10.1029/97gl00504.

Mishra, A. K., and V. P. Singh (2010), A review of drought concepts, *J. Hydrol.*, *391*(1-2), 202-216, doi: 10.1016/j.jhydrol.2010.07.012.

Mitchell, K. E. (2005), The Community Noah Land-surface Model. User's Guide, Public Release Version 2.7.1, edited, Accessed September 02, 2009. Available at ftp://ftp.emc.ncep.noaa.gov/mmb/gcp/ldas/noahlsm/ver_2.7.1.

Mitchell, K. E., D. Lohmann, P. R. Houser, E. F. Wood, J. C. Schaake, et al. (2004), The multi-institution North American Land Data Assimilation System (NLDAS): Utilizing multiple GCIP products and partners in a continental distributed hydrological modeling system, *J. Geophys. Res.*, *109*(D7), D07S90, doi: 10.1029/2003jd003823.

Mo, K. C., and R. W. Higgins (1998), Tropical influences on California precipitation, *J. Clim.*, *11*(3), 412-430, doi: 10.1175/1520-0442(1998)011<0412:TIOCP>2.0.CO;2.

Mo, K. C., M. Chelliah, M. L. Carrera, R. W. Higgins, and W. Ebisuzaki (2005), Atmospheric moisture transport over the United States and Mexico as evaluated in the NCEP regional reanalysis, *J. Hydrometeorol.*, *6*(5), 710-728, doi: 10.1175/jhm452.1.

Namais, J. (1966), Nature and possible causes of the northeastern United States drought during 1962–65, *Mon. Weather Rev.*, *94*(9), 543-554, doi: 10.1175/1520-0493(1966)094<0543:NAPCOT>2.3.CO;2.

Namais, J. (1967), Further studies of drought over the northeastern United States, *Mon. Weather Rev.*, *95*(8), 497-508, doi: 10.1175/1520-0493(1967)095<0497:FSODON>2.3.CO;2.

Neal, E. G., M. Todd Walter, and C. Coffeen (2002), Linking the pacific decadal oscillation to seasonal stream discharge patterns in southeast Alaska, *J. Hydrol.*, *263*(1-4), 188-197, doi: Doi: 10.1016/s0022-1694(02)00058-6.

Neelin, J. D. (2010), *Climate Change and Climate Modeling*, Cambridge University Press, Cambridge, GBR.

Nelsen, R. B. (2006), *An Introduction to Copulas*, Springer Verlag, New York, N.Y., U.S.A.

Newman, M., G. P. Compo, and M. A. Alexander (2003), ENSO-forced variability of the Pacific Decadal Oscillation, *J. Clim.*, *16*(23), 3853-3857, doi: 10.1175/1520-0442(2003)016<3853:EVOTPD>2.0.CO;2.

Nielsen-Gammon, J. W. (2009), The changing climate of Texas, in *The Impact of Global Warming on Texas*, edited by J. Schmandt, J. Clarkson and G. R. North, University of Texas Press, Austin, Tex., U.S.A.

Nielsen-Gammon, J. W. (2011), The 2011 Texas Drought. A Briefing Packet for the Texas Legislature *Rep.*, 43 pp, The Office of the State Climatologist, College of Geosciences, Texas A&M University, College Station, Tex., U.S.A.

NIST/SEMATECH (2012), e-Handbook of Statistical Methods, edited by C. Croarkin and P. Tobias, Available at http://www.itl.nist.gov/div898/handbook/.

Noilhan, J., and S. Planton (1989), A simple parameterization of land surface processes for meteorological models, *Mon. Weather Rev.*, *117*(3), 536-549, doi: 10.1175/1520-0493(1989)117<0536:ASPOLS>2.0.CO;2.

O'Brien, J. (2002), Definition(s) of La Niña, in *La Niña and its Impacts: Facts and Speculation*, edited by M. H. Glantz, United Nations University Press, Tokyo, Japan.

Özger, M., A. K. Mishra, and V. P. Singh (2009), Low frequency drought variability associated with climate indices, *J. Hydrol.*, *364*(1-2), 152-162, doi: 10.1016/j.jhydrol.2008.10.018.

Pan, H. L., and L. Mahrt (1987), Interaction between soil hydrology and boundary-layer development, *Bound.-Lay. Meteorol.*, *38*(1), 185-202, doi: 10.1007/bf00121563.

Pan, M., J. Sheffield, E. F. Wood, K. E. Mitchell, P. R. Houser, et al. (2003), Snow process modeling in the North American Land Data Assimilation System (NLDAS): 2. Evaluation of model simulated snow water equivalent, *J. Geophys. Res.*, *108*(D22), 8850, doi: 10.1029/2003jd003994.

Patiño-Gomez, C. (2005), GIS for Large-Scale Watershed Observational Data Model, Ph.D. thesis, 282 pp, University of Texas, Austin, Tex., U.S.A.

Patten, J. M., S. R. Smith, and J. J. O'Brien (2003), Impacts of ENSO on snowfall frequencies in the United States, *Wea. Forecasting*, *18*(5), 965-980, doi: 10.1175/1520-0434(2003)018<0965:IOEOSF>2.0.CO;2.

Peters-Lidard, C., P. Houser, Y. Tian, S. Kumar, J. Geiger, et al. (2007), High-performance Earth system modeling with NASA/GSFC's Land Information System, *Innovations in Systems and Software Engineering*, *3*(3), 157-165, doi: 10.1007/s11334-007-0028-x.

Piechota, T. C., and J. A. Dracup (1996), Drought and regional hydrologic variation in the United States: Associations with the El Niño-Southern Oscillation, *Water Resour. Res.*, *32*(5), 1359-1373, doi: 10.1029/96wr00353.

Pielke, R. A., and C. N. Landsea (1999), La Niña, El Niño and Atlantic hurricane damages in the United States, *Bull. Am. Meteorol. Soc.*, *80*(10), 2027-2033, doi: 10.1175/1520-0477(1999)080<2027:lnaeno>2.0.co;2.

Pinker, R. T., J. D. Tarpley, I. Laszlo, K. E. Mitchell, P. R. Houser, et al. (2003), Surface radiation budgets in support of the GEWEX Continental-Scale International Project (GCIP) and the GEWEX Americas Prediction Project (GAPP), including the North American Land Data Assimilation System (NLDAS) project, *J. Geophys. Res.*, *108*(D22), 8844, doi: 10.1029/2002jd003301.

Quiring, S., and G. Goodrich (2008), Nature and causes of the 2002 to 2004 drought in the southwestern United States compared with the historic 1953 to 1957 drought, *Climate Res.*, *36*(1), 41-52, doi: 10.3354/cr00735.

Rasmusson, E. M., and T. H. Carpenter (1982), Variations in tropical sea surface temperature and surface wind fields associated with the Southern Oscillation/El Niño, *Mon. Weather Rev.*, *110*(5), 354-384, doi: 10.1175/1520-0493(1982)110<0354:VITSST>2.0.CO;2.

Redmond, K. T., and R. W. Koch (1991), Surface climate and streamflow variability in the western United States and their relationship to large-scale circulation indices, *Water Resour. Res.*, *27*(9), 2381-2399, doi: 10.1029/91wr00690.

Revenga, C., J. Nackoney, E. Hoshino, Y. Kura, and J. Maidens (2003), *Watersheds of the World*, World Resources Institute, Washington D.C., U.S.A.

Rivera, N., S. Ray, J. Jensen, A. Chan, and W. Ayers (2004), Detection of cyclic patterns using wavelets: An example study in the Ormskirk Sandstone, Irish Sea, *Math. Geol.*, *36*(5), 529-543, doi: 10.1023/b:matg.0000037735.34280.42.

Robock, A., L. Luo, E. F. Wood, F. Wen, K. E. Mitchell, et al. (2003), Evaluation of the North American Land Data Assimilation System over the southern Great Plains during the warm season, *J. Geophys. Res.*, *108*(D22), 8846, doi: 10.1029/2002jd003245.

Rodell, M., P. R. Houser, U. Jambor, J. Gottschalck, K. Mitchell, et al. (2004), The Global Land Data Assimilation System, *Bull. Am. Meteorol. Soc.*, *85*(3), 381-394, doi: doi:10.1175/BAMS-85-3-381.

Ropelewski, C. F., and M. S. Halpert (1986), North American precipitation and temperature patterns associated with the El Niño/Southern Oscillation (ENSO), *Mon. Weather Rev.*, *114*(12), 2352-2362, doi: 10.1175/1520-0493(1986)114<2352:NAPATP>2.0.CO;2.

Ropelewski, C. F., and P. D. Jones (1987), An extension of the Tahiti–Darwin Southern Oscillation Index, *Mon. Weather Rev.*, *115*(9), 2161-2165, doi: 10.1175/1520-0493(1987)115<2161:aeotts>2.0.co;2.

Sahoo, A. K., P. A. Dirmeyer, P. R. Houser, and M. Kafatos (2008), A study of land surface processes using land surface models over the Little River Experimental Watershed, Georgia, *J. Geophys. Res.*, *113*(D20), D20121, doi: 10.1029/2007jd009671.

Salvadori, G., C. D. Michele, N. T. Kottegoda, and R. Rosso (2007), *Extremes in Nature: An Approach Using Copulas*, Springer Verlag, Dordrecht, The Netherlands.

Sandoval-Solis, S., D. C. McKinney, R. L. Teasley, and J. Schuldes (2010), Memo: Comparison of Annual Naturalized Flows for the Rio Grande/Rio Bravo Basin *Rep.*, 54 pp, TCEQ-CONAGUA, Center for Research in Water Resources, Bureau of Engineering Research, The University of Texas at Austin, Austin, Tex., U.S.A.

SAS/ETS (2011), User's Guide, edited, SAS® Publishing, Cary, N.C., U.S.A., Available at http://support.sas.com/documentation/.

Schaake, J. C., V. I. Koren, Q.-Y. Duan, K. Mitchell, and F. Chen (1996), Simple water balance model for estimating runoff at different spatial and temporal scales, *J. Geophys. Res.*, *101*(D3), 7461-7475, doi: 10.1029/95jd02892.

Schaake, J. C., Q. Duan, V. Koren, K. E. Mitchell, P. R. Houser, et al. (2004), An intercomparison of soil moisture fields in the North American Land Data Assimilation System (NLDAS), *J. Geophys. Res.*, *109*(D1), D01S90, doi: 10.1029/2002jd003309.

Schepsmeier, U., and E. C. Brechmann (2012), Statistical inference of C- and D-vine copulas, edited, Available at http://cran.r-project.org/web/packages/CDVine/index.html.

Schoennagel, T., T. T. Veblen, W. H. Romme, J. S. Sibold, and E. R. Cook (2005), ENSO and PDO variability affect drought-induced fire occurrence in Rocky Mountain subalpine forests, *Ecol. Appl.*, *15*(6), 2000-2014, doi: 10.1890/04-1579.

Schonher, T., and S. E. Nicholson (1989), The relationship between California rainfall and ENSO events, *J. Clim.*, *2*(11), 1258-1269, doi: 10.1175/1520-0442(1989)002<1258:TRBCRA>2.0.CO;2.

Schubert, S. D., M. J. Suarez, P. J. Pegion, R. D. Koster, and J. T. Bacmeister (2004), On the cause of the 1930s Dust Bowl, *Science*, *303*(5665), 1855-1859, doi: 10.1126/science.1095048.

Selkowitz, D. J., D. B. Fagre, and B. A. Reardon (2002), Interannual variations in snowpack in the Crown of the Continent Ecosystem, *Hydrol. Processes*, *16*(18), 3651-3665, doi: 10.1002/hyp.1234.

Sellers, P. (1991), Modeling and observing land-surface-atmosphere interactions on large scales, in *Land Surface-Atmosphere Interactions for Climate Modeling - Observations, Models and Analysis*, edited by E. F. Wood, pp. 85-114, Kluwer Academic Publishers, The Netherlands.

Sheffield, J., M. Pan, E. F. Wood, K. E. Mitchell, P. R. Houser, et al. (2003), Snow process modeling in the North American Land Data Assimilation System (NLDAS): 1. Evaluation of model-simulated snow cover extent, *J. Geophys. Res.*, *108*(D22), 8849, doi: 10.1029/2002jd003274.

Shiau, J.-T., and H. W. Shen (2001), Recurrence analysis of hydrologic droughts of differing severity, *J. Water Resour. Plann. Manage.*, *127*(1).

Shiau, J. (2006), Fitting drought duration and severity with two-dimensional copulas, *Water Resour. Manage.*, *20*(5), 795-815, doi: 10.1007/s11269-005-9008-9.

Shiau, J. T. (2003), Return period of bivariate distributed extreme hydrological events, *Stoch. Environ. Res. Risk Assess.*, *17*(1), 42-57, doi: 10.1007/s00477-003-0125-9.

Shiau, J. T., and R. Modarres (2009), Copula-based drought severity-duration-frequency analysis in Iran, *Meteorol. Appl.*, *16*(4), 481-489, doi: 10.1002/met.145.

Shukla, S., and A. W. Wood (2008), Use of a standardized runoff index for characterizing hydrologic drought, *Geophys. Res. Lett.*, *35*(2), L02405, doi: 10.1029/2007gl032487.

Sklar, A. (1959), Fonctions de repartition à n dimensions et leurs marges, *Publications de l'Institut de Statistique de l'Université de Paris*, *8*, 229-231.

Smith, S. R., and J. J. O'Brien (2001), Regional snowfall distributions associated with ENSO: Implications for seasonal forecasting, *Bull. Am. Meteorol. Soc.*, *82*(6), 1179-1191, doi: 10.1175/1520-0477(2001)082<1179:RSDAWE>2.3.CO;2.

Stone, J. R., and S. C. Fritz (2006), Multidecadal drought and Holocene climate instability in the Rocky Mountains, *Geology*, *34*(5), 409-412, doi: 10.1130/g22225.1.

Texas Water Development Board (2012), Water for Texas. 2012 State Water Plan *Rep.*, Austin, Tex., U.S.A.

Torrence, C., and G. P. Compo (1998), A practical guide to wavelet analysis, *Bull. Am. Meteorol. Soc.*, *79*(1), 61-78, doi: 10.1175/1520-0477(1998)079<0061:APGTWA>2.0.CO;2.

Trenberth, K. E. (1984), Signal versus noise in the Southern Oscillation, *Mon. Weather Rev.*, *112*(2), 326-332, doi: 10.1175/1520-0493(1984)112<0326:svnits>2.0.co;2.

Trenberth, K. E. (1990), Recent observed interdecadal climate changes in the Northern Hemisphere, *Bull. Am. Meteorol. Soc.*, *71*(7), 988-993, doi: 10.1175/1520-0477(1990)071<0988:ROICCI>2.0.CO;2.

Trenberth, K. E. (1997), The definition of El Niño, *Bull. Am. Meteorol. Soc.*, *78*(12), 2771-2777, doi: 10.1175/1520-0477(1997)078<2771:TDOENO>2.0.CO;2.

Trenberth, K. E., and T. J. Hoar (1996), The 1990-1995 El Niño-Southern Oscillation event: Longest on record, *Geophys. Res. Lett.*, *23*(1), 57-60, doi: 10.1029/95gl03602.

US Army Corps of Engineers (2008), Forgotten Reach of the Rio Grande, Fort Quitman to Presidio, Texas *Rep.*, 169 pp, US Army Corps of Engineers, Albuquerque, N.Mex., U.S.A.

Verdon, D. C., A. M. Wyatt, A. S. Kiem, and S. W. Franks (2004), Multidecadal variability of rainfall and streamflow: Eastern Australia, *Water Resour. Res.*, *40*(10), W10201, doi: 10.1029/2004wr003234.

von Storch, H., and F. W. Zwiers (2003), *Statistical Analysis in Climate Research*, Cambridge Univ Press, Cambridge, U.K.

Weng, H., K. Ashok, S. Behera, S. Rao, and T. Yamagata (2007), Impacts of recent El Niño Modoki on dry/wet conditions in the Pacific rim during boreal summer, *Clim. Dyn.*, *29*(2), 113-129, doi: 10.1007/s00382-007-0234-0.

Wolf, A. T. (2002), *Atlas of International Freshwater Agreements*, United Nations Environment Programme, Nairobi, Kenya.

Wolter, K., and M. S. Timlin (1993), Monitoring ENSO in COADS with a seasonally adjusted principal component index, in *17th Climate Diagnostics Workshop*, edited, pp. 52-57, NOAA/NMC/CAC, NSSL, Oklahoma Clim. Survey, CIMMS and the School of Meteor., Univ. of Oklahoma, Norman, Okla., U.S.A.

Wolter, K., and M. S. Timlin (1998), Measuring the strength of ENSO events - how does 1997/98 rank?, *Weather*, *53*, 315-324.

Woolhiser, D. A., T. O. Keefer, and K. T. Redmond (1993), Southern oscillation effects on daily precipitation in the southwestern United States, *Water Resour. Res.*, *29*(4), 1287-1295, doi: 10.1029/92wr02536.

Wurbs, R. A. (2006), Methods for developing naturalized monthly flows at gaged and ungaged sites, *J. Hydrol. Eng.*, *11*(1), 55-64, doi: 10.1061/(asce)1084-0699(2006)11:1(55).

Yeh, S.-W., J.-S. Kug, B. Dewitte, M.-H. Kwon, B. P. Kirtman, and F.-F. Jin (2009), El Niño in a changing climate, *Nature*, *461*(7263), 511-514, doi: 10.1038/nature08316.

Yue, S., T. B. M. J. Ouarda, and B. Bobée (2001), A review of bivariate gamma distributions for hydrological application, *J. Hydrol.*, *246*(1–4), 1-18, doi: 10.1016/s0022-1694(01)00374-2.

Zhang, Y., J. M. Wallace, and D. S. Battisti (1997), ENSO-like interdecadal variability: 1900–93, *J. Clim.*, *10*(5), 1004-1020, doi: 10.1175/1520-0442(1997)010<1004:ELIV>2.0.CO;2.

Zobler, L. (1986), A World Soil File for Global Climate Modelling *Rep.*, 35 pp, NASA Goddard Institute for Space Studies, New York, N.Y., U.S.A.